

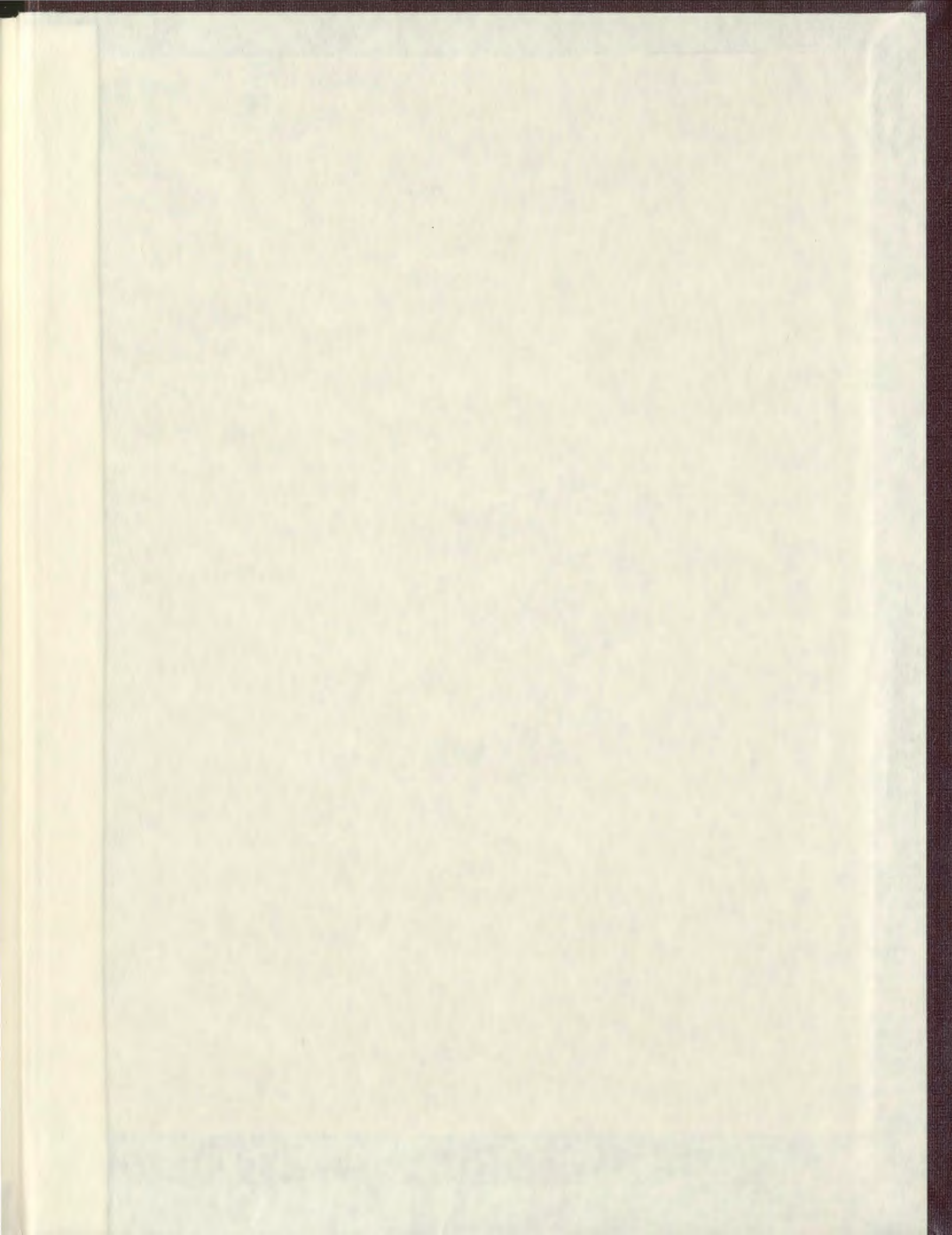
NEOGENE TECTONIC AND SEDIMENTARY EVOLUTION
OF THE OUTER CILICIA BASIN,
EASTERN MEDITERRANEAN SEA

CENTRE FOR NEWFOUNDLAND STUDIES

**TOTAL OF 10 PAGES ONLY
MAY BE XEROXED**

(Without Author's Permission)

STACEY L. MANSFIELD



Neogene Tectonic and Sedimentary Evolution of the Outer Cilicia Basin, Eastern Mediterranean Sea

by

Stacey L. Mansfield

A thesis submitted to
the School of Graduate Studies
in partial fulfillment of the
requirements for the degree of
Masters of Science

Earth Science/ Memorial University of Newfoundland/ Science

Memorial University of Newfoundland and Labrador

November 2005

St. Johns

Newfoundland





Library and
Archives Canada

Bibliothèque et
Archives Canada

Published Heritage
Branch

Direction du
Patrimoine de l'édition

978-0-494-19380-8

395 Wellington Street
Ottawa ON K1A 0N4
Canada

395, rue Wellington
Ottawa ON K1A 0N4
Canada

Your file *Votre référence*

ISBN:

Our file *Notre référence*

ISBN:

NOTICE:

The author has granted a non-exclusive license allowing Library and Archives Canada to reproduce, publish, archive, preserve, conserve, communicate to the public by telecommunication or on the Internet, loan, distribute and sell theses worldwide, for commercial or non-commercial purposes, in microform, paper, electronic and/or any other formats.

The author retains copyright ownership and moral rights in this thesis. Neither the thesis nor substantial extracts from it may be printed or otherwise reproduced without the author's permission.

AVIS:

L'auteur a accordé une licence non exclusive permettant à la Bibliothèque et Archives Canada de reproduire, publier, archiver, sauvegarder, conserver, transmettre au public par télécommunication ou par l'Internet, prêter, distribuer et vendre des thèses partout dans le monde, à des fins commerciales ou autres, sur support microforme, papier, électronique et/ou autres formats.

L'auteur conserve la propriété du droit d'auteur et des droits moraux qui protègent cette thèse. Ni la thèse ni des extraits substantiels de celle-ci ne doivent être imprimés ou autrement reproduits sans son autorisation.

In compliance with the Canadian Privacy Act some supporting forms may have been removed from this thesis.

Conformément à la loi canadienne sur la protection de la vie privée, quelques formulaires secondaires ont été enlevés de cette thèse.

While these forms may be included in the document page count, their removal does not represent any loss of content from the thesis.

Bien que ces formulaires aient inclus dans la pagination, il n'y aura aucun contenu manquant.


Canada

Abstract

The Neogene structural and sedimentary evolution of the Outer Cilicia Basin is investigated using marine multi-channel seismic data collected during a 1992 survey. The Cilicia Basin is a relatively shallow Neogene basin, which is located on the Aegean-Anatolian microplate in the fore-arc region of the Cyprean Arc. The basin's evolution is recorded in four main stratigraphic units each separated by laterally extensive erosional unconformities. These units from youngest to oldest are: *Unit 1* - Pliocene-Quaternary aged siliclastics, *Unit 2* - Messinian aged evaporites, *Unit 3A* - mid- to late-Miocene aged marls and chalks, and *Unit 3B* - Oligocene to mid-Miocene aged marls and turbidite deposits. The deformation of these sequences, throughout the basin's history, gives rise to both compressional and extensional structures, largely affected by the ductile salt layer

The structural evolution of the Outer Cilicia Basin can be separated into two main phases. The first is a compressional phase which began in Miocene time in association with convergence along the Cyprean Arc. During this phase, a south-verging thrust belt developed directly south of the Outer Cilicia Basin. Since the mid-late Miocene, the basin has evolved on the back limb of the thrust system. A second evolutionary phase began in Pliocene time, coinciding with the initiation of westward escape and rotation of the Aegean-Anatolian microplate. The Pliocene-Quaternary succession is primarily affected by two main types of structures: 1) Transtensional faults, which provide accommodation for strain induced in the basin by the westward escape of the microplate,

and 2) Salt tectonic structures, which develop in association with the basin-ward flow of salt, driven by gravitational forces and sedimentary loading.

Acknowledgments

I extend sincere appreciation to my supervisors Dr. Jeremy Hall and Dr. Ali Aksu for giving me the opportunity to work in such an exciting area. This research would not have been possible without their ongoing support and guidance. I would also like to thank them for inviting me to be a part of the 2001 research cruise on the K. Piri Reis research vessel. It is an experience that will never be forgotten.

I would like to thank Dr. Sharon Deemer, for her much-needed help during the data processing stage of my thesis, and Tony Kocurko, for his invaluable technical support. I also wish to acknowledge Paul Barnes who was responsible for the processing of some seismic data from this area, collected during the 1991 and 1992 research cruises. Thank-you, as well, to the captain and crew of the K. Piri Reis research vessel during the 1992 survey.

For financial support, I would like to thank Dr. Jeremy Hall and Dr. Ali Aksu (funded through NSERC grants), the School of Graduate Studies, Canada-Newfoundland Offshore Development Fund, ASARCO Incorporated and the Provincial Government of Newfoundland and Labrador. This thesis also benefitted from seismic processing software donated to the Department of Earth Sciences by Landmark Graphics.

I would like to express thanks to my fellow graduate students, for their support and for making grad school fun and memorable. To my friends and family, thank-you for always being there for me. And finally to my parents, your unconditional love and support makes everything in my life possible.

Table of Contents

Title Page	i
Abstract	ii
Acknowledgments	iv
Table of Contents	v
List of Figures	viii
List of Appendix	xi
Chapter 1	1
1.1 Introduction and Outline of the Problem	1
1.2 Plate Tectonic Setting	3
1.3 Tectonic Evolution of the North-Eastern Mediterranean	4
1.4 Plate Boundaries in the Eastern Mediterranean	12
1.4.1 Interaction of the Aegean-Anatolian and African plates	12
1.4.1.1 The Hellenic Arc	13
1.4.1.2 The Cyprean Arc	16
1.4.2. Interaction of the Aegean-Anatolian and Arabian plate	23
1.4.2.1 Eastern Anatolian Convergent Zone (EACZ)	24
1.4.2.2. Eastern Anatolian Transform Fault (EATF)	25
1.4.3. Interaction between the African and the Arabian plates	26
1.4.4. Interaction of the Aegean-Anatolian and Eurasian plates	30
1.5 Relative Plate Motions in the Eastern Mediterranean	31
1.6 Purpose and Scope	33
Chapter 2	35
2.1 Regional setting	35
2.2 The basins of the northeastern Mediterranean Sea	38
2.2.1 The Iskenderun Basin	39
2.2.2 Latakia Basin	39
2.2.3 The Adana and Cilicia Basin	41
2.3 Structural Elements of the northeast Mediterranean Sea	47
2.3.1 Misis-Kyrenia Thrust Belt	48
2.3.2 Kyrenia Range	49
2.3.3 Misis Mountain Complex	50

2.3.4. The Taurus mountain range and Ecemis Fault zone	52
2.3.5. Anamur-Kormakiti Complex	54
2.3.6. Amanos Fault Zone	55
2.3.7. Amanos-Larnaka Ridge	55
2.4 Models for the formation of the Cilicia basin	56
Chapter 3	59
3.1 Data Acquisition	59
3.2 Data Processing	62
3.2.1 Data Processing scheme	62
3.2.2 Definition of Trace Headers	65
3.2.3 Trace Editing	65
3.2.4 Static Corrections	67
3.2.5 Band-Pass Filtering	67
3.2.6 F-K Filtering and Muting	71
3.2.7 Predictive Deconvolution	75
3.2.8 Multiple Attenuation	85
3.2.8 (2) Wave equation multiple rejection	91
3.2.9 Velocity Analysis and Stacking	100
3.2.10 Migration	110
3.2.11 Time Variant Filtering	123
3.2.12 Trace Mixing and Decimation for Plotting	123
3.3 Summary of Data Processing	125
Chapter 4	127
4.1 General Description of Outer Cilicia Basin	131
4.1.1. Bathymetry	131
4.1.2 Morphology of the Outer Cilicia Basin	133
4.2 Description of seismic sequences and stratigraphy	137
4.2.1. Unit 1	139
4.2.1.1 Unit 1: Sequence A	146
4.2.1.2 Unit 1: Sequence B	147
4.2.1.3 Unit 1: Sequence C	149
4.2.1.4 Unit 1: Sequence D	152
4.2.2 Unit 2	153
4.2.3 Unit 3A	158
4.2.4 Unit 3B	160
4.3 Description of faults and structural elements for each zone	163
4.3.1 Structural systems found on the Turkish Shelf	170
4.3.2 Structural systems found in the Northern Basin	173
4.3.3 Structural systems found in the central fold zone	177

4.3.4 Structural systems found in the Southern Basin	181
4.3.5 Structural systems found on the Cyprean Shelf	185
4.3.6 Structural systems in the Anamur-Kormakiti zone	186
Chapter 5:	195
5.1 Pre- to early-Neogene evolution of the Cilicia Basin	197
5.2 The major structural systems of the Outer Cilicia Basin	198
5.2.1 Structural systems formed due to far-field forces	202
5.2.1.1 Normal faults at basin margins	202
5.2.1.2 East-west oriented transtensional faults	208
5.2.1.3 North to northeast trending extensional/ transtensional faults	210
5.2.1.4 South-southwest verging compressional faults	214
5.2.2 Structural systems related to salt tectonics	215
5.2.2.1 Thin-skinned listric normal faults	217
5.2.2.2 Salt-cored anticlines and folds	218
5.2.2.3 Northward verging thrust fault systems	219
5.3 Neogene Evolution of the Outer Cilicia Basin	223
Chapter 6:	234
6.1 Conclusions	234
6.2 Recommendations	236
References	238

List of Figures

Chapter 1

Figure 1.1 - Simplified tectonic map of the eastern Mediterranean	2
Figure 1.2 - Paleotectonic map during the Jurassic period.	6
Figure 1.3.- Paleotectonic map during the early Cretaceous period	7
Figure 1.4 - Paleotectonic map during the late-Cretaceous to Paleocene period	9
Figure 1.5 - Paleotectonic map during the middle Miocene-Pliocene period.	11
Figure 1.6 - Map showing boundaries and plate motions in the Cyprus area.	21
Figure 1.7 - Ridges related at boundary of African and Aegean-Anatolian plates	22
Figure 1.8 - Faults and structural features onshore Turkey.	27
Figure 1.9 - Simplified tectonic map showing Sinai Microplate.	29

Chapter 2

Figure 2.1 - Bathymetry map of Cilicia and Latakia basins.	36
Figure 2.2 - Basins and structures of the north-east Mediterranean.	37
Figure 2.3 - Main structural and physiographic features of the Cilicia Basin.	42
Figure 2.4 - Inner Cilicia basin and the major surrounding fault systems.	43
Figure 2.5 - Simplified geological and tectonic map of Cyprus.	51

Chapter 3

Figure 3.1 - Seismic lines from the Outer Cilicia Basin	60
Figure 3.2 - Seismic acquisition parameters for line 67 and line 23.	61
Figure 3.3 - Seismic acquisition parameters for lines 423, 489, 501 and 517.	62
Figure 3.4 - Schematic Processing Flow.	63
Figure 3.5 - Trace kill command.	66
Figure 3.6 - Trace kill command.	68
Figure 3.7 - Static time corrections.	69
Figure 3.8 - Data before band-pass filtering.	70
Figure 3.9 - Band-pass filtered data.	72
Figure 3.10 - Spatial Aliasing effect	73
Figure 3.11 - Top mute applied.	74
Figure 3.12 - F-K filtering.	76
Figure 3.13 - Non-deconvolved data	78
Figure 3.14 - Non-deconvolved autocorrelation function and frequency spectrum	79
Figure 3.15 - Autocorrelation function and frequency spectrum after spiking deconvolution.	80

Figure 3.16 - Various prediction lags and time gates attempted for predictive deconvolution.	82
Figure 3.17 - Autocorrelation function and frequency spectrum of predictive deconvolution results.	83
Figure 3.18 - Autocorrelation function and frequency spectrum of predictive deconvolution results.	84
Figure 3.19 - Predictive Deconvolution result	86
Figure 3.20 - Seismic data showing multiple energy	87
Figure 3.21 - Seismic data showing multiple energy.	88
Figure 3.22 - Predictive deconvolution for the removal of short period multiples ...	90
Figure 3.23 - Near Trace gather	92
Figure 3.24 - Near trace gather after the wave equation multiple rejection.	93
Figure 3.25 - Extracted wavelets of primary and multiple energy.	95
Figure 3.26 - Frequency spectrums of primary and multiple energy	96
Figure 3.27 - Wavelet extracted from Butterworth filtered data.	98
Figure 3.28 - Near trace gather after Butterworth filter and wave equation multiple rejection applied.	99
Figure 3.29 - Stacked seismic data.	101
Figure 3.30 - Velocity analysis	103
Figure 3.31 - Velocity analysis.	105
Figure 3.32 - Velocity analysis	106
Figure 3.33 - Stacked section showing stacking velocities	107
Figure 3.34 - Stacked section showing stacking velocities.	108
Figure 3.35 - Stacked section showing stacking velocities	109
Figure 3.36 - Comparison of near trace gather and stacked section	111
Figure 3.37 - Stacked section	113
Figure 3.38 - 1500 m/s constant velocity migrated stack	114
Figure 3.39 - Constant velocity migrated stack showing the RMS velocities	116
Figure 3.40 - Migrated stack using RMS velocities	117
Figure 3.41 - Stacked section	118
Figure 3.42 - 1500 m/s constant velocity migrated stack.	119
Figure 3.43 - Constant velocity migrated stack showing the RMS velocities	120
Figure 3.44 - Migrated stack using RMS velocities	121
Figure 3.45 - Migrated stack showing time-variant filter time gates	122
Figure 3.46 - Migrated stack after time variant band pass filter applied.	124

Chapter 4

Figure 4.1 - All available seismic data from the Outer Cilicia Basin	128
Figure 4.2 - Seismic data with fix numbers	129
Figure 4.3 - Bathymetry map of the Outer Cilicia Basin.	132

Figure 4.4 - Seismic profile showing five morphological zones.	134
Figure 4.5 - Time structure of M-reflector in the Outer Cilicia Basin	135
Figure 4.6 - Seismic reflection configurations and termination patterns	138
Figure 4.7 - Exploration wells	140
Figure 4.8 - Seismic showing sequences and sequence boundaries	141
Figure 4.9 - Well data from Inner Cilicia Basin	142
Figure 4.10 - Isochron map of Unit 1.	144
Figure 4.11 - Prograding clinoforms	151
Figure 4.12 - Isochron map of Unit 2	155
Figure 4.13 - Isochron map of Unit 3A.	159
Figure 4.14 - Erosional truncation across the N-reflector	161
Figure 4.15 - Fault map of the Outer Cilicia basin	164
Figure 4.16 - Colour-coded fault map of the Outer Cilicia Basin	165
Figure 4.17 - Geometry of a simplified listric growth fault	166
Figure 4.18 - Schematic of a fault bend fold	168
Figure 4.19 - Schematic of a idealized strike-slip fault	169
Figure 4.20 - Extensional fault on the Turkish shelf	171
Figure 4.21 - M-reflector displaced vertical strike slip faults	182
Figure 4.22 - Inter-sequence detachment surfaces	188
Figure 4.23 - Bathymetry of the Anamur-Kormakiti region	190

Chapter 5

Figure 5.1 - Tectono-stratigraphic chart of Outer Cilicia Basin	196
Figure 5.2 - Piggy back basin	199
Figure 5.3 - Normal faults at basin margins	200
Figure 5.4 - East-west oriented transtensional faults	201
Figure 5.5 - Messinian aged north verging thrust faults.	203
Figure 5.6 - Central fold zone.	204
Figure 5.7 - Listric growth faults	205
Figure 5.8 - South verging thrusts in the Anamur-Kormakiti complex.	206
Figure 5.9 - North to north-east trending transtensional faults.	207
Figure 5.10 - Tectonic map showing possible extension of the transform fault at the west boundary of Sinai Microplate into the Aegean-Anatolian plate..	211
Figure 5.11 - Tectonic map showing how extension arises in the Outer Cilicia Basin through the counterclockwise rotation.	212
Figure 5.12 - The development of Messinian salt layer during late Miocene time ...	224
Figure 5.13 - Tectono-stratigraphic chart of western Outer Cilicia Basin	225
Figure 5.14 - Paleotectonic map during mid-Miocene time	227
Figure 5.15 - Paleotectonic map from Pliocene to present time.	230

List of Appendix

Appendix 1 - In envelope at back of thesis

A1 - Figure 1 - Line 4948, fix #'s 6-123

A1 - Figure 2 - Line 67, fix #'s 198-291

A1 - Figure 3 - Line 534, fix #'s 1459-1513

A1 - Figure 4 - Line 517, fix #'s 1456-1406

A1 - Figure 5 - Line 501, fix #'s 1352-1405

A1 - Figure 6 - Line 489, fix #'s 1346-1304

A1 - Figure 7 - Line 467, fix #'s 1248-1295

A1 - Figure 8 - Line 423, fix #'s 1246-1189

A1 - Figure 9 - Line 412, fix #'s 1140-1194

A1 - Figure 10 - Line 401, fix #'s 1129-1064

A1 - Figure 11 - Line 389, fix #'s 1000 -1049

A1 - Figure 12 - Line 534, fix #'s 1535-1514

A1 - Figure 13 - Line 534, fix #'s 1560-1535

A1 - Figure 14 - Line 567, fix #'s 1569-1604

A1 - Figure 15 - Line 23, fix #'s 121-154

A1 - Figure 16 - Line 23, fix #'s 183-156

A1 - Figure 17 - Line 23, fix #'s 184-196

Chapter 1

1.1 Introduction and Outline of the Problem

The Cilicia Basin lies directly between Cyprus and Turkey in the Eastern Mediterranean Sea (see Figure 1.1). It has formed since the mid to late Miocene in a fore arc region associated with the subduction of the African plate beneath the Anatolian plate along the Cyprus arc (Biju-Duval et al., 1978). This plate boundary is in the process of changing from subduction to collision as continental fragments, such as Eratosthenes seamount, arrive at the subduction zone (Ben-Avraham et al., 1988,1995). The situation is further complicated by a 45-degree clockwise rotation in the convergence vector since the early Miocene (Le Pichon and Angelier, 1979; Rotstein, 1984). Studying this area should give insight into the changing evolution of fore arc basins during both the transition from subduction to collision and the rotation of the convergence vector. In the Cilicia basin, this transition will be examined through changes in the sedimentation and deformation patterns in Neogene sediment. The interpretable sedimentary packages that are affected by this transition are the late Miocene evaporite dominated layer and the succeeding Pliocene to Quaternary clastics, which were deposited in the basin from the adjacent continental margins. The deposition and deformation of these two sedimentary packages gives rise to remarkable internal structure involving both contractional and extensional tectonics that are largely affected by the ductile salt layer (Evans et al., 1978; Aksu et al., 1992 a). Determining the relationship between these compressional and extensional structures and their relation to the sedimentary history of the basin will be

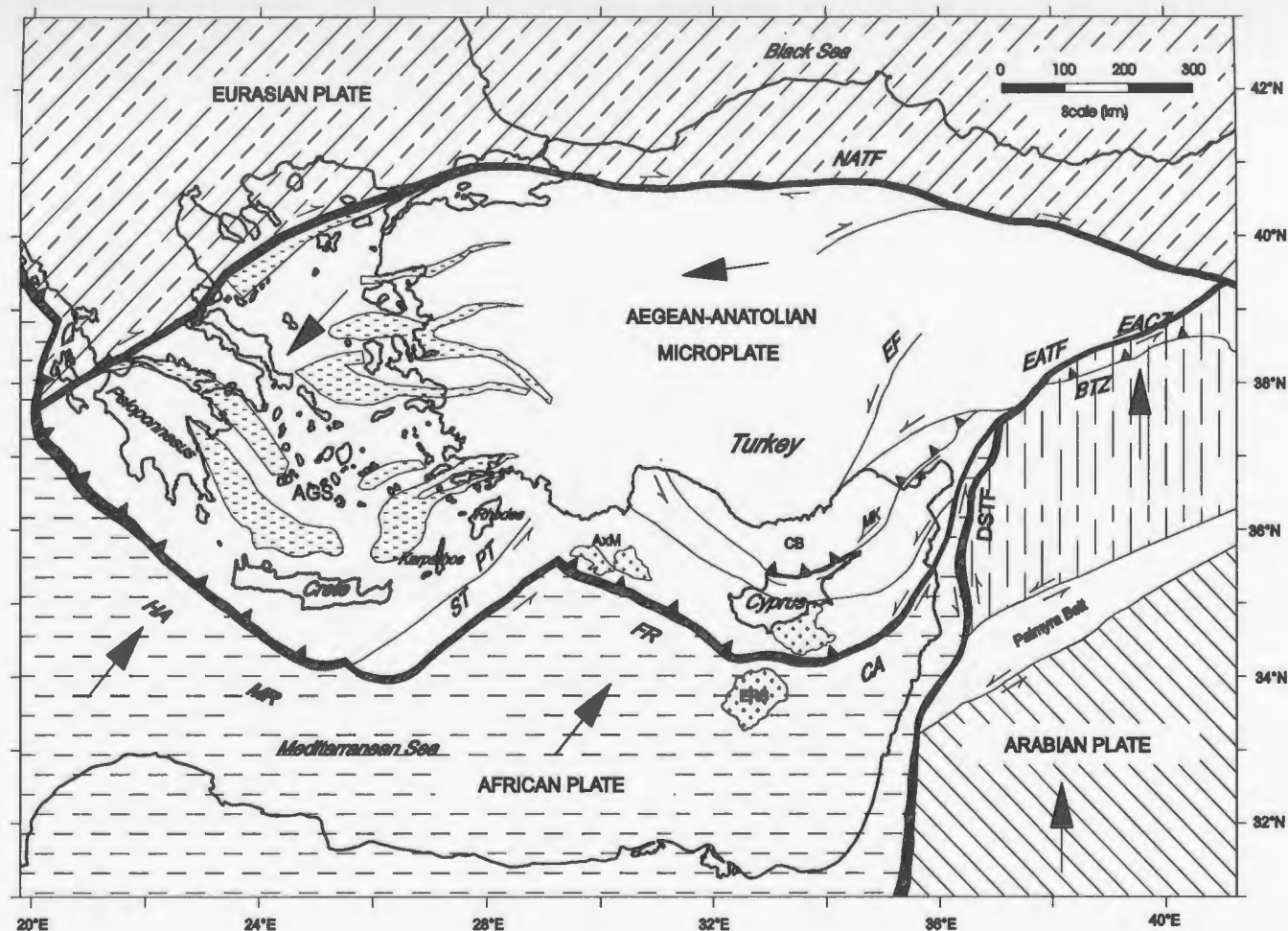


Figure 1.1: Simplified tectonic map of the eastern Mediterranean (edited from Aksu et al, work in progress). Map compiled from Sengör and Yilmaz (1981), Hancock and Barka (1981) and Dewey et al. (1986). AGS = Aegean Graben System, AxM = Anaximander mountains, BTZ = Bitlis thrust zone, CA = Cyprus Arc, CB = Cilicia Basin, DSTF = Dead Sea transform fault, EATF = East Anatolian Transform Fault, EACZ= East Anatolian Convergent Zone EF = Ecemis Fault, ERS = Eratosthenes seamount, FR= Florence rise, HA = Hellenic Arc, MK = Misis-Kyrenia fault, MR = Mediterranean Ridge, PT = Pliny Trench, ST = Strabo Trench, NATF = North Anatolian Transform fault. Large arrows indicate the sense of plate motion relative to a fixed Eurasian plate; half arrows indicate strike-slip.

vital in determining the evolution of this basin. My proposed research will involve using seismological images to map and interpret this active, structurally complex area.

1.2 Plate Tectonic Setting

The Cilicia is one of four related basins that lie in the Northeast Mediterranean Sea. The three other basins (Adana, Latakia and Iskenderun basins) will be discussed in more detail in the next chapter. These basins form broadly in a fore-arc setting, but their evolution is complicated by a complex plate tectonic framework. The four basins lie within the Aegean-Anatolian microplate, which is deformed and displaced due to interactions with four surrounding plates (see Figure 1.1). Two of the main interactions are with Eurasian plate and with the African plate, which moves in a north-north-east direction with respect to the Eurasian plate. The boundary between the Eurasian and Aegean-Anatolian plates involves mainly right lateral strike slip movement along the North Anatolian transform fault (NATF) (Şengör et al., 1985). The convergent plate boundary between the African and the Aegean-Anatolian plates is delineated by the Hellenic Arc in the west and the Cyprean Arc in the east. Along these boundaries a combination of subduction related convergence, strike slip movements and collision takes place (Kempfer and Garfunkel, 1994; Ben-Avraham et al., 1988, 1995). The other important plate interaction occurs between the Aegean-Anatolian and the Arabian plate at the south east margin of the Aegean-Anatolian micro-plate. Along the boundary between the Arabian and the Aegean-Anatolian plates, both continental collision, along the Bitlis

suture zone, and strike-slip activity, along the East Anatolian transform fault (EATF), have occurred concurrently since mid to late Miocene time (Dewey et al., 1986). Internal deformation also occurs within the Arabian plate, in southern Syria, along the east-west trending Palmyran belt (see Figure 1.1) (Dewey et al., 1986). Due to the motion along the NATF and the EATF, the Aegean-Anatolian microplate is thought to be escaping westwards and rotating counter-clockwise due to the forces applied at its margins by the surrounding plates (Şengör et al., 1979, 1985; Rotstein, 1984). A combination of these plate interactions create the deformational forces responsible for the present day structure of the Aegean-Anatolian plate and the formation of the above mentioned basins.

1.3 Tectonic Evolution of the North-Eastern Mediterranean

The present day plate tectonic setting of the northeast Mediterranean is a result of a long history that began in the Permian and continues up to present day. The evolution involved the opening and subsequent closure of at least two major oceans: the Paleo-Tethys and the Neo-Tethys. The geology of both Turkey and Cyprus record this evolution and contain the remnants of ocean floors, passive margins, carbonate platforms, and volcanic and sedimentary rocks related to both subduction and rifting.

During the Permian, the Paleo-Tethys opened between Eurasia and Gondwana, as a branch of the super ocean Panthalassa, due to Eurasia's right lateral motion with respect to Africa. Subduction of this ocean soon followed, beginning sometime between Late Permian and early Triassic (Şengör and Yilmaz, 1981; Robertson, 1998 a). Concurrent

with the closing of the Paleo-Tethys, the southern strand of the Neo-Tethys began to open. The opening began in the Triassic with the rifting and compartmentalization of the northern Gondwanan passive margin. These rifted fragments, including the Anatolide-Tauride, form the northern margin of the southern Neo-Tethyan ocean (Şengör and Yilmaz, 1981) (see Figure 1.2). Active ocean floor spreading in the basin began by late Triassic time. To the southeast, the rifting was associated with the formation of the Levant basin as well as the separation of the Eratosthenes seamount from the Levant margin began during Triassic time (Robertson and Dixon, 1984; Robertson, 1998 a).

During the early Jurassic, rifting leading to the formation of the northern Neo-Tethyan ocean began to occur. This rifting separated the northerly rifted Gondwanan fragments from the more southerly ones (including the Anatolide-Tauride fragment). During the Jurassic, both branches of the Neo-Tethyan ocean expanded while the Paleo-Tethys closed. By the late Jurassic-Early Cretaceous period, the Pontides were thickening and affected by volcanism while the rifted fragments were sites of carbonate deposition (Robertson, 1998 a) (see Figure 1.3).

During early-mid Cretaceous, the African and Eurasian plates began to converge as a result of the opening of the South Atlantic ocean. This convergence led to the initiation of north dipping intra-basin subduction in the southern Neo-Tethyan ocean (Robertson and Dixon, 1984; Robertson, 1998 a). During the late Cretaceous, the eastern portion of this intra-basin subduction zone collided with the Arabian margin

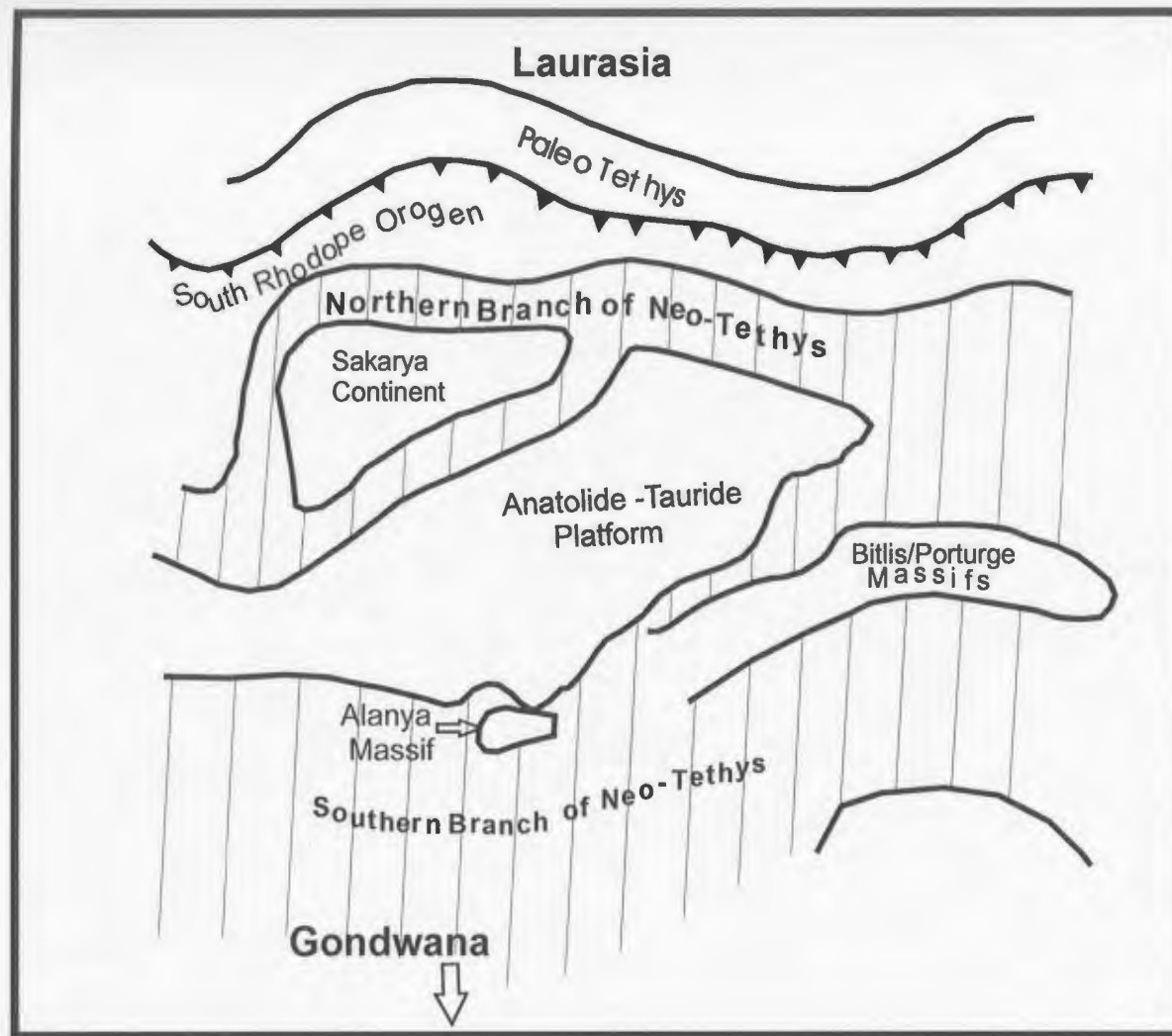


Figure 1.2: Schematic Paleotectonic Map of the Eastern Mediterranean during the Jurassic Period (edited from Sengör et al., 1985).

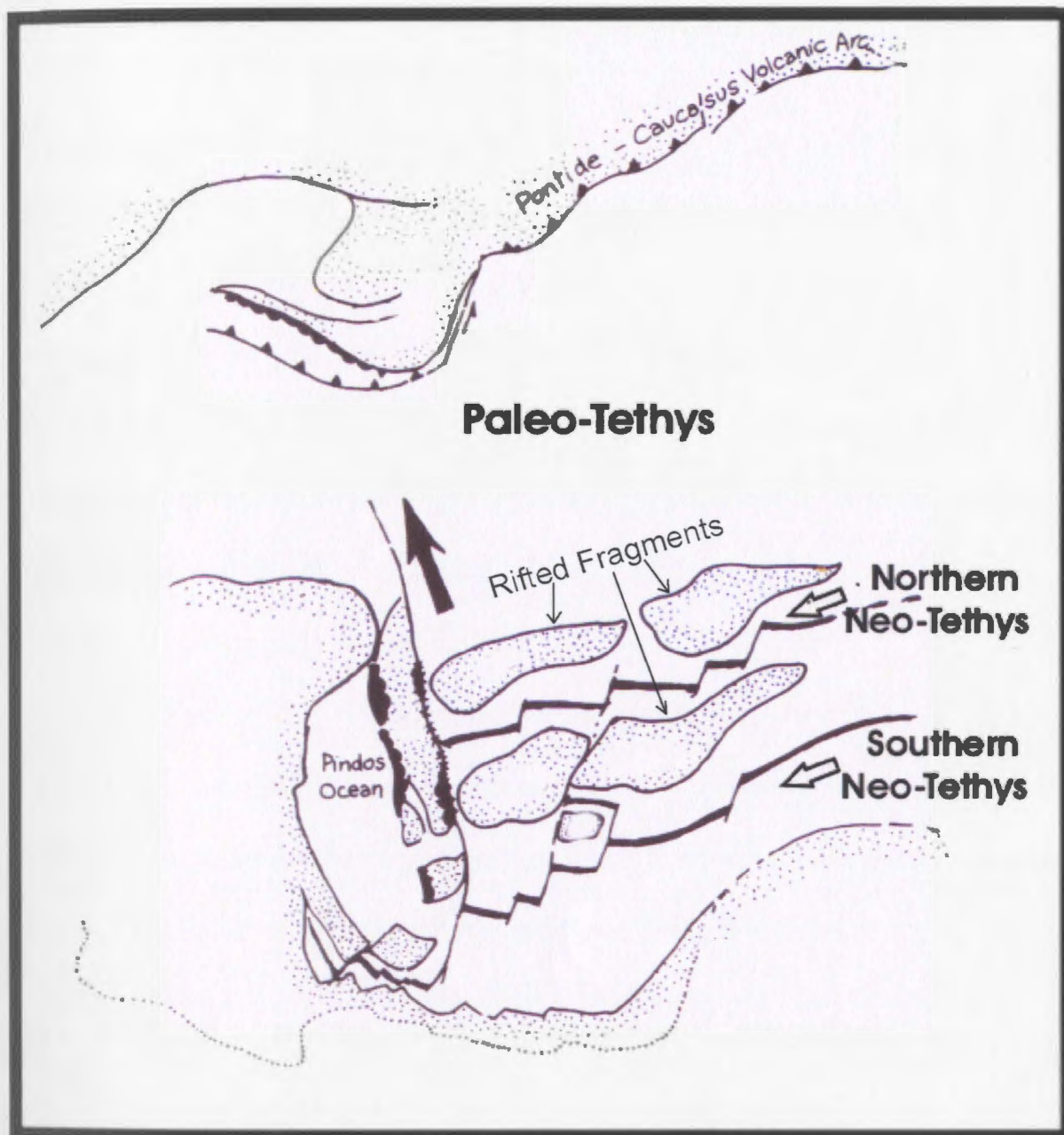


Figure 1.3: Schematic paleotectonic map of Eastern Mediterranean during the early Cretaceous period (edited from Robertson and Dixon, 1984).

causing the sediment associated with the trench to be thrust southwards with ophiolites thrust on to the northern Arabian margin (Robertson, 1998 a). Along the non-collided western portion of the intra-basin subduction zone, subduction slowed forcing a north dipping subduction zone to form at the northern margin of the southern Neo-Tethys basin (Şengör and Yilmaz, 1981) (see Figure 1.4). The remaining trench, from which the Troodos ophiolite later emerged, began to pivot counter-clockwise due to the continued convergence. By latest Cretaceous, Troodos had accreted to the Anatolide-Tauride's southern margin. Within the northern Neo-Tethys, the convergence also forced the cessation of spreading and the beginning of northerly directed subduction. This caused the formation and obduction of ophiolites onto the northern Anatolide-Tauride fragment (Robertson and Dixon, 1984; Şengör and Yilmaz, 1981).

The Paleocene to Eocene is marked by continued subduction of the remaining north Neo-Tethyan and Paleo-Tethyan ocean floor. Collision of the Anatolide-Tauride block with the Eurasian continent ensued in the mid-late Eocene, with the collision migrating from east to west (Şengör and Yilmaz, 1981; Robertson, 1998 a). By late Eocene to Miocene all rifted fragments from Gondwana had collided with the Eurasian margin leaving both the Paleo-Tethys and the northern branch of the Neo-Tethys closed. The Oligocene was mainly a time of subsidence for many Eastern Mediterranean features, such as the Kyrenia range of northern Cyprus (Robertson, 1998 a).

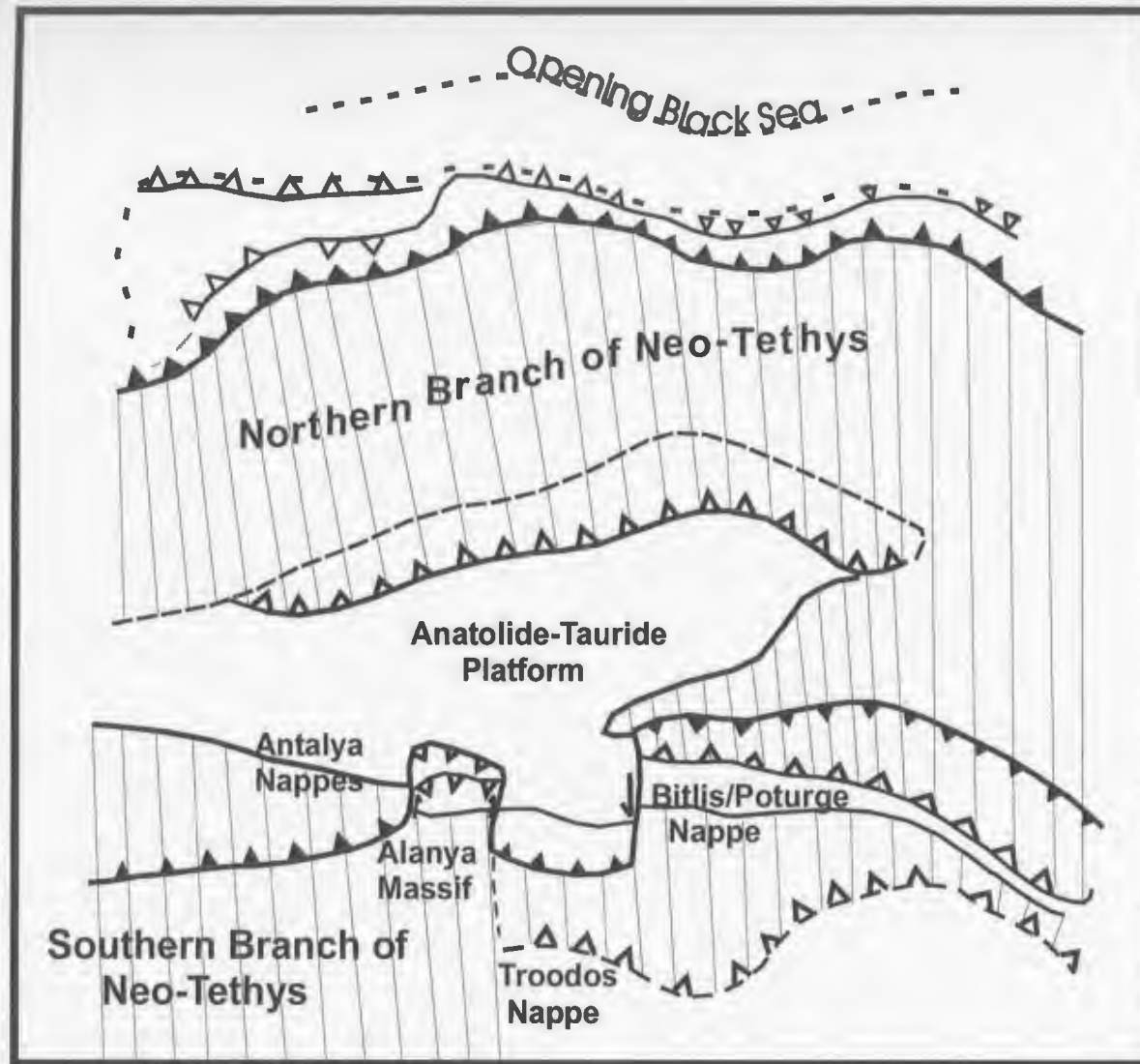


Figure 1.4: Schematic Paleotectonic map of the Eastern Mediterranean during the late-Cretaceous to Paleocene Period (edited from Sengör et al., 1985).

By Miocene time, the southern branch of the Neo-Tethys was the only remaining ocean floor in the North-East Mediterranean (see Figure 1.5). Continued convergence between Africa and Eurasia was accommodated by continued north-dipping subduction within this ocean basin. For the first time, subduction activity occurred along the present day positions of Hellenic and Cyprean Arcs (Robertson, 1998 a). For the Cyprean Arc, this involved a southern migration of the subduction zone leaving Cyprus on the overriding, rather than subducting, plate. Continental collision, between the Arabian and Aegean-Anatolian plates, then ensued in mid to late Miocene beginning in the east, along the Bitlis Suture zone, and progressing toward the west (Dewey et al., 1986). Following the collision, sometime between the mid Miocene and early Pliocene, the North and East Anatolian faults formed and the westward expulsion and rotation of the Aegean-Anatolian micro-plate began (Şengör et al., 1979, 1981, 1985). This caused the subduction direction to change from north to north-east. Also during this time, basins in the north-east Mediterranean; such as the Mersin, Antalya, Latakia and Cilicia, began to subside (Robertson, 1998 a). In latest Miocene, the entire Eastern Mediterranean desiccated depositing a thick evaporite deposit in all deep basins that had formed by this time.

The main event within the north-east Mediterranean during the Pliocene involved the collision of the Eratosthenes seamount with the Cyprean Arc (Ben Avraham et al., 1988, 1995, Robertson, 1998 b,c). This caused a slowdown or cessation of subduction along the arc and the rapid uplift of both southern Cyprus and the Kyrenia range. The

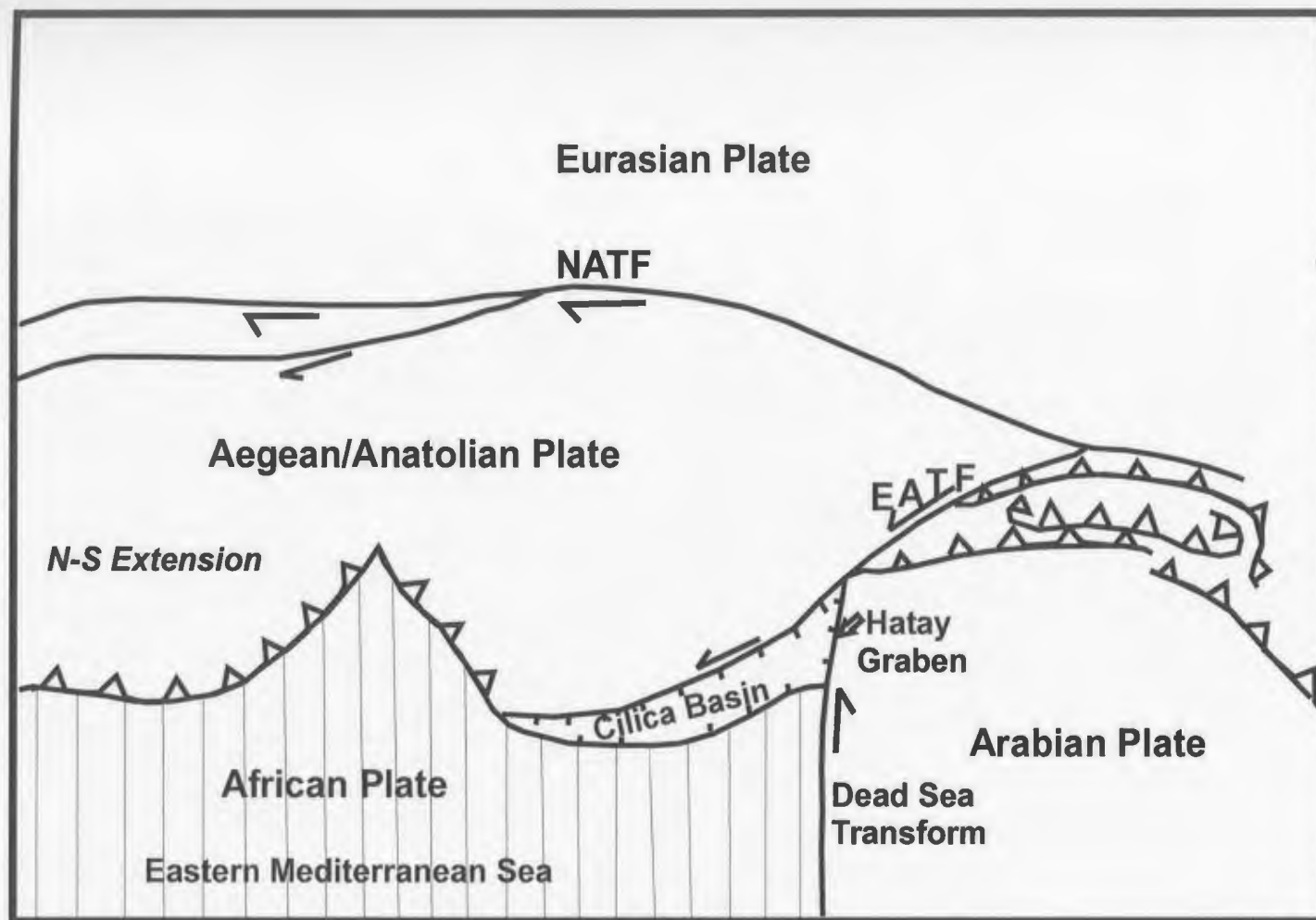


Figure 1.5: Schematic paleotectonic map of the Eastern Mediterranean during the middle Miocene-Pliocene period (edited from Sengör et al., 1985).

3

Pliocene also saw continued subsidence of the basins formed between the late Miocene and early Pliocene and continued uplift within Turkey and along the Bitlis suture zone (Robertson, 1998 a). From the Pleistocene period onwards, the current plate boundaries and plate motions, described in the following sections, have dominated the structure of the north-east Mediterranean.

1.4 Plate Boundaries in the Eastern Mediterranean

The current plate interactions and boundaries in the Eastern Mediterranean control the tectonic framework and the structural systems seen in the area. The plate boundaries mentioned in the introductory section will now be discussed in more detail.

1.4.1 Interaction between the Aegean-Anatolian and African plates

The interaction between the Aegean-Anatolian and the African plates involves mainly convergence, leading up to the ultimate collision of continental parts of the two plates. The boundary between the plates can be found on the sea floor of the Eastern Mediterranean sea along two arcs, the Hellenic and the Cyprean Arc (see Figure 1.1). The Cyprean Arc will be of greater focus in this section, due to its relationship with the Cilicia Basin, however the structure of both arcs will be addressed.

1.4.1.1 The Hellenic Arc

The Hellenic arc forms the western convergent boundary between the African and Aegean-Anatolian plates. The convergence of Africa and Europe began between 120 and 83 Ma (Rosenbaum et al., 2002). The convergence rate has varied through time, with at least two periods of rapid convergence (120-67 Ma and 52.4-19.2 Ma) followed by relatively slow convergence from the early Miocene to present time (Rosenbaum et al., 2002). The evolution of the Hellenic arc occurred quite late in this period and is thought to have begun with the initiation of subduction of the African plate beneath the Aegean-Anatolian in the late Miocene. The relative motion at that time was north-south at the front of the arc and oblique along the western branch. By Pliocene time, subduction was locked to the south inducing left lateral motion along the south margin and subduction along the western arc (Mascle et al., 1986). The Hellenic arc has many of the features characteristic of subduction zones, such as associated sedimentary and volcanic arcs, as well as seismic activity both at the surface and at depth. There is also an associated broad ridge, called the Mediterranean ridge, that extends along the entire arc, from the southwest coast of Greece to the northwest corner of Cyprus. The ridge is about 1300 km long, 150 to 300 km wide and contains about 10 to 12 km of sediment that has been deformed in a compressional setting. Most authors interpret the ridge to be an accretionary prism scraped from the down-going plate at the subduction trench (Lallemant et al., 1994; Huguen et al., 2001). Along the present day Hellenic arc system, the mode of convergence changes from normal subduction and compressive regimes in

the west to strike-slip and collisional regimes in the east. The Hellenic arc is separated into 2 main branches: the western Ionian branch and the eastern Levantine Branch (Peters et al., 1985)

The Ionian branch is northwest-southeast trending feature located at the base of the continental slope along the west coast of Peloponnesus. It is made up a series of discontinuous depressions, with a maximum depth of 5000 m, separated by ridges (Peters et al., 1985). Earthquake data suggests that both active subduction and right lateral transverse motion, mainly along the Cephalonia transform fault, occurs along this branch of the arc (Sachpazi et al., 2000; Papazachos et al., 2000).

The Levantine Branch of the Hellenic Arc extends from just south of the island of Crete, northeastwards towards the island of Rhodes in the Eastern Mediterranean sea. In general, this branch consists of a system of subparallel narrow troughs that lose their distinctive trench morphology, become deeper, and merge to the northeast along the arc. South and east of Crete, the Hellenic margin is characterized by two trenches, namely the Pliny Trench to the north and the Strabo trench to the south, separated by a wide and sedimented plateau (Masclé et al., 1986). The Pliny trench has a depth of up to 4000 m and is characterized by steep walls that dip up to 13 degrees toward the trench floor (Peters et al., 1995). It is made up of small, relatively sedimented depressions that generally form an en echelon arrangement (Masclé et al., 1986). The trench opens to the east into a wide, sedimented, graben like feature. South of the Pliny trench lies the

shallower and less infilled Strabo trench. The Strabo trench is up to 3000 m deep and has steep walls dipping toward the trench floor (Peters et al., 1995). Like the Pliny trench, it is made up of a series of diversely oriented segments in a general en echelon arrangement. The thin sediment infill in the trench is highly deformed and indicates recent tectonic activity (Masclé et al., 1982). To the east, the trench terminates against topographical highs south of the island of Karpathos. Most workers agree that the Strabo trench is the active deformation zone, along which subduction activity has occurred (Masclé et al., 1982; Peters et al., 1995). South of the island of Rhodes, at the eastern end of the Hellenic trench, the systems described above have merged into a trough called the Rhodes basin, which is about 4000 m deep and contains more than a kilometre of Pliocene-Quaternary sediment, but lacks a Messinian salt layer (Masclé et al., 1986; Woodside et al., 2001; Winsor, 2004). Although some workers have interpreted this basin as the remnant of a subduction trench (Masclé et al., 1986), its origin is still debated.

Earthquake and structural data suggest that both strike-slip and compressional tectonics occur along the eastern Hellenic arc. Earthquake mechanisms show dominantly left lateral strike slip with a thrust component, suggesting a dominantly transpressional regime (Papazachos, 2000). The en echelon arrangement seen in both trenches is also suggestion of strike slip activity. Earthquake data show that both shallow and deeper earthquakes have been recorded along the eastern arc, suggesting that subduction has occurred in this area. A north-northeast dipping layer of oceanic crust has also been interpreted, from wide angle seismic data, below the island of Crete further supporting

that subduction had occurred (Bohnhoff et al., 2001). There is evidence of a gap in seismicity between 80 and 100 km depth, which suggests that fragmentation of the down going slab may have occurred. Slab fragmentation, along with evidence that the Mediterranean ridge is thrusting northward south of the Rhodes basin, suggests that collisional processes may have begun along the eastern Hellenic arc (Papazachos, 2000; Mascle et al., 1986).

1.4.1.2 The Cyprean Arc

The Cyprean Arc marks the eastern boundary between the Aegean-Anatolian and African plates. Like the Hellenic Arc, it is a convergent boundary along which subduction has occurred since Miocene time. When compared with the Hellenic Arc however, convergence occurs at a much slower rate (about 7 mm/year; McClusky et al., 2000) and there is a decreased amount and more dispersed pattern of present seismicity (Rotstein and Kafka, 1982). The Cyprean Arc also lacks subduction related features, such as a well defined volcanic arc, that have been documented along the Hellenic Arc (Woodside et al., 2002). The Mediterranean ridge continues, from the Hellenic Arc, to follow the southern boundary of the Cyprean Arc on the western margin, but is not obvious along the central or eastern segments. All of the above evidence suggests that convergence and subduction along the Cyprean Arc is more complex, and consequently less well understood, than that along the Hellenic Arc. There is evidence, in the form of intermediate depth earthquakes, that subduction has occurred during the arc's evolution

(Rotstein and Kafka, 1982), but it is likely that subduction has slowed, or perhaps ceased, in recent times (Ben Avraham et al., 1988, 1995). The mode of convergence changes from subduction, to strike-slip, to collisional processes along the Cyprean Arc. The arc can be divided into 3 main segments, each with its own morphology and controlling processes. They will be described as the western, central and eastern segments.

The western segment of the arc runs from the conjunction between the Cyprean and Hellenic arcs, just southwest of the island of Rhodes, to south of the western margin of Cyprus. This segment of the arc is characterized by a trench, called the Pytheus Trench, that lies just south of the Anaximander mountains in the northwest and the Florence Rise farther to the southeast (Anastasakis and Kelling, 1991). In the north west, the trench is made up of a chain of elongate, flat floored depressions, which are about 5 km wide and 30 km long, in an en echelon arrangement. To the south-east, the trench is represented by flat sea floor that is only slightly deeper than the surrounding floor (Anastasakis and Kelling, 1991). Some workers have interpreted this feature as a strongly deformed basin rather than a trench (Woodside et al., 2002). The Anaximander mountains are an actively uplifting structure, made up of 3 submarine peaks that rise to 1000 m below sea level. They are interpreted by most workers to be transpressional structures (Woodside et al., 2002; Anastasakis and Kelling, 1991). The Florence rise is a 200-300 m high, north-west to west trending, broad asymmetric swell that is thought to be a subduction related feature, and the local equivalent of the Mediterranean ridge. The swell separates the Pytheus trench from the Antalya basin to the north. The pre-

Messinian strata within the rise are folded and cut by north dipping thrust faults, however the recent strata are more affected by strike-slip faulting (Woodside et al., 2002). The Antalya is a Neogene basin filled with thick sediment packages that dip toward the northeast. The basin is relatively deep with a seabed that lies approximately 2500 m below the water surface. Most deformation in this basin is associated with salt structures and not with the deformation that affects the Florence rise just south of the basin (Woodside et al., 2002; Taviani and Rossi, 1989). Recorded seismic activity indicates a change in seismicity along the Cyprean Arc in the Antalya bay region. West of Cyprus, an 80 km thick dipping zone of shallow and intermediate earthquake hypocentres extends between 50 km and 150 km depths, indicating that active subduction of African plate beneath the Aegean-Anatolian plate, is occurring this area (Ben-Avraham et al., 1988; Rotstein and Kafka, 1982). Also, a distinct Benioff zone is observed dipping toward the northeast at an angle of 10 degrees at shallow depths and 40 degrees down to depths of 130 km, within Antalya bay (Papazachos and Papaioannou, 1999). West of Antalya Bay there is a decrease in the amount of recent seismicity suggesting a less seismically active plate boundary in this area. The recent deformation in the structures, such as within the Florence rise and Anaximander mountains, suggests that lateral shearing is occurring within a wrench zone along the inferred plate boundary. This suggests although subduction has been active in the past, strike slip motions currently dominate this area. The lateral motion is likely the result of a slowdown or cessation of subduction, possibly due to the collision between the Eratosthenes seamount and the central Cyprean Arc

and/or stretching or detachment of the subducting plate (Woodside et al., 2002; Anastasakis and Kelling, 1991).

The central segment of the Cyprean Arc is an east-west oriented plate boundary that runs along the south coast of Cyprus and north of the Eratosthenes seamount. The Eratosthenes seamount is a very important feature as it is thought to be obstructing subduction along this portion of the arc. The seamount is an uplifted, faulted block that is elongated in a northwest-southeast direction and rises 1200-1700 m above the sea floor (Anastasakis and Kelling, 1991; Ben-Avraham et al., 1988). It is generally accepted to be made up of a shallow water carbonates overlying a thinned continental crust (Robertson, 1998 b,c). The seamount is thought to have rifted from the North African platform during Mesozoic time and has developed as a shallow water carbonate platform since the Cretaceous (Robertson, 1998 b,c). Eratosthenes is separated from Cyprus by a 2 km deep, asymmetric, sediment filled trench named by some workers as the Cyprus trench (Vidal et al., 2000; Anastasakis and Kelling, 1991).

The tectonic model for the central portion of the Cyprean Arc suggests that normal subduction has been interrupted by collision with the Eratosthenes seamount. Since Pliocene time, the northern margin of the continental fragment has been undergoing subduction leading to the uplift of Cyprus (Robertson, 1998 a). Evidence supporting this model include: 1) seismicity with a compressional thrust component recorded at depths up to 100 km concentrated in the zone between Cyprus and the Eratosthenes seamount

(Ben-Avraham et al., 1988; Papazachos and Papaioannou, 1999), 2) a strong reflection, which extends 10 km beneath the upper plate, has been imaged in this area of the arc and interpreted as the top of the subducting seamount (Vidal et al., 2000). Fault plane solutions for earthquakes at the south-west coast of Cyprus suggest that a linear, northeast striking zone with a dextral strike slip and thrust components may also exist in this area (Papazachos and Papaioannou, 1999) (see Figure 1.6). This would suggest that the convergent margin may be broken by a transform fault in this area and that Cyprus is moving southwest with respect to the African plate.

The eastern segment of the Cyprean arc has the least seismicity, and is an arcuate, northeast-southwest trending segment that extends from south of the south-east coast of Cyprus up to Iskenderun bay. It is characterized by a series of northward tilted basins and asymmetric ridges that merge together toward the east. The structures from north to south are: the Misis-Kyrenia ridge, the Latakia basin, the Amanos-Larnaka ridge, the Cyprean basin, the Latakia ridge, and the Levant basin (Ben-Avraham et al., 1995) (see Figure 1.7). Most of these structures will be discussed in more detail in the following chapter. The active deformation front is thought to lie along the Latakia ridge (Ben-Avraham et al., 1995; Vidal et al., 2000). This ridge is a sub-horizontal elevation that rises above the sea floor along the easternmost arc and continues westward as part of a bathymetric escarpment, which likely extends into the asymmetric trench along the central part of the arc. The feature, which formed before Messinian time, is made up of Paleogene thrust sheets that are covered by a thin veneer of Pliocene-Quaternary

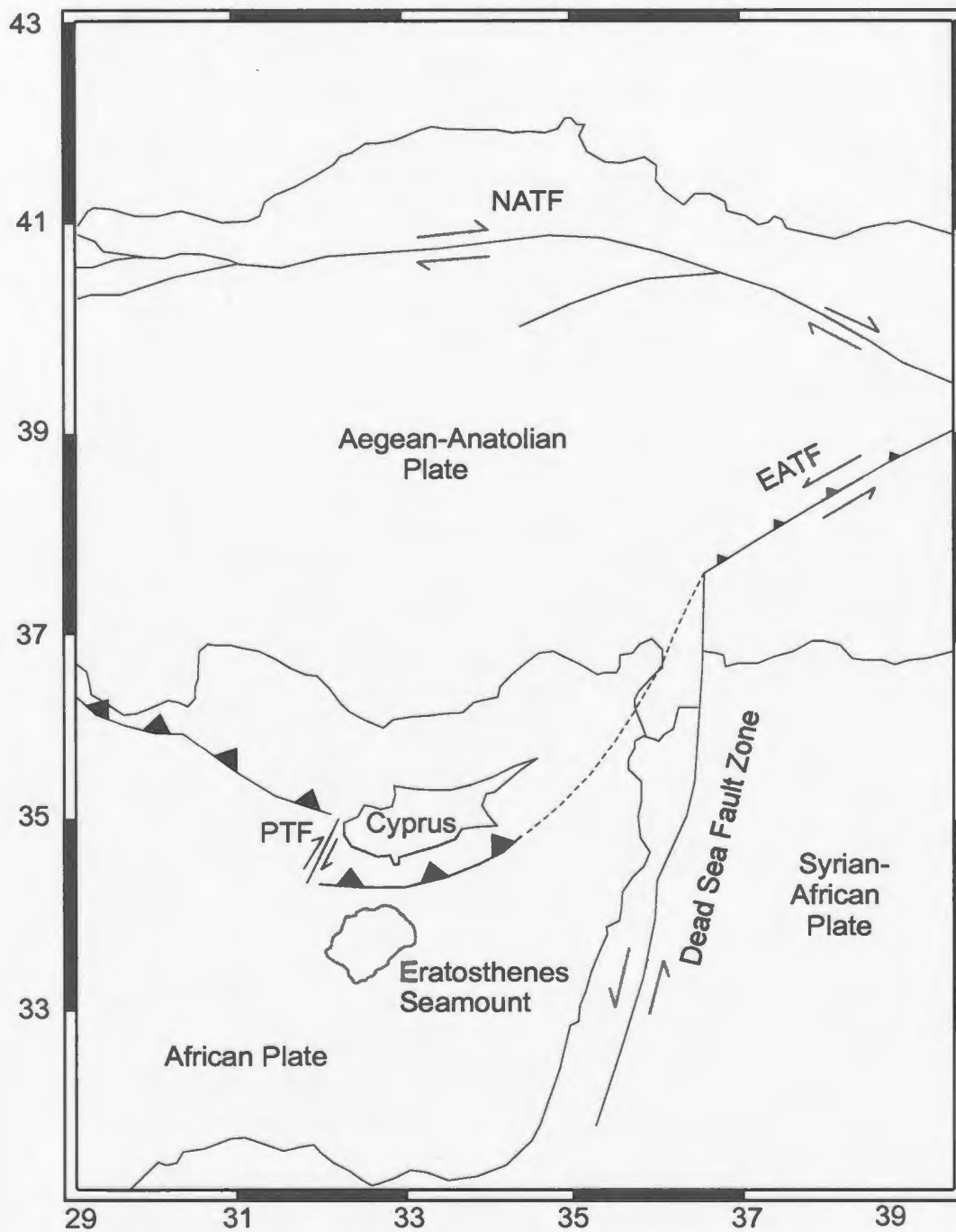


Figure 1.6: Map showing lithospheric boundaries and plate motions in the Cyprus area (edited from Papazachos and Papaioannou, 1999). EATF=East Anatolian transform fault, NATF=North Anatolian transform fault, PTF=Paphos transform fault.

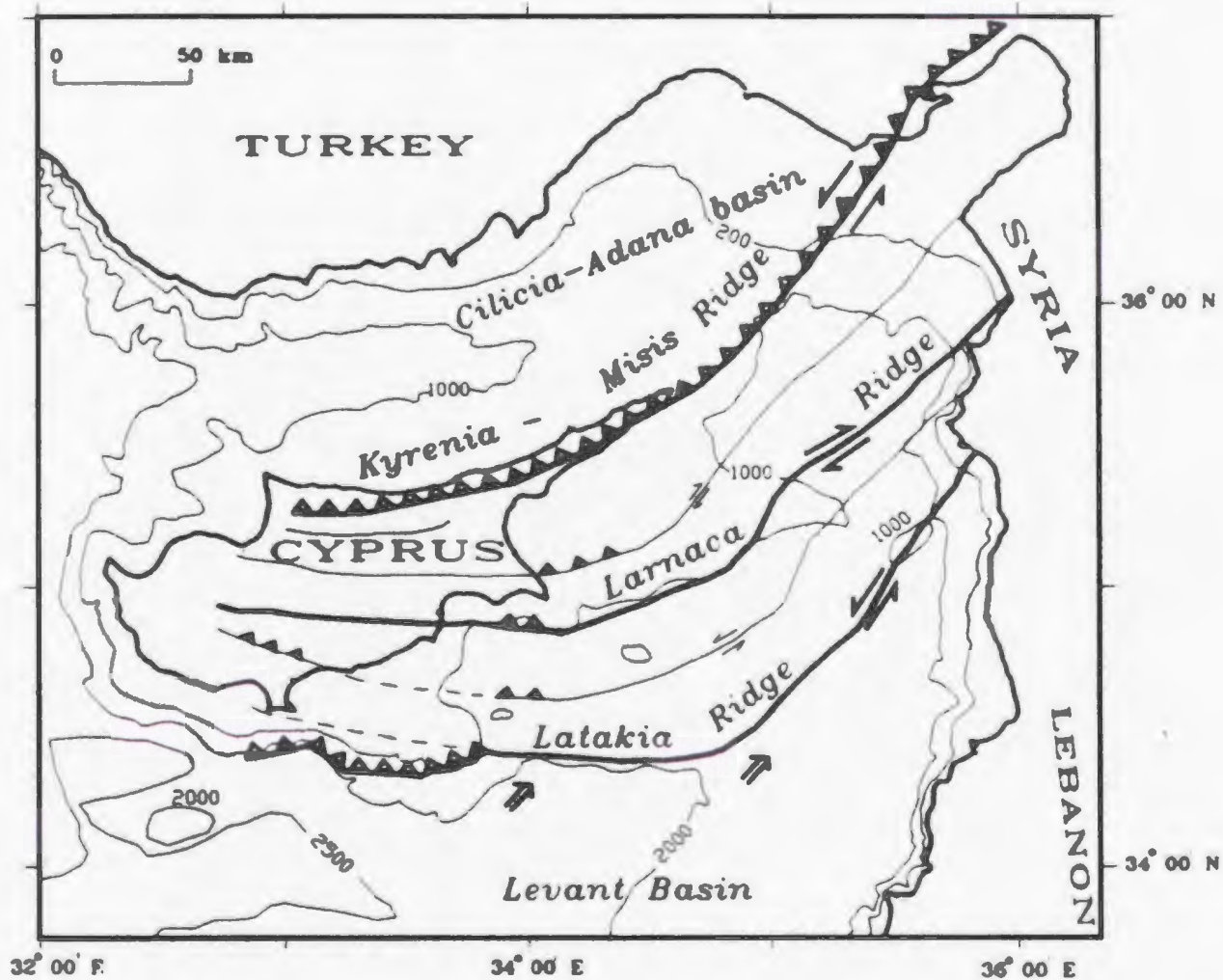


Figure 1.7: Map showing the morphological ridges related to the boundary between the African and Aegean-Anatolian plates north-west of Cyprus (edited from Ben-Avraham et al., 1995).

sediment. The post-Miocene faulting associated with this structure appears to be high angle and strike-slip related (Ben-Avraham et al., 1995). Further evidence that this ridge is indeed a plate boundary is the change in basement structure across the ridge, which suggests that the two sides had different tectonic histories prior to the Tertiary (Vidal et al., 2000). Earthquake data in this area show no strong intermediate depth earthquakes, suggesting that subduction is not taking place along this portion of the arc (Papazachos and Papaioannou, 1999). The shallow seismicity recorded is scattered over a broad zone and does not give conclusive evidence for the location of the plate boundary (Rotstein and Kafta, 1982). The structure of the Latakia and the other associated ridges suggest that they formed as large thrust systems prior to the late Miocene, but strike-slip faulting dominates their more recent activity (Ben-Avraham et al., 1995). The intervening basins show varied dimensions, lateral changes in the thickness of sediment infill, and both compressional and extensional structures (Ben-Avraham et al., 1995). This evidence suggests that the eastern Cyprian arc is presently mainly a strike-slip margin.

1.4.2. Interaction between the Aegean-Anatolian and Arabian plate

The interaction between the Aegean-Anatolian and Arabian plates involves both continental collision and strike slip activity. In the far eastern portion of the Aegean-Anatolian plate, north dipping subduction of the Arabian plate occurred from the late Cretaceous to Middle Miocene, followed by continental collision along the Bitlis suture zone in mid to late Miocene time (see Figure 1.1) (Dewey et al., 1986). The

compressional features associated with this collisional process are concentrated in the East Anatolian convergent zone (EACZ) (Dewey et al., 1986). North and southwest of the collision zone, left lateral strike slip activity has dominated along the East Anatolian transform fault (EATF) since the Pliocene (Dewey et al., 1986). This area is characterized by earthquakes with focal mechanisms suggesting both reverse and strike-slip movement (Rotstein and Kafka, 1982).

1.4.2.1 Eastern Anatolian Convergent Zone (EACZ)

The Eastern Anatolian convergent zone is a generally east-west trending area of north-south crustal shortening and uplift within Eastern Anatolia. The south boundary of the zone is uplifting and is made up of a complicated, 150 km wide zone of southward propagating, shallowly dip thrusts which affect the basement rocks (Dewey et al., 1986). The foreland basin contains a sedimentary sequence that is also affected by south vergent folds and thrusts (Dewey et al., 1986). North of the main thrust belt lies the East Anatolian plateau, which is characterized by complicated deformation and contains both right lateral and left lateral strike slip faults that accommodate the intra-continental convergent strain produced by the continental collision (Dewey et al., 1986). Within the Arabian plate, folds and faults occur only near the Anatolia-Arabia boundary. South of the boundary area, the plate is relatively undeformed (Lyberis et al., 1992).

1.4.2.2. Eastern Anatolian Transform Fault (EATF)

The East Anatolian Transform fault is a left lateral strike-slip fault that separates the Anatolian block from the Syrian foreland (see Figure 1.1). It formed prior to Pliocene time, due to the collision between Arabia and Eurasia. The fault is over 500 km long and has a width that varies between 10 m and 4 km along the fault trace (Dewey et al., 1986). The offset along the fault is thought to be about 22 km, with most of the separation concentrated through the central part of the fault (Dewey et al., 1986; Perincek and Cemen, 1989). The EATF has numerous features characteristic of strike slip faulting including seismic activity, offset of lithological contacts across the fault, as well as a well defined fault valley. Some authors have divided the fault into zones or parts, each with varying characteristics and morphologies (Şaroğlu et al., 1992). The zones vary in the amount of seismic activity along them and in the presence or absence of such features as bifurcating fault traces, associated pull apart basins and en echelon arrangements (Şaroğlu et al., 1992). The Ececi fault (see Figure 1.1), a left lateral strike-slip fault that lies in south west Turkey, is thought to be related to, and extend from, the larger East Anatolian Transform Fault (Ozer et al., 1974). There is some disagreement about how far the EATF extends to the south west and about its relationship with the Dead Sea Fault (described below). Some workers believe that the strike of the fault zone changes from northeast to north oriented near the town of Maras and extends southwestwards through the Hatay graben to join the Dead Sea Fault (Şengör et al., 1985; Şaroğlu et al., 1992) (see Figure 1.8). Others believe that the fault trace disappears south of Maras, and that an

extension of the EATF (the Amanos fault) and the Dead Sea Fault have a complicated relationship within the Amik basin, which forms the southern part of the Hatay graben (Perincek and Cemen, 1990). Other workers believe that the left lateral strike slip motion along the EATF does not extend even as far as the Maras region and that the fault zone is dominated by compression, with only minor strike-slip components, in that region (Lyberis et al., 1990). Regardless the interpretation of the extent of the fault zone, most authors agree that the EATF's sinistral motion provides the southern accommodation of the westward escape of the Aegean-Anatolian microplate.

1.4.3. Interaction between the African and the Arabian plates

The interaction between the African and Arabian plates involves rifting and strike slip motion along the Dead Sea fault zone. The Dead Sea fault is 1000 km long and extends from the Red Sea in the south, through the Dead Sea and the Gulf of Aqaba, up to the EATF in the north (Lyberis, 1988) (see Figure 1.1). The fault activated in the late Miocene and accommodates the more rapid northern movement of the Arabian plate with respect to the more slowly northward moving African plate (Lyberis, 1988). Most of the fault zone is undergoing active rifting, with the exception of the most northern portion which undergoes only left lateral strike slip motion (Prodehl et al., 1997). This northern portion extends from the Red Sea as a single fault zone but then splinters into several branches at the Syria-Turkey boundary (Perincek and Ceman, 1990) (see Figure 1.8). These branches form the boundaries of north-south oriented, fault bounded basins seen in

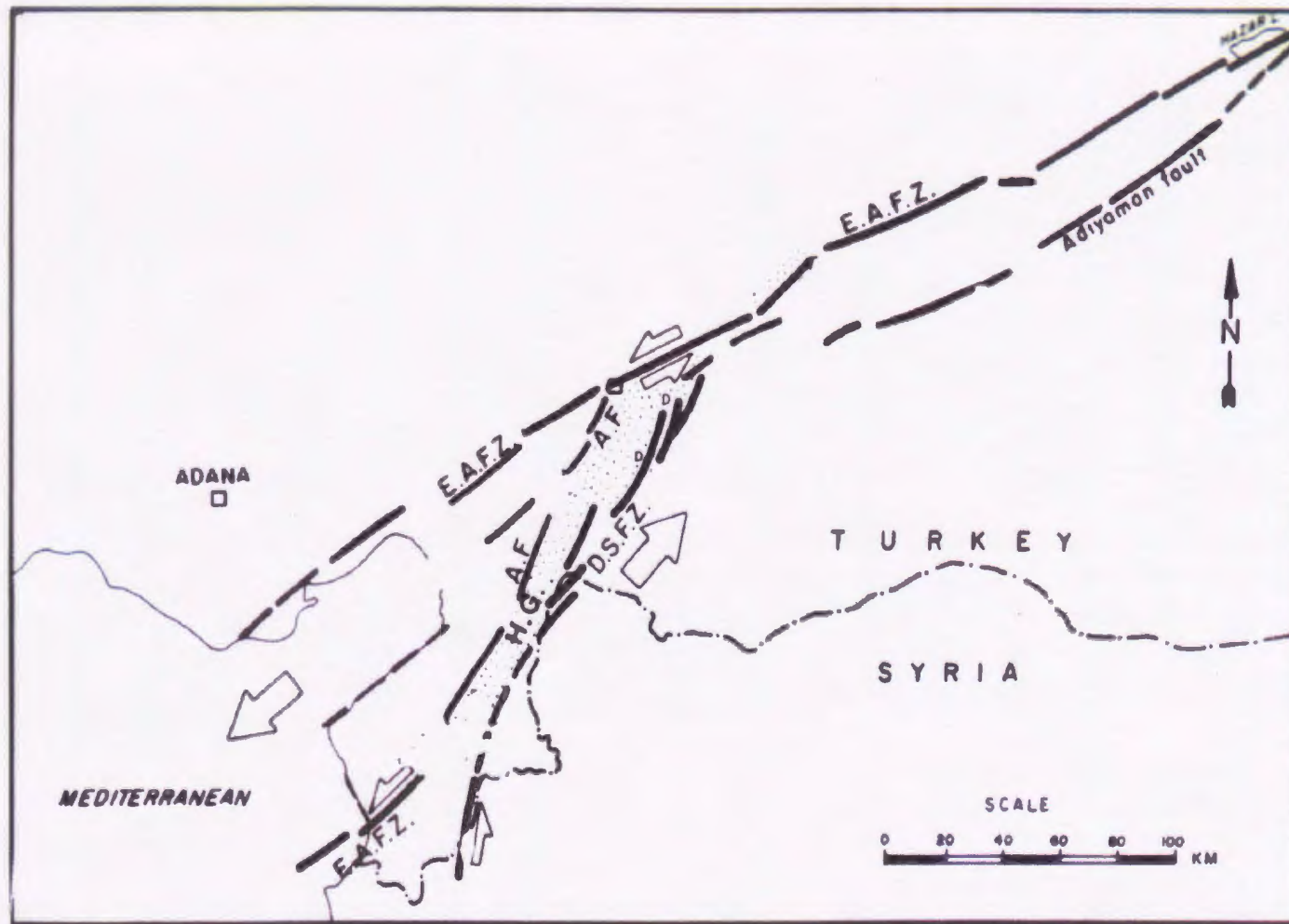


Figure 1.8: Map showing the location and kinematic interpretation of faults and structural features onshore Turkey, near the Turkey/Syria border. A.F.=Amanos fault, D.S.F.Z.=Dead Sea fault zone, E.A.F.Z.= East Anatolian fault zone H.G.=Hatay graben (edited from Perincek and Ceman, 1989)

this area. One of the more important of these basins, is the Amik basin (thought to be a part of the larger Hatay graben) which formed due to interactions between the EATF and the Dead Sea fault and may contain the join between the two faults (Perincek and Cemen, 1990; Şaroğlu et al., 1992). Earthquake fault plane solutions indicate that along the fault trace left lateral strike slip with a strike of N 80-10° E occurs (Nur and Ben-Avraham, 1978). To the west and to the east of the main fault trace, faulting has been recorded with normal components and with thrust components, respectively. Based on stratigraphic and structural evidence, the fault appears to be slipping at a rate between 0.65 and 1.0 cm/yr (Nur and Ben Avraham, 1978).

Some workers (Mascle et al., 2000) suggest the presence of a microplate between the African and Arabian plates, known the as Sinai microplate (see Figure 1.9). The Sinai microplate is bounded by the Dead Sea Transform to the east, the central segment of the Cyprus Arc to the north, the Gulf of Suez rift system to the southwest, and a transtensive fault system cutting through the Nile Deep Sea fan to the northwest. Mascle et al. (2000) theorize that the microplate is a part of the African plate, that broke off in response to the collision between Cyprus and the Eratosthenes seamount. This theory remains controversial due to a lack of seismic activity along northwest boundary of the microplate or a structural indication of connectivity between the Gulf of Suez rift and the fault system mapped through the Nile deep sea fan (Mascle et al., 2000).

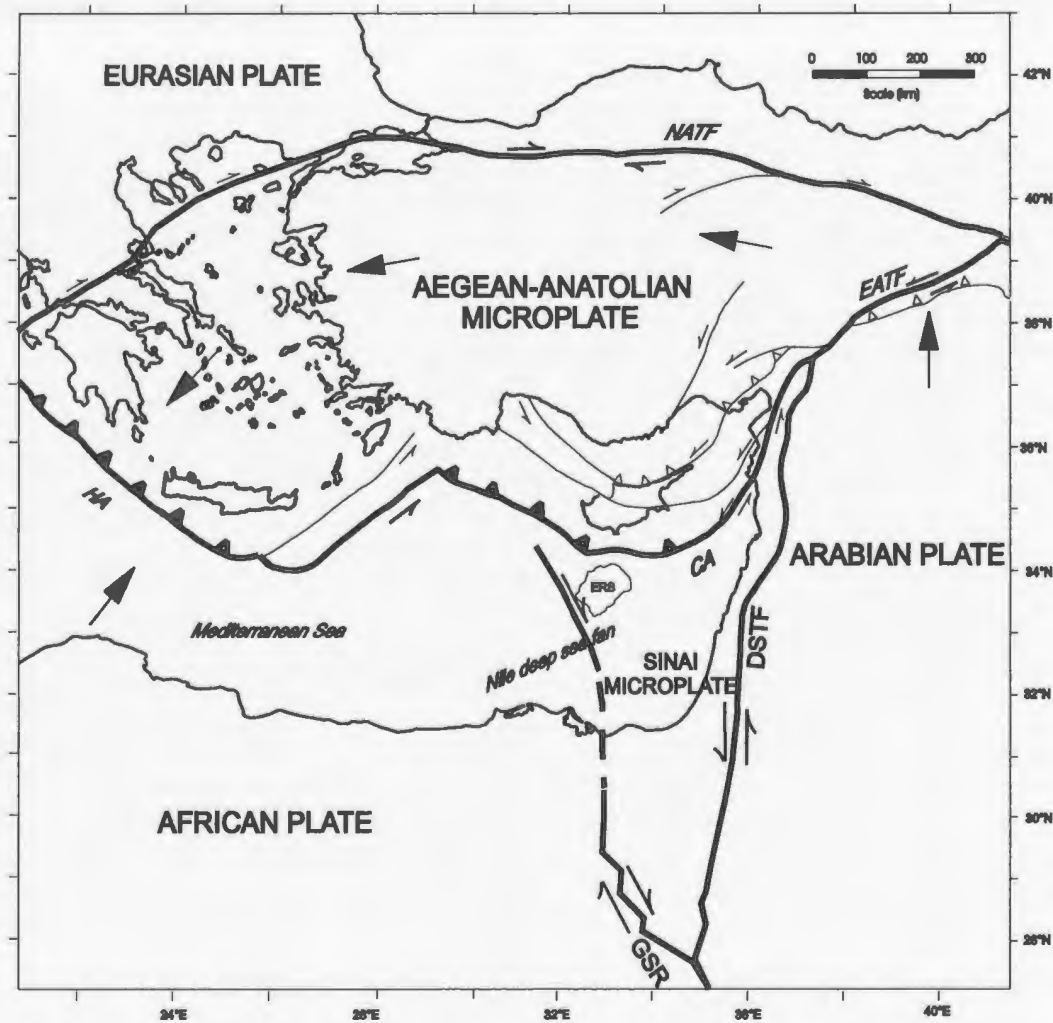


Figure 1.9: Simplified tectonic map of the eastern Mediterranean showing possible presence of Sinai Microplate (edited from Aksu et al., 2005). Map compiled from Sengör and Yilmaz (1981), Hancock and Barka (1981), Dewey et al. (1986), Mascle et al. (2000). CA = Cyprus Arc, DSTF = Dead Sea transform fault, EATF = East Anatolian Transform Fault, ERS = Eratosthenes seamount, GSR= Gulf of Suez rift system, HA = Hellenic Arc, NATF= North Anatolian Transform fault. Large arrows indicate the sense of plate motion relative to a fixed Eurasian plate; half arrows indicate transform/strike-slip faults.

1.4.4. Interaction between the Aegean-Anatolian and the Eurasian plates

The plate boundary between the Aegean-Anatolian and Eurasian plates lies along the North Anatolian transform fault (see Figure 1.1). This fault formed in early late-Miocene in response to the collision between the Arabian and Eurasian plates (Şengör, 1979). The NATF extends 1200-1500 km, from its junction with the EATF in south eastern Anatolia to its western termination in the North Aegean trough (Şengör, 1979). Although the NATF does terminate within the North Aegean trough, the dextral motion that occurs along the fault continues as far as the western margin of the Hellenic Arc. The NATF is more seismically active and has a larger associated offset than the EATF. The NATF has had at least 6 large earthquakes in the last 100 years, resulting in ruptures over 900 km of its length (Hubert-Ferrari et al., 1999; Kiratzi, 1993). The interpreted offset on the fault varies between 40 and 100 km, but decreases from east to west due to the displacement being transferred to numerous splays in the western section (Rotstein, 1984). Two main splays separate just east of the sea of Marmara and are differentiated as the northern and southern North Anatolian Fault strands. This splay separation has led to the formation of narrow graben complexes or transtensional basins in the western portion of the fault zone (Şengör et al., 1985). In the eastern part of the fault zone, fault associated pull-apart or compressional ramp basins are more common.

The earthquake mechanisms indicate that the NATF has right lateral strike-slip motion that is parallel to the fault trace (Şengör and Canitez, 1982). The fault zone has a

distinctive rift morphology, however, indicating that it also has an extensional component. The rift morphology is delineated in a broad zone of sub-parallel and anastomosing faults along the fault valley (Dewey et al., 1986; Şengör et al., 1985).

1.5 Relative Plate Motions in the Eastern Mediterranean

Relative plate motions and plate tectonic models of the Eastern Mediterranean have been estimated by many authors from the analysis of oceanic spreading centres, movement on transform fault systems, earthquake slip vectors and GPS measurements. The plate motions are relative to the Eurasian plate, which is considered stationary for the purpose of determining the motion of other plates. The relative plate motions that will be considered in this section are: the Arabian, the African, and the Aegean-Anatolian plates. The Arabian plate is moving toward the north-northwest at a rate of 20-25 mm/year, while the African plate moves north-northeastward at a slower rate of 10 mm/yr (DeMets et al., 1990, Reilinger et al., 1997). The differential motion between them is taken up in the Dead Sea fault, which separates the two plates. The northward motion of both these plates leads to the formation of a convergent boundary with the Aegean-Anatolian micro-plate along their northern margins. The higher velocity of the Arabian plate leads to collision at its boundary, while a combination of subduction, collision and strike slip activity occurs along the African/Aegean-Anatolian boundary. The collision occurring along the northern Arabian plate generates the forces that induce the westward expulsion

of the Aegean-Anatolian plate along the North and East Anatolian faults. Due to other plate interactions however, the Aegean-Anatolian plate cannot continue to be expelled directly westward. GPS measurements suggest that the motion of the Aegean-Anatolian plate changes from west directed in eastern Anatolia to southwest directed in the western portion of the plate. In the extreme west and southwest of the plate, the GPS measurement indicate a dominantly south-directed motion (Reilinger et al., 1997). The change in the direction of motion across the plate indicates that the Aegean-Anatolian plate is rotating counter-clockwise around a Euler pole which has been defined to lie on the Sinai peninsula (Reilinger et al., 1997; Papazachos, 1999). One challenge to that theory is presented in the Rotstein(1984) paper, which suggests that the presence of internal deformation within the Anatolian block prevents a single pole of rotation from being identified. Regardless of the pole's location, it is obvious that the plate is rotating based on the curvature of the NATF and on the rate and direction of motion recorded for the Aegean-Anatolian plate. The rotation is induced by the Eurasian plate's resistance to the westward expulsion forcing the plate towards the 'free face' of the Hellenic Arc, where the subducting African plate is rolling back (Reilinger et al., 1997; Royden, 1993). This westward expulsion causes the direction of subduction for the African plate to change from north to northeastward, relative to the Aegean-Anatolian plate.

The forced westward expulsion and rotation of the Aegean-Anatolian plate leads to the change in deformation across the plate, as well as the change in the velocity and direction of the plate's motion. It is generally accepted that the Anatolian plate rotates as

a rigid block with an average velocity of at least 22 mm/year, while the Aegean block deforms internally and has a average velocity of 30 mm/year (velocities are 25 mm/year near the coast of Turkey and 30-35 mm/year at the southwestern part of the Hellenic arc) (Papazachos, 1999). The deformation within the Aegean block is mainly in the form of east-west trending grabens created by north-south extension. There is some disagreement over whether the Aegean-Anatolian plate acts as one rotating plate or as two plates separated by a distinctive plate boundary. Reilinger et al. (1997) suggest that the two regions act as one rotating entity and that the increase of internal deformation towards the south-west can be explained by the close proximity of the southwest portion of the plate to the pole of rotation. Papazachos (1999) (as well as Jackson and Mckenzie, 1988) however, suggested that the rate of plate motion in the Aegean region is much higher than can be explained by the single rotating plate theory. They, therefore, suggest that although a distinct boundary has yet to been defined, the two plates must be separate entities. The boundary is thought to lie over a diffuse zone of east-west trending extensional grabens that lie near the south and west coast of Turkey. They also suggest that the Aegean plate's rate of deformation is explained by a combination of the forces translated from the rotating Anatolian plate and from an additional north-south extensional field.

1.6 Purpose and Scope

As mentioned in the introductory section, the purpose of this thesis is to use reflection seismic data to provide an interpretation of the structurally complex Cilicia

Basin. The interpretation should provide insight into the evolution of the basin and of the entire Eastern Mediterranean since Miocene time. The research to be completed for this thesis is part of a research project between the Memorial University of Newfoundland and the Institute of Marine Sciences and Technology at Dokuz Eylül University in Izmir, Turkey. The focus for this project will be data from the Outer Cilicia Basin. The Inner Cilicia and other nearby basins have been investigated more extensively by previous workers within the research group. The seismic data that will be used to complete this analysis was collected mainly during a marine multi-channel seismic reflection survey in 1992. Some of the data collected during this survey, mainly from the inner basin, have been processed and interpreted by previous workers. The remaining unprocessed data are to be taken from shot records to fully interpretable seismic profiles as part of this thesis progress.

Chapter 2

2.1 Regional setting

The Cilicia Basin is one of four genetically related Neogene-Quaternary basins that make up the sea-floor of the north-east Mediterranean Sea (see Figure 2.1). The bathymetry of the seafloor is controlled by major tectonic features and by sediment input from rivers that flow into the area from onland Turkey (Aksu et al., 1992 a,b). These major tectonic features create bathymetric highs on the seafloor and separate the basins into individual depocentres (see Figure 2.2). Within each of the basins the water depth gradually increases from the continental shelf to the central area, where water depths reach a maximum of 1300 m. West of the Cilicia Basin, the water depth drops to well over 2500 m into the Antalya Basin (Aksu et al., 2005).

The underlying crust of the north-east Mediterranean sea is a normal continental type extending from the Asian continent. The continental crust thins rapidly passing from southern Turkey, where it is ~36 km, to south of Cyprus, where it is ~14 km (Riad et al., 1981). South of Cyprus the composition of the crust changes to a more intermediate type and is therefore thought to be a part of the African plate. The crust thickens southwards away from Cyprus towards the Sinai Peninsula (Riad et al., 1981).

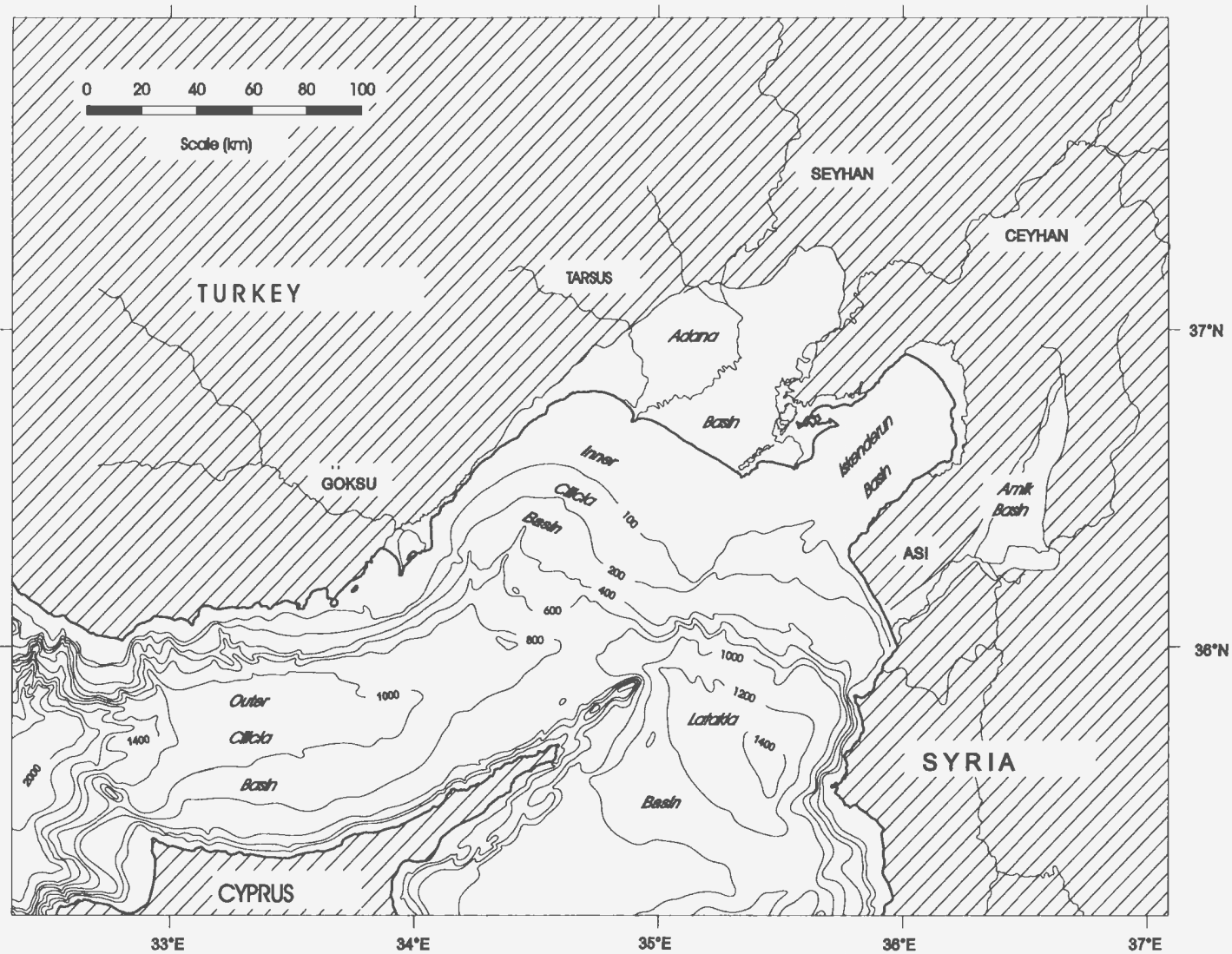


Figure 2.1: Bathymetry map of Cilicia and Latakia basins (edited from Aksu et al., 2005). Compiled using the echo sounder data collected during RV Piri Reis cruises 1991 and 1992 and the International Bathymetric Chart of the Mediterranean (Intergovernmental Oceanographic Commission, 1981).

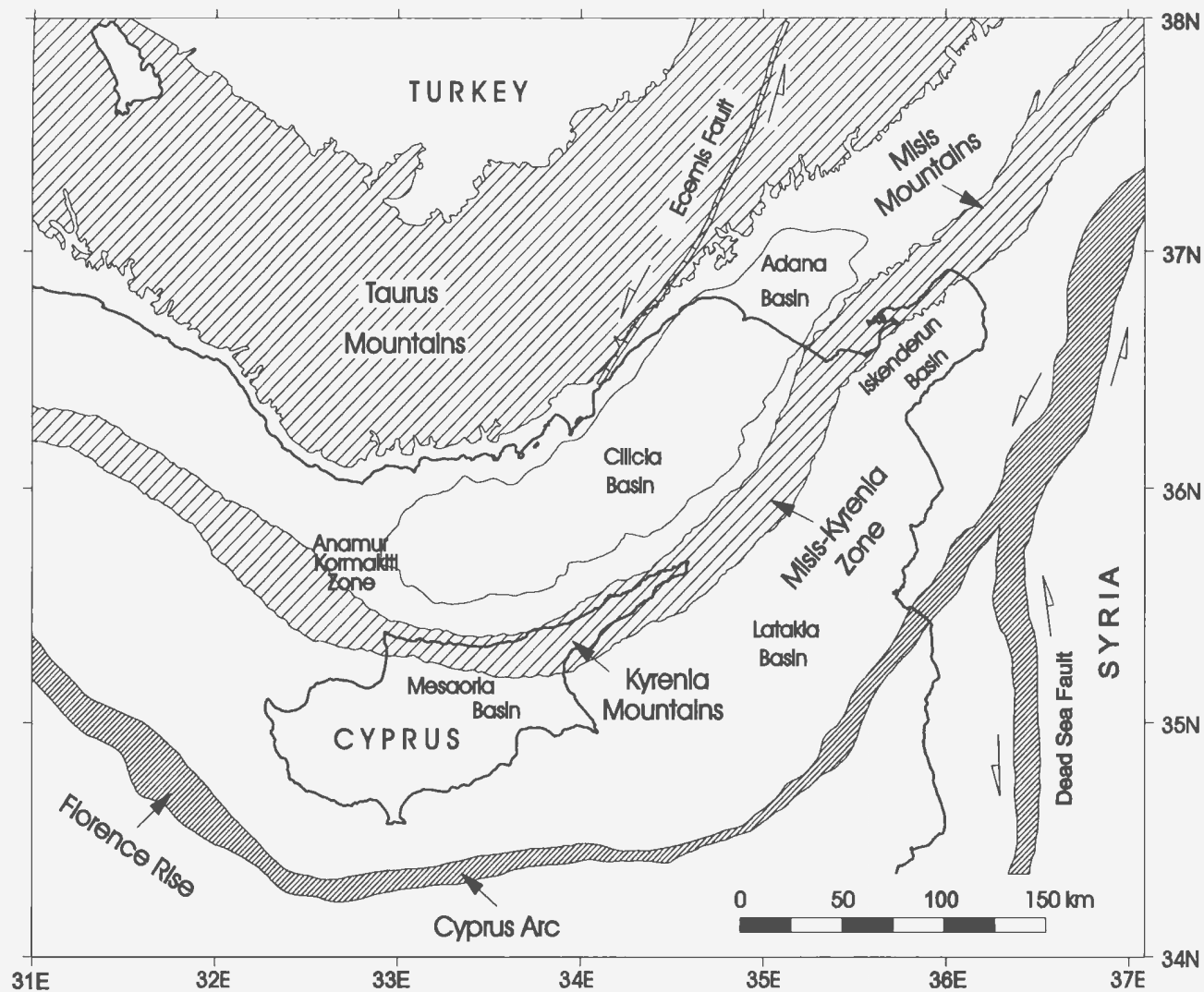


Figure 2.2: Map showing the basins of the north-east Mediterranean and the locations of the main physiographic and structural features in the study area (edited from Aksu et al., 2005).

2.2 The basins of the northeastern Mediterranean Sea

The Neogene-Quaternary basins that lie in the forearc of the Cyprus Arc are, from east to west, the Iskenderun Basin, the Lakakia Basin, and the Adana Basin with its offshore extension, the Cilicia Basin (see Figure 2.1). The Misis-Kyrenia fault, a Miocene compressional feature, separates the Iskenderun and Latakia Basins in the east from the Adana and Cilicia Basins in the west (see Figure 2.2). The Iskenderun and Latakia Basins form a fairly continuous structure, separated by a north-west trending extensional fault zone. The Cilicia and Adana Basins also form a continuous structure, with the onland Adana area being the infilled portion of the basin (Aksu et al., 1992 a). Each of the basins is north-east trending, rectangular to rhombohedral shaped depressions that have been subsiding since mid to late Miocene time. The Miocene to Quaternary stratigraphy is similar for each of the basins and consists of more than 1000 m of early Miocene siliclastics, marls and marly limestones, between 500 m and 1000 m of Messinian evaporites and 300-2000 m of Pliocene-Quaternary deltaic deposits, all overlying a pre-Miocene orogenic belt (Aksu et al., 1992 a; Mulder et al., 1975). There are at least two common erosional unconformities seen in all four basins: the first at the base of the early Miocene succession, the second at the base of the Pliocene-Quaternary succession. Four rivers (Seyhan, Ceyhan, Tarsus and Göksu) provide most of the siliciclastic input into the basins (Aksu et al., 1992 b). Three of the four rivers, namely the Seyhan, Ceyhan and Tarsus Rivers, form a major deltaic complex that occupies the Adana Basin. This leaves a much wider continental shelf in the Adana basin than in the

other three basins (see Figure 2.1). Most of the published data pertaining to these basins has concentrated on the structural and sedimentary evolution of the Pliocene and Quaternary succession.

2.2.1 The Iskenderun Basin

The Iskenderun Basin is bounded by the Misis mountains to the north-west, by a basement high flanking the Amanos fault zone to the south-east, and by an extensional fault zone that separates it from the Latakia Basin to the south-west. The basin has been divided into inner and outer zones based upon changes in structural and stratigraphic architectures (Aksu et al., 1992 a). The inner basin is characterized by an extensional fault zone which controls the sediment deposition in this part of the basin. There are at least two families of steep normal faults that affect the Quaternary succession: 1) a set of north-east trending faults that lie parallel to the Misis lineament, 2) a north trending, east dipping listric fault fan, which splayed from the southeastern boundary fault. Sediment distribution in the Iskenderun Basin is controlled by the architecture of the basin, the subsidence rate, and the distance to the sediment source (Aksu et al., 1992 b). These controls leave most of the coarse grained sediment trapped on the shelf and only finer grained shales in the deeper basin.

2.2.2 Latakia Basin

The Latakia Basin is bounded by the Misis-Kyrenia fault zone to the west, the

Iskenderun Basin to the north-east and the Amanos-Larnaka ridge to the south and east. The onland Cyprus extension of this basin is called the Mesaoria Basin. The structural architecture of the Latakia Basin is complicated and involves both compressional and extensional tectonics (Aksu et al., 1992 a). The internal structure of the basin consists of a fairly narrow shelf in the eastern part of the basin, a 25 km zone dominated by normal faulting associated with the shelf to basin transition, and an outer zone controlled by halokinetic structures (Aksu et al., 1992 a). The extensional fault systems found within the basin are orthogonal to the basin-bounding faults found along the eastern and north-west boundary of the basin. The basin bounding structures are northwest-trending and southwest-dipping normal faults, which are associated with a large rollover structure containing mainly south-westerly dipping faults that cut the Quaternary succession and detach within the Messinian layer (Aksu et al., 1992 a). In the north-west portion of the basin, a thrust front associated with the Misis-Kyrenia fault zone affects the entire succession (Aksu et al., 1992 a).

The Pliocene-Quaternary sediment fill in the Latakia Basin mainly consists of silt and muds that were deposited in pro-delta plumes derived from delta plains within the Adana Basin (Aksu et al., 1992 b). Most of the sediment has been trapped on the subsiding shelf leaving deposition in the outer basin limited to mainly muddy turbidity currents (Aksu et al., 1992 b). The sediment deposition within the outer basin is controlled by, and often records, the growth of their associated salt structures (Aksu et al., 1992 b).

2.2.3 The Adana and Cilicia Basin

The Adana and Cilicia Basins form the onland and offshore portions of a continuous structure and will therefore be addressed together. The basins form an arcuate depocentre bounded to the north by the Taurus mountains and Eceemis fault zone of south Turkey, to the south-east by the Misis-Kyrenia fault zone, to the south by the Kyrenia mountains of northern Cyprus and to the west by a submarine basement high, called the Anamur-Kormakiti complex (Aksu et al., 1992 a) (see Figure 2.2). The Cilicia Basin can be separated into two domains, namely the Inner and the Outer Cilicia Basin, based on differences in structural architecture. These two domains are separated by an elongate salt ridge with an overlying collapse graben (Aksu et al., 1992 a) (see Figure 2.3).

The inner basin extends south-westwards from the Adana Basin, along the Turkish continental shelf. The main structural feature of the Inner Cilicia Basin is a north-west trending imbricate extensional fault fan with north and south dipping synthetic and antithetic listric faults which sole into a Messinian detachment surface (see Figure 2.4) (Aksu et al., 1992 a). The imbricate fan trends perpendicular to the Misis-Kyrenia fault zone and has a cross sectional width of ~ 50 km. The listric faults within the imbricate fan show a large amount of rotation and significant sediment growth throughout the Pliocene-Quaternary succession (Aksu et al., 1992 a). The structure is quite different within the onland Adana Basin, as described by Williams et al. (1995). One trend exists in the northern Adana Basin with a north-northwest-south-

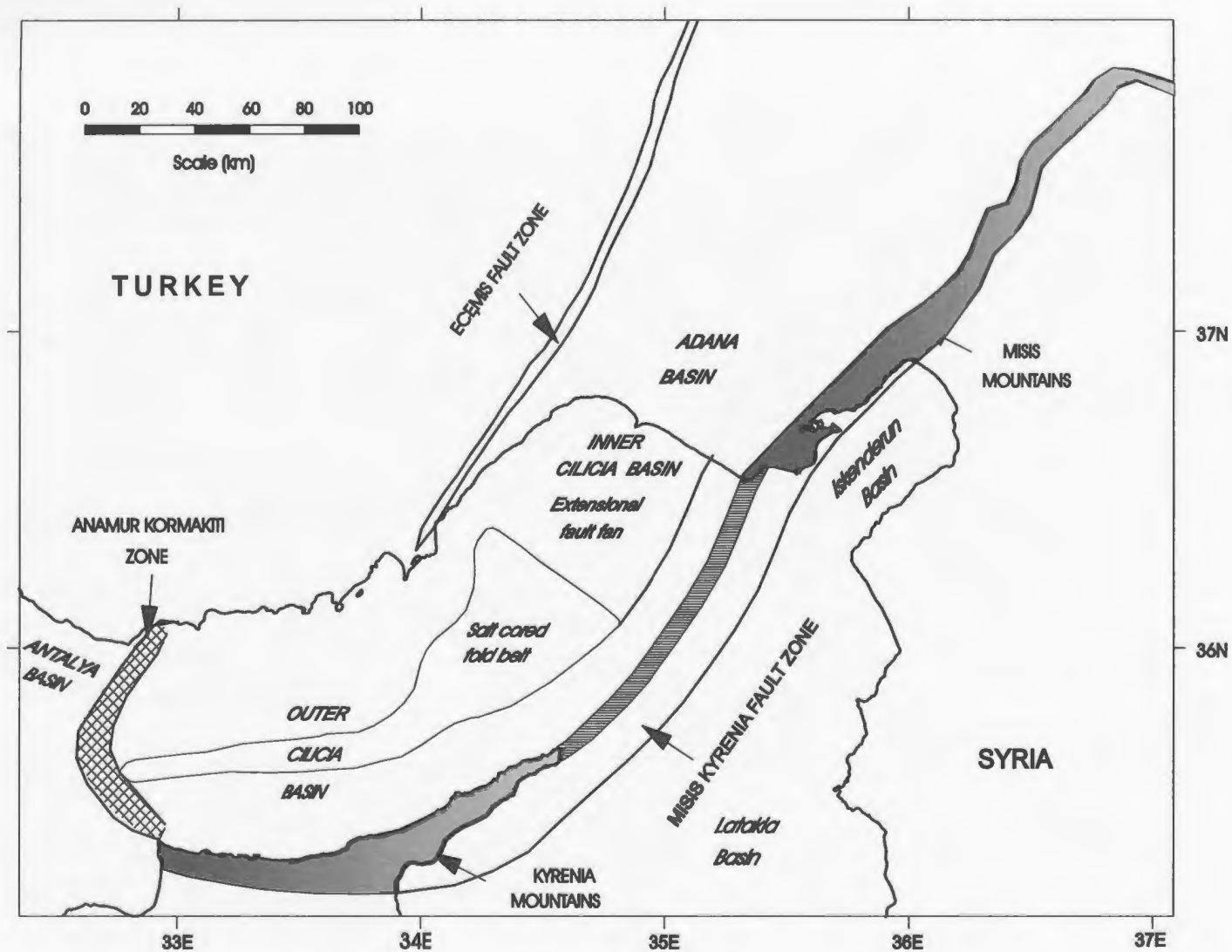


Figure 2.3: Map showing the main structural and physiographic features of the Cilicia Basin (edited from Aksu et al., 2005).

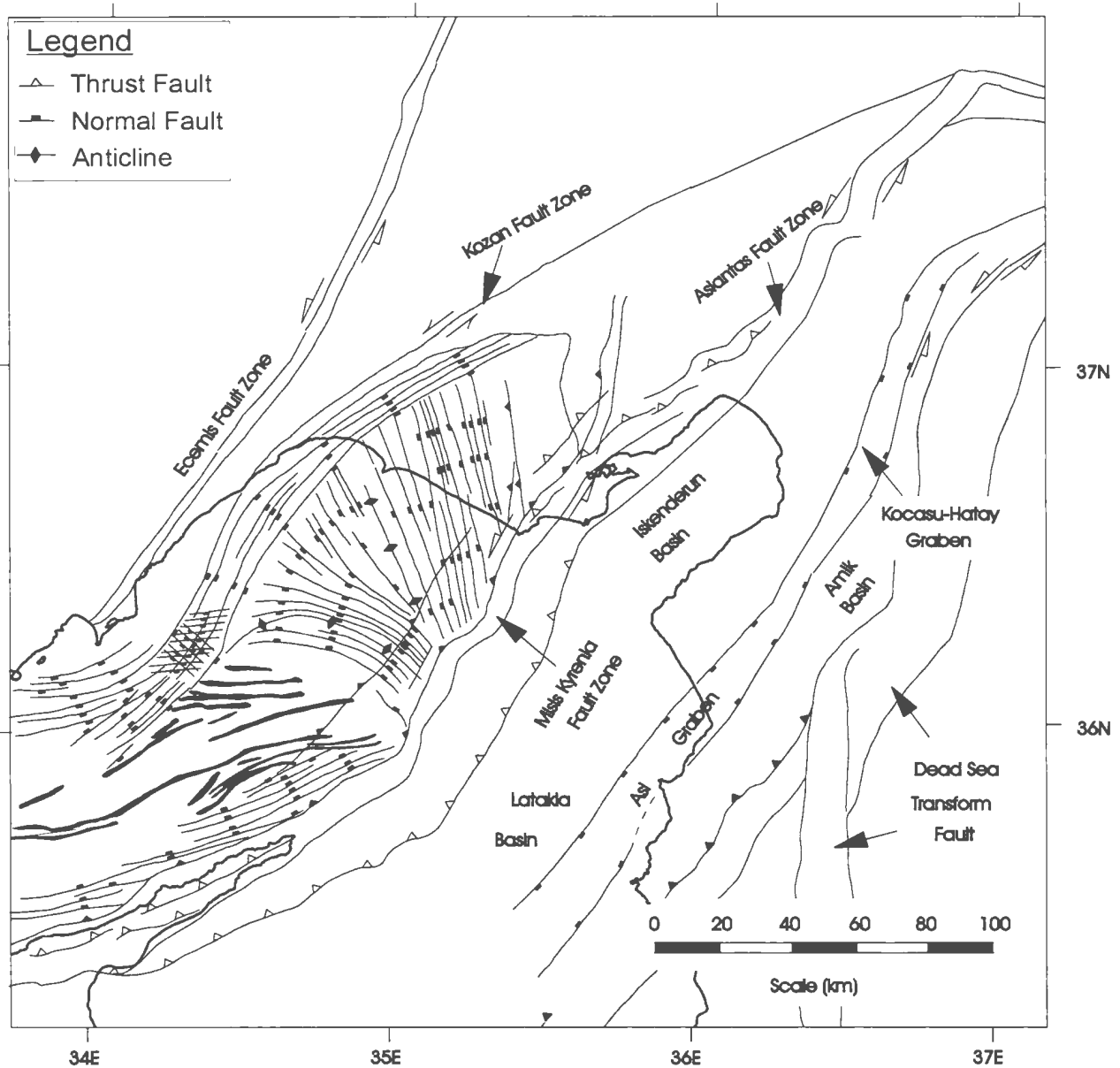


Figure 2.4: Map showing faults of the Inner Cilicia basin and the major surrounding fault systems (edited from Aksu et al., 2005).

southeast trending and west-southwest dipping extensional fault fan. The second trend is called the Imamoglou fault zone and is interpreted as a north-south trending positive flower structure that affects the upper Miocene and younger deposits (Williams et al., 1995).

Due to a southerly dip within the Adana Basin, the sequences that outcrop in the north are at depth to the south in the Inner Cilicia Basin. The stratigraphy of the Adana Basin, as described by Williams et al. (1995), consists of lower Miocene reefal deposits overlain by turbidite sediments all overlain by progradational deltaic deposits.

Exploration drilling results have also proved the presence of the Messinian salt layer directly overlying the Miocene reefal deposits within the basin (Gorur, 1995). Due to the slower subsidence rate and close proximity to sediment supply, Pliocene-Quaternary sedimentation has ‘filled’ the Adana Basin in comparison to the Inner Cilicia Basin. The sediment supply comes from deltas including those of the Seyhan, Ceyhan and Taurus rivers (Aksu et al., 1992 b). Although the Goksu river delta is a significant sediment source for the Outer Cilicia Basin, it deposits too far to the south-west to largely affect Adana’s or the Inner Cilicia Basin’s sediment fill (see Figure 2.1).

Modern sedimentation within the Inner Cilicia Basin predominantly occurs within 30 km of the shoreline and consists of silt and mud from pro-delta plumes, with limited sand sheet deposition occurring during major transgressions (Aksu et al., 1992 b).

Sedimentation is concentrated near the shoreline because subsidence rates across the delta

plain are sufficient to create accommodation space, leaving only limited sediment available to pass into the deep basin. The depositional architecture of the older sequences suggest that similar deposition processes operated throughout the Quaternary. The Cilicia Basin's average subsidence rate was calculated to be 0.33 cm/ 1000 yr, with a higher subsidence rate calculated for the inner basin (Aksu et al., 1992 b).

The Outer Cilicia Basin lies between the continental shelf of Turkey to the north and the continental shelf of Cyprus to the south (see Figure 2.1). The outer basin is deeper than the inner part of the basin at about 1000 m and contains a thinner Pliocene-Quaternary sediment package (Aksu et al., 1992 a). The top of Messinian evaporites is also about 1000 m shallower than in the inner basin (Aksu et al., 1992 a). As mentioned above, the structures found in the basin are mainly controlled by salt diapirism. East-west trending diapirs with transparent cores were noted by Smith (1977) and were interpreted to be salt cored based on the velocity of the rising sediment. Evans et al. (1978) used seismic data to classify the same system of diapirs into one of several east-west trending morphologic zones within the Outer Cilicia Basin. The zones, from north to south, include the Turkish continental shelf, which is underlain by well stratified sediment cut by a zone of faults at its outer edge. Farther south, along the continental slope there is a zone of well stratified sediments that develop by progradation of the shoreline and shows complicated slumping features. Also in this zone, a keystone graben forms at right angles to the shelf just west of the Goksu delta. The next zone occupies the central basin, at the base of the slope, and is characterized by well stratified sediment folded into low

amplitude east-west trending anticlines and synclines. Farther south, into the next zone described, the anticlines increase in amplitude and many are salt-cored. These anticlines were interpreted to be asymmetric, with limbs being steeper, and possible thrusting, to the south. The zone of anticlines then ends fairly abruptly leaving flat lying sediment for the next zone. Farther south, the flat-lying sediment is cut by north dipping, low angle faults and finally growth faults at the foot of the slope. In this zone, there are surface depressions over highs in the M-reflector. They interpreted these to be either solution related collapse structures or as toes of rotational slumps. The next, and most southerly zone, is the narrow slope and shelf of Cyprus.

The most distinctive feature of the Outer Cilicia Basin is the salt cored anticline zone described above by both Smith (1977) and Evans et al. (1978). These anticlines are oriented approximately 45 degrees to both the basin bounding faults and the extensional imbricate fan seen in the inner basin. This suggests that the formation of these salt structures is not related to the deformational forces that form other structures in the basin (Aksu et al., 1992 a). The salt structures are thought to be related to diapirism triggered by the underlying pre-Messinian basement structure (Evans et al., 1978, Aksu et al., 2005).

Evidence suggests that the basin was infilled asymmetrically from a sediment source in the north-north-east, with little contribution from Cyprus or western Turkey (Evans et al., 1978). As mentioned above, the sediment source is from the delta plains of

the Seyhan, Ceyhan and Taurus rivers, as well as the Goksu river delta, which deposits just south-west of the Adana basin. The sediment found in the basin is mainly silt and mud deposited when the paleoshorelines were furthest south in the Cilicia Basin (Aksu et al., 1992 b). During these times, limited sandy turbidites may also have been deposited through turbidity current channels in the west part of the basin. Evidence for the sand deposits include thin reflective units with a ponded depositional style between the salt anticlines (Aksu et al., 1992). Turbidite basins, formed along these current channels, are one of the two main types of depocentre found in the Outer Cilicia Basin. The other type is controlled by halokinesis and appear as rim synclines on the flanks of rising salt structures (Aksu et al., 1992 a). The thickness and architecture of sediments deposited within these depocentres is controlled only by salt movement in the flanking structures. The main seismic stratigraphic configuration seen in the Outer Cilicia Basin is laterally continuous parallel reflections. The only exception is just seaward of the shelf edge where the stratigraphic signature is influenced by depositional processes and a more complex progradational, sigmoid-oblique pattern develops (Aksu et al., 1992 b).

2.3 Structural Elements of the northeast Mediterranean Sea

An understanding of how the basins described above form and develop can only be addressed in relation to other structural elements found in the area and in the context of the structural history of the entire Eastern Mediterranean. The structural elements in the general vicinity of the basins will be discussed in the following section.

2.3.1 Misis-Kyrenia Thrust Belt

The Misis-Kyrenia thrust belt is a northeast-southwest trending submarine ridge extending from the Kyrenia mountains of northern Cyprus to the Misis mountains of south-east Turkey (see Figure 2.2). The thrust belt's rugged submarine topography and internal structure is reminiscent of both mountain chains suggesting that they all form parts of a genetically related south to south-east verging thrust system (Anastasakis and Kelling, 1990; Kelling et al., 1987; Evans et al., 1978,). As described above, the Misis-Kyrenia belt forms the boundary separating the Iskenderun and Latakia Basins in the west from the Adana and Cilicia Basins in the east. The ridge ranges from 3-8 km in width and rises between 10 and 50 m above the adjacent sea floor (Aksu et al., 1992 a). Both edges of the structure are marked by steep normal faults characterized by significant throw and associated sediment growth, with the north eastern edge being the steeper of the two (Aksu et al., 1992 a; Ben-Avraham et al., 1988). The thrust belt cuts through pre-late Miocene successions, with only minimal Messinian evaporites and Pliocene-Quaternary sediments lying in depressions along the top of the ridge. This suggests that the belt has been a positive feature at least since late Miocene time. Most authors view the history of the belt to involve thrusting in the Eocene or Miocene, followed by uplift occurring into the Quaternary (Robertson and Woodcock, 1986). Networks of sub-vertical faults with straight, north-east trending traces in plan view have also been noted across the structure. These have been interpreted as recent strike-slip faults, suggesting that although the structure likely formed under compressive stress, the more recent activity involves strike-

slip motion (Aksu et al., 1992 a). Some authors also support a strike-slip origin for the Misis-Kyrenia fault belt, suggesting the belt forms a positive flower structure flanked by the surrounding basins (Kempler and Garfunkel, 1994) .

2.3.2 Kyrenia Range

The Kyrenia is a narrow, elongate, east-west trending mountain range found along the northern coast of Cyprus (see Figure 2.2). As already described, it forms the southern boundary of the Cilicia Basin and is related to the Misis-Kyrenia thrust zone. The mountain range originated in the Eocene or early Miocene but has experienced most of its uplift since the late Pliocene-Pleistocene in relation to the uplift of the entire land mass of Cyprus (Robertson, 1998 a; Robertson et al., 1991). The western and central zones of the range have experienced more uplift and contain more steeply tilted stratigraphic units, than those in the eastern zone. The units within the range show reverse faulting, with vergence toward the south, and folding against the units at the southern margin of the range (Robertson, 1998 a). The stratigraphy of the mountain chain includes Permian-early Tertiary carbonates and volcanics, Oligocene to mid-Miocene age terrestrial to shallow marine and turbidite deposits of the Kythrea group, mid-late Miocene marls and chinks of Pakhna formation, and Pliocene marine sediments of the Mirtou formation (Robertson, 1998 a; Robertson et al., 1991). Both the stratigraphy and structure of this mountain chain suggest that its history has involved at least two periods of uplift separated by a marine depositional phase. The evidence that the reverse faulting affects

only the early carbonate and Oligocene terrestrial deposits suggests that the area was uplifted prior to Miocene time. The turbiditic Miocene deposits indicate that full marine conditions had been reestablished by that time (Robertson, 1998 a; Robertson et al., 1991). Recent uplift, in conjunction with the uplift of the entire island of Cyprus, is interpreted to have started in the late Pliocene or Pleistocene, as indicated by the presence of open marine Pliocene sediments found within the uplifted mountain chain (Robertson, 1998 a; Robertson et al., 1991).

South of the Kyrenia range lies the Mesaoria Basin followed by the Troodos Ophiolite complex (see Figure 2.5). The Mesaoria basin formed in Miocene- Pliocene time and occupies an intra-montane setting between the Kyrenia range and the Troodos complex (Robertson, 1998 a). The basin extends into the Latakia basin to the east and the Antalya basin to the west. The Troodos Complex had accreted to southern margin of the Anatolian plate by late Cretaceous time and now forms the basement of the Mesaoria basin (Robertson, 1998 a).

2.3.3 Misis Mountain Complex

The Misis Mountain Complex is a northeast-southwest trending structural high in southeast Turkey that extends into the genetically related Andirin complex to the northeast (Kelling et al., 1987) (see Figure 2.2). It forms the landward extension of the Misis-Kyrenia fault belt to the north, as well as the northern boundary of the

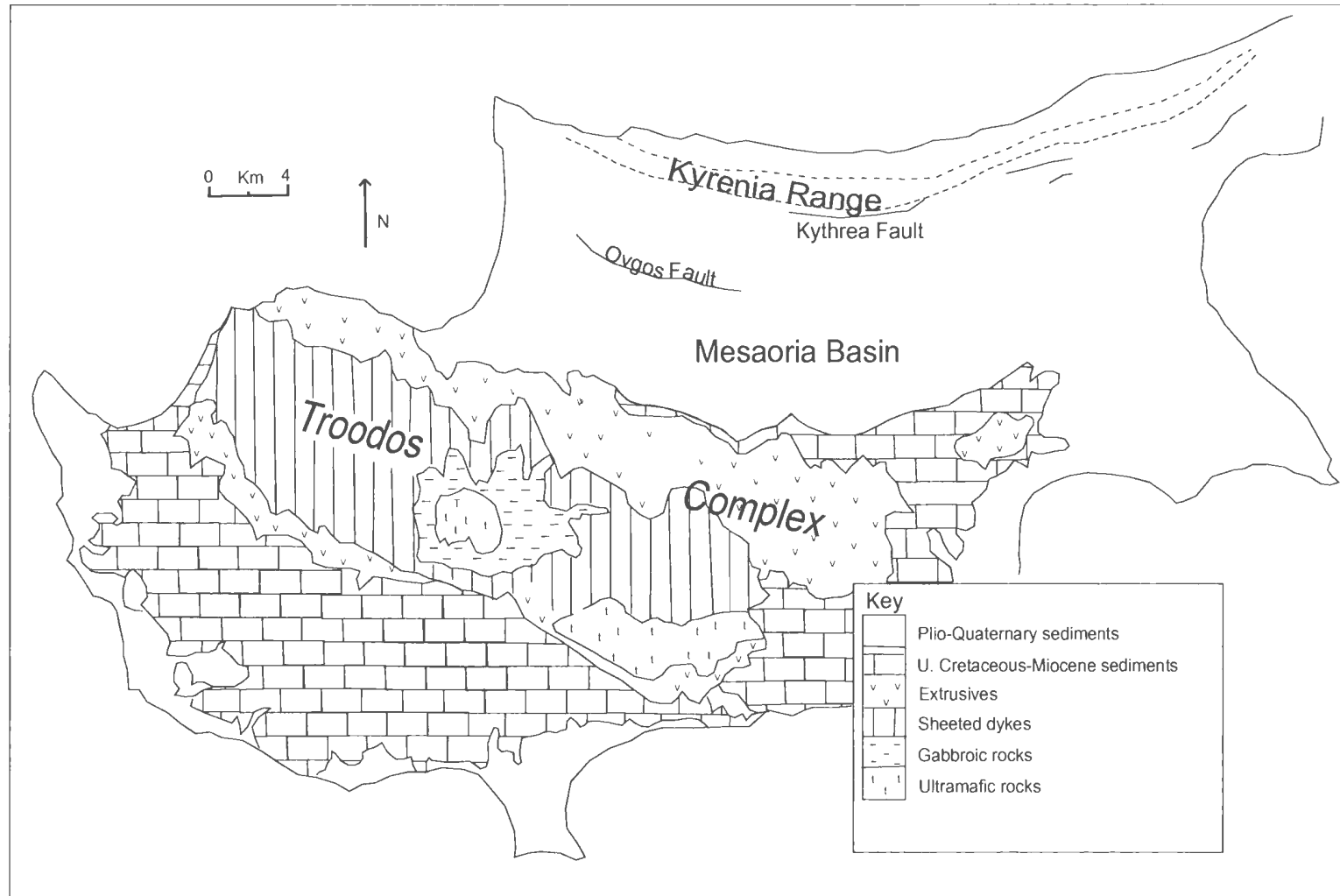


Figure 2.5: Simplified geological and tectonic map of Cyprus showing features mentioned in the text (modified from Robertson et al., 1993, 1996).

Iskenderun Basin. Within the complex, there is evidence of both reverse and strike-slip faulting suggesting that it has been uplifting in a transpressional regime since the Miocene (Kelling et al., 1987). The structure consists mainly of thick (more than 2 km) packages of steeply dipping, northwest inclined strata bounded by south directed major thrusts and reverse faults, which separate stratigraphically younger slices in an updip direction (Kelling et al., 1987). The presence of narrow fault slices of steeply dipping older rocks in the otherwise uniform stratigraphy gives evidence that strike-slip faulting occurred before and during the regional thrusting. The main stratigraphic units exposed in the range are of Tertiary age and consist of two main parts. A lower part dominated by distal volcanogenic turbidites of mid to late Miocene in age (Karatas Formation), tectonically overlain by a melange containing large blocks, derived from a Miocene volcanic arc and back arc setting, within a calcareous claystone matrix (Isali Formation) (Robertson, 1998 a; Kelling et al., 1987). The sedimentary successions found in the Misis complex are basically equivalent to the successions found in the Kyrenia range, suggesting deposition under similar conditions. The transpressional deformation in the Misis complex, however, commenced much earlier than the uplift in the Kyrenia range (Kelling et al., 1987).

2.3.4. The Taurus mountain range and Ecemis Fault zone

The Taurus mountains and Ecemis fault zone lie in south-east Turkey and form the north-west boundary of the Adana and Inner Cilicia Basins. The Taurides also extend across the south coast of Turkey and form the northern boundary of the Outer Cilicia

Basin. The Taurides formed mainly during the Oligocene period are one of the two east-west trending mountain ranges found in Turkey (the other is older, is found to the north and is known as the Pontide mountain range) (Robertson, 1998 a). The mountain chains record a complicated history involving a number of convergent events during closure of at least two major oceans. The continental portion of the Tauride chain is thought to have been part of the Mesozoic passive margin of Gondwana which rifted and moved northwards during the opening and subsequent closure of the southern branch of the Neo-Tethyan ocean (Şengör and Yilmaz, 1981; Robertson and Dixon, 1984). The ultimate closure of the ocean occurred during Eocene time. Due to their complicated history, the Taurides contain a variety of rock types and structures. North of the Cilicia Basin, the basement is mainly made up of the low and high grade metamorphic rocks of the Alanya Massif, along with occurrences of ophiolite successions (Robertson, 1998 a). The Alanya Massif is a nappe stack made up of three large thrust sheets that have been thrust northwards over the unmetamorphosed Mesozoic rocks of the Antalya complex, which made up the southern passive margin of the Eurasian continent. Overlying the basement rocks, Neogene extensional or foreland flexural basins that contain Miocene to Pliocene open marine sediments occur in some areas within the Taurides (Robertson, 1998 a).

The Ecemis fault zone trends northeast-southwest and extends from eastern Turkey to the northwest boundary of the Adana and inner Cilicia basins. The Ecemis is a left lateral strike-slip fault that is thought to be related to, and extend from, the larger East

Anatolian Transform Fault (Ozer et al., 1974). Other workers suggest that the Ecemis is older than both the North and East Anatolian Transform Faults and that it accommodated the internal deformation of Anatolia long before the other faults formed (Jaffey and Robertson, 2001). These workers suggest that strike slip faulting along the Ecemis fault zone began in mid-Miocene time, but that the later history of the fault is dominated by east-west extension with lesser components of strike slip. The surface expression of the fault zone is characterized by a horst-graben structure with significant vertical throws. An offshore extension of this fault zone has not been documented (Ozer et al., 1974; Aksu et al., 1992 a).

2.3.5. Anamur-Kormakiti Complex

The Anamur-Kormakiti complex is a north to north-west trending basement high that extends from the north-west coast of Cyprus to the south coast of Turkey, near Anamur Bay. The basement high separates the Cilicia Basin in the east from the deeper Antalya Basin in the west. The complex rises about 2 km above the adjacent seafloor with edges marked by a sudden break in slope, and has only a thin sediment cover (Evans et al., 1978; Koçyigit and Beyhan, 1998). Some workers have suggested that the complex is directly related to an onshore, late Cretaceous aged thrust fault called the Anamur fault, which separates the Alanya massif from the Antalya complex in southern Turkey (Ediger et al., 1993; Anastasakis and Kelling, 1990). Others have suggested that the basement high is related to an onshore, left lateral, strike-slip fault system called the Central Anatolian Fault zone, which was described to be the extension or reactivation of the older

Ecemis fault zone (Koçyiğit and Beyhan, 1997). Evidence exists, such as slumping in the Pliocene-Quaternary succession, that the lineament is an active structure but further work is required to confirm this.

2.3.6. Amanos Fault Zone

The Amanos is a left-lateral, northeast trending fault zone that stems from the East Anatolian transform fault (EATF) and extends along the south east boundary of the Iskenderun basin (see Figure 1.8). The Amanos fault is thought to be a major ‘left step’ of the EATF and runs parallel to the Dead Sea fault along the Syria/Turkey border (Perinçek and Cemen, 1990). Between the Amanos and Dead Sea fault, an extensional basin called the Amik basin forms. This basin is significant as it is thought to contain the NW-trending faults that provide a connection between the Amanos and Dead Sea faults and hence is the location of a triple junction between the African, Arabian and Aegean-Anatolian plates (Perinçek and Cemen, 1990). The morphology of the Amanos fault zone is a horst and graben structure characterized by significant vertical throw (Perinçek and Eren, 1990).

2.3.7. Amanos-Larnaka Ridge

The Amanos-Larnaka ridge is a submarine basement high that extends from the Amanos fault of south Turkey to the west coast of Cyprus (see Figure 1.7). The ridge forms the south and east margin of the Latakia Basin and parallels both the Misis-Kyrenia thrust belt and the Latakia ridge to the south. The ridge is associated with large gravity and magnetic anomalies which suggests a possible ophiolite core possibly extending from

ophiolites onshore Cyprus, such as the Troodos complex (Ergün et al., 2005, Ben-Avraham et al., 1995). Modeling of the gravity and magnetic anomalies suggest that the ophiolite has reduced thickness in the Amanos-Larnaka structure in comparison to those onshore Cyprus. The ridge was emplaced by south to southeast thrusting, likely as a part of a late Cretaceous to Miocene thrust system that led to the emplacement of ophiolites throughout the Eastern Mediterranean (Dilek and Moores, 1990).

2.4 Models for the formation of the Cilicia basin

The Cilicia basin formed and evolved in relation to the surrounding basins and structural features described above. It is generally agreed that the Cilicia Basin formed before latest Miocene time, based on the presence of a Messinian salt layer within the basin. The mechanisms for its formation and evolution, however, are debated. In this section, some of the existing theories for the formation of the basin will be briefly discussed.

The early theories on the evolution of the Cilicia Basin suggest that it originated through incompatibility problems arising from the generation of the FFF plate triple junction just north-east of the basin. Şengör et al. (1985) suggest that when strike slip faults meet within the continental lithosphere, incompatibility problems arise due to the buoyancy and low shear strength of the lithosphere. Their kinematic analysis, which considered the rates and directions of plate movements in the area, suggested that oblique, north to northwest directed extension should result in the area of the Adana-Cilicia

Basin. Dewey et al. (1986) support the conclusions of Şengör's kinematic analysis and suggest that although the basin could have formed as a pull apart along left lateral transform faults extending from the EATF, it is more likely that the formation resulted from incompatibility issues at the triple junction due to the westward escape of the Aegean-Anatolian micro-plate. Kelling et al. (1987) believe that the formation of the basin occurred earlier than proposed in the above models, and that it was the result of a Oligocene-Miocene phase of extension that preceded the south directed thrusting in the Kyrenia range. Karig and Kozlu (1990) also support an early Miocene transtensional phase that affected the area along the lineament of the Misis-Kyrenia fault belt and led to the formation of the Cilicia Basin. They believed that the transtensional phase was succeeded by a late Miocene transpressional phase, which produced the fold and thrust belt, and was in turn succeeded by a second transtensional phase since Miocene time. Kempler and Garfunkel (1994) believed that the Cilicia Basin has been subsiding only since mid to late Miocene time and that the Misis-Kyrenia thrust belt is an extensional feature that reached its current location through strike slip motion in late Eocene to early Oligocene time. They supported a transtensional origin for the basin, and the fault belt, and relate the origin of the extension to the orientation of the plate boundary in relation to the plate motion in the area. They suggested that since the Inner Cilicia Basin has a general northeast-southwest orientation, near parallel to the plate motion, transtensional forces will dominate. For the east-west oriented Outer Cilicia Basin, in which transpressional stress should dominate according to their theory, they explain the lack of

compressive structure by assuming that the majority of the compressive stress is absorbed within Cyprus. Ben Ayraham et al. (1995) also supported a mid to late Miocene initiation of subsidence in the Cilicia Basin. They suggested that the Misis-Kyrenia thrust belt, and its associated ridges, formed as Oligocene to mid-Miocene thrust sheets that were later overprinted by strike-slip activity. The basin then formed, as a half graben, in relation to the transform motion along the thrust belt.

Although the theories presented above vary both temporally and in the mechanism proposed for initial subsidence, most relate the formation of the Cilicia Basin to strike slip (transtensional) activity. There have been theories presented more recently that suggest the basin's formation is related to extensional forces that lack the transverse component. One of these theories is presented by Williams et al. (1995) and mainly pertains to the onland extension of the Adana Basin. They suggest that the basin formed during the early Miocene in response to load induced flexure resulting from renewed thrusting in the Tauride mountains. Another theory presented by Robertson (1998) suggests that the basin formed due to extensional forces caused by the southward retreat or 'roll back' of the subducting African plate. The variability in the theories presented for the evolution of the Cilicia Basin shows that no one theory has satisfied the data or the minds of researchers who focus on the area. The lack of good well and seismic data has prevented the development of a theory that would satisfy all characteristics of the basin and its surrounding structure. The seismic data to be analyzed for the purpose of the thesis will hopefully shed light on the evolution of this basin.

Chapter 3: Data Acquisition and Processing

The reflection seismic data processed for this thesis were collected during a 1992 marine multi-channel reflection survey. In this survey, there were over 1000 km of seismic data shot along 10 main profiles within this basin. Some of these profiles, mainly from the inner basin, have been processed by previous workers. The remaining unprocessed data, including 6 profiles or just over 600 km of reflection data, were taken from shot records to interpretable seismic profiles. The lines processed are shown in Figure 3.1.

3.1 Data Acquisition

As mentioned above, the seismic data were collected during a 1992 survey conducted with the research vessel K. Piri Reis, operated by the Institute of Marine Sciences and Technology in Izmir Turkey, using equipment provided by Memorial University of Newfoundland. The equipment included a source air gun array, a receiver/hydrophone array and a digital recording device used to write the data to disk. The air gun array included seven high pressure Halliburton sleeve guns, (a set of 2 x 40 inch³; 1 x 20 inch³; 2 x 10 inch³) working at a pressure of 2000 psi and rendering a source bandwidth of 50-250 Hz. The air guns were towed 50 meters behind the stern of the ship at a 3 metre depth below the water surface. The 3 meter towing depth allowed optimal reinforcement of the primary pulse and the pulse reflected from the air sea interface at a source frequency of 120 Hz. Shots were fired at fixed time intervals, with the interval adjusted every 10 minutes at the time of recording GPS navigation fixes, for a target shot

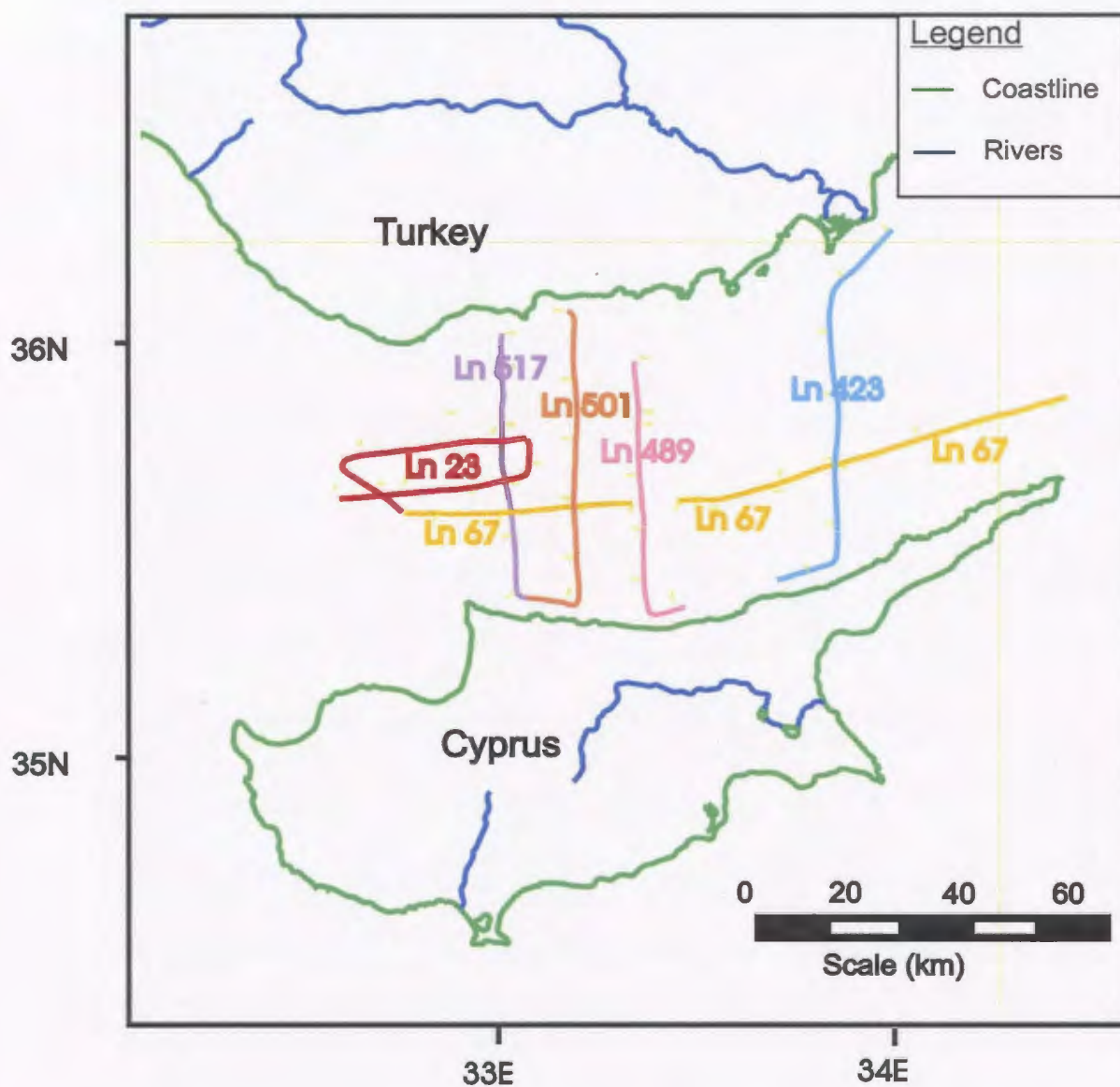


Figure 3.1: Seismic lines from the Outer Cilicia Basin processed as part of this thesis (edited from Aksu et al., 2005).

spacing of 25 metres. The fix location represents the latitude and longitude of the research vessel at the time the shot was fired. The receiver array included a 600 metre long streamer towed behind the stern of the ship and held at a 3 metre depth by streamer birds. The analog streamer consists of 48 recording channels separated by a group interval of 12.5 meters. For two lines (line 23 and 67), in order to achieve line length at the expense of fold, only the last 19 channels were deployed in the water. Along these lines, there is only a few metre offset between the source and receiver, as the first channel lies directly adjacent to the source array, and a 237.5 metre far offset (see Figure 3.2). For the lines 423, 489, 501 and 517, only data from the last 12 channels was recorded. The near and far offsets for this array is 156 metres and 306 metres, respectively (see Figure 3.3). The data were recorded with a sample rate of 1 ms and with a record length of 3 seconds. An appropriate recording delay, dependent on the water depth in the area, were applied to the data in order to record the maximum possible sub-seabed data allowed by the 3 second record length. The data were recorded on a T.I. DFS5 instrument in SEG-D format and stored on re-writable optical discs by intercepting the original 9 track magnetic tape output.

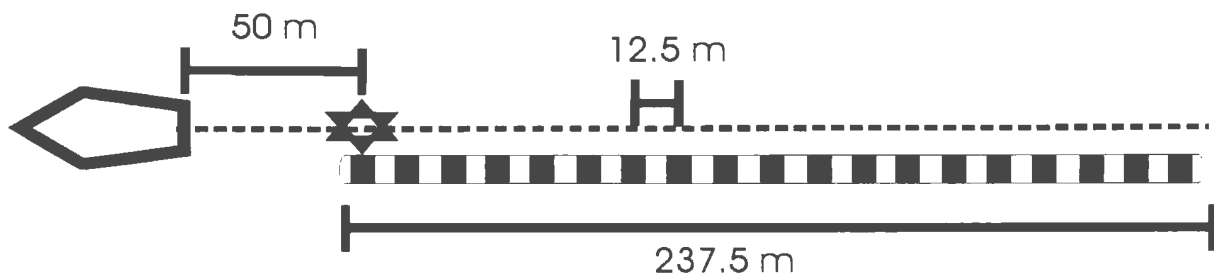


Figure 3.2: Seismic acquisition parameters for lines 23 and 67.

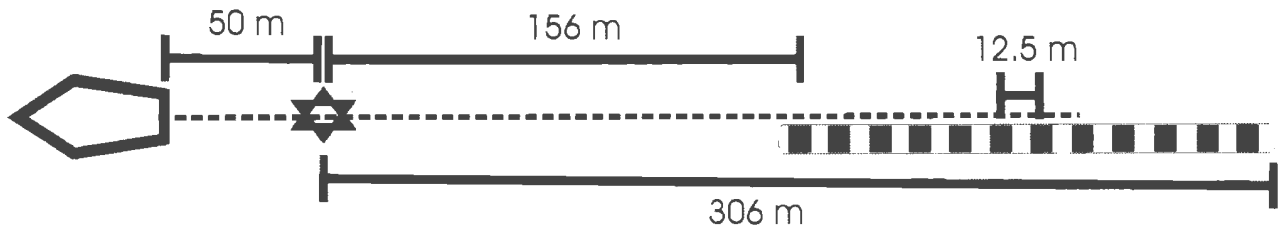


Figure 3.3: Seismic acquisition parameters for lines 423, 489, 501 and 517.

3.2 Data Processing

The data processing to be completed for this thesis involved bringing raw seismic data from shot records to fully interpretable seismic images. The Landmark based computer program, Promax, was used to complete this task. The processing flow involved a complete scheme determined through analysis of the data and changes somewhat from line to line.

3.2.1 Data Processing scheme

The general processing flow used is shown in Figure 3.4. Further discussion of certain steps are discussed in the following section.

(1) Demultiplex data. The data were recorded on optical discs in SEG-Y format. To be usable by the Promax processing package, the data had to be read from the discs and converted to the appropriate format. The converted SEG-Y data was then written to and stored on DLT tapes.

(2) Analysis of Data Quality. The data was analyzed to locate noisy traces, other noise

Data Processing Scheme

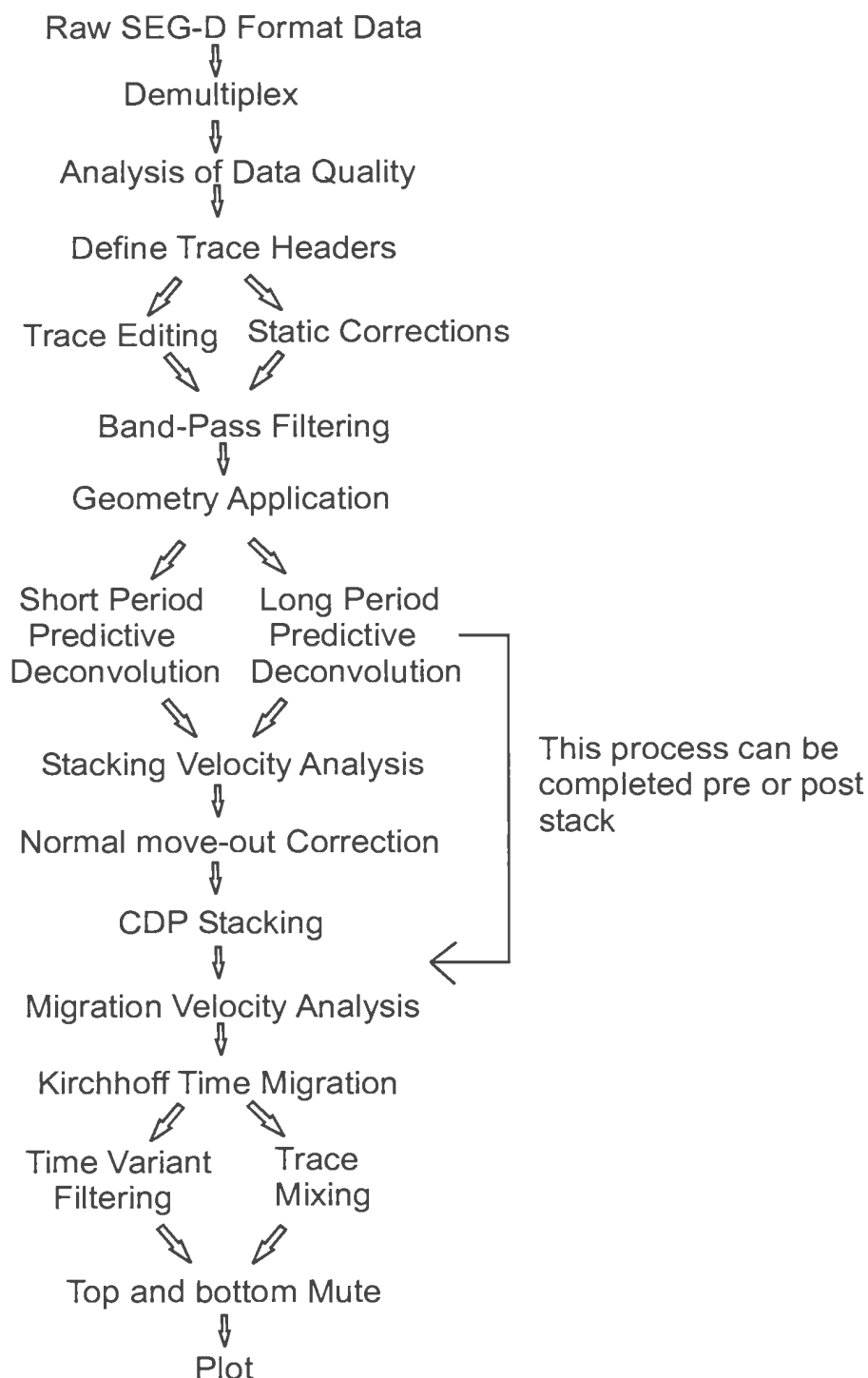



Figure 3.4: Schematic Processing Flow applied to each of the seismic lines processed for this thesis. The  symbol indicates that the below processes may not have been applied to all lines processed, their application depended on need and data quality.

problems and static shifts created by changes in recording delays.

(3) Definition of Trace Headers. Field file identification numbers and channels numbers are defined.

(4) Trace editing. Involves killing or cropping bad traces

(5) Static Corrections. Static time shifting to bring all data to the same datum.

(6) Filtering. Band Pass filter are applied to eliminate low and high frequency noise. In some cases, F-K filtering and muting is used to eliminate aliased signals.

(7) Geometry application. Geometry applied to assign source-receiver offsets and common depth points (CDP's) to the data.

(8) Predictive Deconvolution. Predictive deconvolution with short time lag applied to data for wavelet shortening. Predictive deconvolution with a longer time lag applied in some cases to eliminate short period multiples.

(9) Multiple Attenuation. Various techniques are attempted to eliminate the sea bed multiples.

(10) Velocity analysis. Involves generating semblance spectra and constant velocity stacks to pick appropriate stacking velocities.

(11) Normal Moveout Correction. Correction applied to convert data to zero offset

(12) Stack. Summing all traces for the same common depth point to increase the signal to noise ratio.

(13) Migration. Kirchhoff time migration algorithm applied to restore dipping reflectors to their true subsurface positions.

(14) Filtering. In some cases, time variant filtering is used to eliminate noise generated through migrating the data.

(15) Trace Mixing. Adjacent traces are averaged to make the reflections appear more continuous.

(16) Muting. Data is muted immediately above the sea bed.

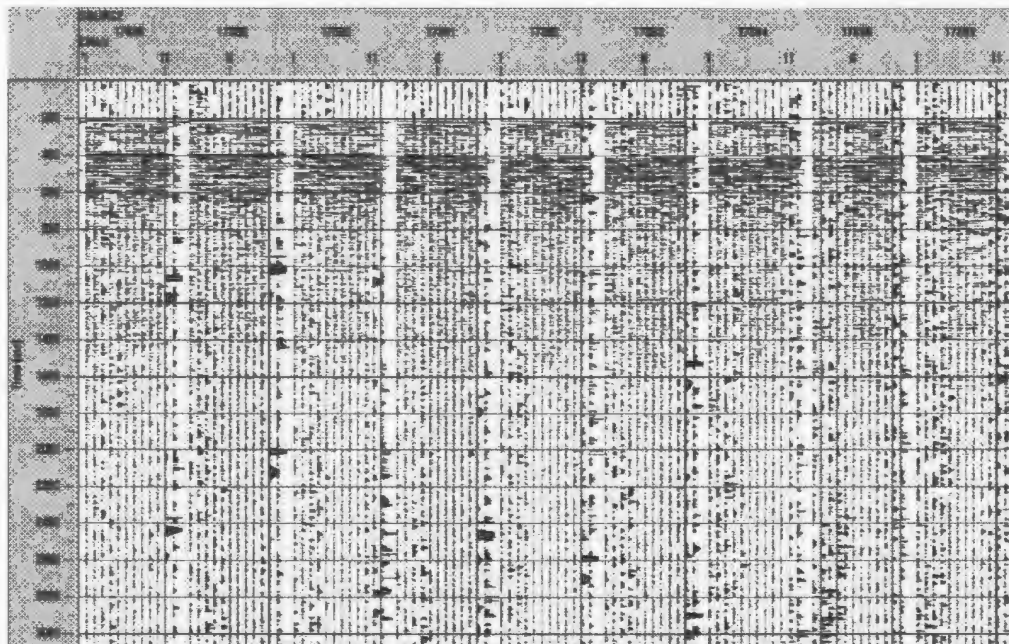
3.2.2 Definition of Trace Headers

In the data recorded for this thesis, some trace headers that are necessary for geometry application are empty. These trace headers include field identification numbers (FFIDs) and channel numbers. These headers are designated using the 'Trace Header Math' command utilizing other trace headers that have already been defined during recording. The FFID headers are defined as equal to the source identification numbers. The channel numbers are defined as equal to the sequence number in ensemble header.

3.2.3 Trace Editing

All of the lines processed required some trace editing due to noise problems in select traces. Spurious noise spikes, likely created by random noise, are a problem along certain traces. They are usually random, sometimes affecting an entire trace, sometimes just affecting a short time period along a trace. If the entire trace is affected, the trace is zeroed using the trace kill command (see Figure 3.5). If only a short time interval is affected, that interval can be selected using the windowed processing command and only that time interval of the trace is killed. In some cases, the same channel had noise

(A)



(B)

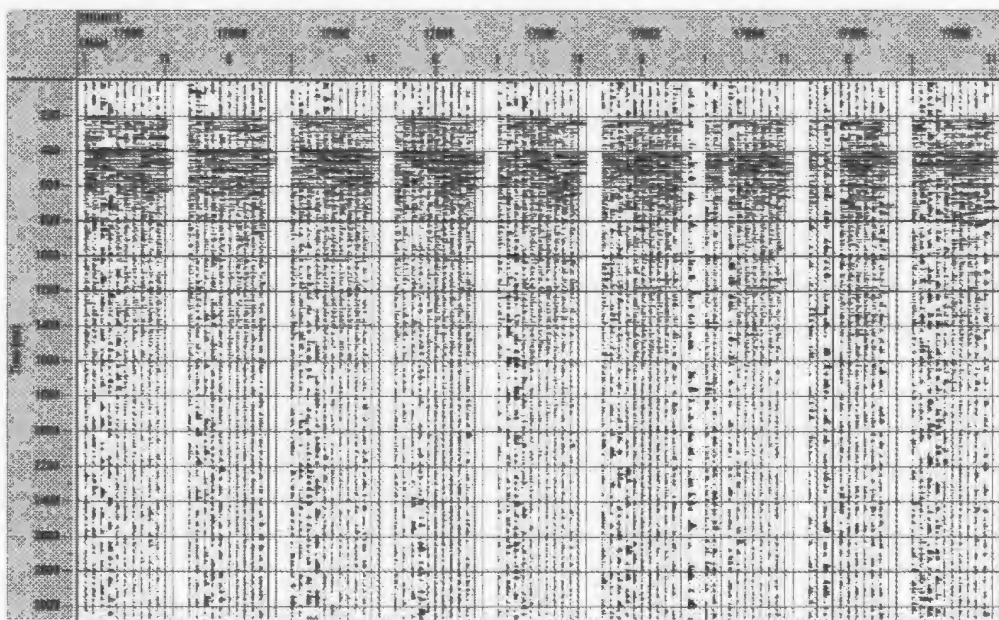


Figure 3.5: (A) Shot numbers 17888 to 17896 on line 501 showing spurious noise spikes on random channels, (B) Shot numbers 17888 to 17896 on line 501 after the trace kill command was used to zero noisy channels.

problems across numerous shots suggesting a problem with the channel during acquisition. These noise dominated channels generally do not have usable reflection data recorded even if the noise is eliminated by frequency filtering. Therefore, it is warranted to kill the noisy trace across all affected shots (see Figure 3.6).

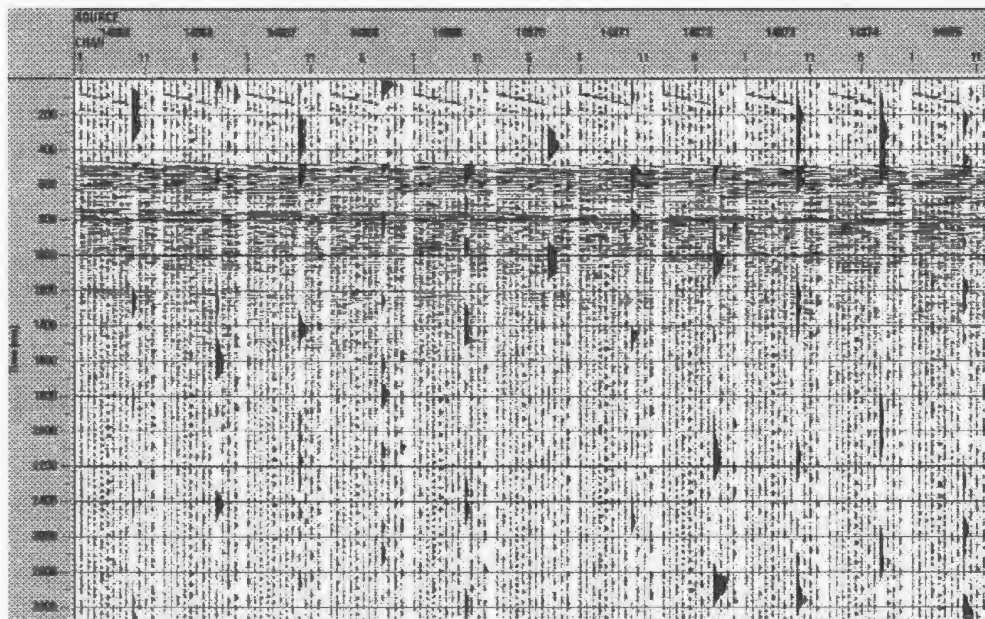
3.2.4 Static Corrections

Each of the lines processed for this thesis require some degree of static correction. Some of the adjustments were recorded as time delays in the recording log and are easily applied to the affected shots. Other required static corrections are more random and not documented in the recording logs. These corrections are needed due to jumps in the starting time of random shots caused by problems with the recording and shot pulse generator device. The amount required for these corrections varies between 60 and 70 ms and have to be determined and applied individually for each shot (see Figure 3.7).

3.2.5 Band-Pass Filtering

Pre-stack band pass filtering was applied to all profiles to eliminate low and high frequency noise. The filter type and filter parameters were picked through analysis of the raw data and using amplitude and frequency spectra. The chosen filter was an Ormsby band-pass with a sufficiently great frequency bandwidth as to not limit the temporal resolution. The low cut filter parameters were set at 40 and 60 Hz with the high cut parameters set at 250 and 350 Hz: a minimum of two octaves is preserved. Figure 3.8

(A)



(B)

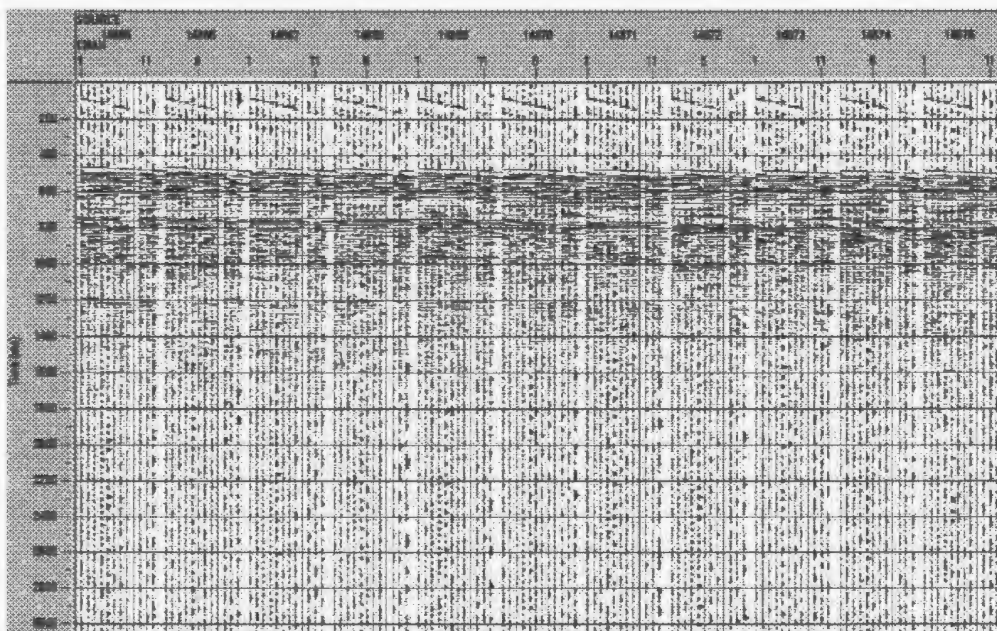
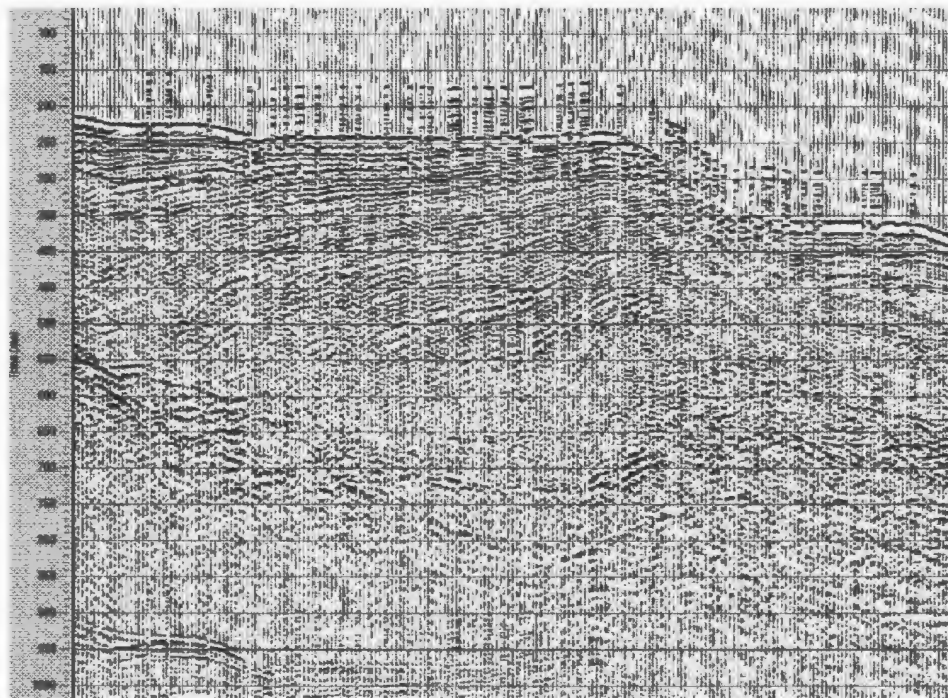


Figure 3.6: (A) Original shot numbers 14865 to 14875 on Line 501 showing a repeating noisy channel 9, (B) Shot numbers 14865-14875 on Line 501 with channel 9 effectively zeroed using the Trace Kill command.

(A)



(B)

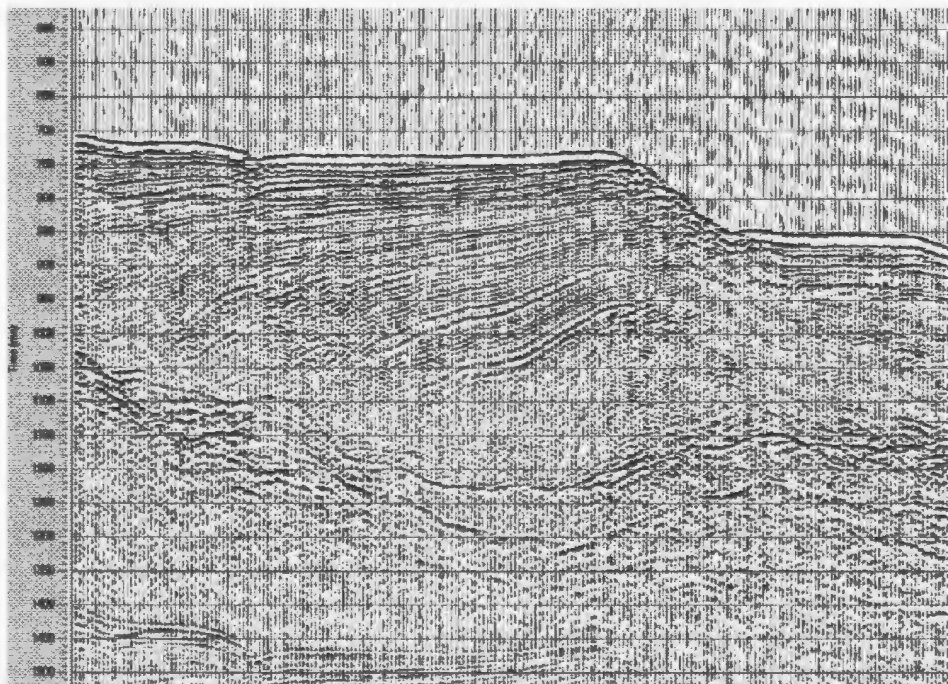
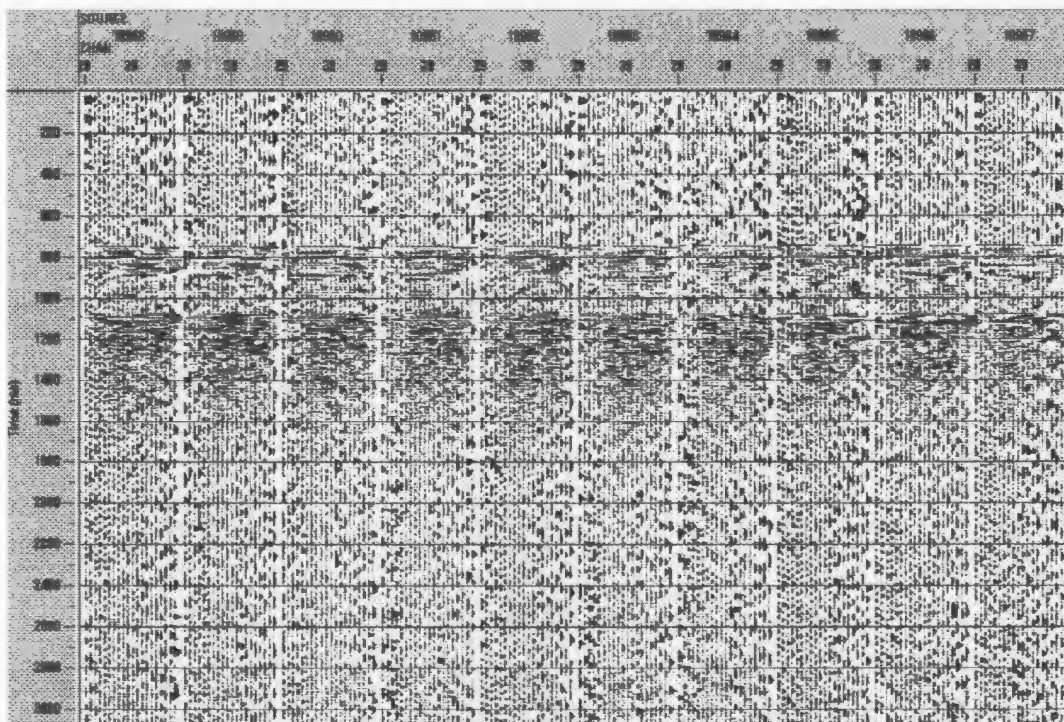


Figure 3.7: (A) Near trace gather of shots 11026-11246 on line 489 showing the random jumps in record starting time, (B) Near trace gather of shots 11026-11246 on line 489 after static time shift corrections

(A)



(B)

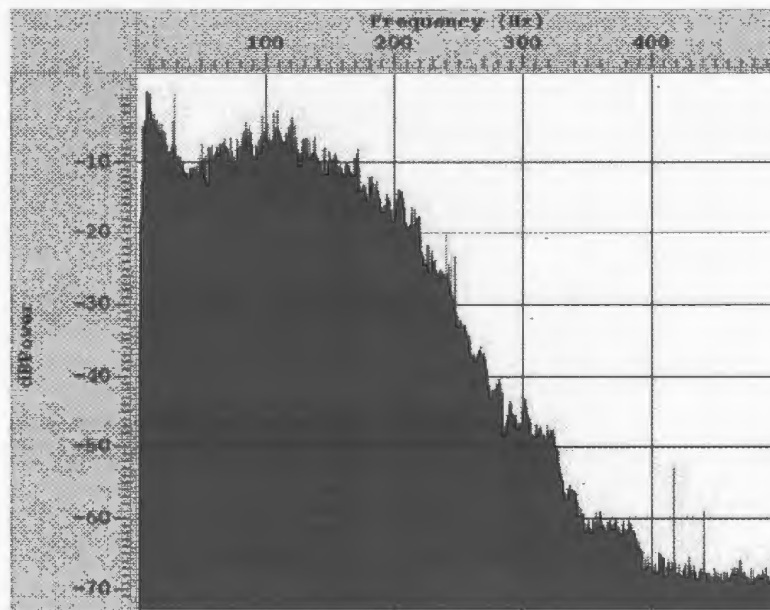


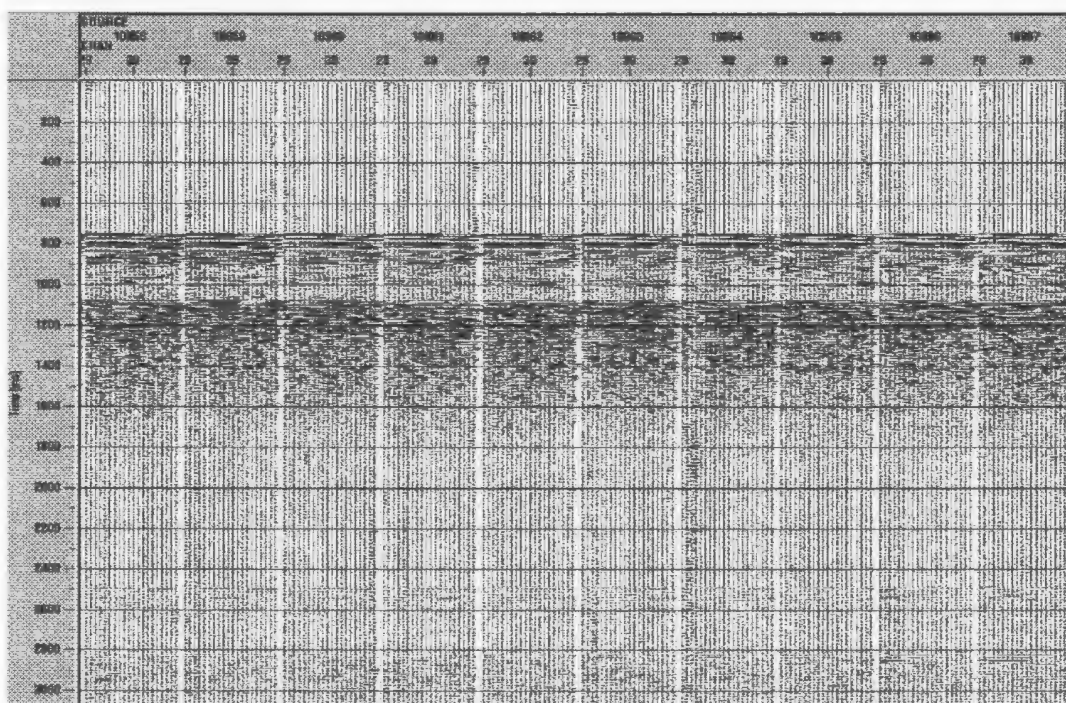
Figure 3.8: (A) Original unfiltered data for selected shots along line 67, (B) amplitude spectrum of the shot gathers shown in (A).

shows some original shot gathers from along line 67 without any filtering applied. Figure 3.9 shows the same shot gathers after band-pass filtering. The filter was effective mainly in attenuating the low frequency noise in the data.

3.2.6 F-K Filtering and Muting

F-k filtering and muting were necessary on line 423 and line 501 to remove the effects of spatial aliasing of the shallow reflections. In both lines, spatial aliasing occurs in areas where the sea bed is very shallow near the Turkish margin. The shots affected are shots 62-415 on line 423 and shots 21243-21274 on line 501. Spatial aliasing occurs in these areas due to under-sampling of the shallow subsurface created by a source-receiver offset and a group interval that are too large to sufficiently sample the shallow layers. Figure 3.10 shows the spatial aliasing effect on the shot gathers and on the frequency spectrum from line 423. Spatial aliasing is obvious on the shot gathers shown in Figure 3.10 (A), as the peaks marking the early reflections are difficult to track across all channels as they began to merge with the reflection peaks below at the far offset channels. Aliasing can also be noticed in the f-k spectrum shown in Figure 3.10 (B), where the aliased energy wraps around to the opposite quadrant past the Nyquist wavenumber. To remove the spatial aliasing, both muting and f-k filtering were attempted. The muting technique minimizes aliased energy by deleting the early arrivals of the far offset aliased channels. Figure 3.11 (A) shows the top mute picked on shots

(A)



(B)

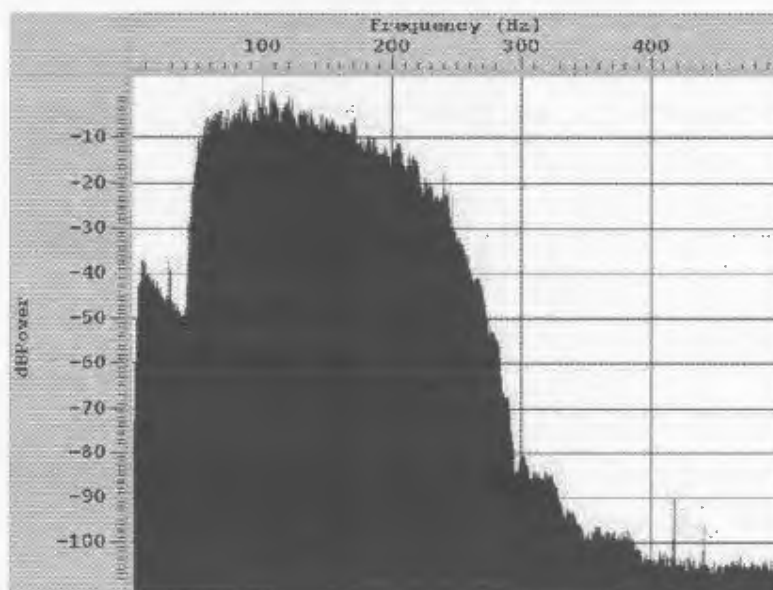
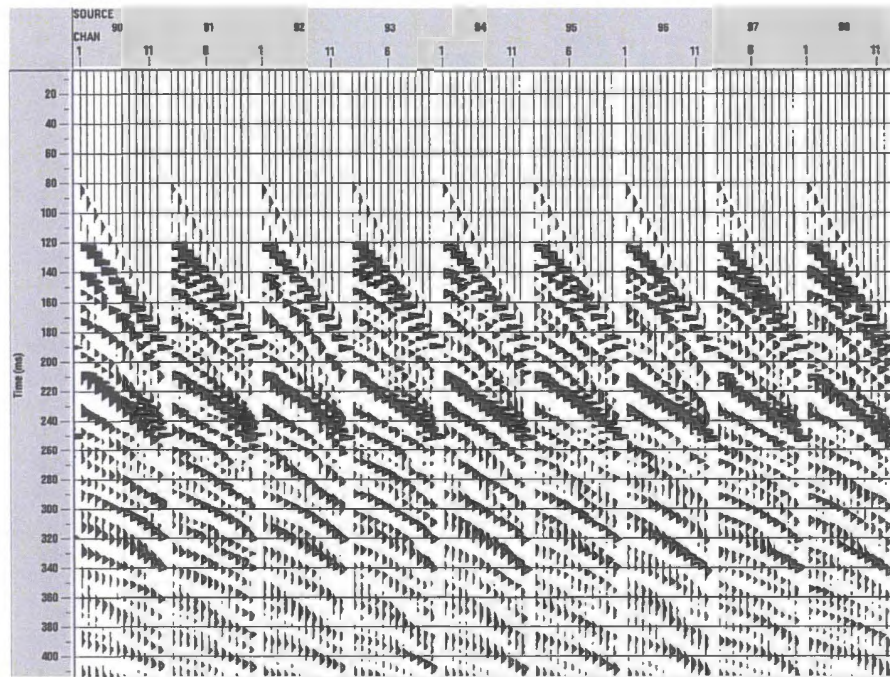
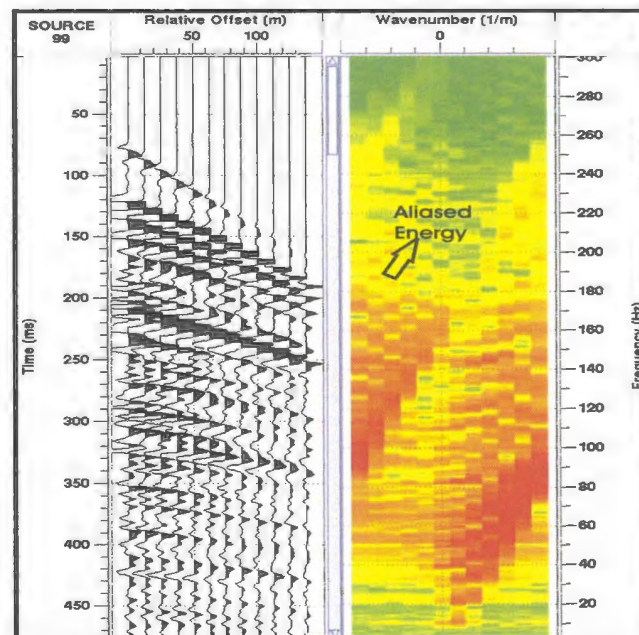


Figure 3.9: (A) Band-Pass filtered data of selected shots along line 67, (B) amplitude spectrum of the shot gathers shown in (A).



(A)



(B)

Figure 3.10: (A) Shot gathers from line 423 showing the effect of spatial aliasing in about the first 200 ms of data on the far offset channels, (B) The f-k spectrum of shot gathers shown in (A) showing the appearance of spatial aliasing in the frequency domain.

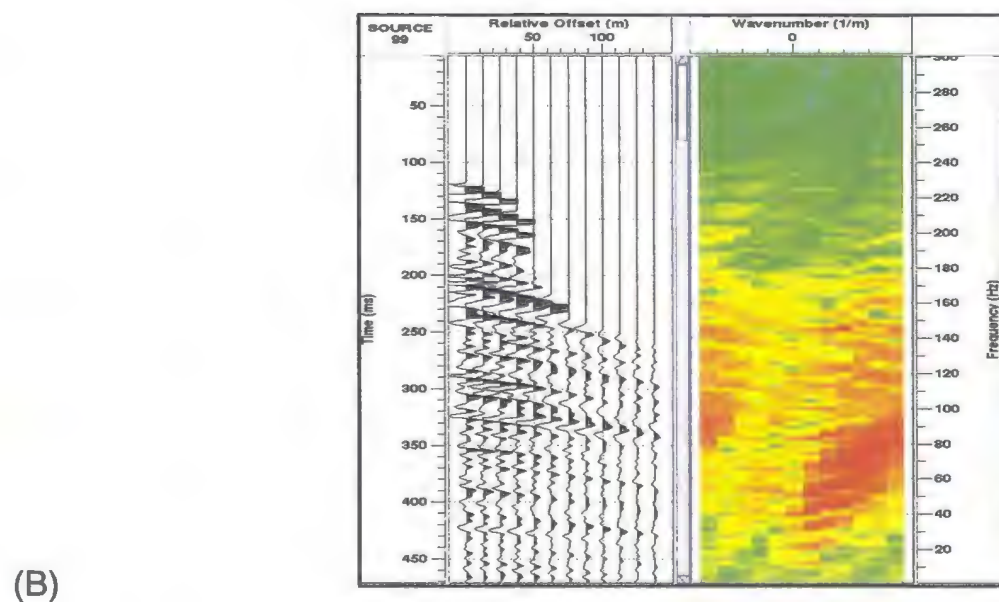
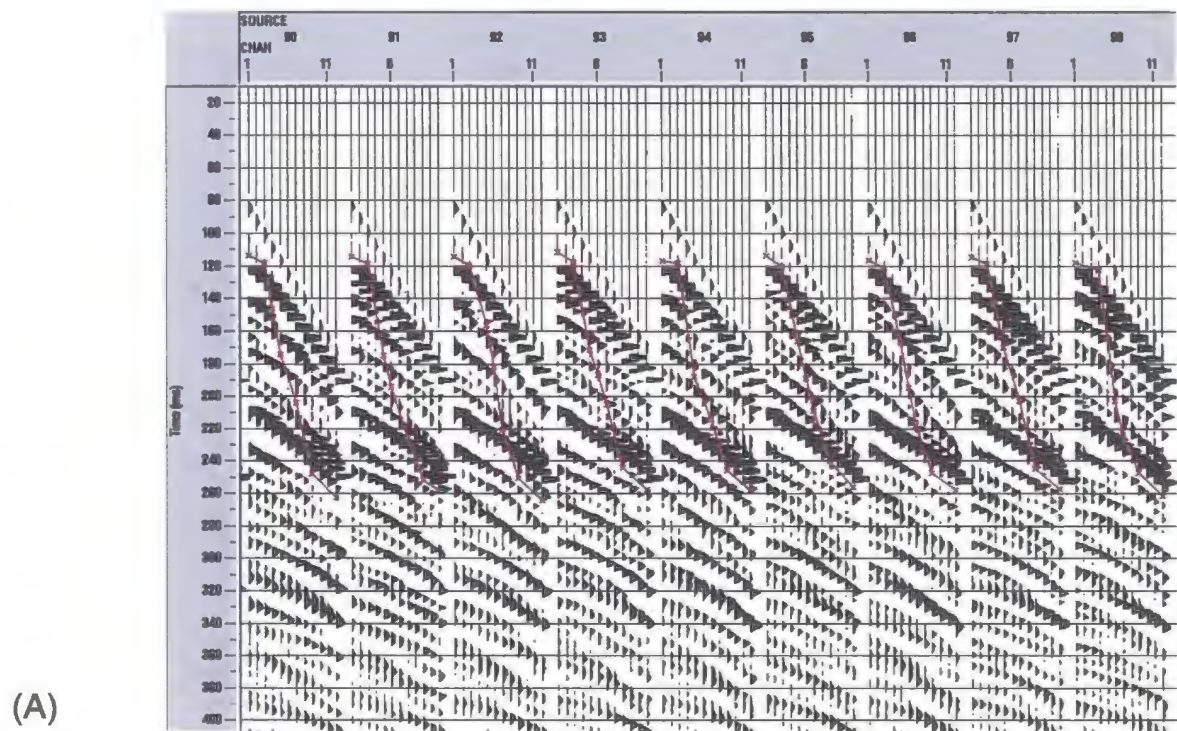


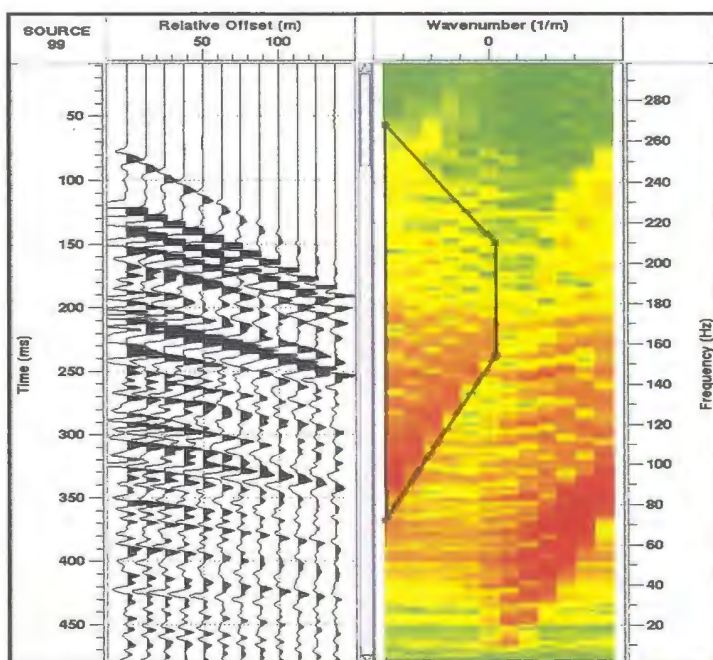
Figure 3.11: (A) Shot gathers from line 423 showing the top mute picked to remove the channels affected by spatial aliasing, (B) The f-k spectrum of shot gathers shown in (A) after the top mute was applied.

gathers along line 423. The f-k spectrum shown in Figure 3.11 (B) shows that although the muting technique does eliminate some of the unwanted energy some of the aliased energy remains. A combination of muting and F-k filtering proved to be most effective at removing the energy, as demonstrated in the frequency spectrums shown in Figure 3.12.

3.2.7 Predictive Deconvolution

Predictive deconvolution is performed on the data for both wavelet shortening and, in some areas, for the removal of short period multiples. Multiples are a problem in this data as the sea bed is generally at a depth less than 1 km. However, deconvolution was generally only useful when the sea bed appeared at 20 ms or less and the sea bed multiple repeated numerous times in the record. This approach to multiple removal will be further discussed in a following section. Pre-stack deconvolution, for signal enhancement, is performed on all lines processed for this thesis. In theory, spiking deconvolution compresses the basic wavelet to a single spike leaving only the earth's reflectivity in the seismic trace. The process should therefore rid the data of all reverberating energy and increase the temporal resolution, thereby whitening the frequency spectrum. Unfortunately, spiking deconvolution operators often add unwanted high frequencies due to noise already present in the data and due to incorrect assumptions made about the wavelet (Yilmaz, 1987). Short gap predictive deconvolution operators can also be used as a means of compressing the wavelet, often without adding the high frequencies seen when spiking deconvolution operators are used. The main difference in

(A)



(B)

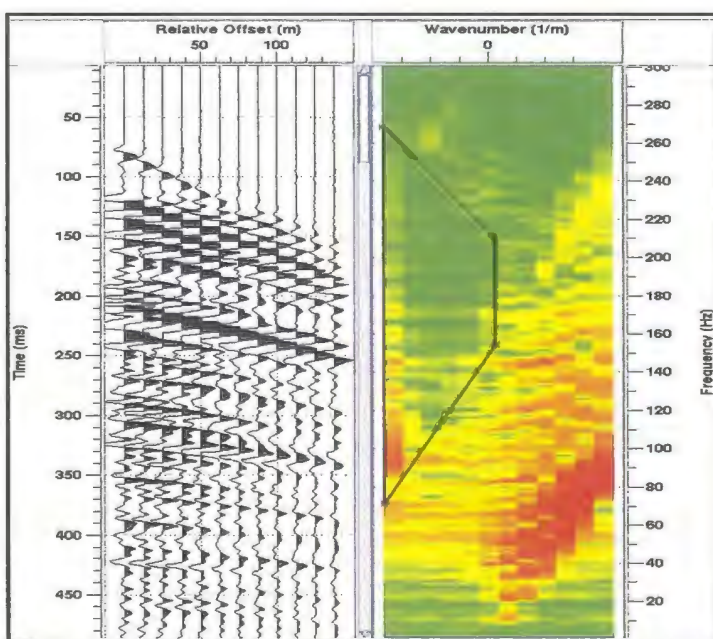


Figure 3.12: (A) F-K spectrum of the shot gathers shown in figure 3.10 showing the polygon filter applied to the data to remove the spatial aliased energy, (B) F-K spectrum of the shot gathers shown in figure 3.10 showing the result of the f-k filtering.

the two methods is that in predictive deconvolution a prediction lag, or a time gap, can be chosen which is effectively skipped in the deconvolution process. In spiking deconvolution, this “gap” is assigned as the sampling rate of your data, which in this case would be 1 ms. For this data, both spiking and predictive deconvolution operators, which both use a Wiener-Levinson least squares algorithm, were applied using various time gates and prediction lags to determine which provides the best result.

Figure 3.13 shows a non-deconvolved near trace gather of 425 shots along line 67. Figure 3.14 shows an autocorrelation function and a frequency spectrum for 20 stacked shot gathers from the same area. The autocorrelation shown in 3.14 (b) shows reverberatory energy, which the deconvolution process aims to attenuate. The same autocorrelation can be used to pick the time gate for the spiking deconvolution as well as the time gate and prediction lag for the short gap predictive deconvolution. Figure 3.14 (b) shows the 64 ms time gate window picked for the spiking deconvolution operator. This time gate is chosen as it appears sufficiently long to deal with the higher amplitude reverberations below the main spike. The result of this process is shown in the autocorrelation, frequency spectrum and deconvolved near trace gather shown in Figure 3.15. Both the autocorrelation function and frequency spectrum show that the deconvolution process was successful at compressing the wavelet and whitening the frequency spectrum, but also show the unwanted frequencies added to the data by the process. The effect of the compressed wavelet can be noticed in the resolution of the strong reflector that occurs at about 1500 ms in Figure 3.15 (c). However, the effect of

Line 67

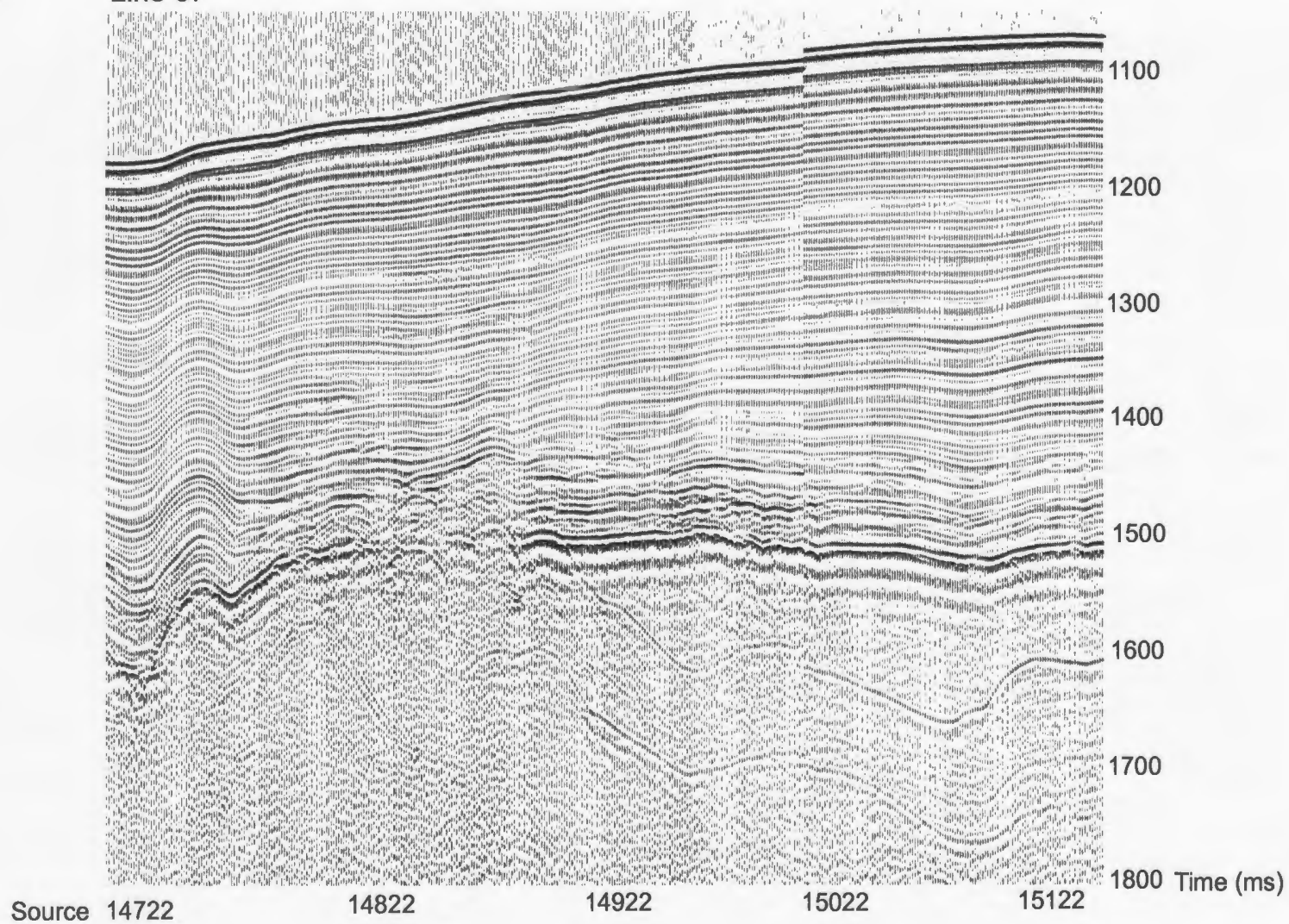


Figure 3.13: Near trace gather of non-deconvolved shots 14722-15149 from line 67.

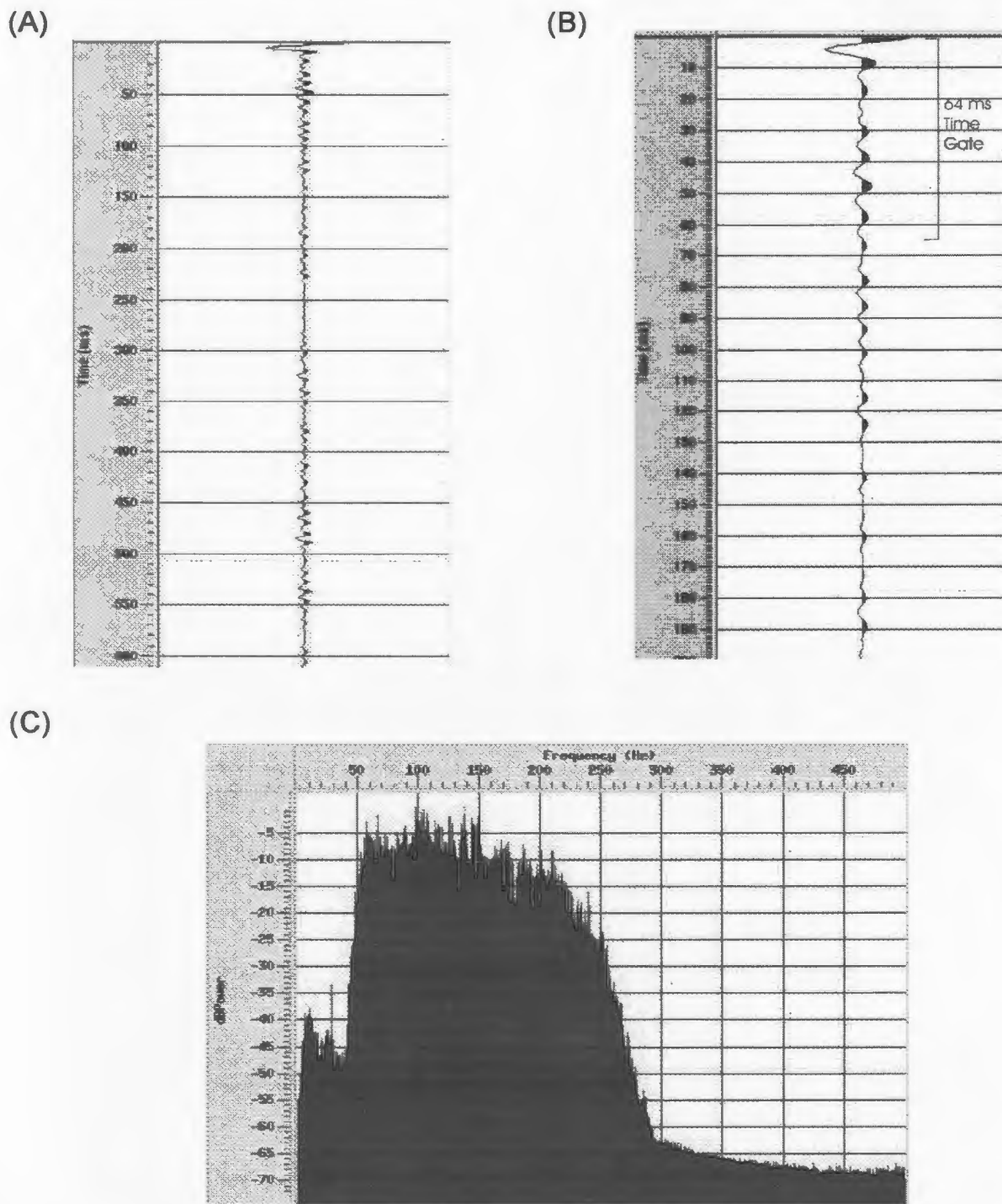


Figure 3.14: (a) 600 ms autocorrelation function calculated from shots 14800-14820 of line 67. (b) 200 ms autocorrelation function calculated from shots 14800-14820 of line 67, showing the chosen 64 ms time gate used for the spiking deconvolution (c) Frequency spectrum derived from shots 14800-14820 of line 67.

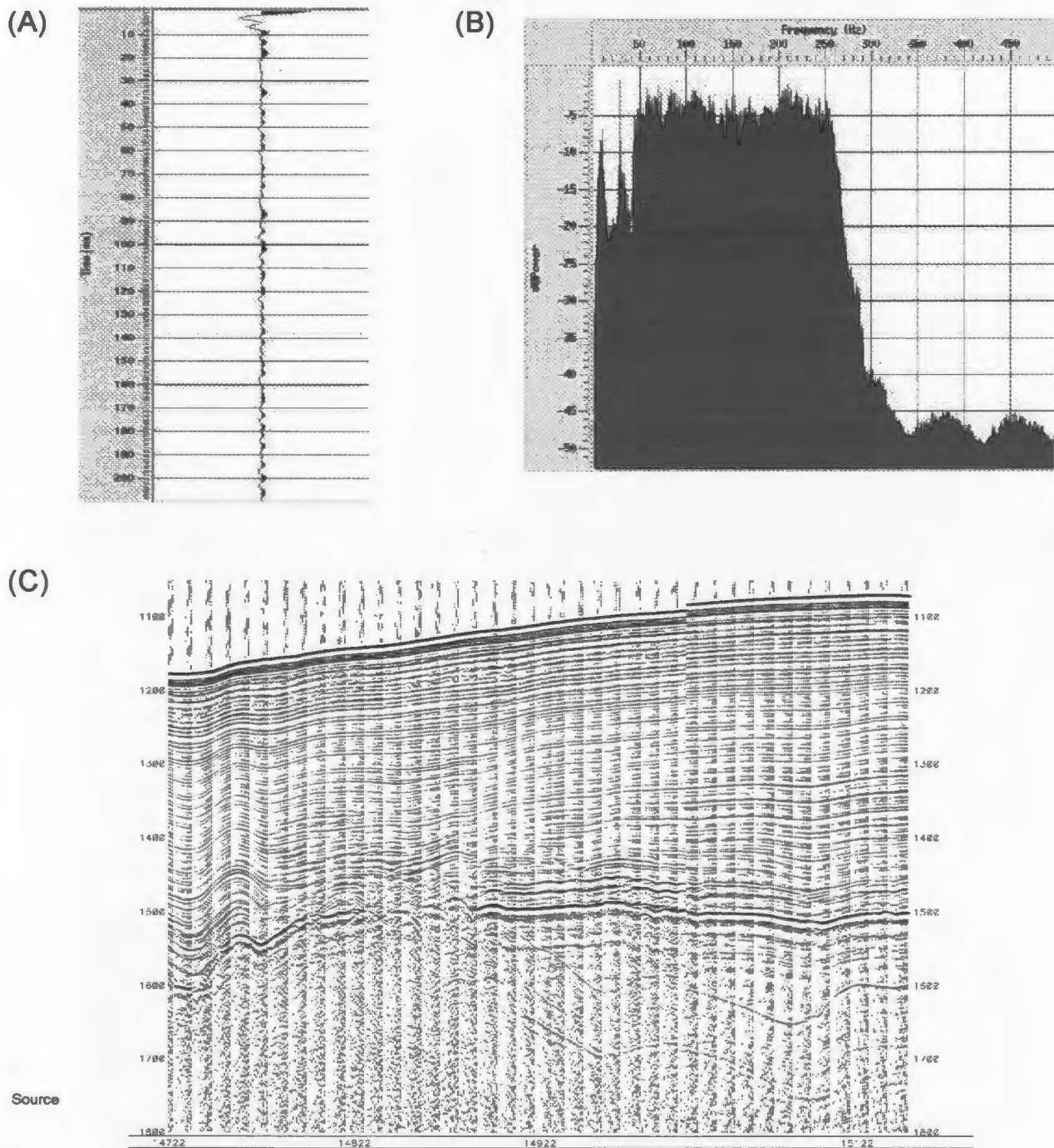


Figure 3.15: (A) 200 ms autocorrelation function calculated from shots 14800-14820 of line 67 after spiking deconvolution is applied, (B) Frequency spectrum derived from shots 14800-14820 of line 67, after spiking deconvolution is applied. (C) Near Trace Gather of shots 14722-15149 from line 67 after spiking deconvolution is applied.

added high frequencies can be seen in the near trace gather mainly in the upper part of the section from 1100 ms to 1500 ms. Deconvolution operators with either longer and shorter time gate windows were attempted but did not improve the result found with the 64 ms time gate.

Due to the inefficiencies of the spiking deconvolution operators, short gap predictive deconvolution was attempted to see if better resolution could be achieved. Operators with various prediction lags and time gates are attempted to find the best balance between a well compressed wavelet and a minimal amount of added unwanted frequencies. Some of the prediction lag and time gates attempted are shown Figure 3.16. The resultant autocorrelation functions and frequency spectrums are shown in Figure 3.17 and 3.18. Changing the prediction lag has a major impact on the data, best exhibited in the autocorrelation functions. The predictive deconvolution with a 4 ms lag has a similar effect on the data as spiking deconvolution, in that unwanted high frequencies are added. This suggests that the 4 ms lag is not a long enough to deal with this data. The 12 ms lag, however, appears to be too long as much of the high amplitude reverberation below the main spike remains after the deconvolution is applied. The 8 ms lag appears to do the best job of attenuating the reverberatory energy without adding major high frequencies to the data. Changing the time gate also impacts the data as can be seen in both the autocorrelation functions and frequency spectrums shown in Figure 3.18. The 36 ms time gate deconvolution attenuates the reverberatory energy beneath the main spike but adds an undesirable effect seen in the higher frequency portion of the frequency

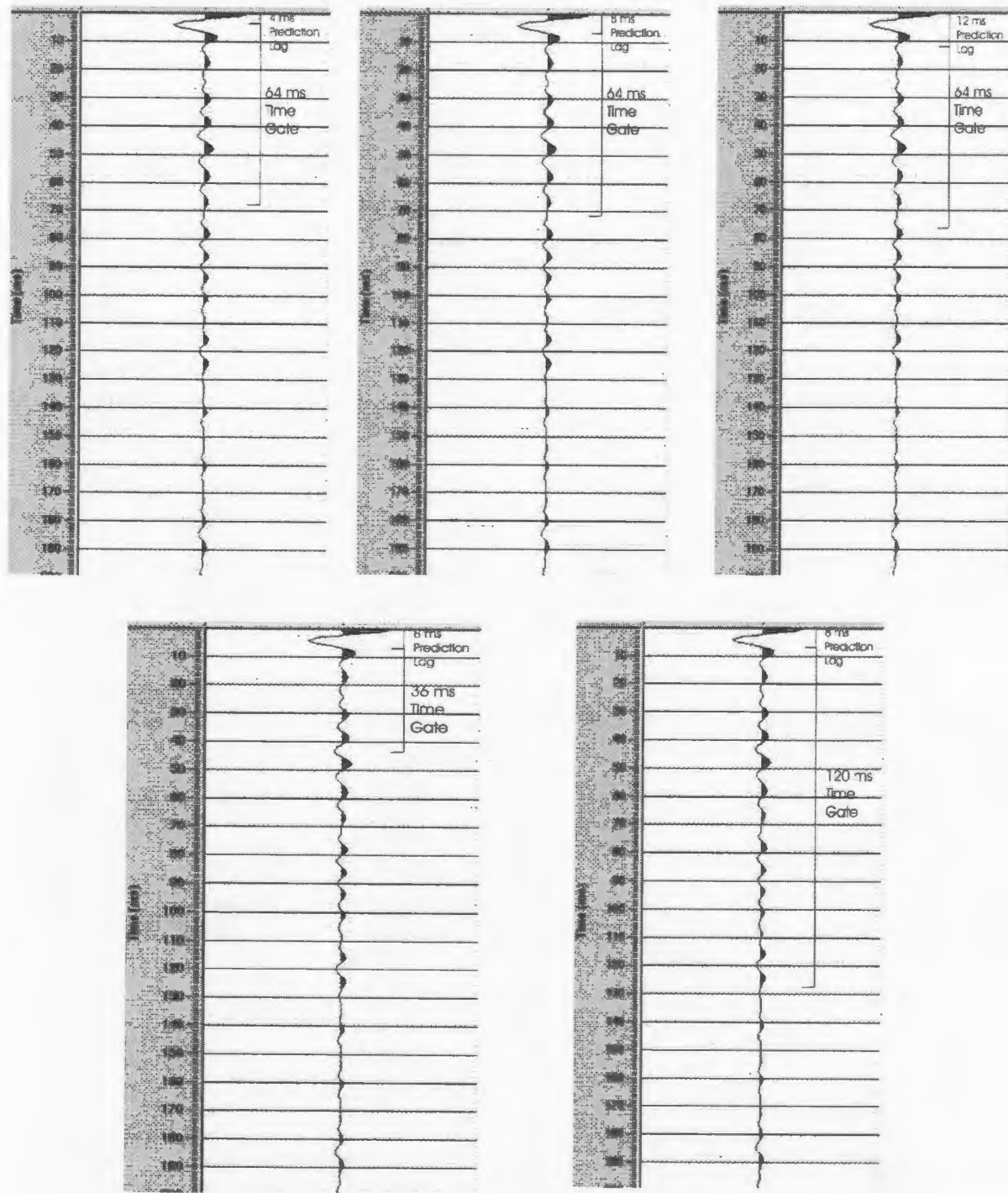
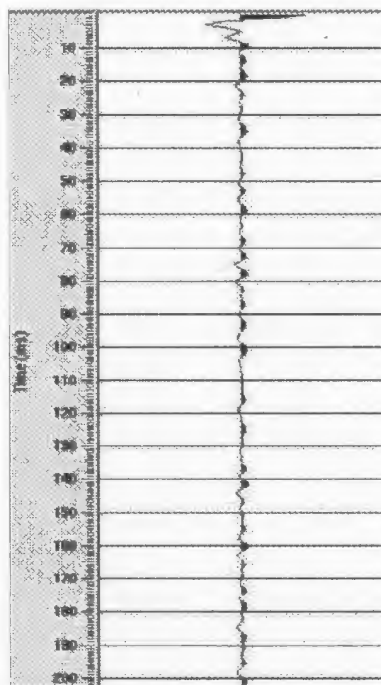
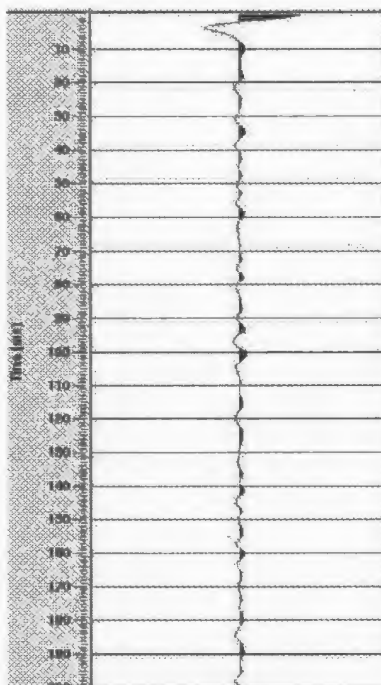


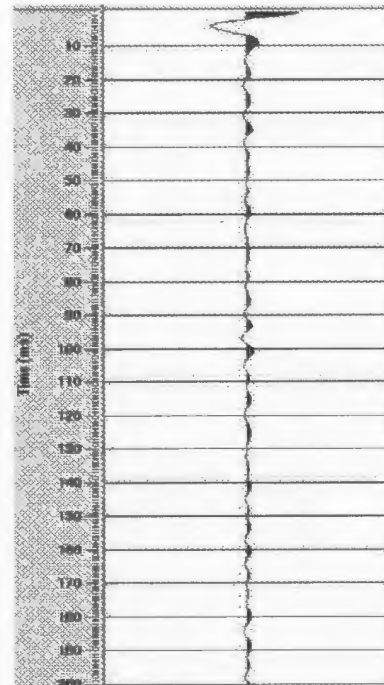
Figure 3.16: 200 ms autocorrelation function calculated from shots 14800-14820 of the non-deconvolved data of line 67 showing the various prediction lags and time gates attempted for the short gap predictive deconvolution operators.



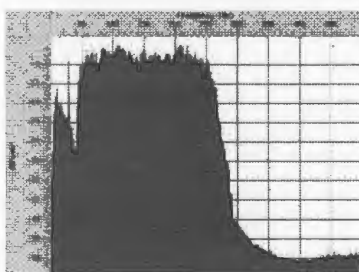
A (i)



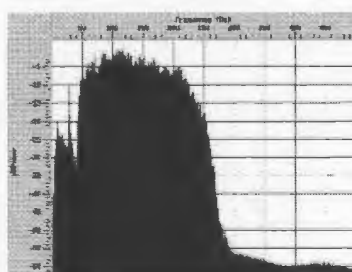
B (i)



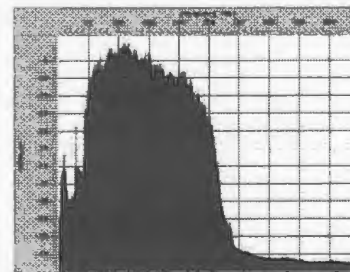
C (i)



A (ii)

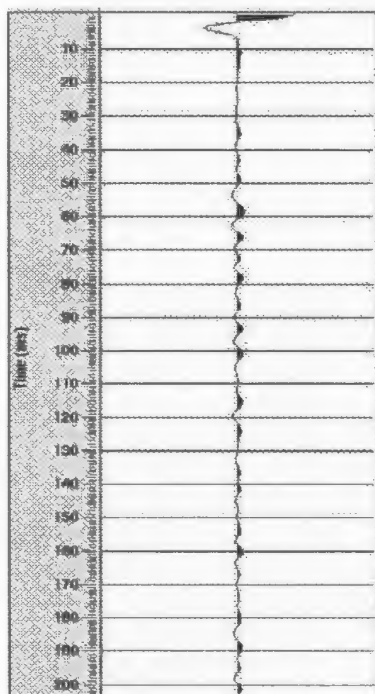


B (ii)

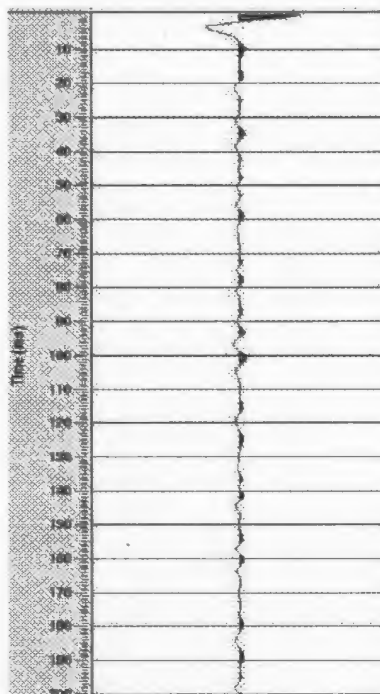


C (ii)

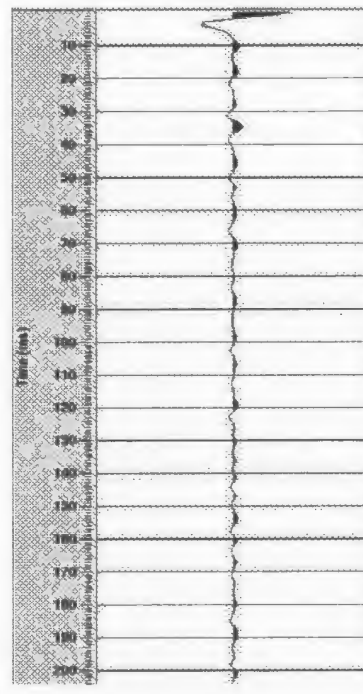
Figure 3.17: A (i) 200 ms autocorrelation function and (ii) frequency spectrum calculated from shots 14800-14820 of line 67 after predictive deconvolution, with a prediction lag of 4 ms and a time gate of 64 ms, is applied. B (i) 200 ms autocorrelation function and (ii) frequency spectrum calculated from shots 14800-14820 of line 67 after predictive deconvolution, with a prediction lag of 8ms and a time gate of 64 ms, is applied. C (i) 200 ms autocorrelation function and (ii) frequency spectrum calculated from shots 14800-14820 of line 67 after predictive deconvolution, with a prediction lag of 12 ms and a time gate of 64 ms.



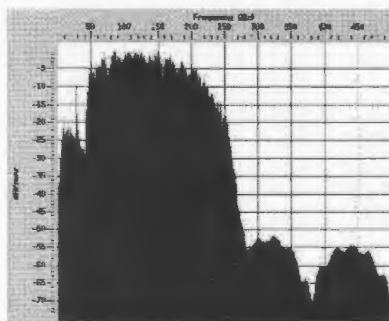
A (i)



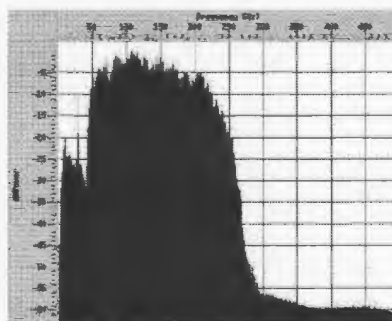
B (i)



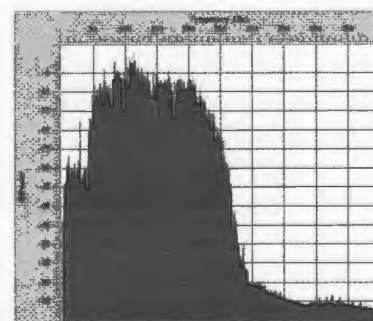
C (i)



A (ii)



B (ii)



C (ii)

Figure 3.18: A(i) 200 ms autocorrelation function and (ii) frequency spectrum calculated from shots 14800-14820 of line 67 after predictive deconvolution, with a prediction lag of 8 ms and a time gate of 36 ms, is applied. B (i) 200 ms autocorrelation function and (ii) frequency spectrum calculated from shots 14800-14820 of line 67 after predictive deconvolution, with a prediction lag of 8ms and a time gate of 64 ms, is applied. C (i) 200 ms autocorrelation function and (ii) frequency spectrum calculated from shots 14800-14820 of line 67 after predictive deconvolution, with a prediction lag of 8 ms and a time gate of 120 ms.

spectrum. The 64 ms time gate appears to both attenuate the reverberations obvious on the autocorrelation function and moderately whiten the frequency spectrum. There is no obvious improvement with the longer, 120 ms time gate which may even add noise to the data as seen in the spikiness of the frequency spectrum. Overall, the best result is found with predictive deconvolution with the 8 ms lag and the 64 ms time gate. The near trace gather of the deconvolved data seen in Figure 3.19 shows how compressing the wavelet has reduced the reverberations in the data, especially at and beneath the reflection at about 1500 ms.

3.2.8 Multiple Attenuation

Sea bed multiples are a problem in these data as the sea bed reflection generally occurs at shallow times ranging between 100 ms and 1500 ms. This leads to multiple sea bed reflections that occur at the same time and within the same frequency bandwidth as the primary reflections. This overshadowing of important primary reflections is particularly a problem in shallow areas along shelf margins and in areas with thick Pliocene-Quaternary sediment packages (see Figure 3.20 and Figure 3.21). In theory, the removal of the multiple energy will bring the primary energy to the foreground and allow those reflections to be interpreted. However, in order to remove the multiple energy there needs to be identifying characteristics to discriminate them from the primaries. There are numerous techniques possible for the removal of multiples, most of which utilize either the differential move-out between the primary and multiple reflections or the periodicity of the multiples. The techniques that utilize differential movement of the primary and

Line 67

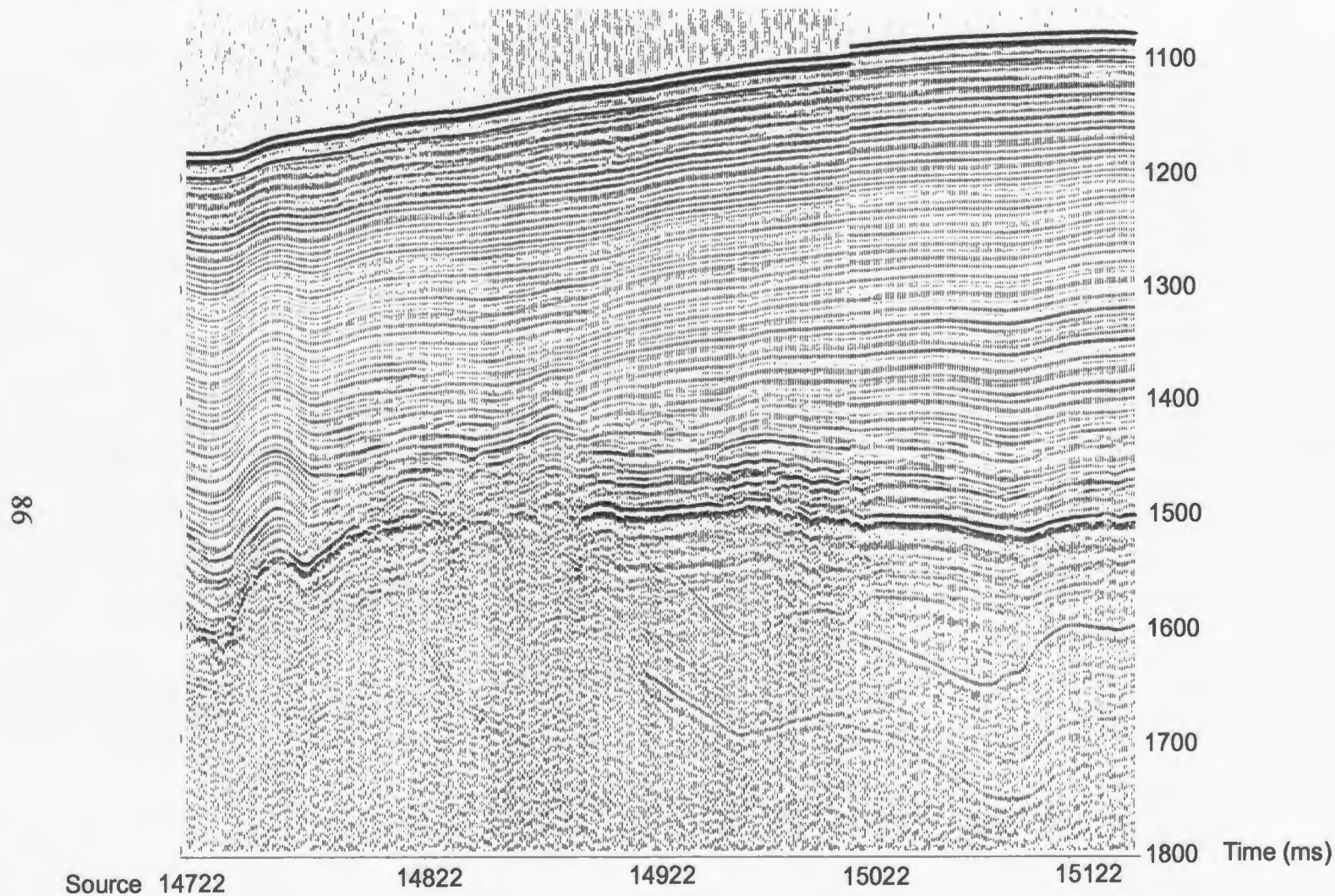
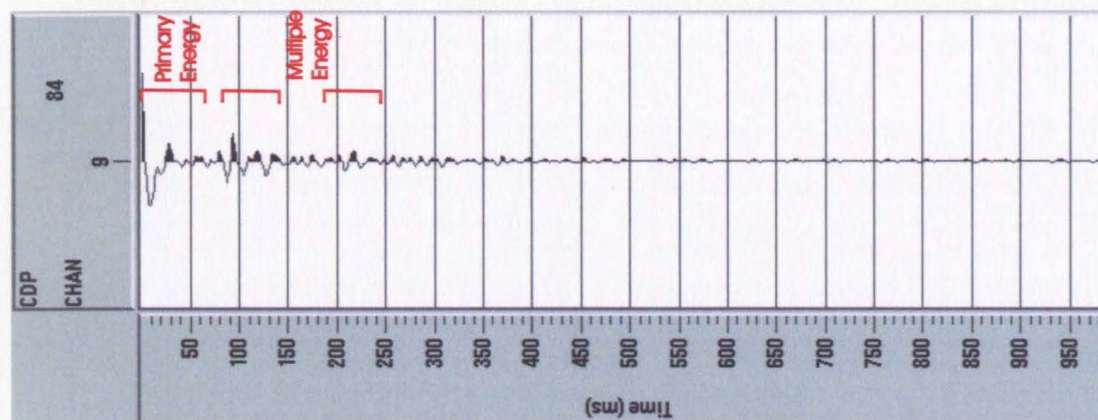


Figure 3.19: Near trace gather of shots 14722-15149 from line 67 after a short gap predictive deconvolution, with a prediction lag of 8 ms and a time gate of 64 ms, was applied. .

(B)



(A) Line 412

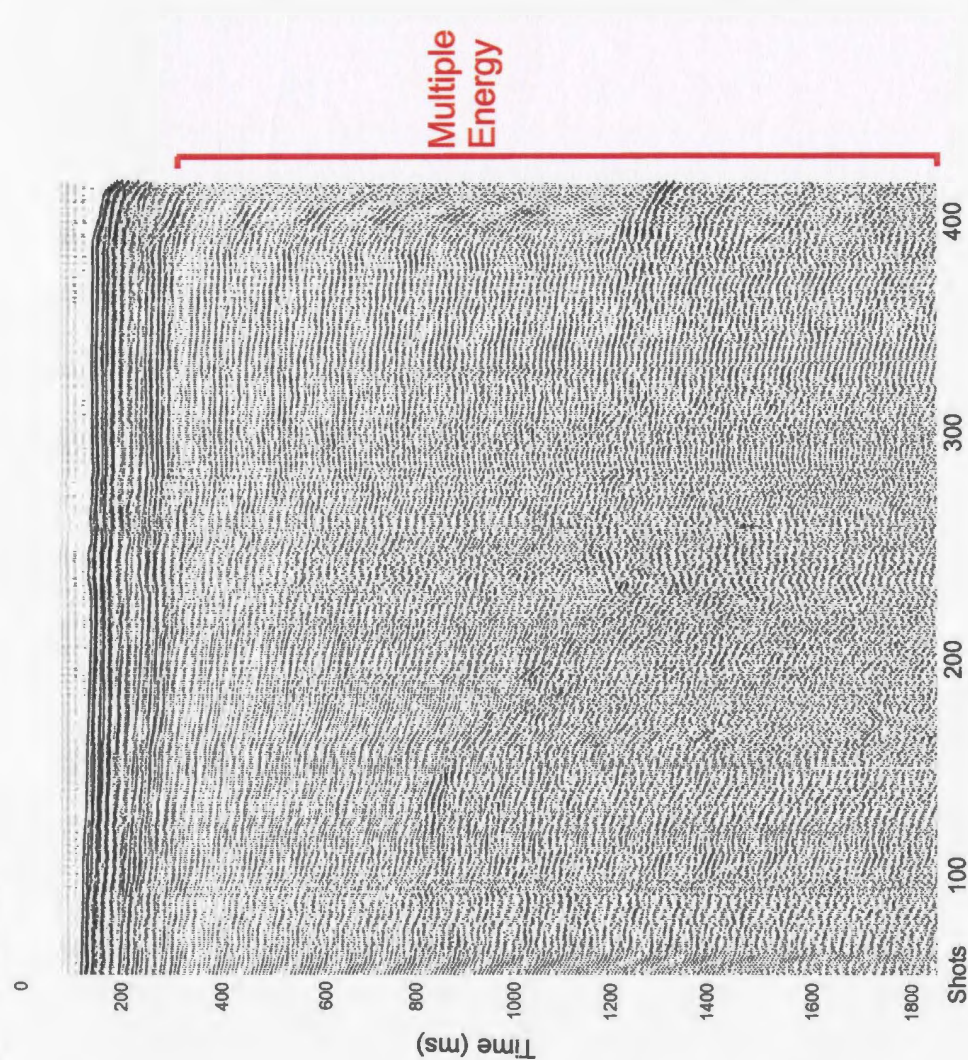


Figure 3.20: (A) Near Trace gather of shots 63–411 showing multiple energy along a shallow shelf margin (B) A 600 ms autocorrelation function calculated from shots 100–120 along line 412.

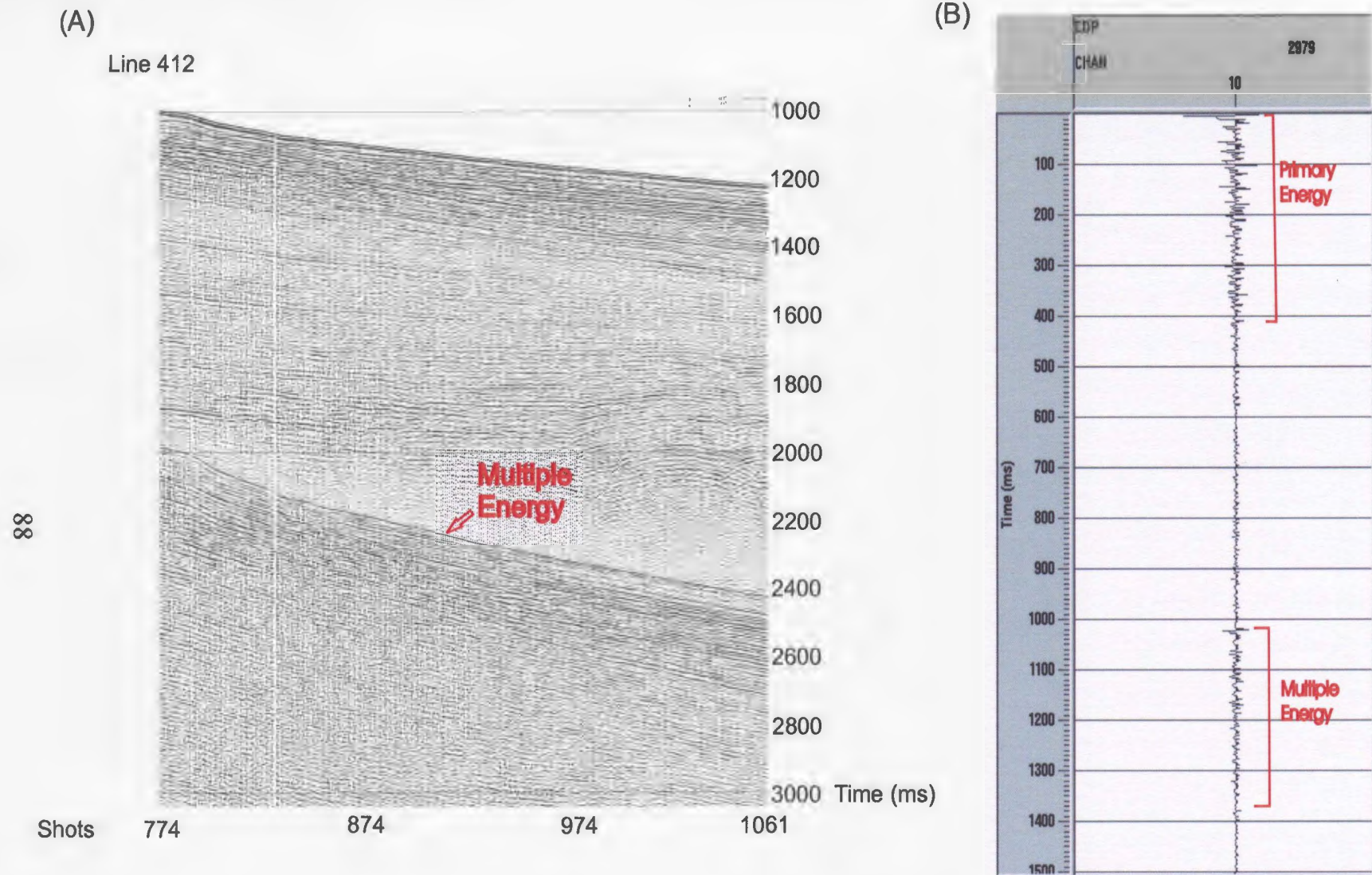


Figure 3.21: (A) Near Trace gather of shots 774-1061 showing multiple energy in an area with a thick Plio-Quaternary succession (B) A 600 ms autocorrelation function calculated from shots 900-920 along line 412.

multiple energy are not useful in the data processed for this thesis as, due to the small number of channels used for the recording and therefore the short offset between the source and the receivers, there is no appreciable difference in the amount of move-out. Techniques that utilize the periodicity of the multiple, however, can be useful on certain parts of this data for the removal of short period multiples. A short period multiple is defined as one that has a repeat interval that is only a few times the length of the source wavelet, and can therefore be discriminated on the basis of its periodicity using predictive deconvolution (Backus, 1959). For this data, predictive deconvolution with a prediction lag equal to the sea bed arrival time was attempted in shallow areas along each of the lines processed for thesis. The deconvolution operators are tested on both pre-stack and post-stack data to determine which provides the best result. Figure 3.22 shows the resultant data and autocorrelation function of 1200 CDP's along line 412 after predictive deconvolution, with a prediction lag ranging from 80 to 120 ms and a gate length of 300 ms, was applied to post stack data. When compared with the original non-deconvolved data seen in Figure 3.20, it is obvious that the deconvolution was successful at attenuating the short period multiple and bringing out primary reflections that were hidden beneath the multiple energy. Unfortunately, this method only proves to be beneficial where the sea bed appears at times less than 200-300 ms and the multiple repeats numerous times in this section.

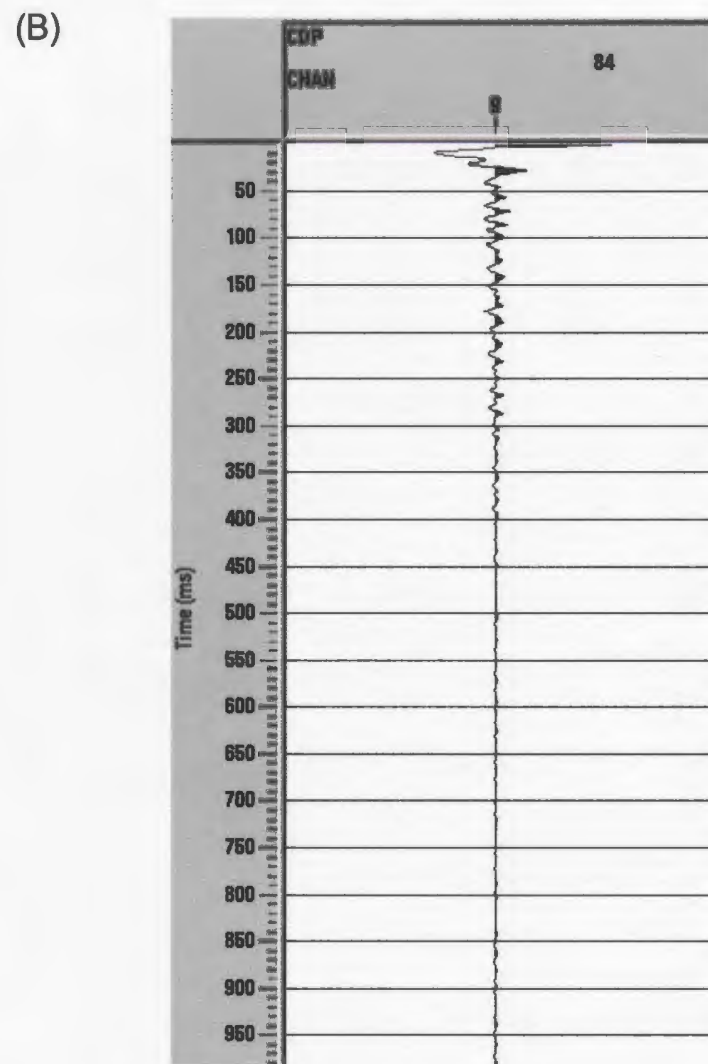
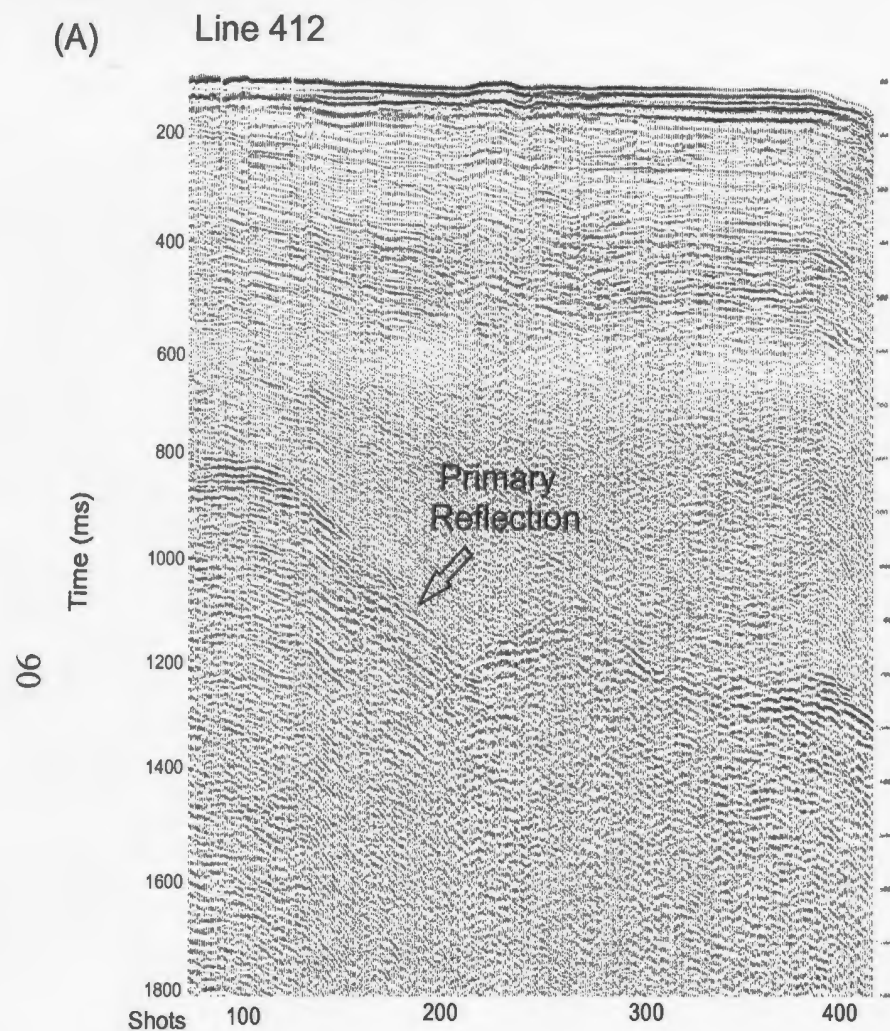


Figure 3.22: (A) Near Trace gather of CDPs 1-1400 (shots 63-411) after predictive deconvolution with a prediction lag equal to the sea bed reflection time and a gate length of 300 ms was applied (B) A 600 ms autocorrelation function calculated from the deconvolved shots 100-120 along line 412.

3.2.8 (2) Wave equation multiple rejection

For the removal of the long period multiples, which predominate in this dataset, a method that utilizes neither the differential movement of the primary and multiple energy nor the periodicity of the multiple must be introduced. One such method involves using the acoustic wave equation to estimate water bottom reflectivity, and from this to predict an appropriate model of the sea bed multiple in terms of time, amplitude and phase. The predicted multiple model can then be subtracted from the original data to theoretically obtain a multiple free dataset. There are, however, known limitations to this method due to assumptions made to decrease computation time, such as the assumption that the water bottom is flat and that it creates the only multiple in the data-set. Therefore, this method does not deal well with dipping reflectors or with peg leg multiples derived from deeper reflections beneath the sea bed (Promax 3D reference guide, 1998). To attempt this method on the data processed for this thesis, an area with a fairly flat sea bed and well defined multiple is chosen. The original near trace gather of shots 11244-11744 along line 67 is shown in Figure 3.23. Prior to estimating a multiple model, a number of processes must be applied to the data including: 1) generation of a receiver water depth trace header, 2) padding or infill of traces to produce traces at near, far and between offset zones on the receiver record, and 3) top muting everything above the water bottom to remove any water surface waves or refracted arrivals. The multiple estimation process, followed by the elimination process, can then be applied to the data. The result of the initial attempt on shots 11244-11744 of line 67 is shown in Figure 3.24. When compared

Line 67

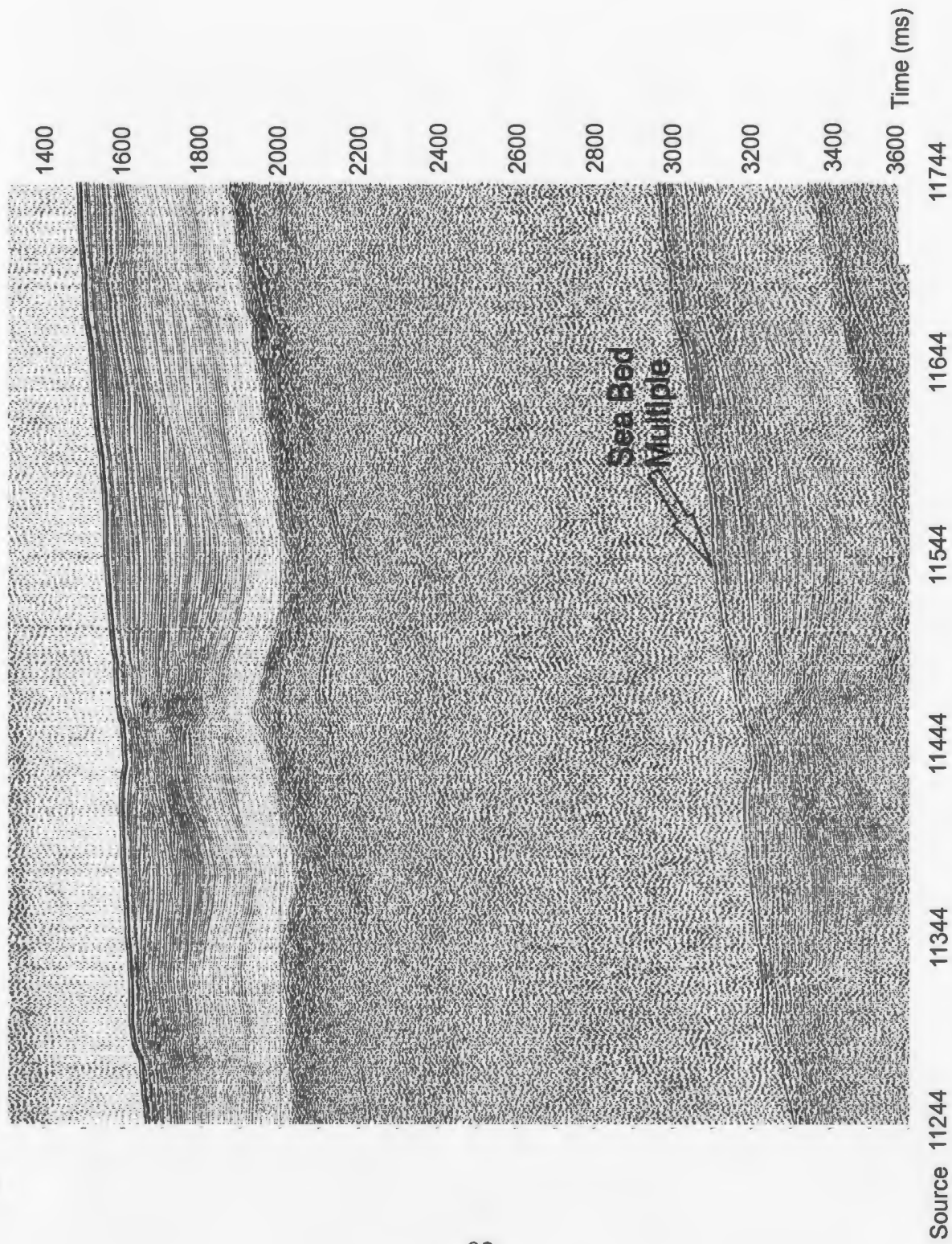


Figure 3.23: Near Trace gather of Shots 11244-11744 along line 67.

Line 67

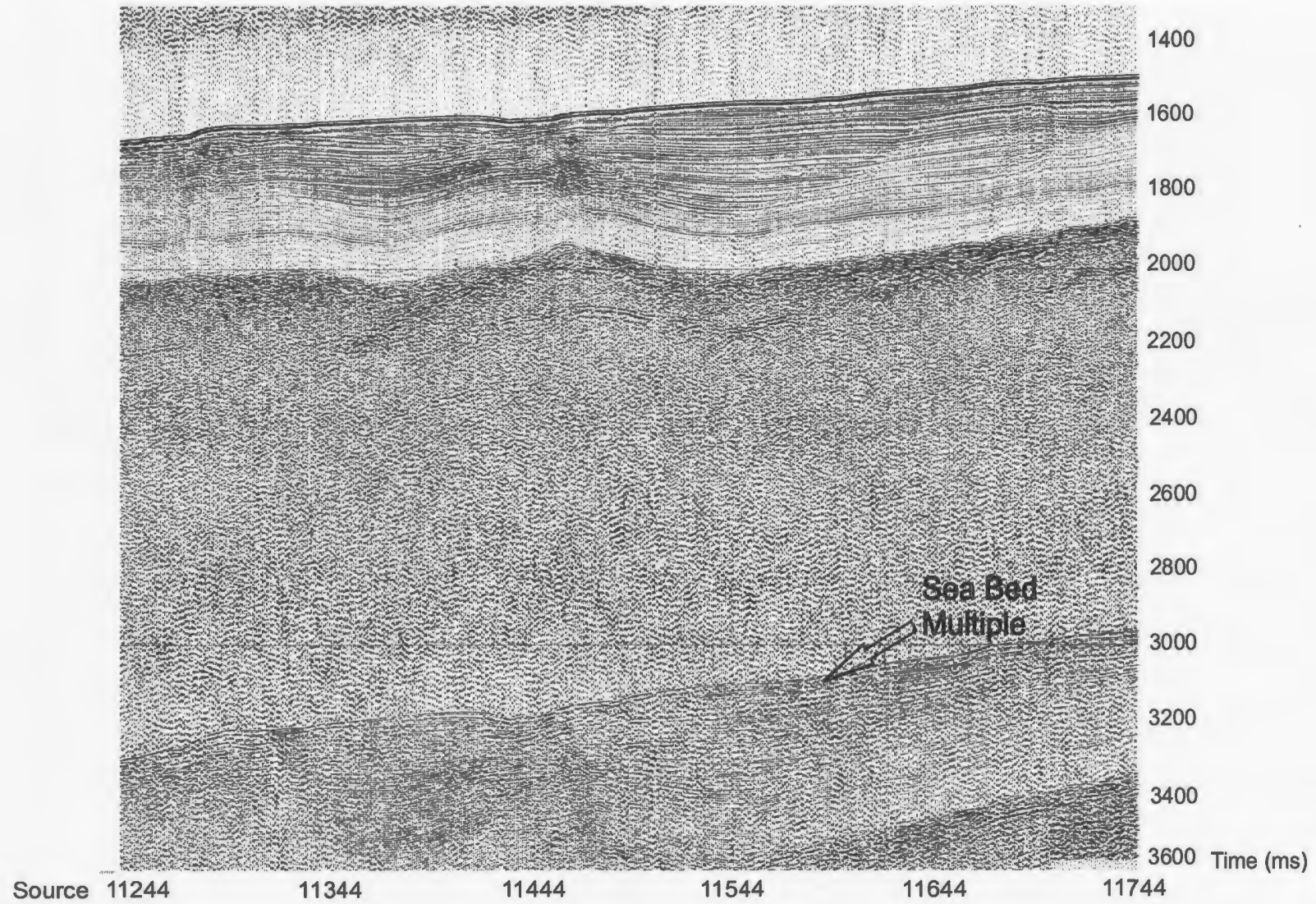


Figure 3.24: Near trace gather of shots 11244-11744 along line 67 after the wave equation multiple rejection process has been applied

with the original data, it is obvious that although the multiple energy is somewhat attenuated, it still dominates over the primary energy wherever the multiple appears. A similar result is found when the process is attempted in other areas along line 67 and along other seismic profiles in the basin. This indicates that the process is not successful for this dataset and therefore has limitations other than those discussed above. One such possible limitation is a difference in the phase and frequency content between the primary and multiple energy. In theory, a source wavelet extracted from the multiple energy should be a lower amplitude and reversed polarity version of the wavelet extracted from the primary energy. Figure 3.25 shows the wavelets extracted from 1000 ms time gates centered over both the primary and multiple energy along shots 11244-11744 on line 67 using the wavelet extraction process in the Promax package. This wavelet extraction process uses a fourth order, time domain statistical approach to separate the wavelet from the reflectivity data. Basically, a parametric model of a wavelet is matched to the fourth order cumulants (which are high order covariance functions that retain phase information) in a minimum mean squared sense (Lazear, 1993). The process requires a fairly large number of data samples and assumes that the reflectivity coefficients are a non-Gaussian random series. Figure 3.25 shows an obvious phase difference between the two wavelets in that the primary wavelet has a general minimum phase character, with a large trough before the main positive peak that is larger in amplitude than the trough below, while the multiple wavelet has more of a zero phase character, with negative peaks below and above the main positive peak that are closer in amplitude. The frequency spectra

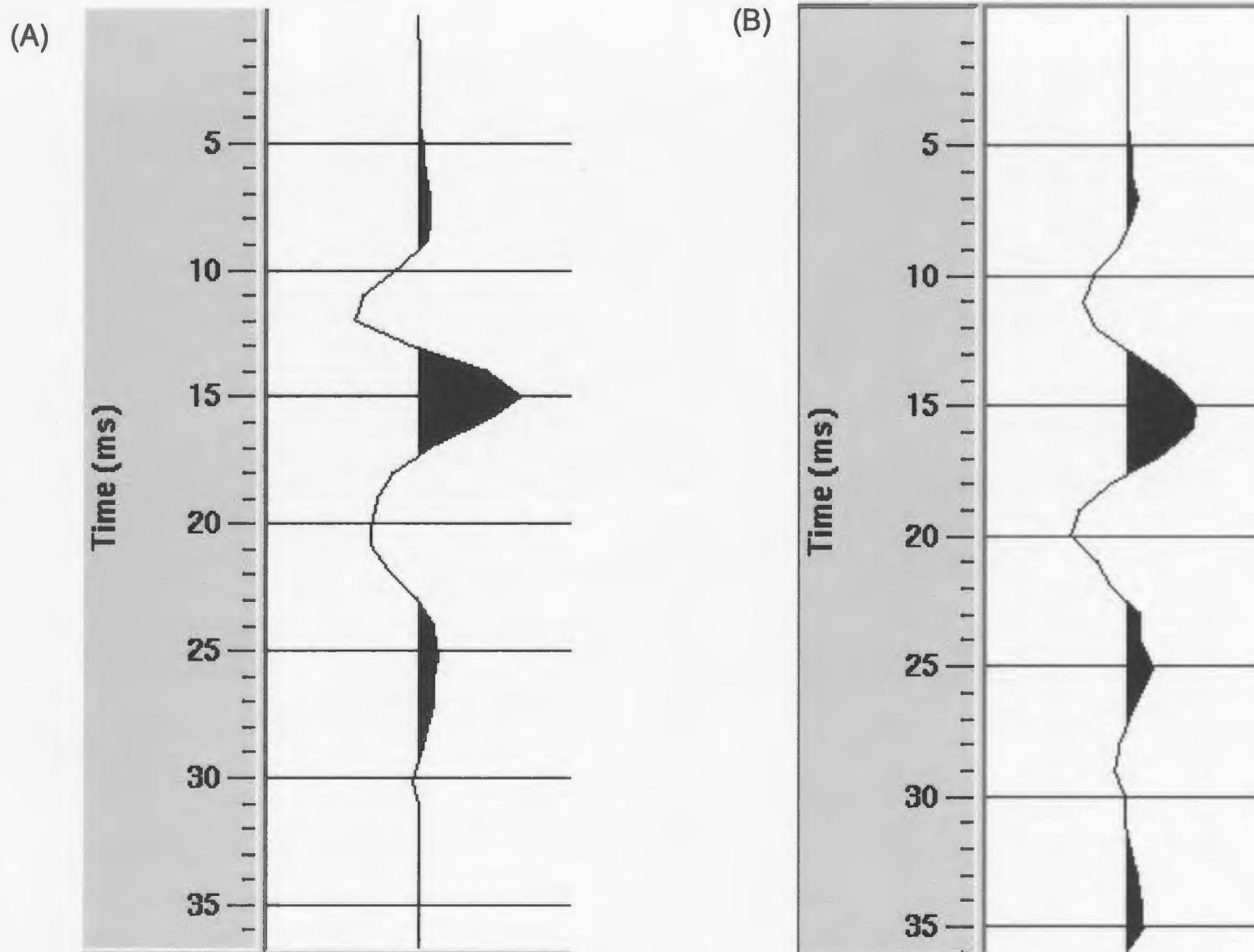


Figure 3.25: (A) 30 ms wavelet extracted from a 1000 ms time gate starting at the primary sea bed reflection along shots 11244-11744 on line 67. (B) 30 ms reverse polarity wavelet extracted from a 1000 ms time gate starting at the sea bed multiple along shots 11244-11744 on line 67

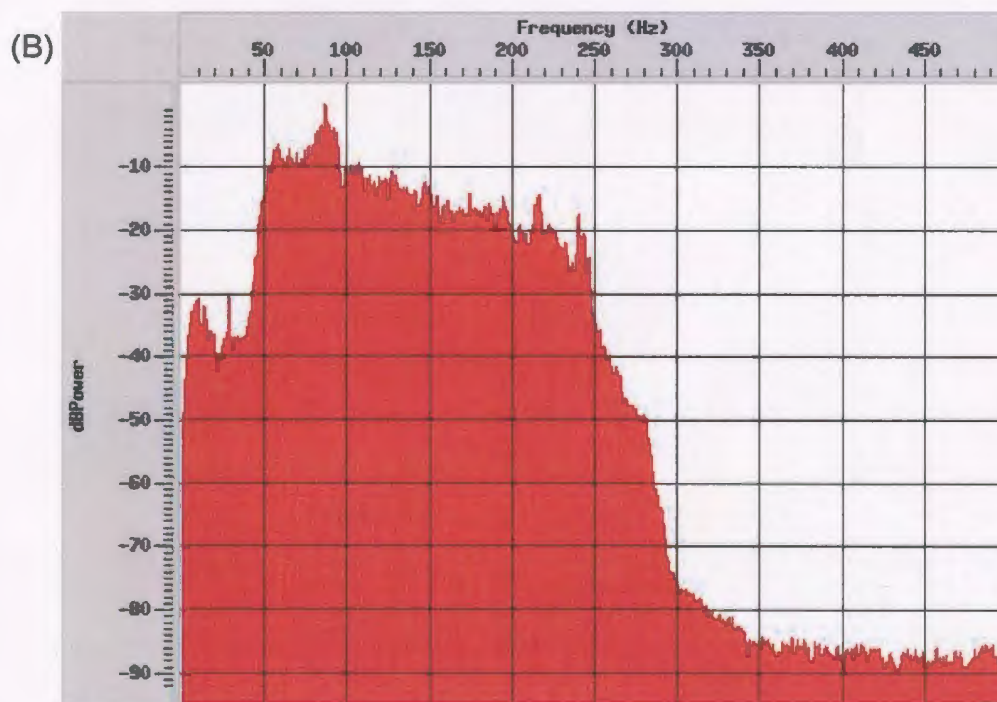
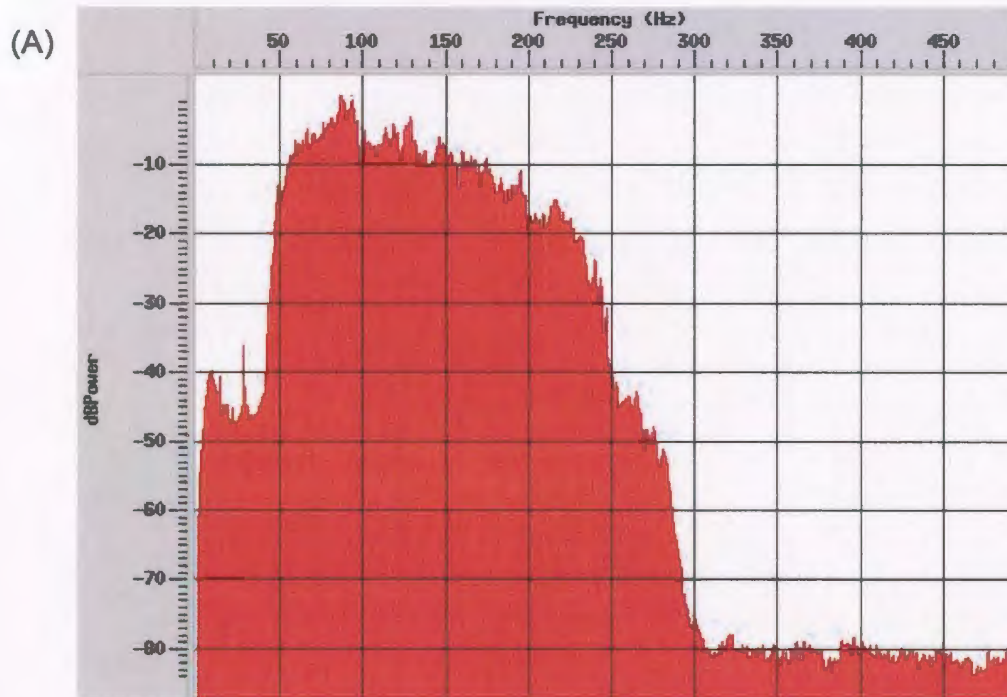


Figure 3.26: (A) Frequency spectrum for primary energy of shots 11244-11744 on line 67, (B) Frequency spectrum for multiple energy of shots 11244-11744 on line 67.

extracted from 1000 ms time gates representing the primary and multiple energy are shown in Figure 3.26. The spectra show a subtle, but noticeable, change in the frequency content of the primary and multiple energy, especially at frequencies higher than 100 Hz. This suggests that there is a frequency attenuation or a filtering effect creating the apparent phase difference between the primary and multiple energy. The wave equation multiple estimation process accommodates for differences in amplitude and polarity that are expected between the primary and multiple reflections, but does not accommodate for such phase changes. This leads to a multiple model, derived using the acoustic wave equation and estimated water bottom reflectivity, that is not equivalent to the multiple energy in the data and is therefore not eliminated during the subtraction process.

An attempt can be made to make the primary and multiple energy more comparable in terms of frequency content and phase by applying a frequency filter to the primary reflections lying above the multiple. A Butterworth filter with a high cut of 100 Hz and a slope of 8 db/Hz is chosen based on the frequency spectrums, shown in Figure 3.26, and applied to the data in a time window extending from just above the multiple up to the sea bed reflection. The wavelet extracted from the primary reflections of the filtered dataset is shown in Figure 3.27, along with the reversed polarity wavelet extracted from the multiple reflections. The phase of the filtered primary wavelet is now much more comparable to the wavelet extracted from the multiple energy of original dataset. Reapplying the wave equation multiple rejection process to the filtered data gives the result shown in Figure 3.28. The multiple is now slightly better attenuated than in the

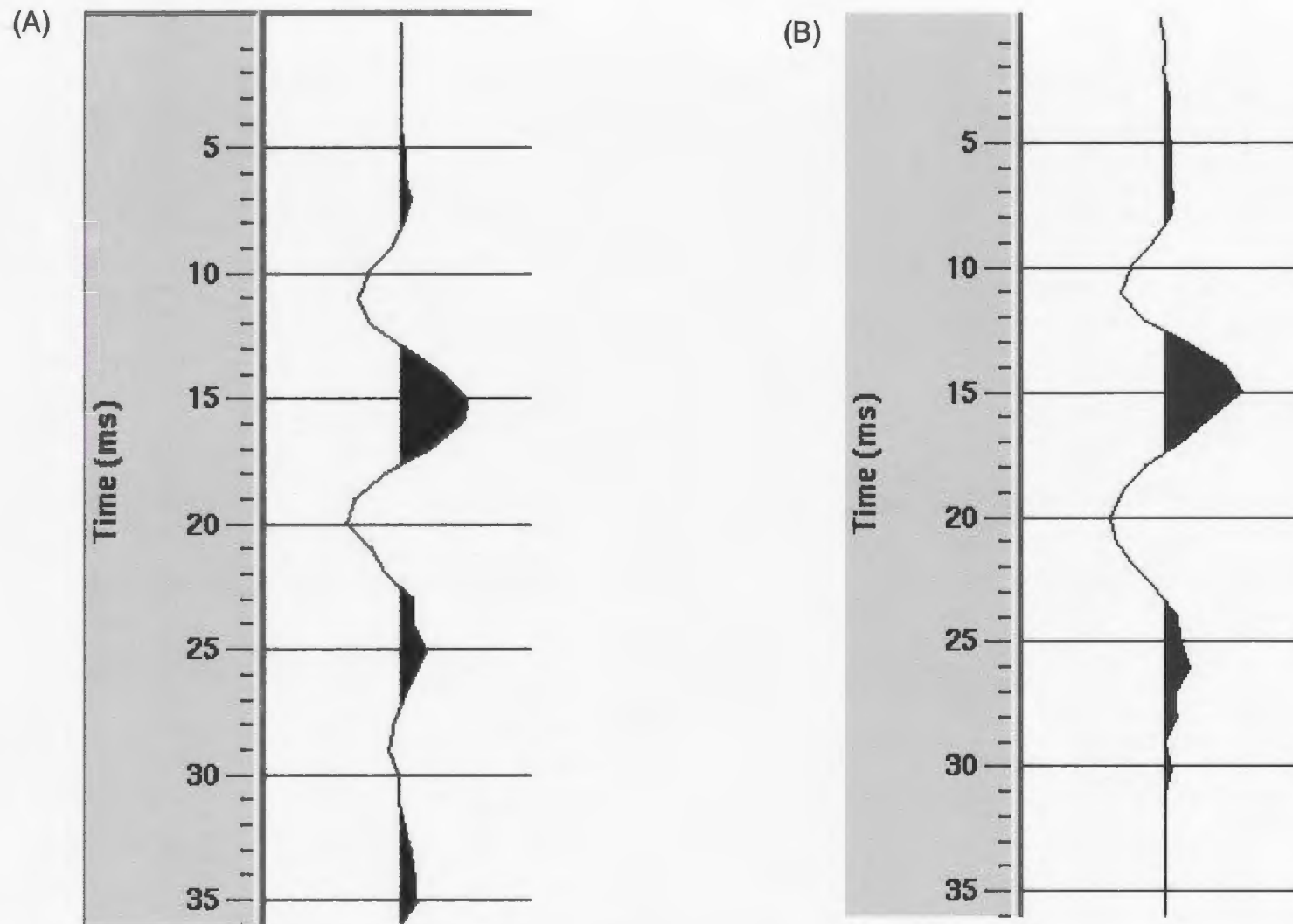


Figure 3.27: (A) 30 ms long reverse polarity wavelet extracted from a 1000 ms time gate starting at the sea bed multiple along shots 11244-11744 on line 67 (B) 30 ms wavelet extracted from a 1000 ms time gate starting at the primary sea bed reflection along shots 11244-11744 on line 67 after a Butterworth filter, with a high cut defined at 100 Hz and a slope of 8 db/Hz, has been applied.

Line 67

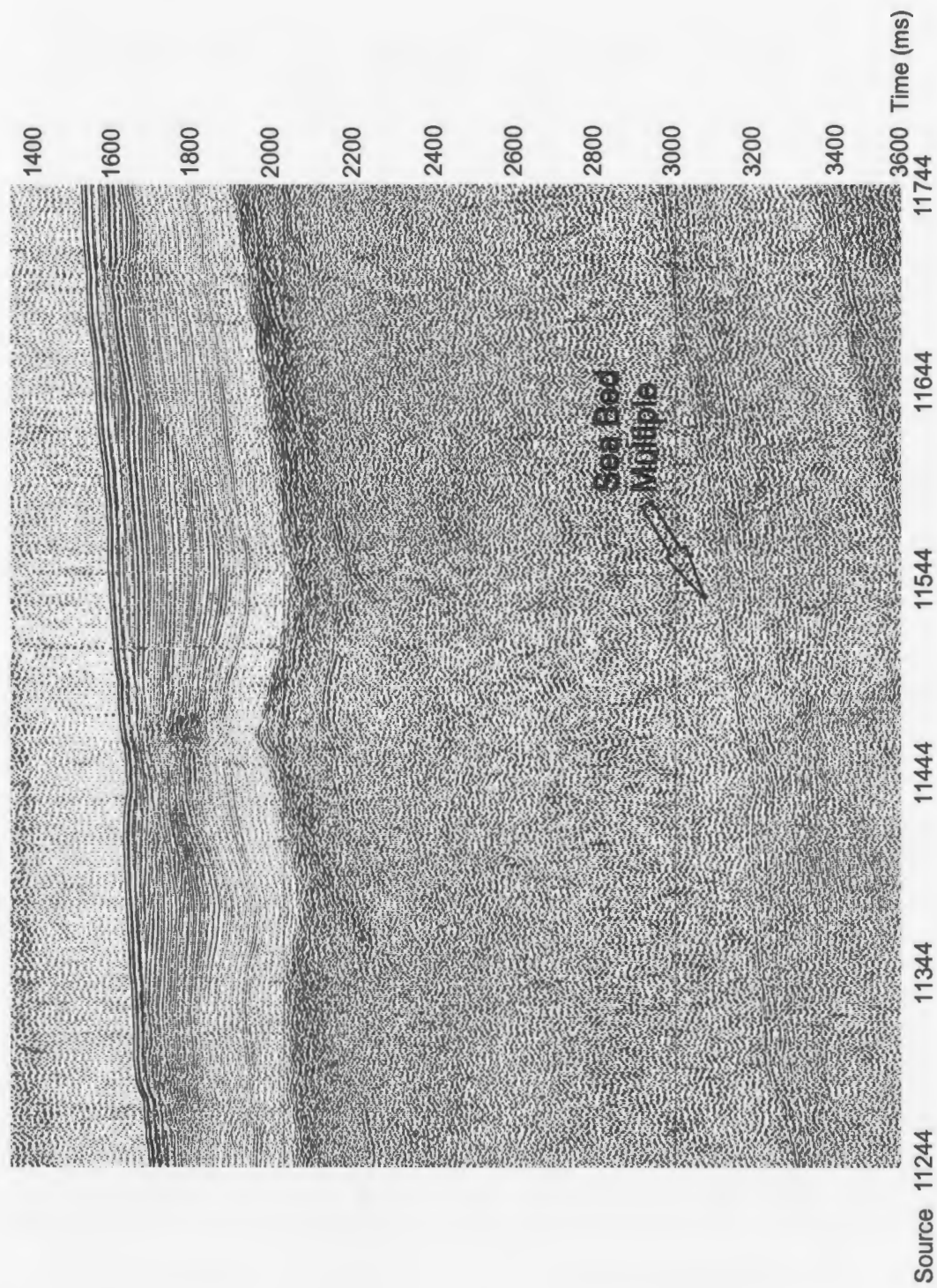


Figure 3.28: Near trace gather of shots 11244-11744 along line 67 after the data was Butterworth filtered, with a high cut of 100 Hz and a slope of 8 db/Hz, and wave equation multiple rejection has been applied.

initial attempt at the multiple rejection process shown in Figure 3.24, however the multiple is still obvious and becomes even more so after the data has been stacked (see Figure 3.29). Considering how minimal the improvement is between the Butterworth filtered data and the original dataset and considering the frequency limiting effect that the filter has on the data, it is not beneficial to filter the data prior to applying the multiple rejection process. Overall, the wave equation multiple rejection process is unsuccessful at removing the sea bed multiple in the data processed for this thesis.

3.2.9 Velocity Analysis and Stacking

Stacking involves averaging all traces for the same common depth point to increase the signal to noise ratio. In theory, the higher the fold of the data the better resolved the subsurface will be. In the case of the data processed for this thesis, the fold ranges from 3-fold for lines 412, 489, 517 and 501 to 4-fold for lines 23 and 67. Stacking velocities can be derived directly from seismic data and are related to normal move-out velocities, which are used to correct travel times for non-zero offsets. The velocities are chosen based on a velocity hyperbola that best fits the data over the spread length. Unfortunately, velocity estimation is limited by both spread length and stacking fold, both of which are relatively low in this data-set. The lack of large offsets, and therefore lack of significant move-out, limits the ability to discriminate velocities, while the low stacking fold limits the resolution that can be achieved in the velocity spectra (Yilmaz, 1987). The spectral resolution issue can be remedied by using supergathers in the velocity analysis instead of individual CDPs. Averaging adjacent CDPs into a supergather increases the

Line 67

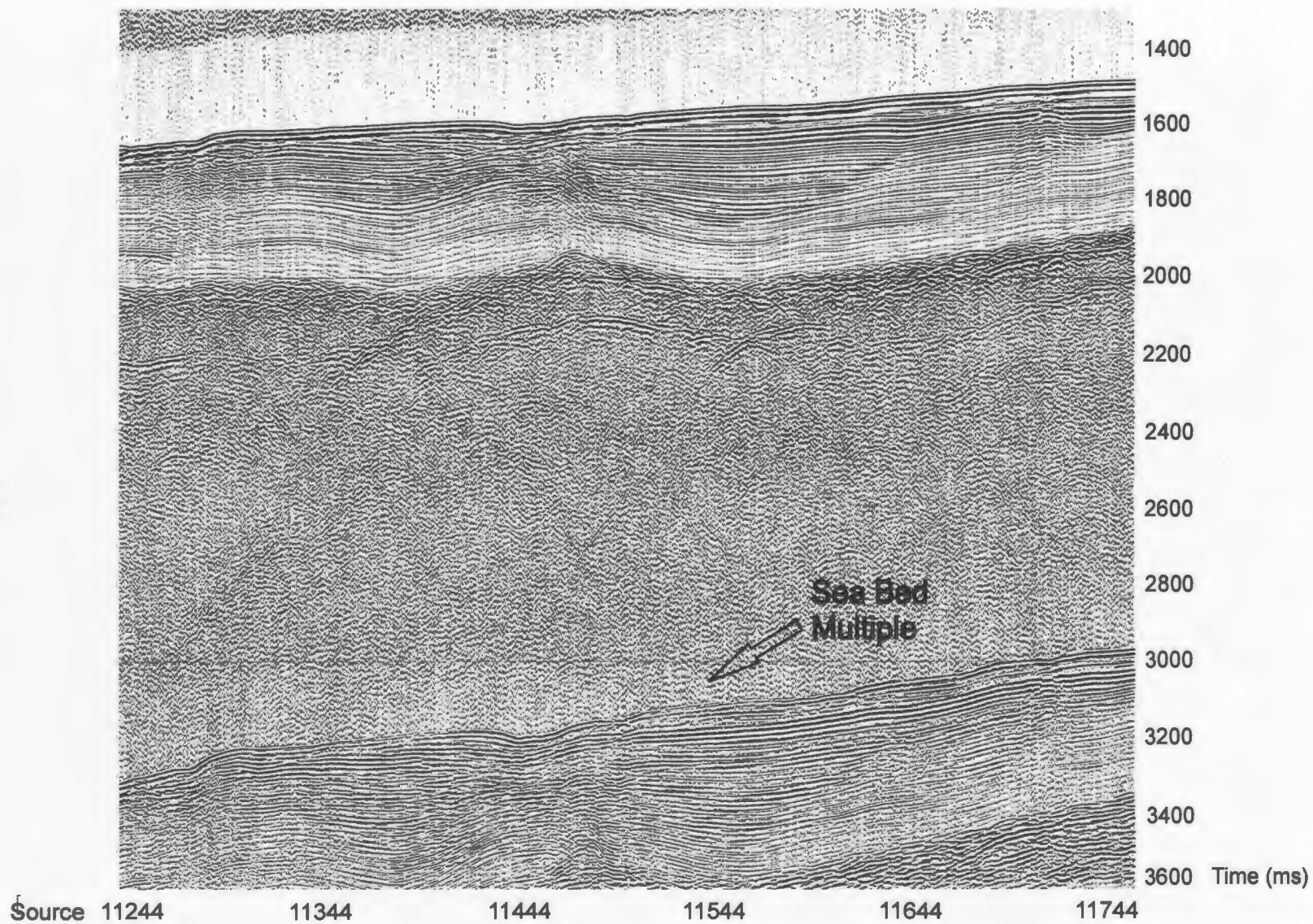


Figure 3.29: Stacked section of shots 11244-11744 on line 67 after the data was Butterworth filtered, with a high cut frequency of 100 Hz and a slope of 8 dB/Hz, and the wave equation multiple rejection process was applied.

signal to noise ratio and gives the impression of higher fold data. It is especially useful in areas of low dip where there is little variation in the arrival time of events. In the data processed for this thesis, supergathers of 3, 5 and 11 CDPs are utilized depending on the dip and structural complexity of the subsurface.

To interpret stacking velocities in the Promax package the interactive velocity analysis tool is used. This tool has four display panels each of which can be used to pick the appropriate velocities (see Figure 3.30). The first display panel is a semblance plot which displays the stack response as a function of time and velocity in a contour plot (Promax 3D reference guide, 1998). The maximum semblance peak lies at the velocity which represents the hyperbolic trajectory that best stacks the data, and therefore represents the appropriate stacking velocity. The second display panel represents a common offset stacked supergather of a chosen number of CDP's. A normal movement correction can be interactively applied to the data to determine the degree to which the chosen stacking velocity will flatten the event in question. The third panel is a dynamic stack, which displays an approximation of a stack generated at the specified velocity pick. The fourth panel shows a series of normal move-out corrected gathers at a series of constant velocities. The best normal move-out correction should indicate the most appropriate stacking velocity.

Using a combination of the four display panels described above, the most appropriate stacking velocities can be chosen. However, as mentioned above, the lack of large offsets makes velocity discrimination difficult and often there is little difference in

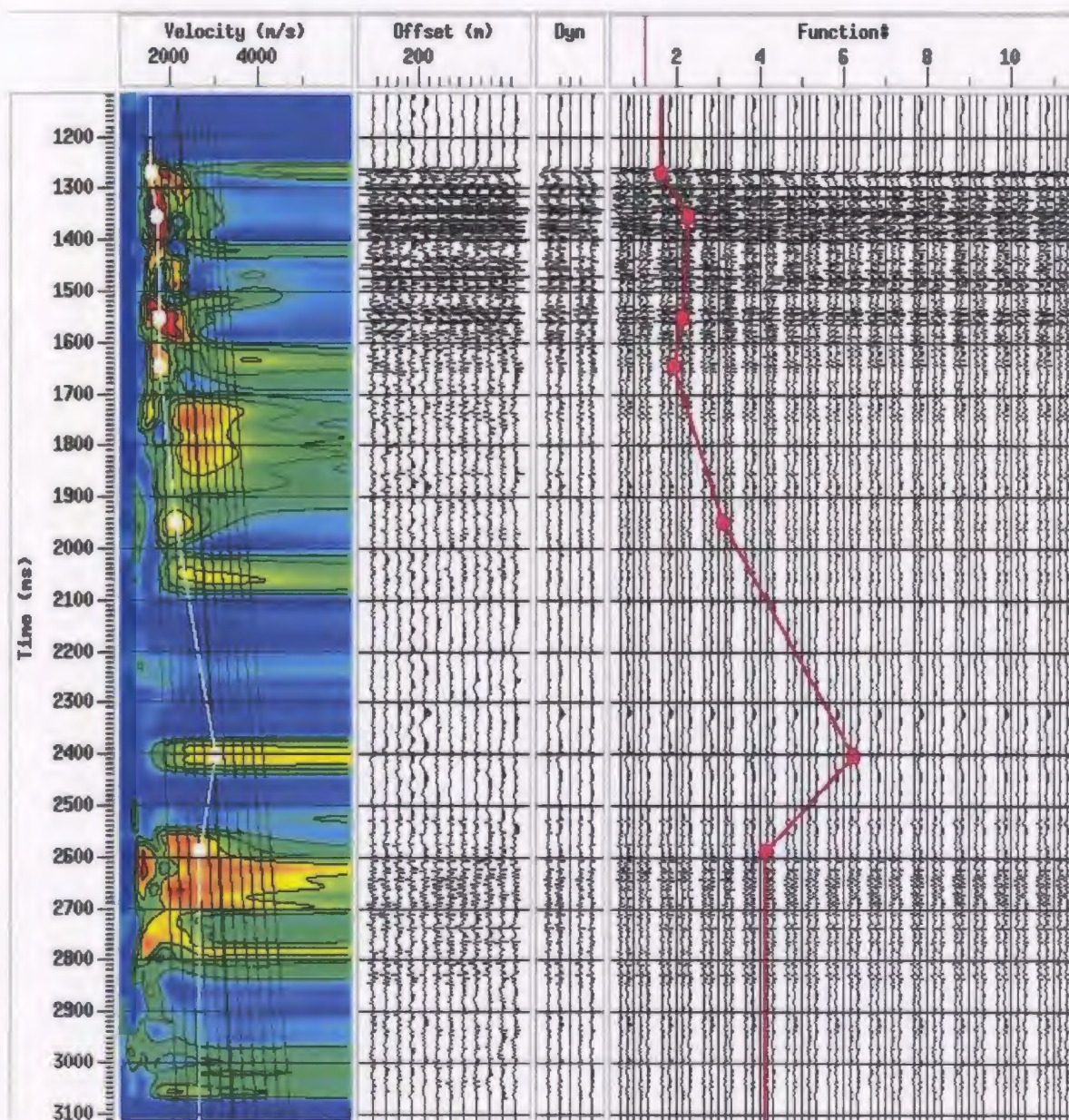


Figure 3.30: Velocity analysis of CDP's 4600-4611 along line 412.

the stacking ability of a series of velocities. The most appropriate velocity was therefore chosen based both on the methods described above and on the known geology of the area. Figure 3.30, 3.31 and 3.32 show the velocity analyses at various points along line 412. Figure 3.30 shows an analysis of a supergather with 11 CDP's in a relatively flat area with a thick Pliocene-Quaternary sequence as shown in Figure 3.33. The chosen rms velocities are shown on both Figure 3.30 and Figure 3.33. The stacking velocities increase steadily through the thick Pliocene-Quaternary succession, increase fairly dramatically at the inferred evaporite layer at 2400 ms, and then decrease at the base of the evaporite layer. Figure 3.31 shows an analysis of a supergather of 5 CDP's in a slightly more dipping area with a thinner Pliocene-Quaternary sequence as shown in Figure 3.34. The chosen rms velocities are shown in both figures, and show generally the same pattern as the previous area with increasing velocities through the now thinner Pliocene-Quaternary succession and a jump in velocity at the inferred evaporite layer at 1450 ms. Figure 3.32 shows a velocity analysis of a supergather with just 3 CDP's in a steeply dipping area with a shallow multiple, as shown in Figure 3.35. Both the dip of the events and the interference between the multiple and the primary energy limits the usefulness of methods available for velocity analysis. Appropriate velocities can be better estimated based on the inferred geology of the area and on velocity picks from correlated reflectors in nearby areas.

The CDP/Ensemble Stack tool is implemented to stack the common depth point traces for this dataset. The stacking algorithm chosen is straight mean stack,

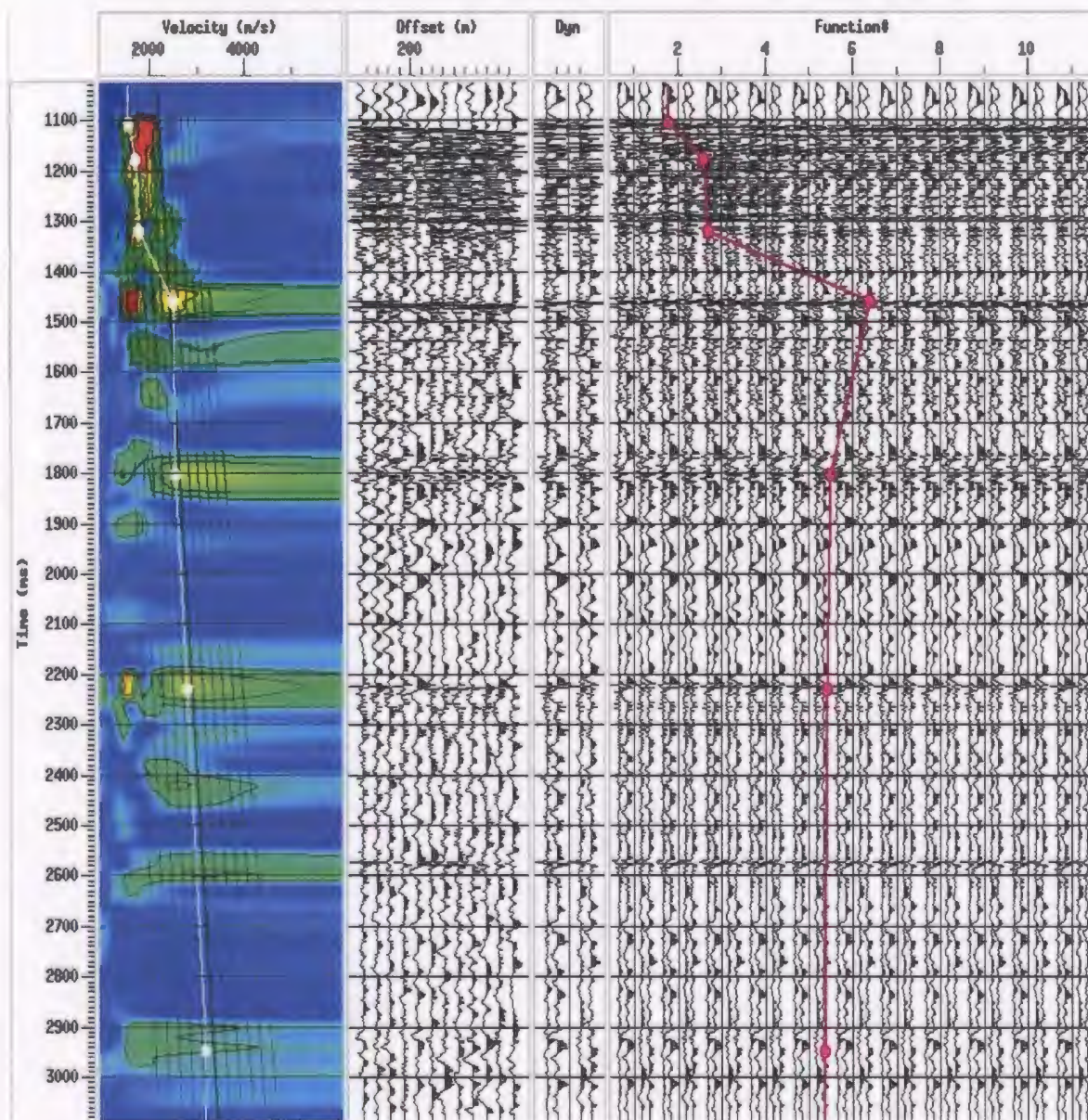


Figure 3.31: Velocity analysis of a supergather of CDP's 10200-10205 along line 412.

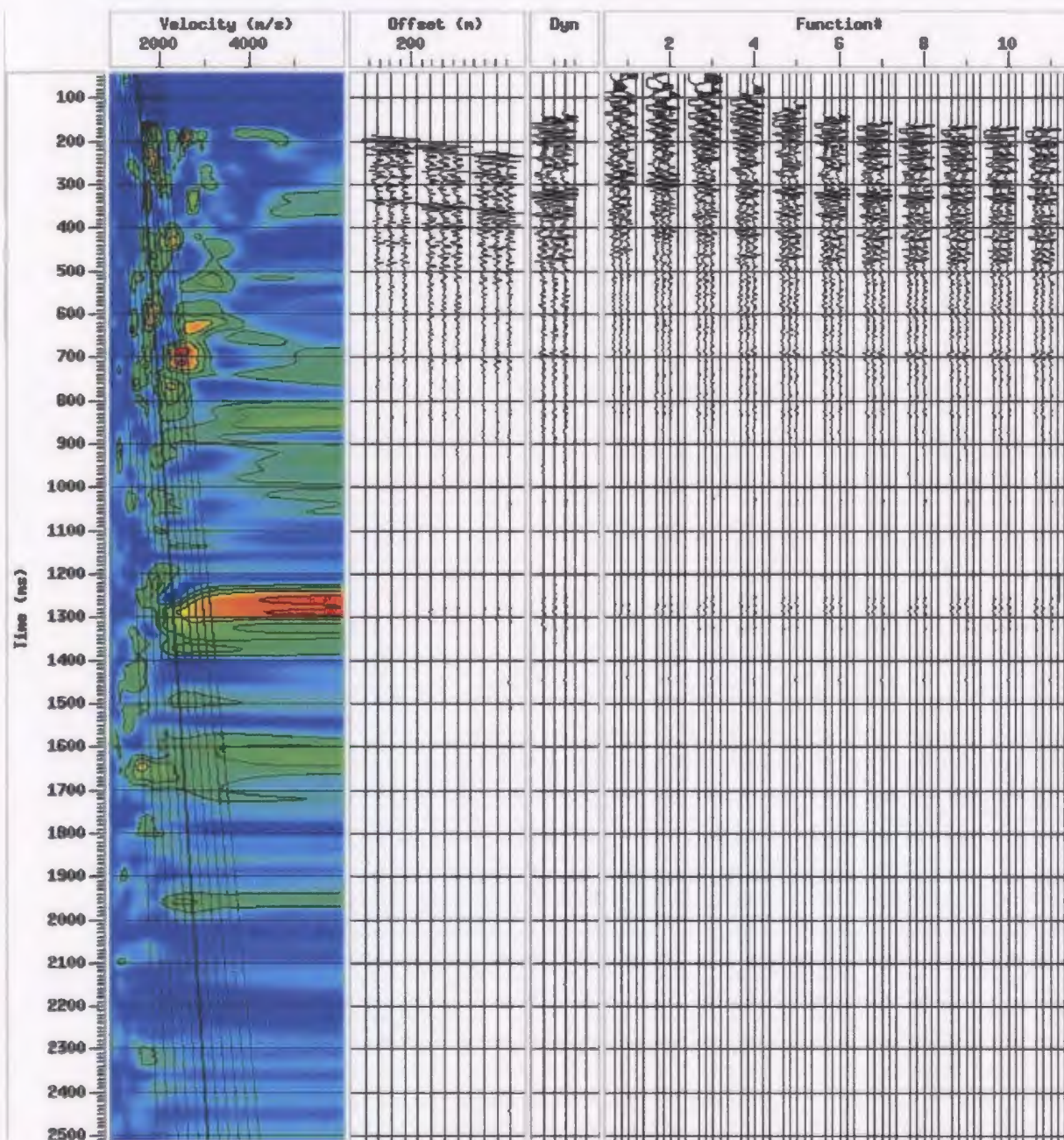


Figure 3.32: Velocity analysis of a supergather of CDP's 1400-1403 along line 412

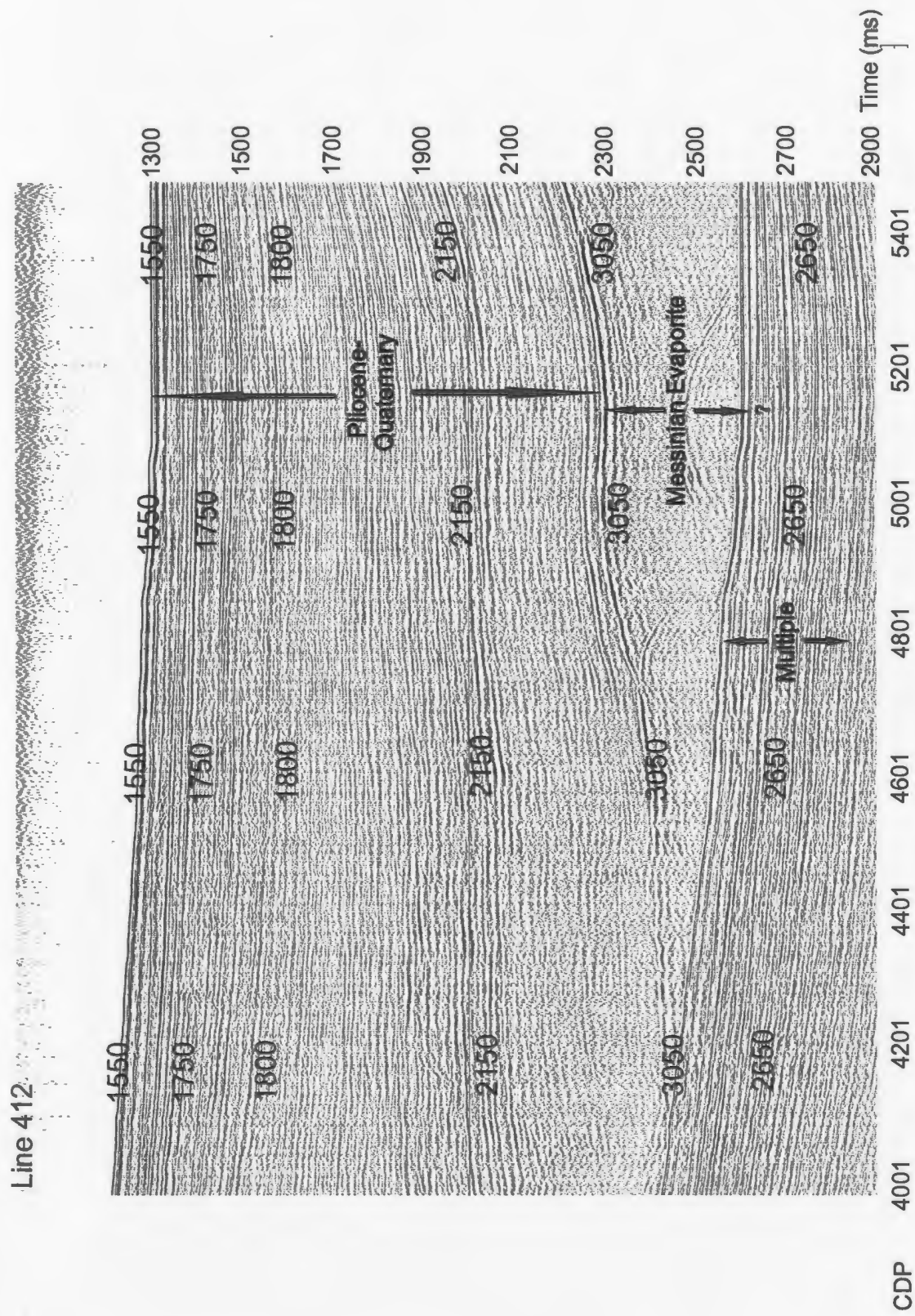


Figure 3.33: Stacked section of CDP's 4001-5500 along line 412 with posted stacking velocities (m/s)

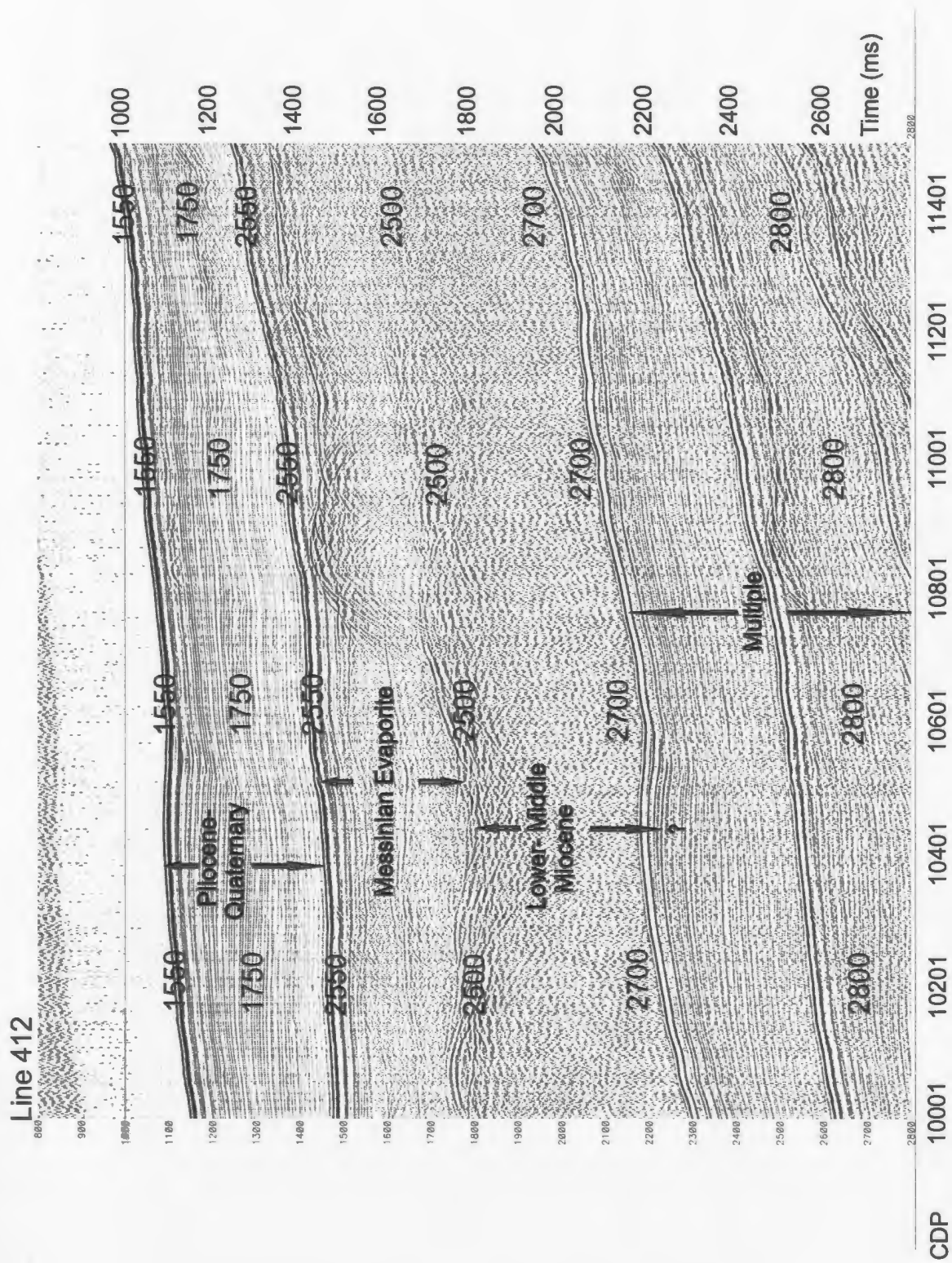


Figure 3.34: Stacked section of CDP's 10001-11500 along line 412 with posted stacking velocities (m/s)

which sums the sample values and divides by the number of samples summed and raised to a power of 0.5 (Promax 3D reference guide, 1998). The stacking process is successful at increasing the signal to noise ratio of the data, as exemplified by comparing the near trace gather and stacked section of CDP's 4000-5500 on line 412 in Figure 3.36.

3.2.10 Migration

Migration is applied to the data to collapse diffractions and bring dipping reflections to their true subsurface position. The aim of migration is to create a seismic image that is most similar to the geological cross section along the same profile. A post-stack Kirchhoff time migration is chosen for this data-set. Kirchhoff algorithms are based on summing seismic amplitudes along diffraction hyperbolas with added amplitude and phase considerations to correct for spherical spreading and wavelet filtering effects (Yilmaz, 1987). These migrations use a vertically and laterally varying RMS velocity field and tend to deal well with steep dips and vertical velocity variations. The main limit of this process is in dealing with lateral velocity variations as they tend to distort the hyperbolic diffraction pattern along which the summing takes place. In data processed for this thesis, lateral velocity variations are minimal and are only a concern in areas where salt cored folds appear. Another benefit of the Kirchhoff migration for this particular data-set is the 'avoid spatial aliasing' option. As mentioned above, spatial aliasing does occur in some areas of the data-set and if this option is not chosen the quality of the migration will degrade.

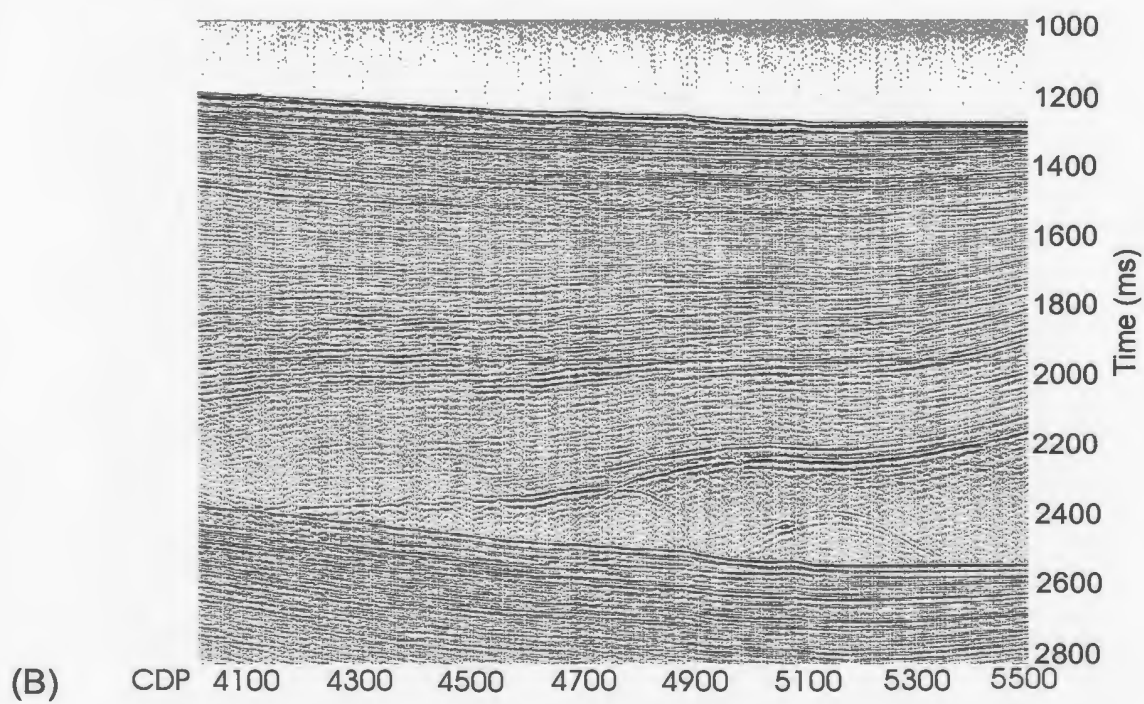
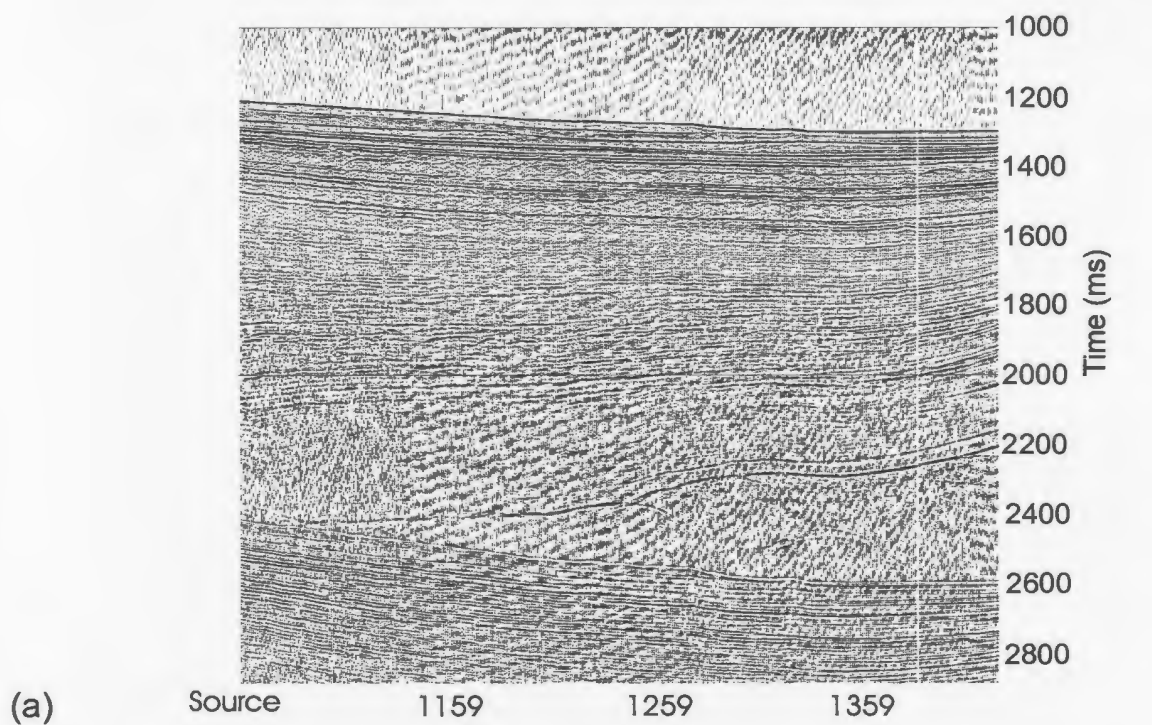


Figure 3.36: (a) Near gather of shots 1059-1409 (CDP's 4000-5500) along line 412 (b) Stacked section of CDP's 4000-5500 along line 412.

Other than RMS velocity fields, the parameters that must be set for Kirchhoff migrations include maximum frequency, maximum dip to migrate, and aperture. The maximum frequency is chosen at 350 Hz based on the high cut of the band pass filter applied to the data. The maximum dip is chosen at 90 degrees, so that potentially steep dips will not be overlooked. An appropriate aperture can be chosen based on maximum aperture values, which are calculated within the Promax package using the user-defined velocity field and the steepest dips present. For each of the lines, the calculated maximum aperture values vary between about 3000 m and 3700 m. To maintain uniform amplitude characteristics, the same aperture value of 3000 m is chosen for all lines. A value higher than 3000 m would not be beneficial as large aperture values can degrade the quality of the migrated section by allowing random noise from deeper times to be brought into the shallow data.

RMS migration velocity fields are chosen through analysis of the data and can vary from simple to detailed depending on the geology and structural complexity of an area. It is a common practice to set migration velocities as a certain percentage of the stacking velocities. However, considering the difficulties described above in choosing appropriate stacking velocities, it is preferable to use another method of velocity picking. A constant velocity migration, initially set at the approximate water velocity of 1500 m/s, is applied to each of the lines and the result is visually inspected to determine where the velocities are too high, too low, or appropriate to successfully migrate the data. Figure 3.37 and Figure 3.38 show a non-migrated and a 1500 m/s constant velocity migration of

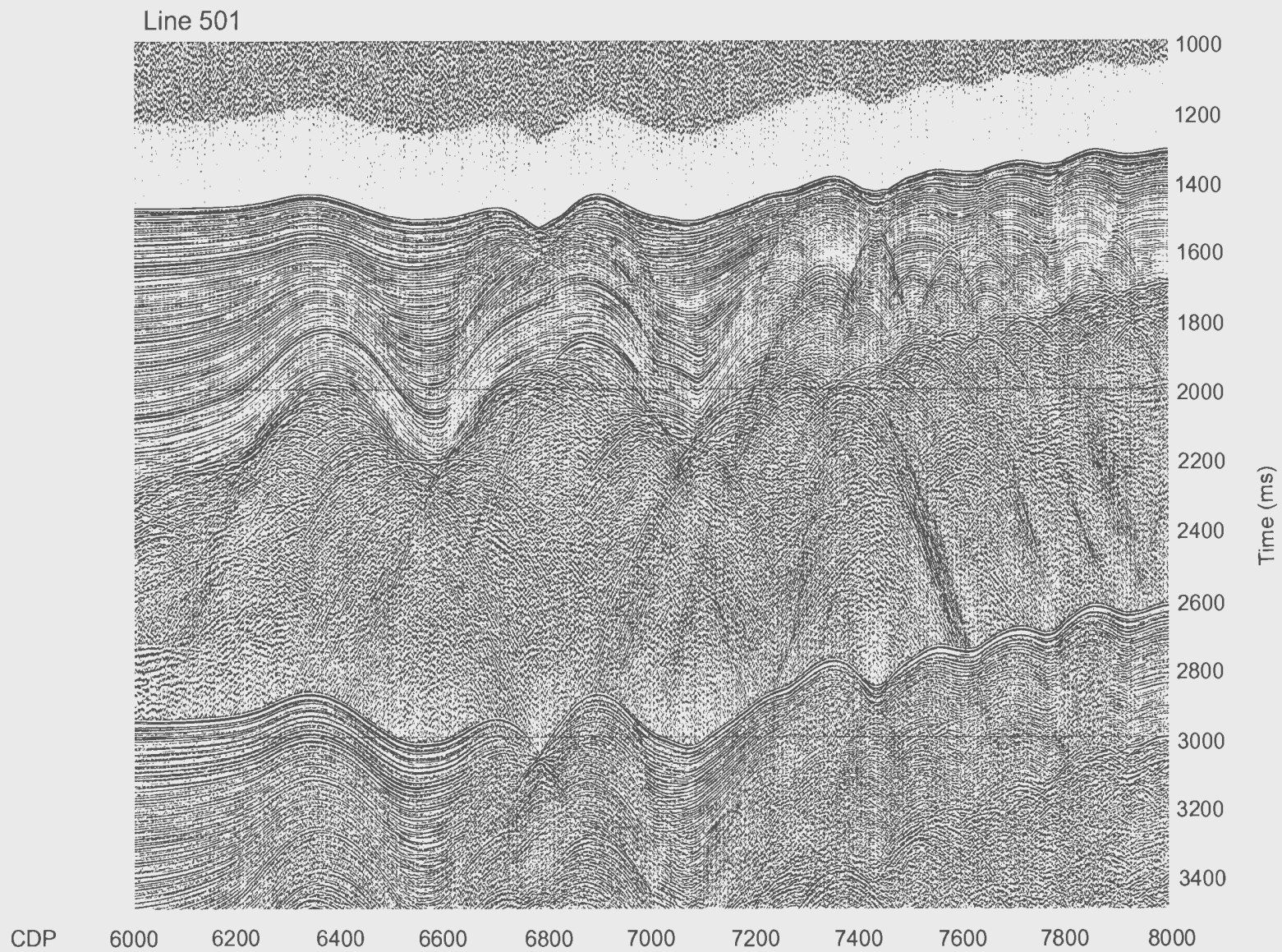


Figure 3.37: Stacked section of CDPs 6000-8000 along line 501.

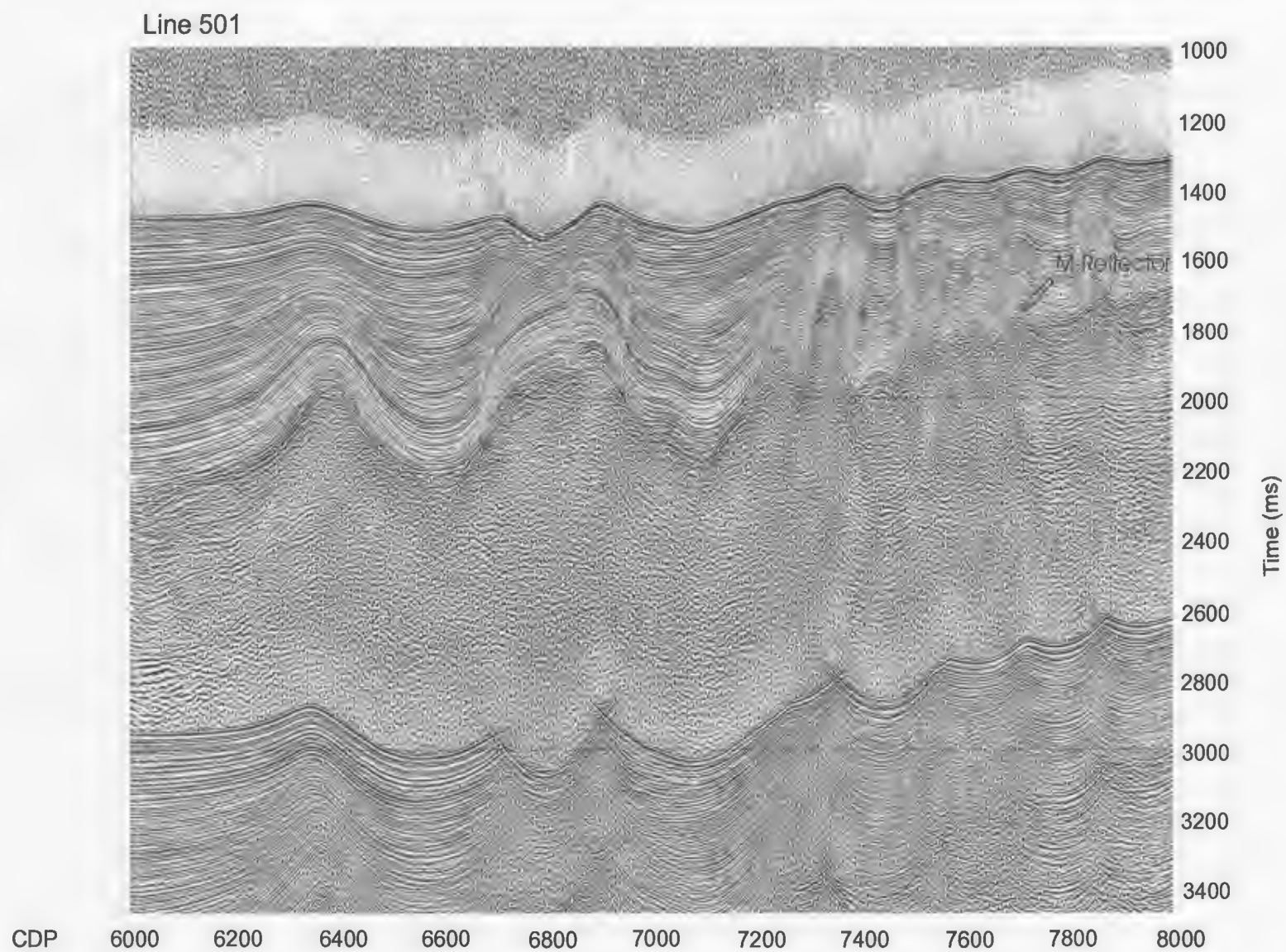


Figure 3.38: 1500 m/s constant velocity migrated stack of CDPs 6000-8000 along line 501.

CDP's 6000-8000 on line 501, respectively. The 1500 m/s velocity is fairly successful at migrating the section in shallow areas but does only a moderate job at collapsing the diffractions at deeper times at and below the M-reflector. To achieve a better migration, velocities in the deeper section are increased iteratively until the most appropriate velocities are found. The RMS velocity field chosen is shown in Figure 3.39, with the final migrated section shown in Figure 3.40. Another example of the migration process is shown with CDP's 19000-22000 along line 67. Figures 3.41 and 3.42 show the stacked section and constant 1500 m/s velocity section, respectively. In this case the constant velocity migration shows evidence of both over-migration, between 1400-1800 ms at CDP locations 19201-19601, and under migration, at a number of locations at times later than 1200 ms. The final velocity field and final migrated section are shown in Figures 3.43 and Figure 3.44, respectively. This section is more complicated than the example shown along line 501 due to out of plane effects caused by crossing 3-dimensional structures at angles not perpendicular to the strike of the structures. If more data were available, a 3-dimensional migration might achieve a better result for these out of plane reflections. With the exception of these complicated areas, the post-stack Kirchhoff time migration achieved good results for all lines processed for this thesis. Even in areas with lateral velocity variations, due to salt diapirism, the migration algorithm was fairly successfully at placing the dipping reflections.

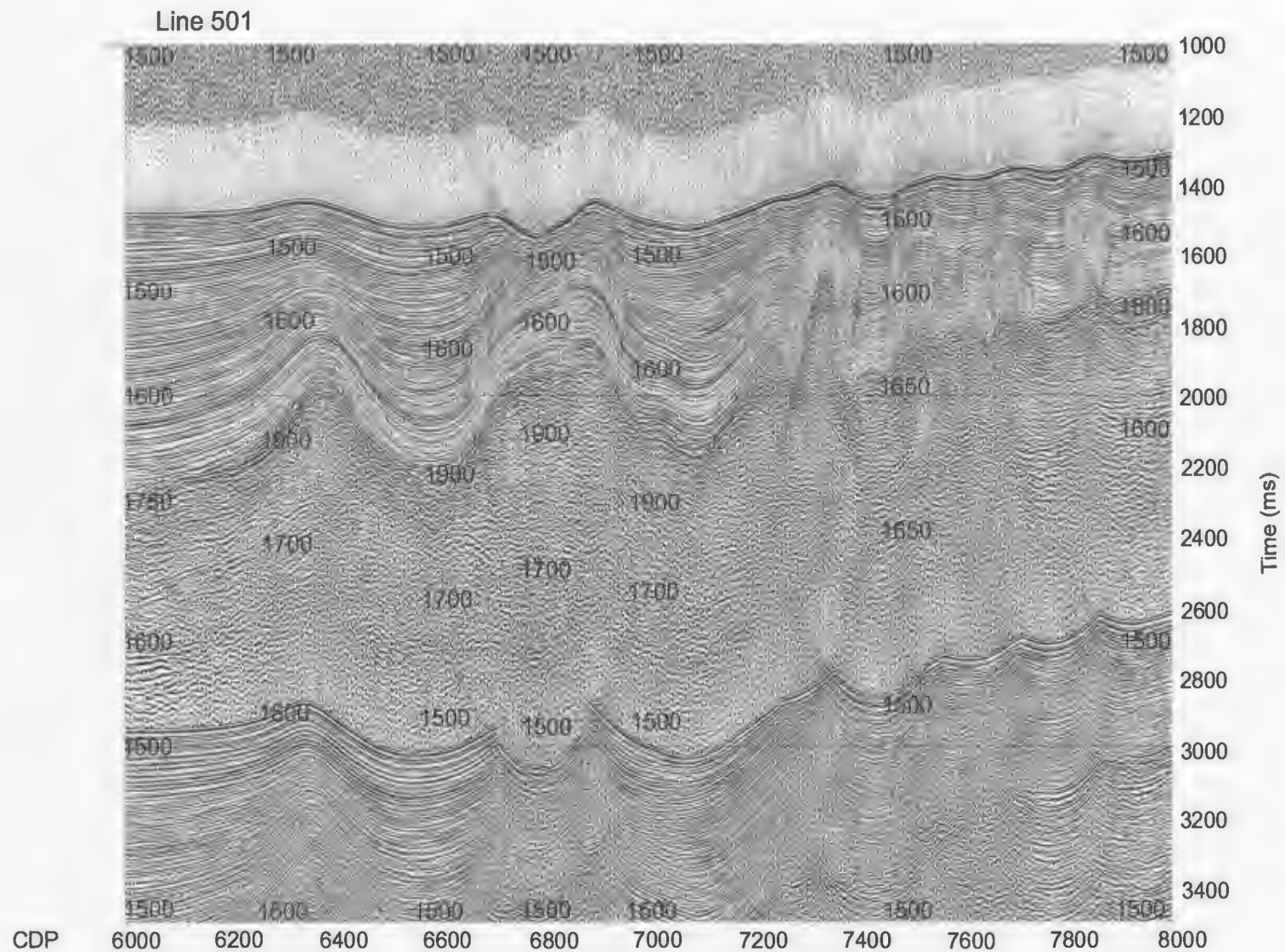


Figure 3.39: Constant velocity migrated stack of CDPs 6000-8000 along line 501 showing the chosen RMS velocity field (all velocities in m/s). Resultant migrated stack using the shown velocity field is given in Figure 3.40.

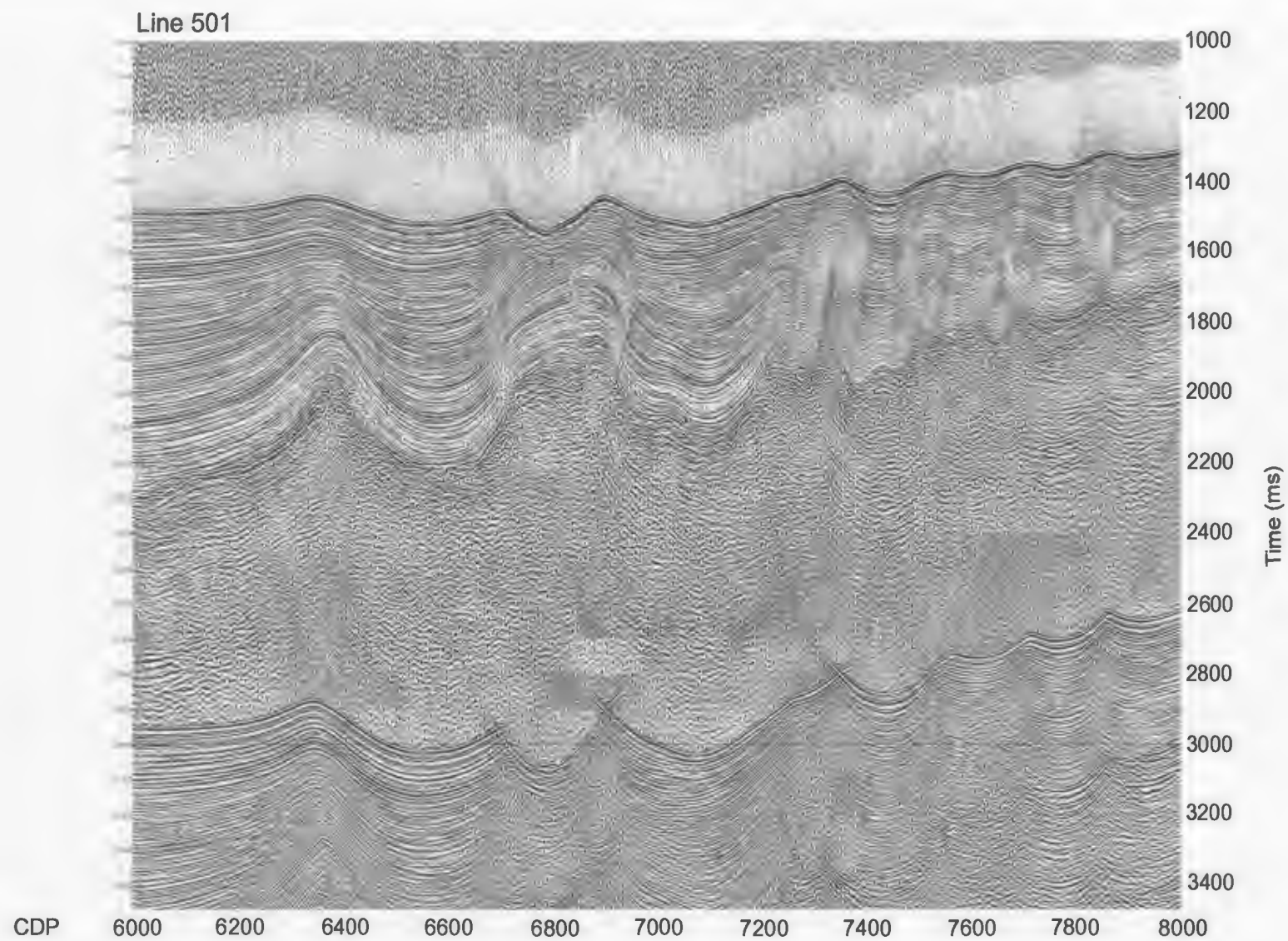


Figure 3.40: Migrated stack of CDPs 6000-8000 along line 501, using RMS velocity field shown in figure 3.39.

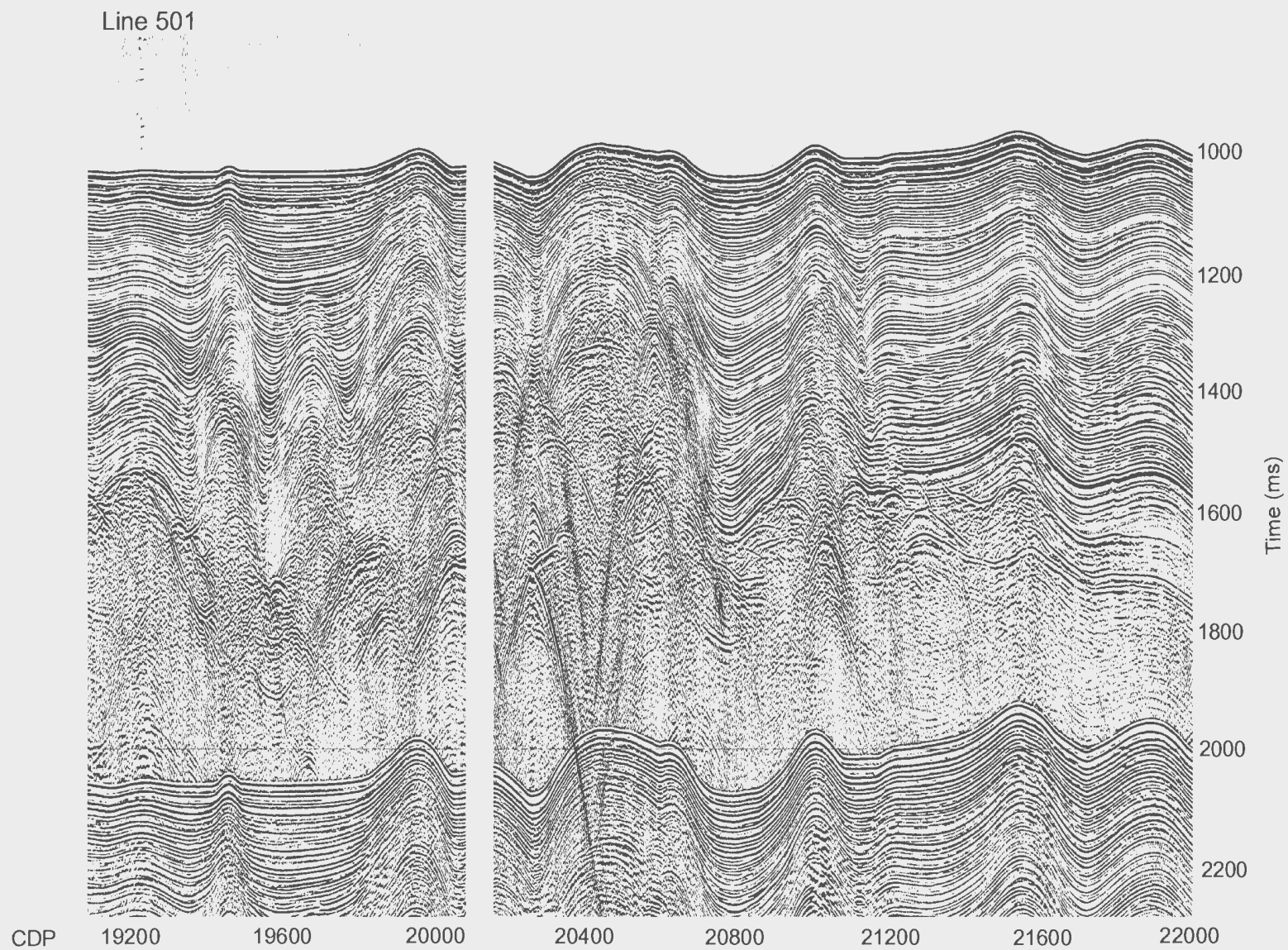


Figure 3.41: Stacked section of CDPs 19000-22000 along line 67.

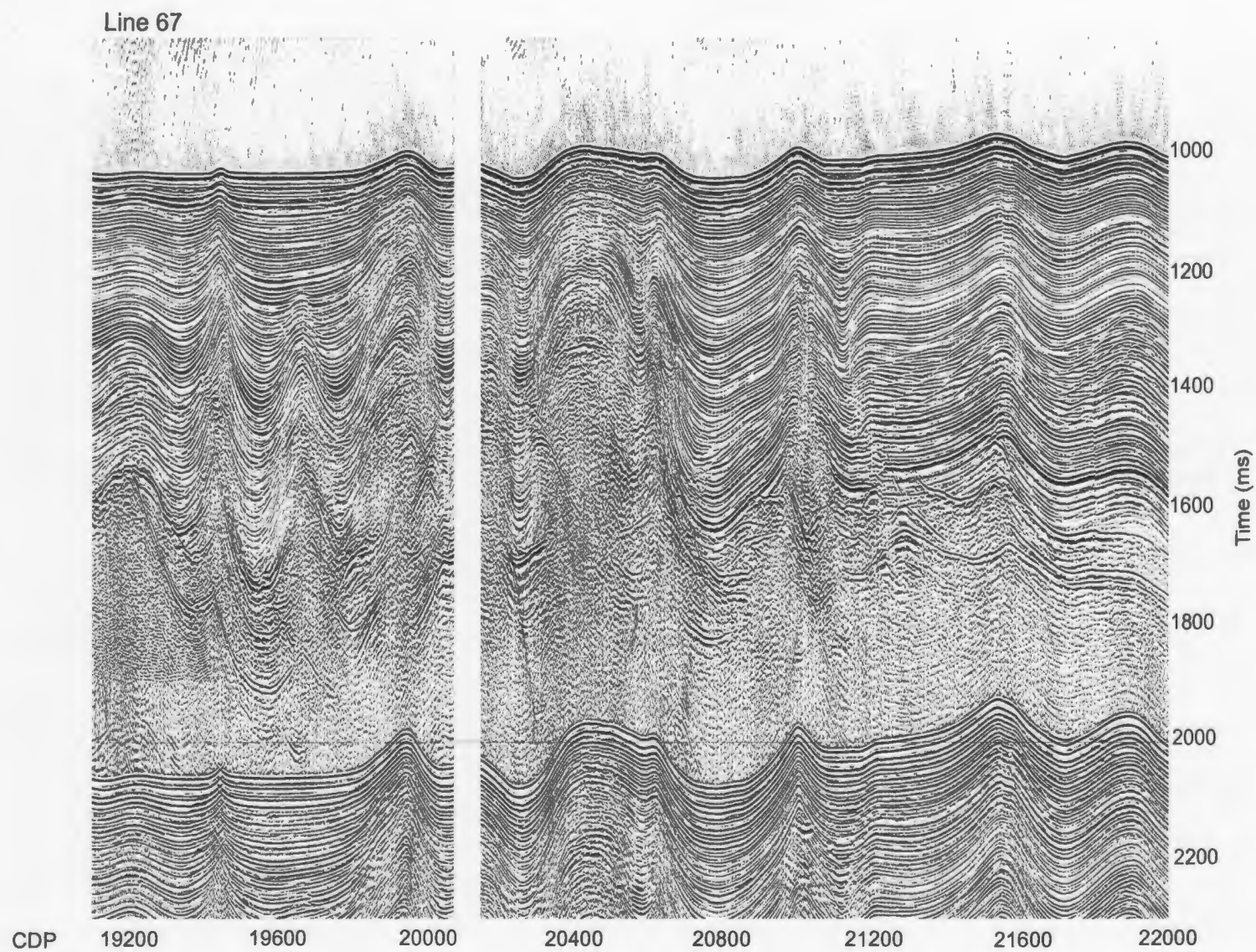


Figure 3.42: 1500 m/s constant velocity migrated stack of CDPs 19000-22000 along line 67.

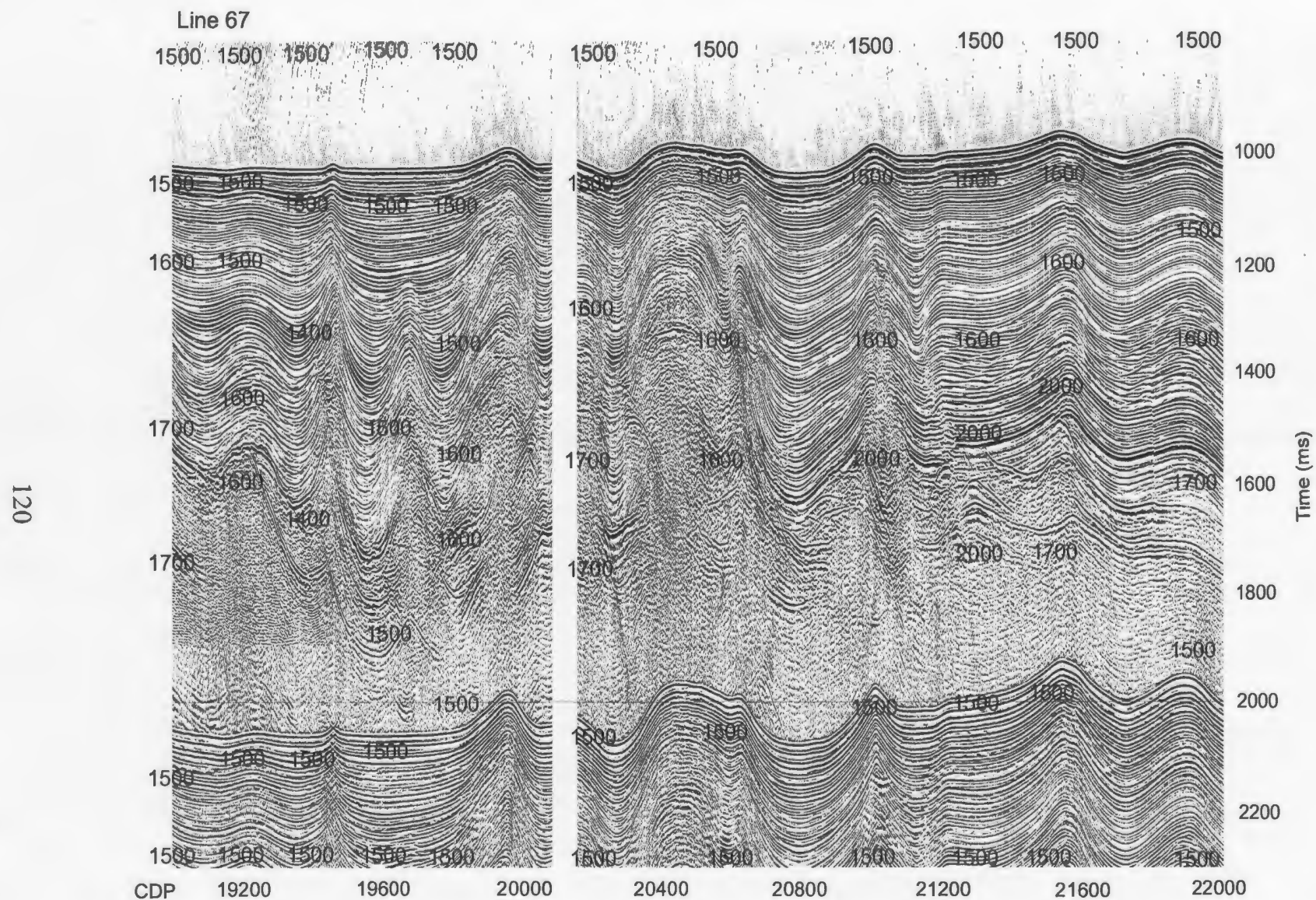


Figure 3.43: Constant velocity migrated stack of CDPs 19000-22000 along line 67 showing the chosen RMS velocity field (all velocities in m/s). Resultant migrated stack using the shown velocity field is given in figure 3.44.

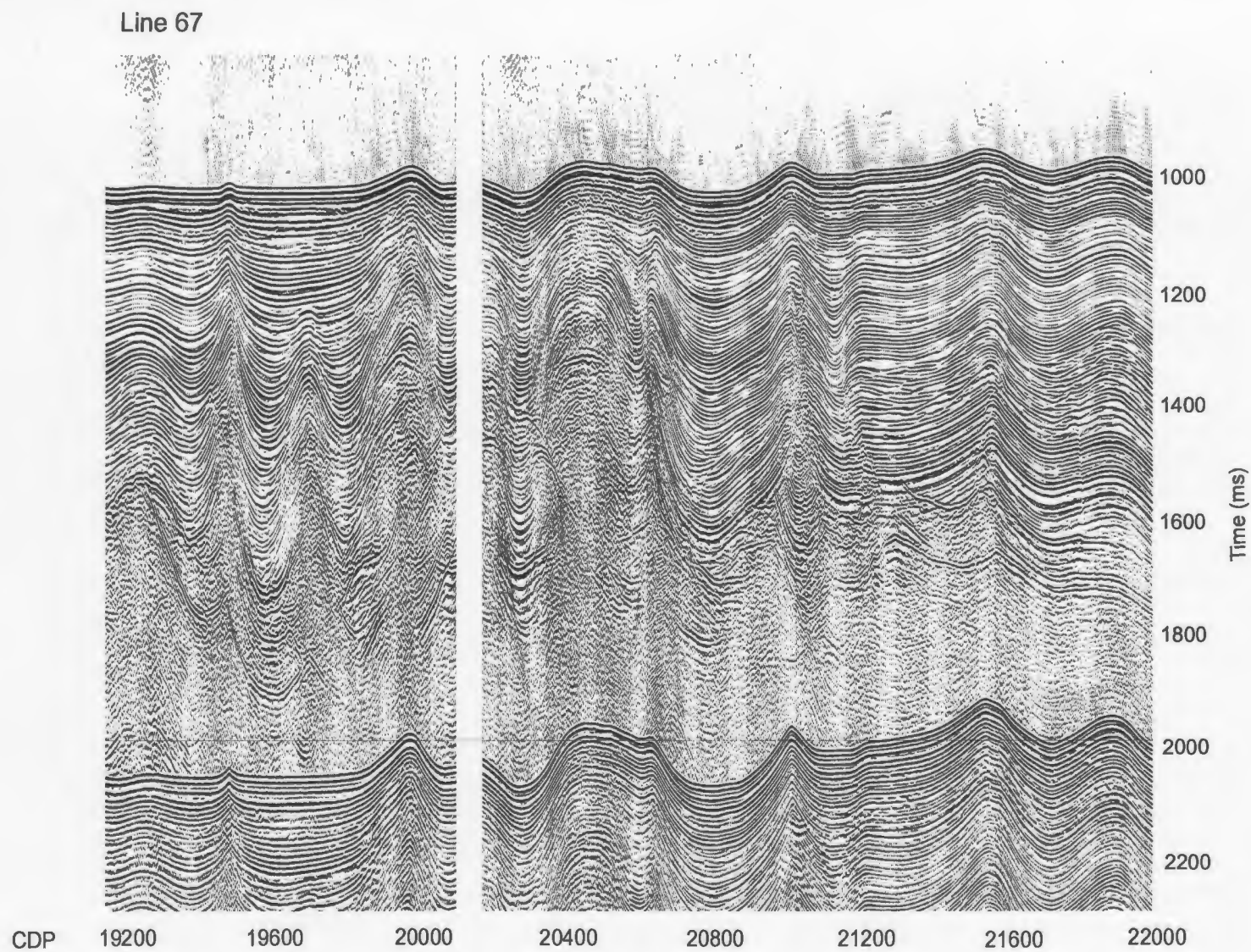


Figure 3.44: Migrated stack of CDPs 19000-22000 along line 67, using RMS velocity field shown in figure 3.43.

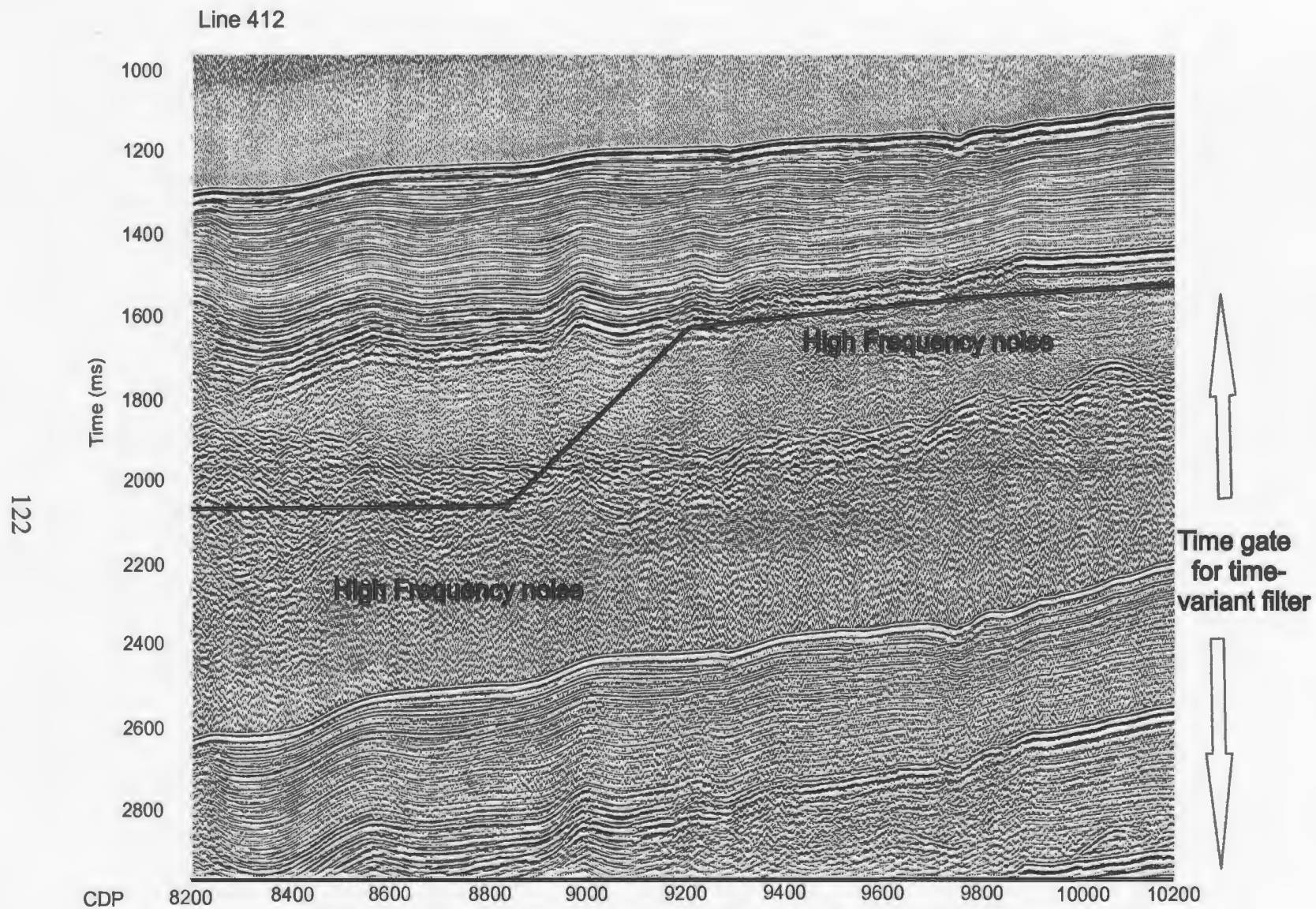


Figure 3.45: Migrated stack of CDP's 8200-10200 along line 412 showing high frequency noise generated during migration. Boundaries show time gates chosen for a time variant filter.

3.2.11 Time Variant Filtering

High frequency noise, not obvious prior to migration, appears in the migrated data at various places and times in each of the lines processed for this thesis. Figure 3.45 shows an example of this noise on CDP's 8200-10200 of a migrated stack along line 412. The noise appears to be an artifact of the migration process, possibly caused by noise from the deeper section being brought into the shallower times due to summing along the diffraction hyperbolas. Fortunately in most places where the noise occurs, it is at times late enough that the primary events have a lower frequency than the generated noise. High frequency filters should therefore not eliminate the primary reflections. To avoid these filters affecting high frequency shallow events the filter must be spatial and temporally limited to affect only the areas affected by the noise. Figure 3.45 shows the time gate chosen for time varying filtering in this portion of line 412. A bandpass filter with parameters 25-50-150-200 was applied between these time gate boundaries. The filtered result, in Figure 3.46, shows that the noise has been attenuated leaving only the primary energy reflections behind.

3.2.12 Trace Mixing and Decimation for Plotting

Trace Mixing involves averaging adjacent traces and is done for two reasons in this data-set. The first reason is to make the reflections appear more continuous by enhancing low dip events. The second reason is for plotting purposes. For the lines processed for this thesis, trace mixing is done with three adjacent CDPs. It is then possible to plot only every second trace after trace mixing.

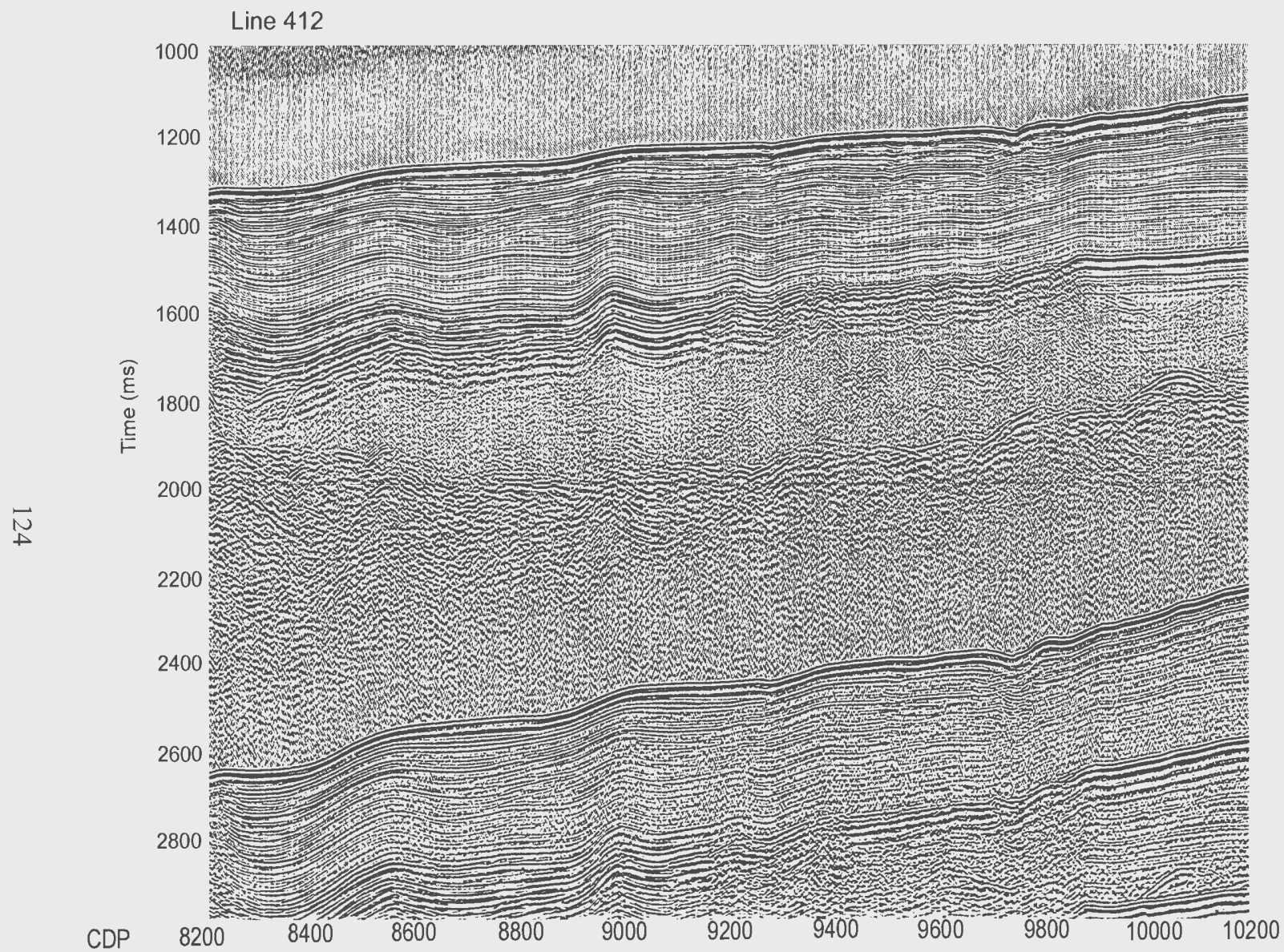


Figure 3.46: Migrated stack of CDP's 8200-10200 on line 412 after time variant band pass filter (25-50-150-200) has been applied.

3.3 Summary of Data Processing

The processing flows for each of the lines processed for this thesis were similar, with minimal changes based on the amount of noise in the sections, the degree of spatial aliasing, and the number of static corrections required. There were also small variances in the filter parameters, predictive deconvolution operators and in stacking and migration velocities. Overall, the processing resulted in quality seismic images despite the modest source volume and CDP stacking fold. Reflections are generally imaged to 2-3 seconds two-way time below seabed, even when water depth is more than 1 km. The main obstacle in the processing, which remains unresolved, is in the removal of long period multiples. The wave equation multiple rejection process attempted on this data was unsuccessful at removing the sea bed multiple. This is likely due to the inability of the algorithms used in the multiple rejection process to deal with even gently dipping sea beds or to deal with multiple energy that differs, in phase and frequency content, even slightly from the primary energy. The limitations of this process, and of other multiple attenuation methods, cause the processes to be unsuccessful when applied to this dataset. In order for multiples to be dealt with in any data collected from this basin there would need to be a change in the acquisition parameters. The desired outcome of changing these parameters would be a dataset with multiple energy that can be more easily differentiated from primary energy, and therefore be more easily eliminated. Some such changes could include increasing the number of receiving channels, which would increase the offset and therefore hopefully create a difference in the amount of move-out between the primary

and multiple reflections. If a noticeable difference in move-out could be achieved, processes such as stacking or radon transform could be useful to suppress the multiple energy. Another possible approach is to implement an increase in the length of the recorded data. This should increase the number of repetitions of the multiple, at least in shallow areas, and make processes like predictive deconvolution more widely beneficial in data collected from this basin.

Chapter 4: Seismic Descriptions

In this chapter, the seismic data located in figures 4.1 (also see figure 4.2) will be utilized to describe and correlate seismic sequences and structures found in the Outer Cilicia Basin. The sequence and fault descriptions will then be used to estimate age relationships for the layers and structures, with adherence to the rules of stratigraphic architecture and structural relationship. Wherever possible, an attempt will be made to correlate these structures and sediment layers with the onland geology. In the chapter following, the descriptions will be discussed further in relation to the origin of the structures and the evolution of the basin during Neogene time.

The descriptions of both sequences and structures are limited to those observed in the Miocene and later. This is due to a relatively short seismic record length, a lack of seismic resolution at depth, and to multiple energy masking the primary energy in many areas. The descriptions are also limited by the seismic coverage in the basin. In general, the north-south directed dip lines are separated by about 15 km, while the east-west directed strike lines are separated by at least twice that amount (with exception of the western portion of the basin where there is better seismic coverage). This coverage should allow correlation of major basin-wide features, but may limit the interpretation of more local features.

All interpretations were made from paper seismic sections plotted in either CGM or TIFF format. Care was taken to make sure that all sections were plotted at the same scale and that all interpretations were done on appropriately scaled sections. Some

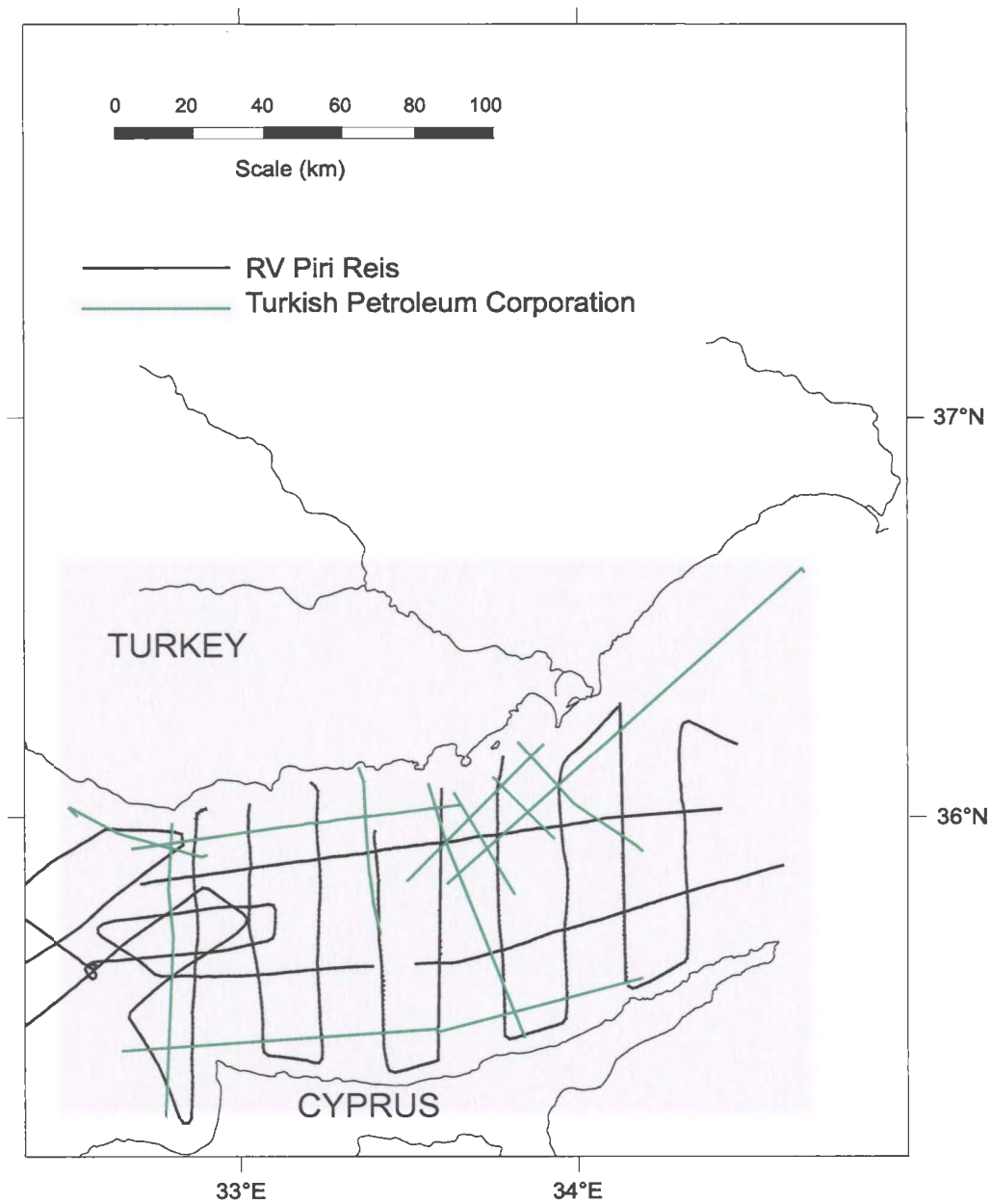


Figure 4.1: All available seismic data from the Outer Cilicia Basin (edited from Aksu et al., 1995).

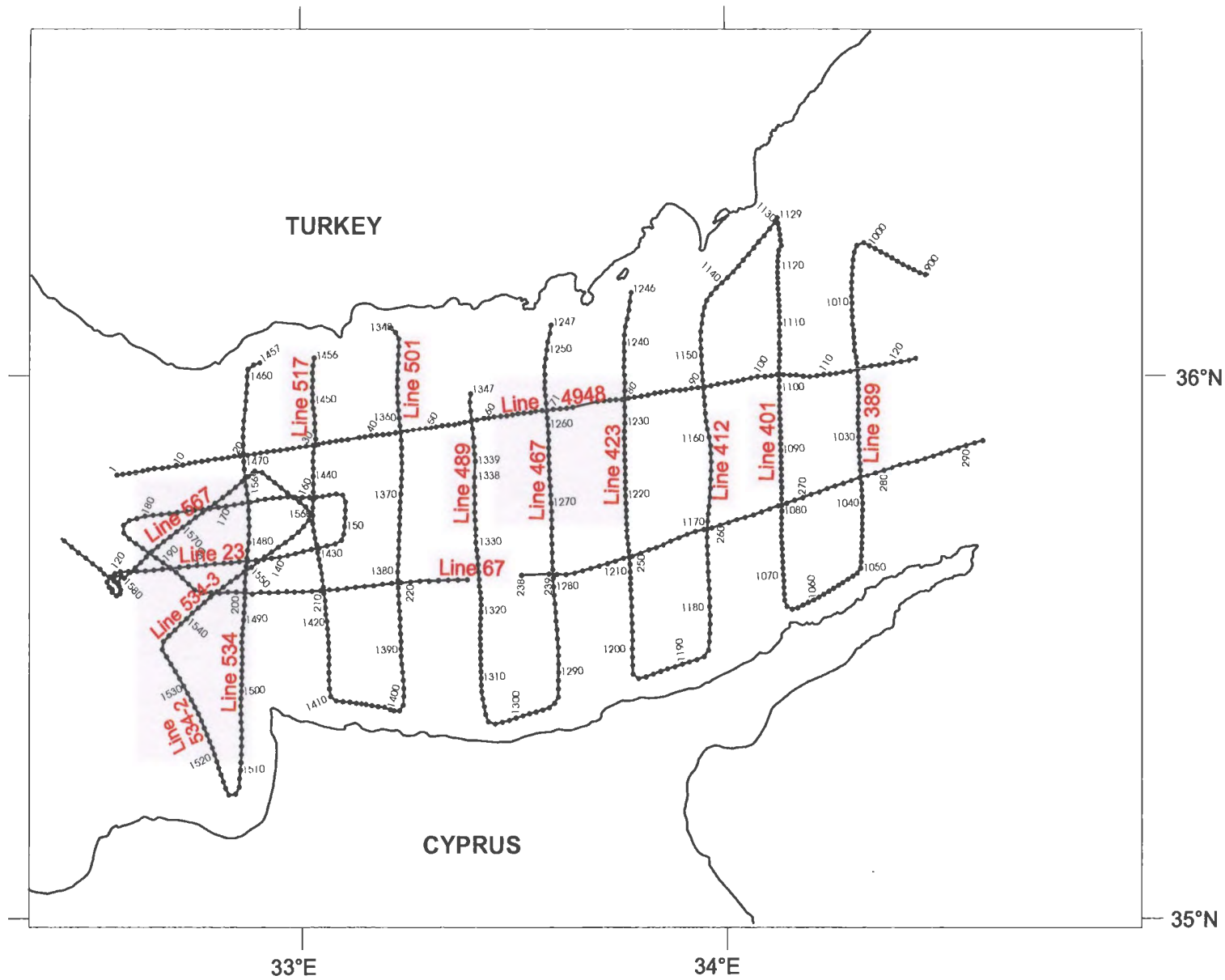


Figure 4.2: Seismic data in the Outer Cilicia Basin collected from the RV Piri Reis showing location of fix numbers (edited from Aksu et al., 2005)

references in this chapter relate to fold-out seismic sections of complete lines, included in Appendix 1 and referenced as A1-Figure 1, etc. These sections are vertically exaggerated by a factor 8X, making faults and structures dip more steeply than they do at true scale. True dip indicators are included on each seismic profile to give a better indication of the actual dip of the structures. It should be noted, however, that the true dip indicators are calculated based on water velocity (1500 m/s), and may therefore be somewhat misleading for deeper structures. Contour maps were created using hand-picked time or isochron values (both in two way travel time), which are then plotted at the appropriate location and hand contoured. Picks were taken at every available navigational fix location, which corresponds to an interval of about 1.7 km. As stated in the previous chapter, the navigational fix locations represent the location of the research vessel at the time the shot was fired. On the seismic profiles of appendix 1, however, the fix numbers are actually plotted at the CDP location of the corresponding shot number. This results in a few hundred metre discrepancy between the actual navigational fix location and the location plotted on the seismic profiles. This issue can create some degree of mistie at crossover points on intersecting seismic profiles. Generally, well-correlated tie points can be found on intersecting seismic profiles within a maximum of one kilometre from the navigational fix location marking where the lines cross.

4.1 General Description of Outer Cilicia Basin

4.1.1. Bathymetry

A bathymetry map of the Outer Cilicia basin, derived from the available seismic data, is shown in figure 4.3. The Cilicia Basin is perched relative to the significantly deeper sea floor of the Antalya Basin, immediately to its west. The sea floor drops from a maximum of 1300 m (assuming a water velocity of 1500 m/s) in the Cilicia basin to about 2500 m in the Antalya Basin to the west. The Outer Cilicia Basin forms the east-west oriented segment of the arcuate Cilicia Basin, and is considered to be the deeper and relatively under-filled portion of the basin. The bathymetry shows the deepening of the sea floor from shelf regions into the central portion of the basin, as well as the deepening toward the western boundary. The sea floor drops from around 150 m along the narrow Turkish Shelf, at the northern extent of the seismic data, reaches over 1000 m near the centre of the basin, then shallows again rapidly toward the coastline of northern Cyprus. The progressive deepening of the sea floor toward the west is obvious in the central zone, where the sea floor drops from 800 m in the east to over 1800 m in the far west portion of the basin. Closely spaced contours, both to the north and south of this western area, indicate a rapid drop in bathymetry into the deep basin. To the north, the sea floor gradually deepens across the Turkish Shelf and then rapidly drops into the basin about 25 km south of the coast of Turkey. To the south, closely spaced contours at the northern extent of a northwest oriented relative bathymetric high, which extends more than 50 km off the northwest coast of Cyprus, represents an up to 750 m drop in bathymetry

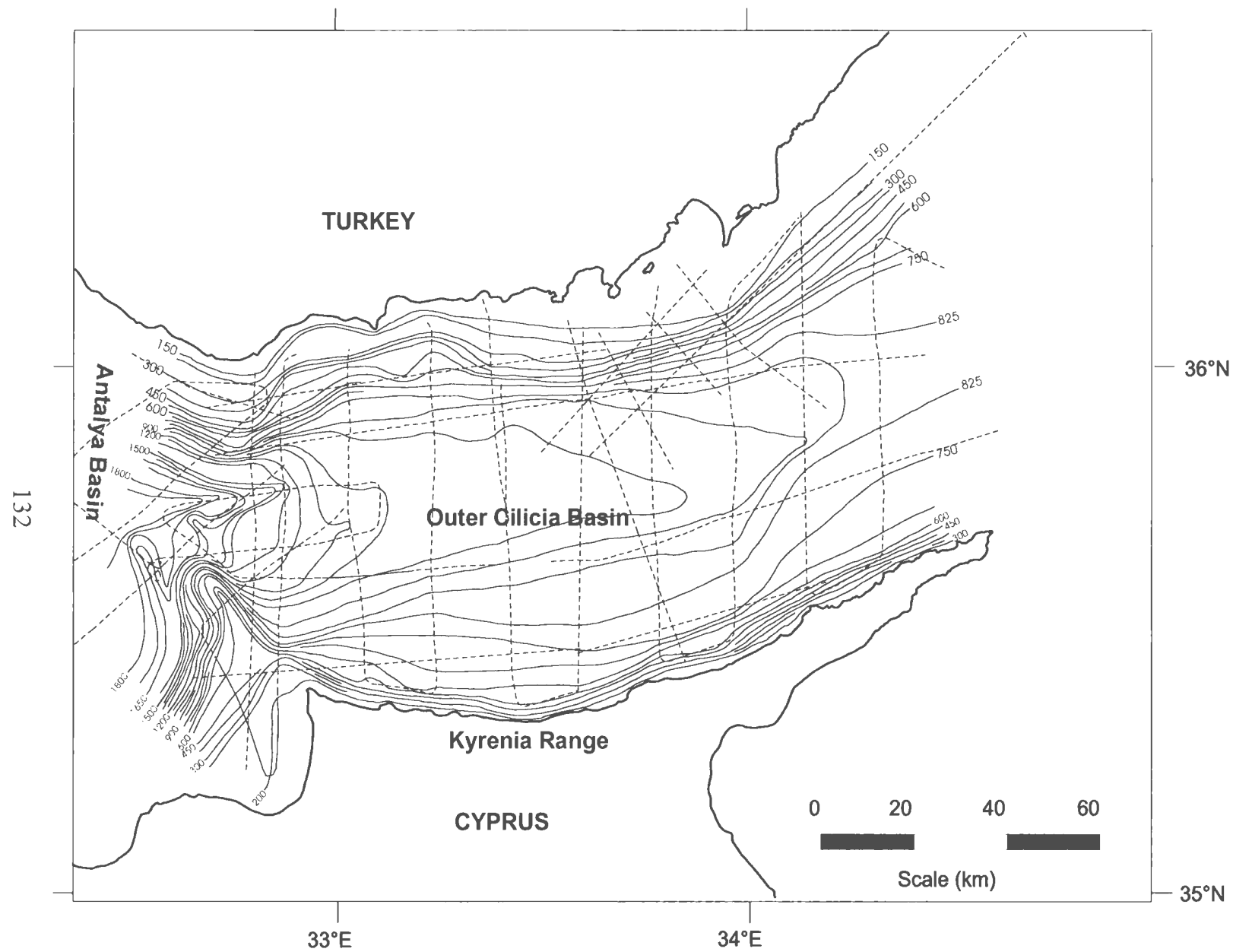


Figure 4.3: Bathymetry map of the Outer Cilicia Basin, contoured with a 75 m contour interval

over a 10 km distance.

4.1.2 Morphology of the Outer Cilicia Basin

The Outer Cilicia Basin is divided into five morphological zones, reduced from the seven defined by Evans et al. (1978) and described in some detail in section 2.2.3. The five zones, from north to south are: 1) the Turkish Shelf, 2) the northern Outer Cilicia Basin, 3) the Central Fold Zone, 4) the southern Outer Cilicia Basin, and 5) the Cyprean Shelf (Figure 4.4). A sixth zone, the Anamur-Kormikiti Zone, is the transition between the Outer Cilicia and Antalya Basins. Each zone is labeled on the time structure map across the M-reflector, shown in Figure 4.5.

The Turkish Shelf extends from the coastline to a transition zone into the deeper basin. The transition is marked by a steep gradient in sea floor bathymetry (shown by closely spaced contours at the northern shelf margin on Figure 4.4). The zone is characterized by a young sedimentary succession, relatively thin in comparison to that seen in the deep basin, directly overlying deformed older rock units. The transition between this zone and the next is marked by deep and surficial extensional faults.

The northern Outer Cilicia Basin lies just south of the Turkish shelf break and is the deepest part of the basin on north-south profiles (Figure 4.4). The zone is characterized by a thick succession of young sedimentary rock units, affected by extensional, compressional and strike slip faulting.

The Central Fold Zone lies along the centre of the basin and separates the basin

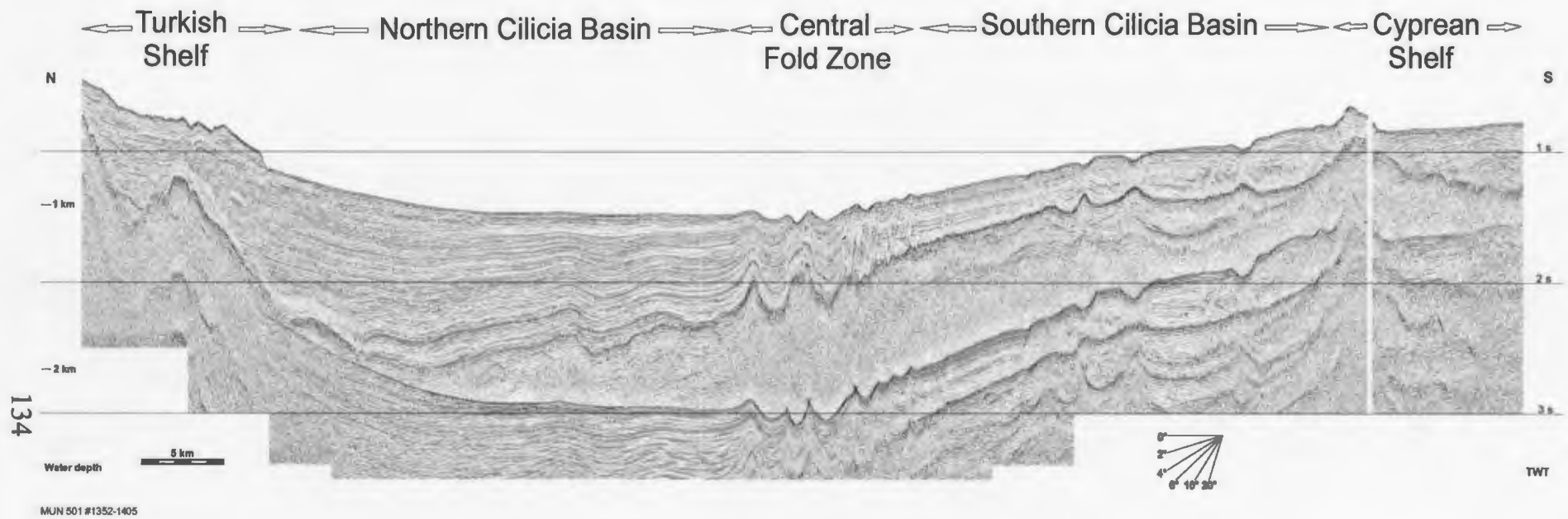


Figure 4.4: Seismic Line 501 showing the five zones making up the Outer Cilicia Basin.

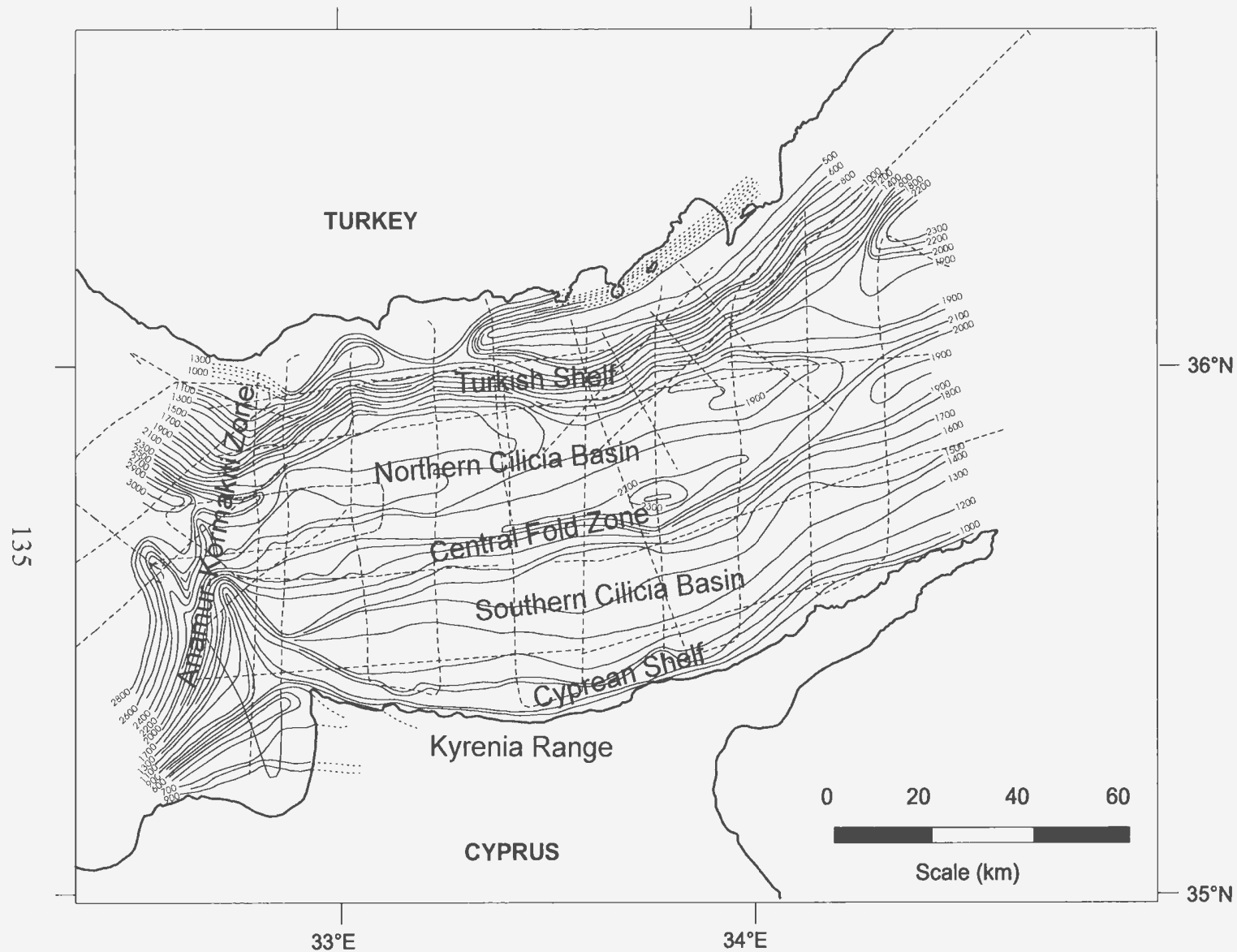


Figure 4.5: Time structure of M-reflector in the Outer Cilicia Basin, contoured with a 100 ms contour interval.

into more simply-structured, north and south divisions (Figure 4.4). The zone is characterized by high amplitude folds, often associated with reverse faulting and less often with overlying extensional faults.

The southern Outer Cilicia Basin is generally shallower and has a thinner succession of young sedimentary rock units than does the northern basin (Figure 4.4). The sedimentary succession is relatively flat lying and undisturbed, except in the most southerly portion of the basin where it is cut by listric, extensional faults.

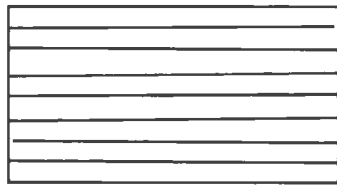
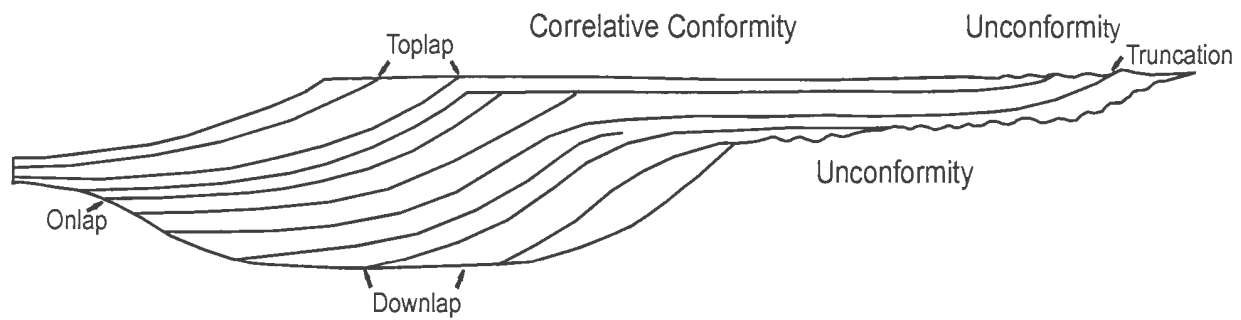
The transition between the southern Cilicia Basin and the Cyprean Shelf is not as easily defined as the northern shelf boundary, as there is generally not a rapid change in the sea-floor bathymetry (Figures 4.3 and 4.4), except at the north end of the Kyrenia mountain range. The transition is most often represented by a noticeable thinning of youngest successions towards the coastline. The Cyprus Shelf itself is characterized by a young sedimentary succession, of comparable thickness to that in the south basin, overlying the older rock units.

The overall basin shape, as represented by both the sea-bed reflector and the youngest sedimentary sequences, is an asymmetrical depression with its deepest point in the northern half of the basin.

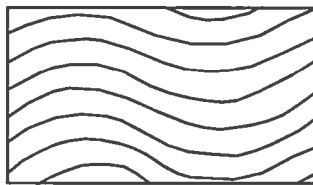
The sixth zone is the transition zone between the Cilicia and Antalya Basins and has been described in literature as the Anamur complex (Anastasakis and Kelling, 1990) or the Anamur-Kormakiti complex (Aksu et al., 2005). The transition is represented by basement highs, which appear to extend from onshore mountain ranges (Figure 4.5).

4.2 Description of seismic sequences and stratigraphy

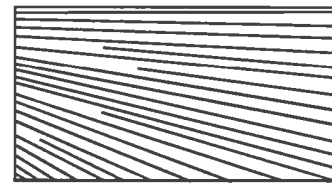
The depositional history of the Outer Cilicia Basin can be broken down into distinct phases using the principles of seismic stratigraphy, correlated with distant wells drilled in the Inner Cilicia and Adana Basins. A seismic sequence is defined as “A stratigraphic unit composed of a relatively conformable succession of genetically related strata bounded at its top and base by unconformities or their correlative conformities” (Mitchum et al., 1977). Sequence analysis first requires sequence boundaries to be defined. An unconformity is a surface along which there is clear evidence that either erosion or non-deposition has taken place, based on the angular discordance of beds above and/or below the boundary. A conformity also separates older from younger strata, but with no evidence of erosion or non-deposition (Mitchum et al., 1977). Schematics of these boundary types, as well as common internal seismic configurations seen in the basin, are shown in Figure 4.6. In the Outer Cilicia Basin, the sequence boundaries are represented as distinct reflectors that cut off the reflectors below and/or above the boundary. The boundaries are not easily defined everywhere because unconformities often become correlative conformities in deeper areas of the basin. In these instances, the sequence boundaries must be traced from areas where they are well determined to places where the reflector is more conformable with sequences that lie above and below it. Sequence boundaries are then correlated around the seismic grid using crossover points to ensure the same reflector is picked on adjacent lines. This tie-line crossover point approach, together with some jump correlation, leads to the definition of basin-wide



Parallel



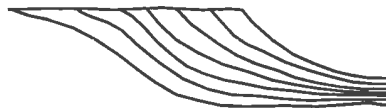
Wavy



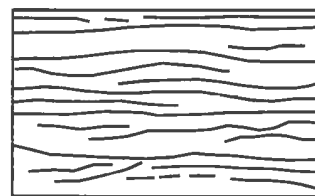
Divergent



Sigmoid



Oblique



Hummocky

Figure 4.6: Seismic reflection configurations and termination patterns commonly seen in the Outer Cilicia Basin (edited from Mitchum et al., 1977).

sequence boundaries. Below, the main stratigraphic units are defined and described, and their age and lithology established by correlation with onland geology and with wells drilled in the Adana and Inner Cilicia Basins (see Figure 4.7).

Four stratigraphic units have been identified: units 1, 2, 3A and 3B (from youngest to oldest) (see Figure 4.8). The corresponding sequence boundaries are: the M-reflector (at the base of unit 1, light green reflector), the N-reflector (at the base of unit 2, blue reflector) and the O-reflector (at the base of unit 3A, dark green reflector). Unit 1 is separated into 4 seismic sequences, each separated by internal sequence boundaries. These are from youngest to oldest: sequence A, sequence B, sequence C, and sequence D, each separated by sequence boundaries: SB-a, SB-b, and SB-c (purple reflectors). It is not possible to separate the older stratigraphic units into seismic sequences, as a lack of seismic resolution at depth makes it difficult to track internal sequence boundaries. Two wells located in the Inner Cilicia Basin were used to correlate the seismic stratigraphic units, described above, with geological units (see figure 4.9). Both wells tie, and show good correlation, with seismic data from the Inner Cilicia Basin. These correlations were then carried into the Outer Cilicia Basin through seismic tie lines.

4.2.1. Unit 1

Unit 1 is the youngest sedimentary package seen in the Outer Cilicia Basin and is characterized by high frequency, acoustically strong, continuous reflections. The unit represents the Pliocene-Quaternary succession, and is likely made up of deep water

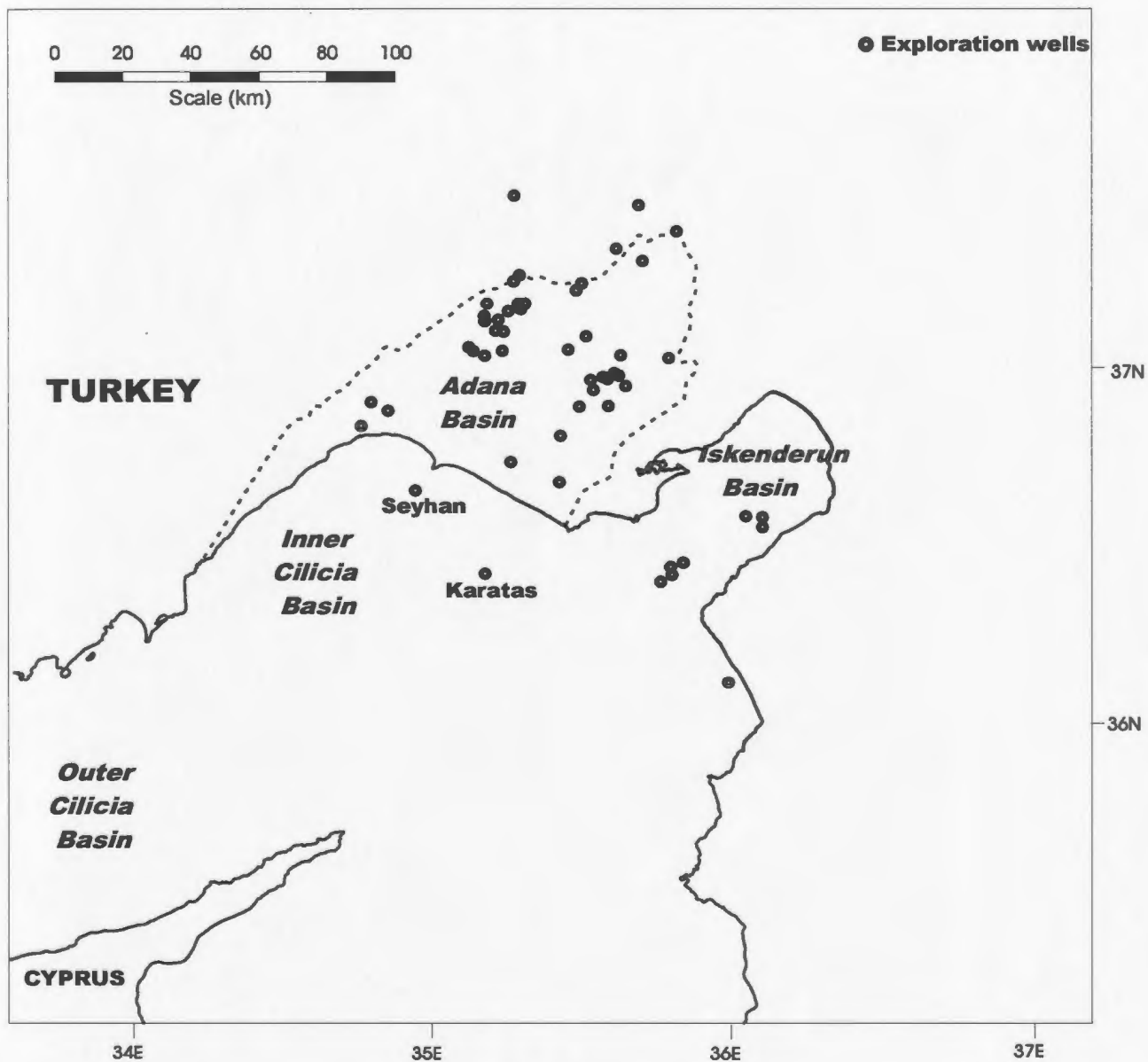


Figure 4.7: All exploration wells drilled in the Adana, Inner Cilicia and Iskenderun Basins (edited from Aksu et al., 1992).

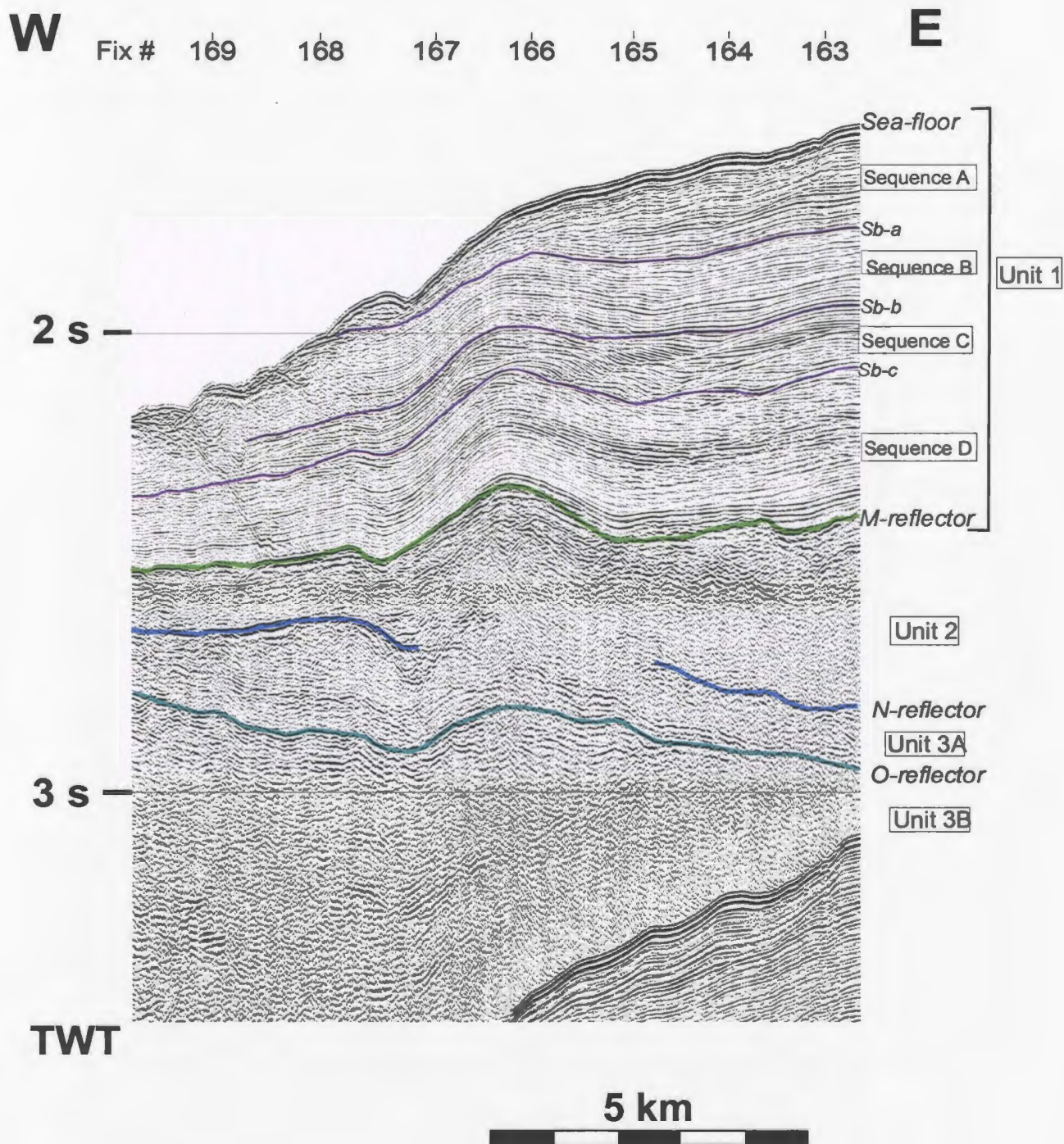


Figure 4.8: Seismic line 23, fix # 163-169 showing each of the sequences and sequence boundaries described from the Outer Cilicia Basin.

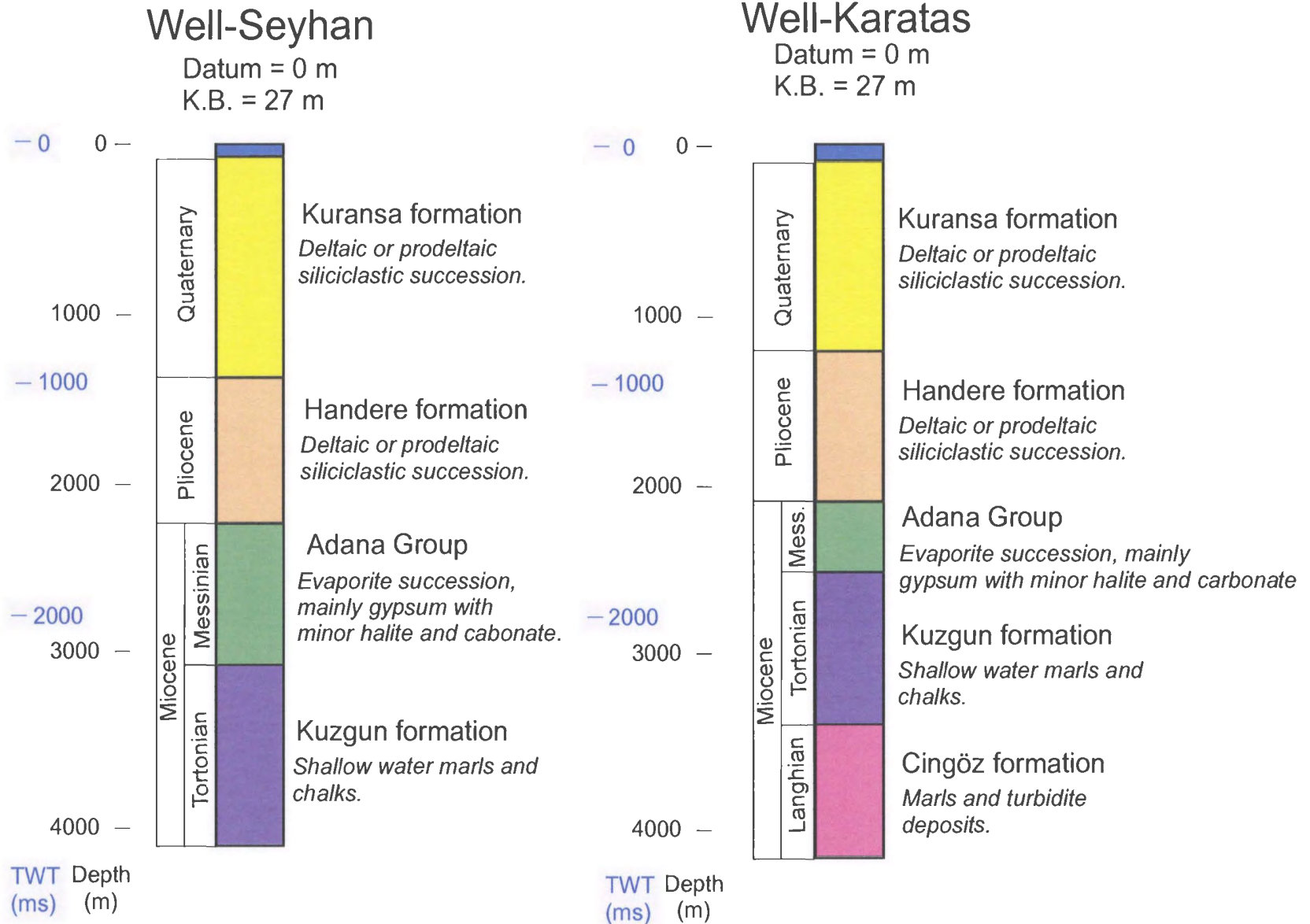


Figure 4.9: Results from two wells drilled in the Inner Cilicia Basin, map locations labeled on figure 4.7 (used with permission from Turkish Petroleum, unpublished data)..

siliciclastics with limited turbidite deposition. The succession continues into the Inner Cilicia Basin, where it is characterized by a prograding wedge of deltaic sediment fed from a number of rivers, onland Turkey (Aksu et al., 1992, 2005). The unit can be correlated with the Handere and Kuranşa Formations of the Adana Basin (Yalçın and Görür, 1984). The isochron thickness map of the Pliocene-Quaternary succession is shown in Figure 4.10. The map shows that the succession is widely distributed in the Outer Cilicia Basin and even blankets the basement highs found in the area, such as the Anamur-Kormakiti complex and the offshore extension of the Kyrenia range. In most areas, the succession continues onto the continental shelves, with the exception of the far south-west portion of the basin where the succession abuts against a major, basin-bounding transtensional fault (see A1-Figure 3, south margin). The succession is thickest along the east-west directed, central axis of the north basin and thins towards the margins in both north and south directions. At the northern margin, the closely spaced contours indicate a fairly rapid increase in thickness from the shelf to central axis. This increase occurs somewhat less rapidly over the Ecemiş high, as labeled on Figure 4.10. At the southern margin, the change in thickness also occurs much more gradually, as shown by the more widely spaced contours. Figure 4.10 also shows that the Pliocene-Quaternary succession reaches greater thicknesses on the eastern part of Turkish Shelf, toward the Inner Cilicia Basin, which is known to have a much thicker Pliocene-Quaternary succession (Aksu et al., 1992). In the Anamur-Kormakiti area, the succession thins towards the basement high, but then thickens substantially in the depocentres that lie

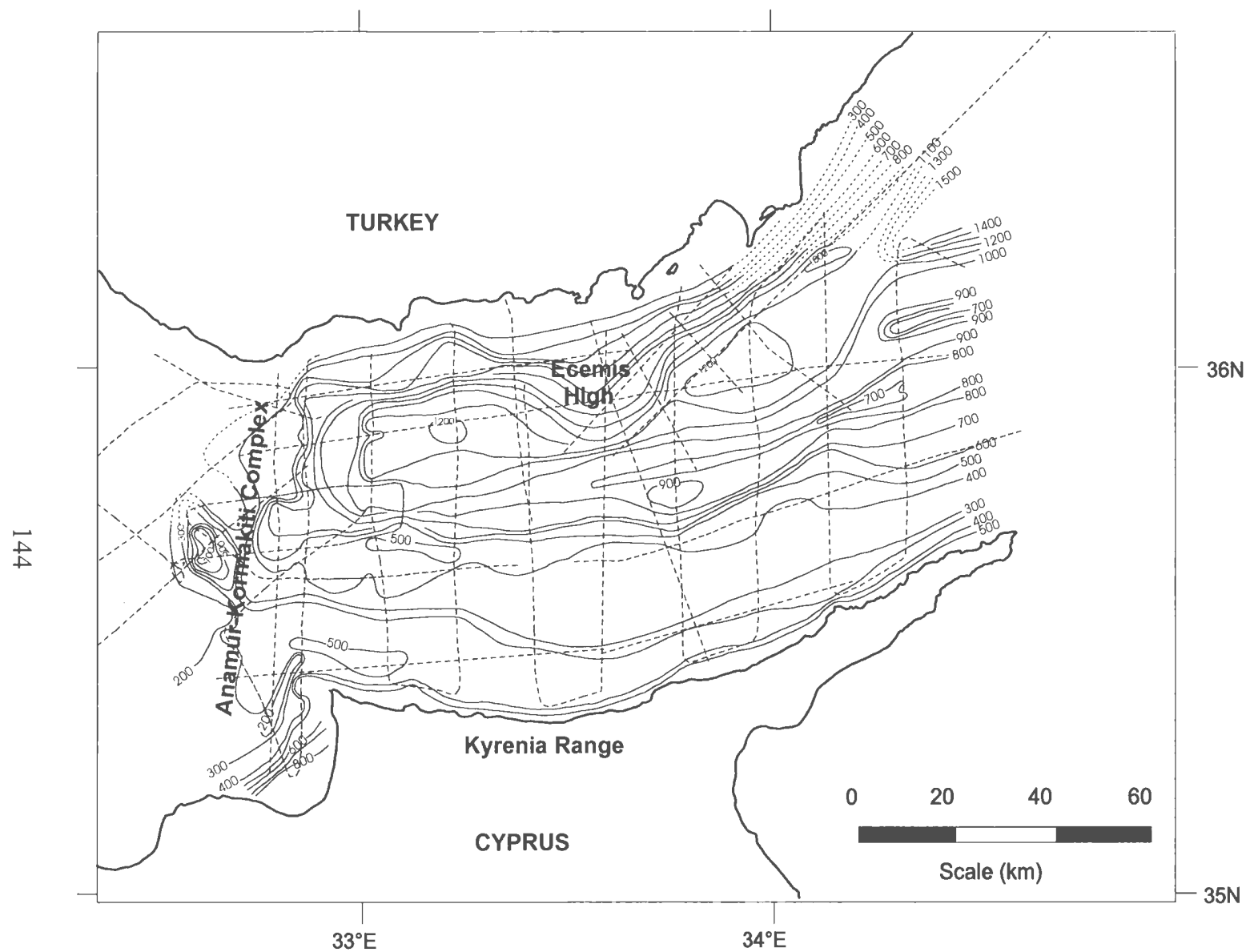


Figure 4.10: Isochron map of unit 1 (Pliocene-Quaternary succession) in the Outer Cilicia Basin, contoured with a 100ms contour interval.

between thrust zone highs. It should also be noted that in areas where the Anamur-Kormakiti complex is not represented by an obvious basement high, the Pliocene-Quaternary successions still thin toward the western boundary of the basin (see A1-Figure 16, fix # 165-180). Smaller scale thickness variations, such as thinning over salt anticlines, are not represented by the isochron map as neither the fix spacing nor the contour interval are fine enough to capture these details. As mentioned above, the Pliocene-Quaternary succession has been divided into 4 seismic sequences, each separated by sequence boundaries.

4.2.1.1 Unit 1: Sequence A

Sequence A is characterized by high amplitude, continuous reflections that are parallel with the upper and lower boundaries in most areas. A notable exception occurs just south of the Turkish Shelf, where the reflections downlap onto the lower boundary as the sediment progrades toward the center basin (e.g., A1-Figure 7, fix # 1252-1255). Other local exceptions occur where reflections show onlapping and toplapping relationships and where the reflections are discontinuous or chaotic. Sequence A represents the youngest sediment deposited in the Outer Cilicia Basin.

The upper boundary of sequence A is represented everywhere as a high amplitude reflector marking the base of the water column. The bathymetry map (Figure 4.3) shows all major changes in the depth to the sea-floor horizon. Smaller scale changes in sea floor bathymetry are caused by surface relief of presently active fault systems, salt diapirism, and erosional processes. Channel cuts, created by either erosional processes or

underlying fault systems, also commonly affect the sea-floor bathymetry, especially in the western portion of the basin.

Sequence A is distributed across the entire basin, including a thick succession deposited on the Turkish Shelf. In the both the east and far-west portions of the basin, the sequence is thickest on the shelf. Most thickness changes seen in sequence A occur in the hanging walls of extensional faults, on top of thrust sheets, or are related to rising salt structures. These thickness changes are mainly accommodated by the convergence or divergence of the internal reflectors (e.g., A1-Figure 7, fix # 1271-1276, A1-Figure 4, fix # 1414-1418). A notable exception is seen both in the eastern fold belt and on top of the offshore extension of the Kyrenia Range, where the reflectors of sequence A onlap onto underlying growth unconformities (e.g., A1-Figure 1, fix # 112-119 and A1-Figure 3, fix # 1503-1506). These local unconformities form at the flanks of the rising salt structures or elevating thrust sheets.

Another feature commonly seen within sequence A, is a patchy, discontinuous, and sometimes chaotic reflector group (A1-Figure 8, fix #1225-1232 and A1-Figure 1, fix # 37-45). These features are only seen in the northern part of the basin and commonly have a fairly flat base and mounded upper surface. In the western and central part of the basin, the features are quite extensive with maximum lengths reaching between 13 and 15 km, and a thickness of over 100 ms. Farther east in the basin, the features tend to be smaller and less continuous. These features are interpreted as gravity flow phenomena, such as debris flows or turbidites, deposited as a result of shelf instability. Within

sequence A, there is evidence of infilled channels cutting through this sequence, in the central and western portions of the northern basin (A1-Figure 8, fix # 1235-1236). The infilling sediment onlaps onto the channel walls and gives rise to generally higher amplitude reflectors. It is possible that these channels may have acted as feeders for the turbidite flow deposits mentioned above.

Primarily in the central and eastern portion of the basin, there is evidence of prograding reflectors, slump deposits and shallow faulting at the boundary between the Turkish Shelf and the deeper basin (A1-Figure 7, fix # 1248-1256 and A1-Figure 10, fix # 1108-1114). This suggests that the sediment of sequence A, initially deposited atop the Turkish shelf, commonly progrades or slumps into the deeper basin.

4.2.1.2 Unit 1: Sequence B

Sequence B is characterized by medium to high amplitude reflections that are parallel and concordant with the upper and lower boundaries in most areas of the basin. Locally, however, the reflections can be wavy, hummocky, discontinuous and even chaotic. The reflections also locally show toplap, onlap and downlap onto both internal reflectors and onto the sequence boundaries.

The upper boundary of sequence B is a distinctive reflector, easily correlatable throughout the Outer Cilicia Basin. The boundary separates the lower amplitude reflections of sequence B, from the high amplitude reflections of sequence A (see A1-Figure 6, fix # 1315-1318). The chrono-stratigraphic significance of this reflector is obvious on an east-west profile extending through the north part of the basin (A1-Figure

1). This profile shows SB-a as an important boundary between the underlying sequences, which are structured and vary in thickness across the profile, and the overlying sequence, which has a relatively constant thickness and is unaffected by most fault systems active in this part of the basin (with the exception of those active in the far east end of the profile). This indicates there was major structural change in the Outer Cilicia Basin between the deposition of sequences A and B.

Sequence B is thickest in the northern part of the Outer Cilicia Basin, and thins toward both basin margins. The thinning toward the basin margins is accommodated by the termination of onlapping reflectors onto the lower boundary and by convergence of the internal reflections (see A1-Figure 4, fix # 1450-1452). Unlike the underlying sequences, sequence B is present on the Turkish Shelf and only pinches out near the northern limit of the data set. The sequence also shows thinning over the Ecemiş high, accommodated by converging reflectors, as there is no evidence of terminating reflectors toward the high. In the area of the Ecemiş high, sequence B is highly structured and the reflectors show complicated relationships involving onlap or baselap onto underlying, folded, internal reflectors and abrupt changes in reflection character. Other complex seismic configurations, such as wavy reflectors (see A1-Figure 4, fix 1433-1435), are common in the western part of the north basin and are likely related to the evolving salt structures and fault systems in the area.

The pockets of discontinuous reflectors (interpreted as debris flows) described for the previous sequence are also present in sequence B (A1-Figure 1, fix # 5-40, A1-Figure

6, fix # 1341-1345). In the western and central part of the basin, the features are quite extensive with lengths and cross sectional widths of up to 10 km and thicknesses up to ~ 80 ms. Similarly to sequence A, the features tend to be smaller and less continuous in the east part of the basin. There is also evidence of infilled channels in the western part of the north basin (A1-Figure 1, fix 30-32 and A1-Figure 4, fix # 1443-1445).

Local thickness changes occur in sequence B, as a result of the movements of salt structures and fault systems found in the basin. The convergence or divergence of internal reflectors accommodate these thickness changes. The sequence thins over the top of salt anticlines, and thickens slightly in the adjacent synclines in some areas of the central fold zone (A1-Figure 6, fix # 1330-1332). The sequence also thickens in the hanging walls of certain extensional or transtensional faults that lie in both the north and south basins. Thickness changes also occur on top of the offshore Kyrenia range, due to the movement of the underlying thrust systems.

4.2.1.3 Unit 1: Sequence C

Sequence C is characterized by high amplitude, continuous reflections that are parallel and concordant with its bounding surfaces, in most areas of the basin. Locally, however, the reflections converge and diverge, as well as showing onlap, downlap, and toplap onto the upper and lower boundaries. Sequence C is either a continuation of Pliocene deposition, or the initial deposition of the Quaternary succession in the Outer Cilicia Basin.

The top of the sequence C is a high amplitude reflector, easily correlated across the entire Outer Cilicia Basin. The SB-b reflector is most easily picked on the Turkish margin where it has the appearance of an erosional unconformity. Underlying reflectors are noticeably terminated by the boundary (e.g., A1-Figure 4, fix # 1445-1447), while overlying reflectors show a strong onlapping relationship (e.g., A1-Figure 4, fix # 1447-1449). In the southern basin, the reflector is picked based on a noticeable amplitude change between sequences B and C (e.g., A1-Figure 5, fix # 1380-1386).

Sequence C shows a similar distribution pattern to sequence B. The sequence thins towards both basin margins and pinches out onto the Turkish shelf (see A1-Figure 3, fix # 1466-1470). The pinch out occurs farther landward than that of sequence D (see below description), which indicates a further relative sea level rise across the northern shelf between the deposition of the two sequences. Thinning toward the basin margins is accommodated by the termination of reflectors as they onlap onto the basin margins. Thinning also occurs towards the Ecemiş high, accommodated by progressive onlap onto the lower boundary towards the high (A1-Figure 1, fix # 65-70). More complicated seismic configurations, such as the onlap, toplap, and downlap of reflectors onto both the sequence boundaries and onto other internal reflectors, are common in the central and in the western portions of the basin. A good example is seen on Figure 4.11 (A1-Figure 4 fix # 1432-1438), where prograding clinoforms appear 5-10 km away from rising salt structures.

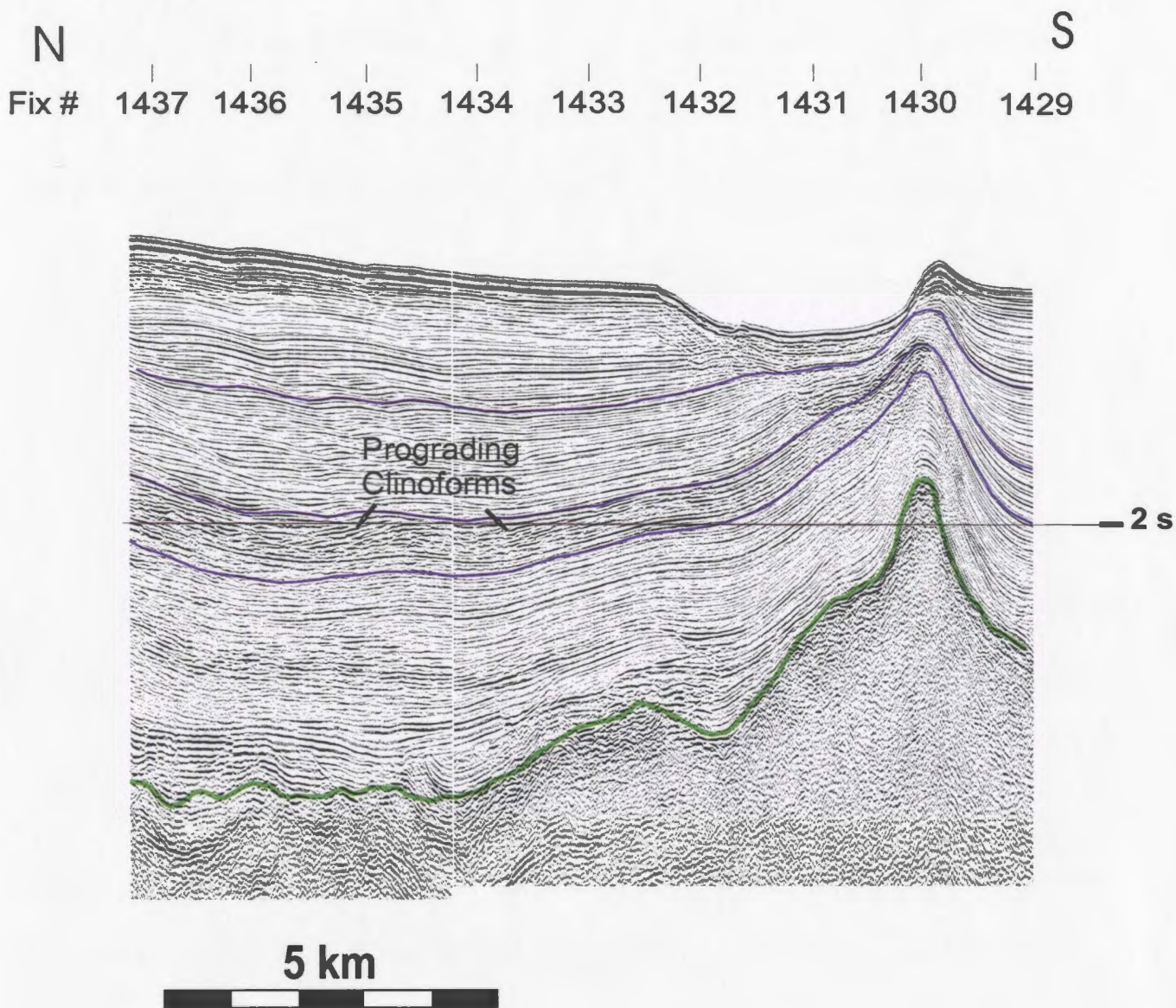


Figure 4.11: Seismic Line 517, fix # 1429-1437 showing prograding clinoforms in sequence C of the Pliocene-Quaternary succession.

Local thickness changes occur in sequence C, as a result of the movements of salt structures and fault systems found in the basin. These thickness changes generally occur over the same structures and by the same means as those of sequence B (see above descriptions).

4.2.1.4 Unit 1: Sequence D

Sequence D is represented by low to medium amplitude reflections with moderate to good continuity. Wherever present, the sequence directly overlies the M-reflector, and therefore represents the earliest Pliocene deposits found in the Outer Cilicia Basin. The internal reflections are mainly parallel and concordant, but do show local converging and diverging patterns where the unit changes in thickness. There is also evidence of onlap or downlap of the reflectors onto the lower boundary, most noticeable at the basin margins (see A1-Figure 7, fix # 1256-1264).

The top of depositional sequence D is a strong, high amplitude reflector that separates the relatively low amplitude reflectors below from the much higher amplitude, continuous reflections of depositional sequence C above. SB-c does not appear to be a major basin-wide erosional unconformity, as there is limited or no evidence of erosion across the boundary. However, the noticeable change in reflection character (e.g., A1-Figure 2, fix # 200-215), combined with the evidence of sequence C's onlap onto the boundary (e.g., A1-Figure 4, fix # 1448-1450), suggest that it represents a basin-wide break in deposition in a progressively deepening basin.

Sequence D is thickest in the northern part of the Outer Cilicia Basin, and thins toward both basin margins. The thinning is accommodated mainly by the progressive landward termination of reflectors as they onlap onto the lower boundary. The sequence's pinch-out onto the northern margin oversteps the deposition of the underlying evaporite sequence suggesting a rise in sea level from late Miocene to Pliocene time. Onlap occurs onto internal reflectors away from basin margins, suggesting deposition in a continuously deepening basin. The sequence also thins dramatically over the Ecemiş high, in the central part of the north basin. This thinning is accommodated by progressive onlap onto the lower boundary towards the high. In areas where this sequence infills Messinian age channels, the reflectors are higher amplitude, and portray an infilling, mounded type character with baselap onto the channels walls (A1-Figure 3, fix # 1470).

Other than the general thinning toward the margins, the sequence keeps a relatively constant thickness throughout the basin. In other words, the sequence does not show appreciable thinning or thickening over salt structures or due to fault systems found in the Outer Cilicia Basin. The only area where thickness changes in sequence D can be related to structural causes is at the offshore extension of the Kyrenia range, where sequence D does show thinning over the top of the basement highs created by the underlying thrust systems (A1-Figure 3, fix # 1500-1508).

4.2.2 Unit 2

The internal seismic configuration of Unit 2 is characterized by variable amplitude and discontinuous reflectors. Where internal reflections can be traced, they are

relatively parallel and concordant with the upper boundary. In areas where the upper boundary is dipping, the internal reflections tend to follow the same pattern. In some places, the discontinuous signature is interbedded with high amplitude and continuous reflectors. Unit 2 correlates with an evaporite layer that was widely deposited throughout the Eastern Mediterranean Sea during Messinian time. In the Cilicia Basin, the unit is known as the Adana Group (see Figure 4.9) and is made up of a combination of halite, gypsum, anhydrite and, in some coastal regions, possibly carbonates (Yalçın and Görür, 1984). The locally high amplitude and continuous reflectors could be the result of muds deposited during hiatuses in the evaporite deposition. Nearing the Turkish margin, in the western part of the basin, the seismic reflectors become more continuous and higher amplitude (this area is outlined between the green contour and the northern extent of the data-set on Figure 4.12). This is likely due to a lithology change from acoustically transparent halite, in the inner basin, to more carbonate or gypsum, at the basin margin. These deposits possibly correlate with Messinian-aged sandstone, gypsum and fossiliferous limestone successions, including the Taşlık, Eskiköy and Gebiz formations, found in the Aksu and Manavgat Basins, onshore Turkey (Akay et al., 1985, Karabıyıkoglu et al., 2000).

The present day distribution of the Messinian evaporites in the Outer Cilicia Basin is outlined by the zero contour on Figure 4.12. It should be noted, however, that due to movement of the ductile layer since it was deposited, the present day boundary is likely

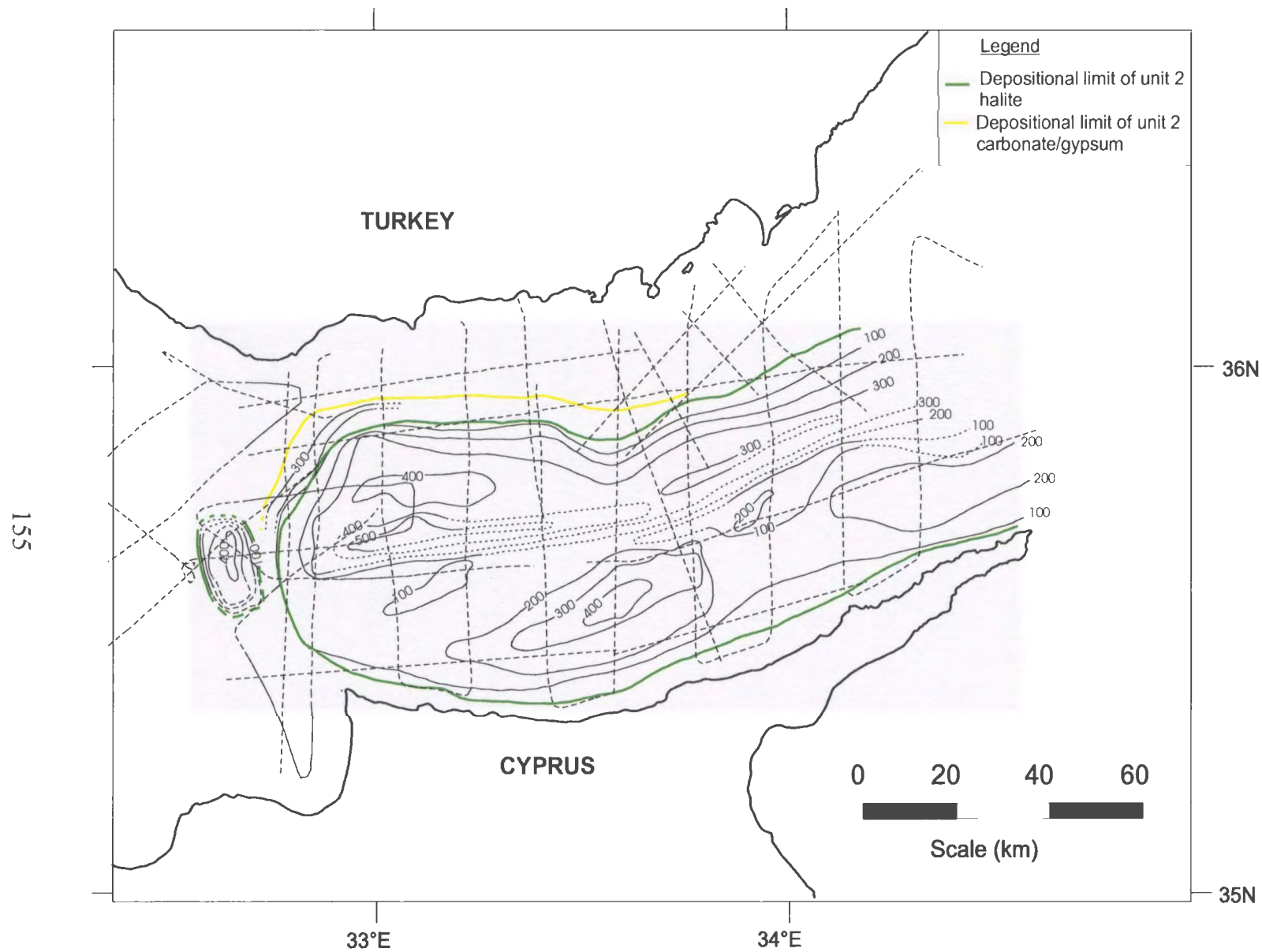


Figure 4.12: Isochron map of Unit 2 in the Outer Cilicia basin, contoured with a 100 ms contour interval.

not equivalent to the original depositional boundary. Considering the most likely direction of salt movement is toward the centre of the basin, the current distribution should be considered the minimum basin size at the time of deposition. The time thickness map shown in Figure 4.12, indicates that Unit 2 is distributed through much of the Outer Cilicia Basin. The unit pinches out onto both the northern and southern margins of the basin, as well as onto the Anamur-Kormakiti high. The northern pinch out is much deeper in the basin than the southern one, which occurs close to the Cyprean shelf (see A1-Figure 7). Previous work has also indicated that the evaporite layer continues well into the Inner Cilicia Basin and pinches out onto the Misis-Kyrenia thrust belt, to the south-east (Aksu et al., 1992, 2005). The evaporites are also present in a small depocentre, lying between two relative basement highs, in the Anamur-Kormakiti complex (A1-Figure 14, fix # 1584-1590). Unit 2 directly overlies Unit 3A in most areas, with the exception of a relatively narrow zone in the northern basin where it lies directly on top of Unit 3B. This suggests that the evaporite layer pinches out higher, or more landward, on the Turkish margin than the older unit below (A1-Figure 7, fix # 1264-1265).

Although the thickness distribution map of the evaporite layer covers most of the basin (see Figure 4.12), the dotted contour lines indicate areas where the thickness is uncertain due to the base salt reflector not being imaged. It should also be noted that the thickness at any particular point might have changed through time due to movement within the ductile layer. Thickness variations may therefore depend upon either

depositional processes, or on later salt movement. This problem will be further addressed in Chapter 5, where salt structures are discussed in more detail. The time thickness map shows the evaporite layer thickening away from both the basin margins and the Anamur-Kormakiti complex. Although the thicknesses can only be estimated, it is likely that the layer is thickest within the salt anticlines in the central fold zone. In the north basin, the layer is at its thickest point near the boundary with the central zone. In the south basin, the layer thickens away from the Cyprus margin, but then thins again toward the centre of the basin. This creates a rather abrupt change in thickness along the central basin line.

The top sequence boundary is a high amplitude, continuous reflector that is easily discernible across the entire study area. The boundary marks the top of the evaporite layer wherever the layer is present. Where the layer is not present, it separates pre-Messinian stratigraphy from the Pliocene succession above. The reflector has been called the M-reflector by Ryan et al. (1973), and is known to be a Mediterranean-wide unconformity separating rocks of the Miocene and Pliocene epochs. Evidence of erosion on the seismic data, such as cut off of underlying, dipping reflectors and channel cuts into the underlying evaporite layer, supports the notion that the sequence boundary is indeed an unconformity. Variations in the structure of the M-reflector are generally the result of either erosional processes, displacement on faults or deformation due to the underlying salt layer.

4.2.3 Unit 3A

Unit 3A directly overlies Unit 3B in all areas where both units are present. The thickness and distribution of Unit 3A is shown in Figure 4.13. The sequence has been correlated with the mid-late Miocene age marls and chalks of the Kuzgun formation of the Adana Basin (Williams et al., 1995) (Figure 4.9) and the Pakhna formation of the foothills of the Kyrenia Mountains (Robertson and Woodstock, 1986). There is a clear pinch out, shown at the zero thickness contour, onto Unit 3B at the northern margin of the basin. The south margin pinch out is generally less well represented, but the absence of this formation in the northern Kyrenia range suggests that the unit does indeed pinch out within the outer Cilicia basin (Robertson and Woodstock, 1986). The sequence also thins towards, but possibly continues, onto the Anamur-Kormakiti complex. Figure 4.13 also shows that the sequence thickens away from the basin margins toward maxima reached in both the central zone of the east portion of the basin and near the Anamur-Kormakiti high. Unit 3A has a thickness of just less than 350 ms in all areas where fully developed. The internal seismic character shows low frequency, low to medium amplitude reflections with limited lateral continuity. The reflections are most continuous at the top of the sequence where they generally follow the upper boundary. Similarly to unit 3B, the reflections appear more continuous at the basin margins and near the Anamur-Kormakiti high than in the central part of the basin.

The top of Unit 3A is known as the N-reflector. This reflector is high amplitude

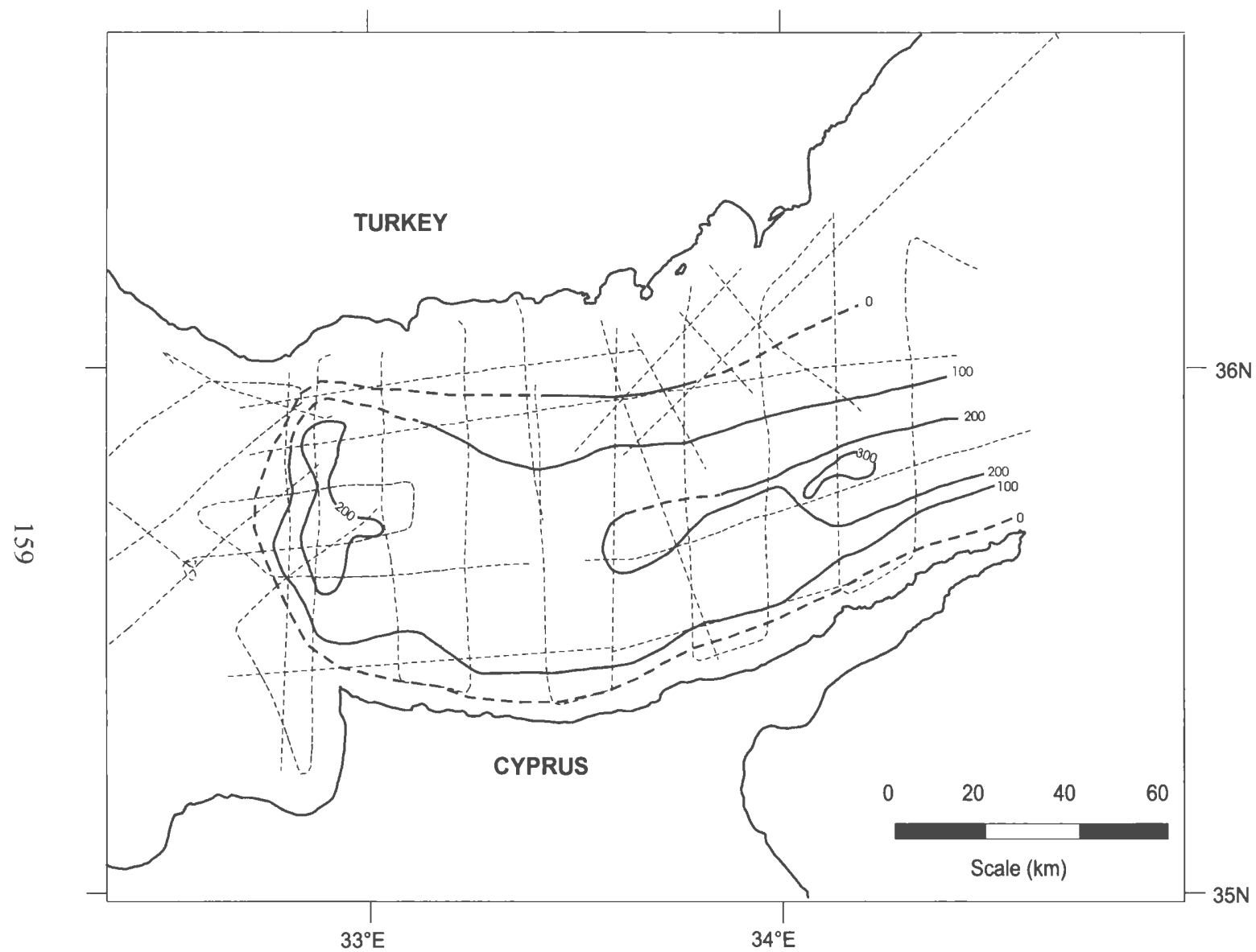


Figure 4.13: Isochron map of Unit 3A in the Outer Cilicia Basin, contoured with a 100 ms contour interval.

and laterally continuous where it is well imaged, but virtually indiscernible in other areas. Figure 4.13 shows dotted line contours in areas where N-reflector is difficult to pick. The poor imaging of this reflector is mainly due to attenuation of signal strength within the overlying high velocity salt layer. This is especially true in areas where the evaporite layer is quite thick, such as in the central folded zone. Overall, the boundary is best imaged in the western part of the south basin and near the Anamur-Kormakiti high. The reflector is generally either flat or gently dipping, except in areas where it is cut by northward verging, low angle thrust faults (further discussed in section 4.3.2). There are also some incidences where the N-reflector follows the topography of the M-reflector above (A1-Figure 5, fix # 1389-1395), but this is more likely due to velocity pull up effects than due to structural causes. There is some disagreement in the literature of whether the N-reflector represents an unconformity or a conformable surface. Robertson et al. (1991) suggest that in some areas the evaporites conformably overlie the underlying succession with no evidence of emergence, but that in other areas there is evidence of conglomerate units and freshwater deposits at the base of evaporites suggesting subaerial exposure and erosion. In our data, there is subtle evidence of underlying reflectors being cut off by the sequence boundary (see Figure 4.14). This suggests that the reflector is an erosional unconformity, at least in some areas of the basin.

4.2.4 Unit 3B

Unit 3B is the oldest definable sequence in this data set. It is distributed over all parts of the basin and clearly continues up the Cyprus Shelf. It is assumed that the unit

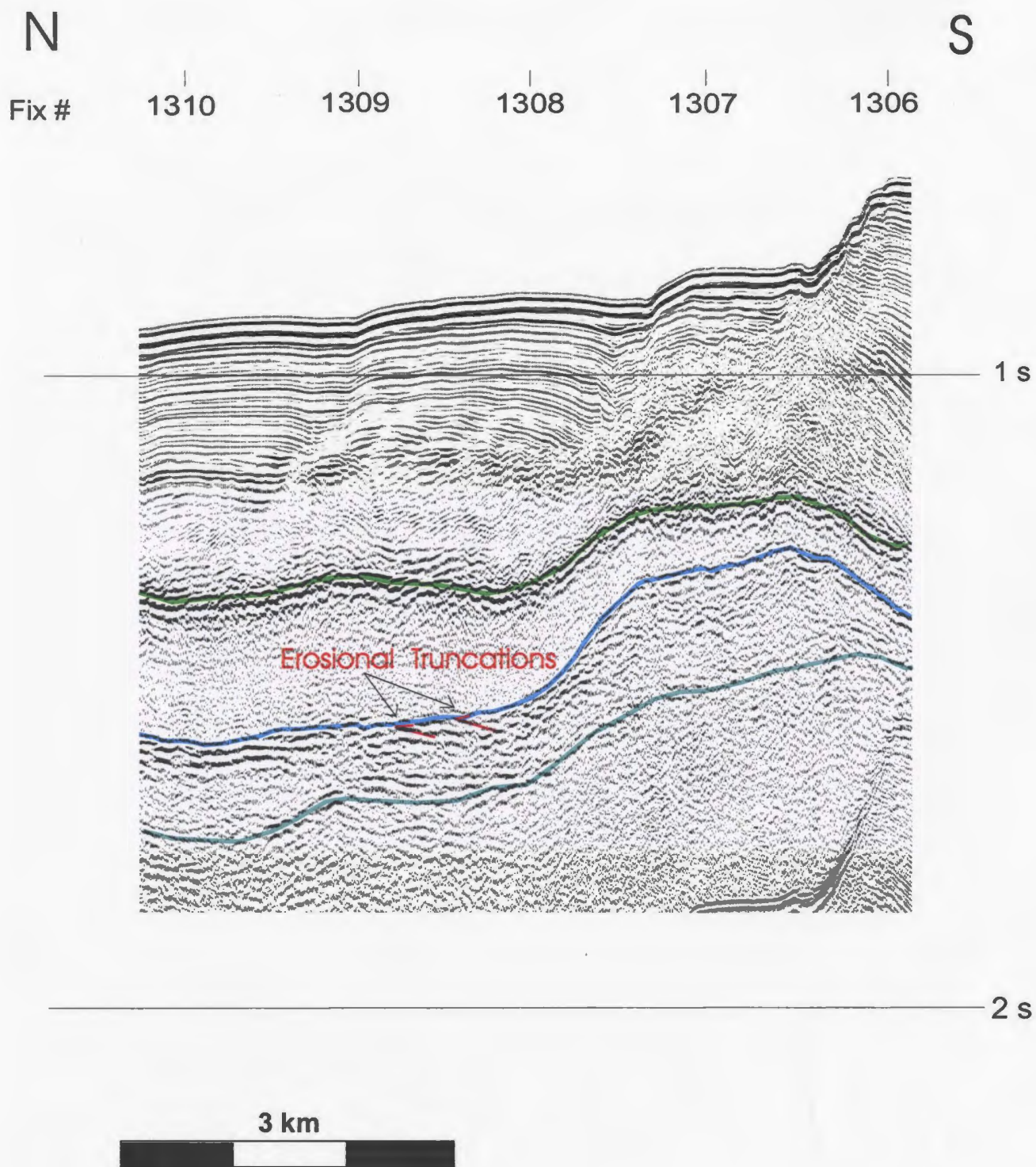


Figure 4.14: Seismic line 489, fix #1306-1310 showing subtle erosional truncation across the N-reflector.

also continues onto the Turkish Shelf, as there is no clear pinch out of the sequence onto the northern margin. This unit is thought to represent Oligocene to mid-Miocene age marls and turbidite deposits, as correlated with the Güvenç and Cingöz formations of the Adana Basin (Williams et al., 1995) (Figure 4.9), the Karataş/Isali- Aslantaş formations of the Misis Mountains (Kelling et al., 1987) and the Kythrea group, first described from Kyrenia Mountains (Robertson and Woodcock, 1986). The thickness of the unit is unknown as the base of the unit is not imaged. The seismic character shows fairly low frequency, medium to high amplitude reflectors with varying continuity. At the margins of the basin the reflectors generally show better lateral continuity than those in the central basin. The amplitude of the reflections decreases in intensity downwards, but this is more likely caused by signal attenuation than by any geological phenomenon.

The top of the sequence, termed the O-reflector for the purpose of this thesis, is mainly a medium to high amplitude reflector with varying degrees of continuity. In the south basin, the reflector is well imaged and continuous in the east part of the basin, but is more discontinuously imaged in the west. In the north basin, the opposite is true, with the reflector being more continuously imaged in the west. The reflector is poorly imaged beneath the central, folded zone everywhere in the basin. The boundary is most likely an erosional unconformity, as evidenced by the cut off of dipping reflectors below (A1- Figure 7, fix # 1285-1287).

4.3 Description of faults and structural elements for each zone

In this section the major faulting systems and other structural features, such as salt-related folds, found in the Outer Cilicia Basin are described. Each of the morphological zones, introduced above, will be discussed separately, as most of the structural elements found in the basin tend to be zone specific. Some of the surrounding onland and pre-defined basinal fault systems, first described in Chapter 2, will be further discussed in this section in reference to the faults mapped during this project.

In the seismic data from the Outer Cilicia Basin, faults are recognized as seismic discontinuities cutting through relatively conformable strata. In order to group the individual faults into consistent fault sets and to correlate the discontinuities basin-wide, the characteristics of each fault must first be established. These characteristics include the type and direction of fault movement, the dip of the fault plane and the extent of the stratigraphy cut. If these characteristics are comparable for faults interpreted on adjacent seismic lines, these faults can be correlated in plan view. Once faults are correlated, the orientation and spatial extent of the fault systems can then be interpreted. A map view of faults correlated throughout the Outer Cilicia Basin is shown Figures 4.15 and 4.16 (color-coded). In most cases the map view location of each fault is represented by the fix location where the fault cuts the M-reflector. In areas where the M-reflector is unaffected, the upper tip or termination point of the fault is used instead.

Episodes of extensional, compressional and strike-slip faulting have affected areas of the Outer Cilicia Basin at various times during its history. The evolution of individual

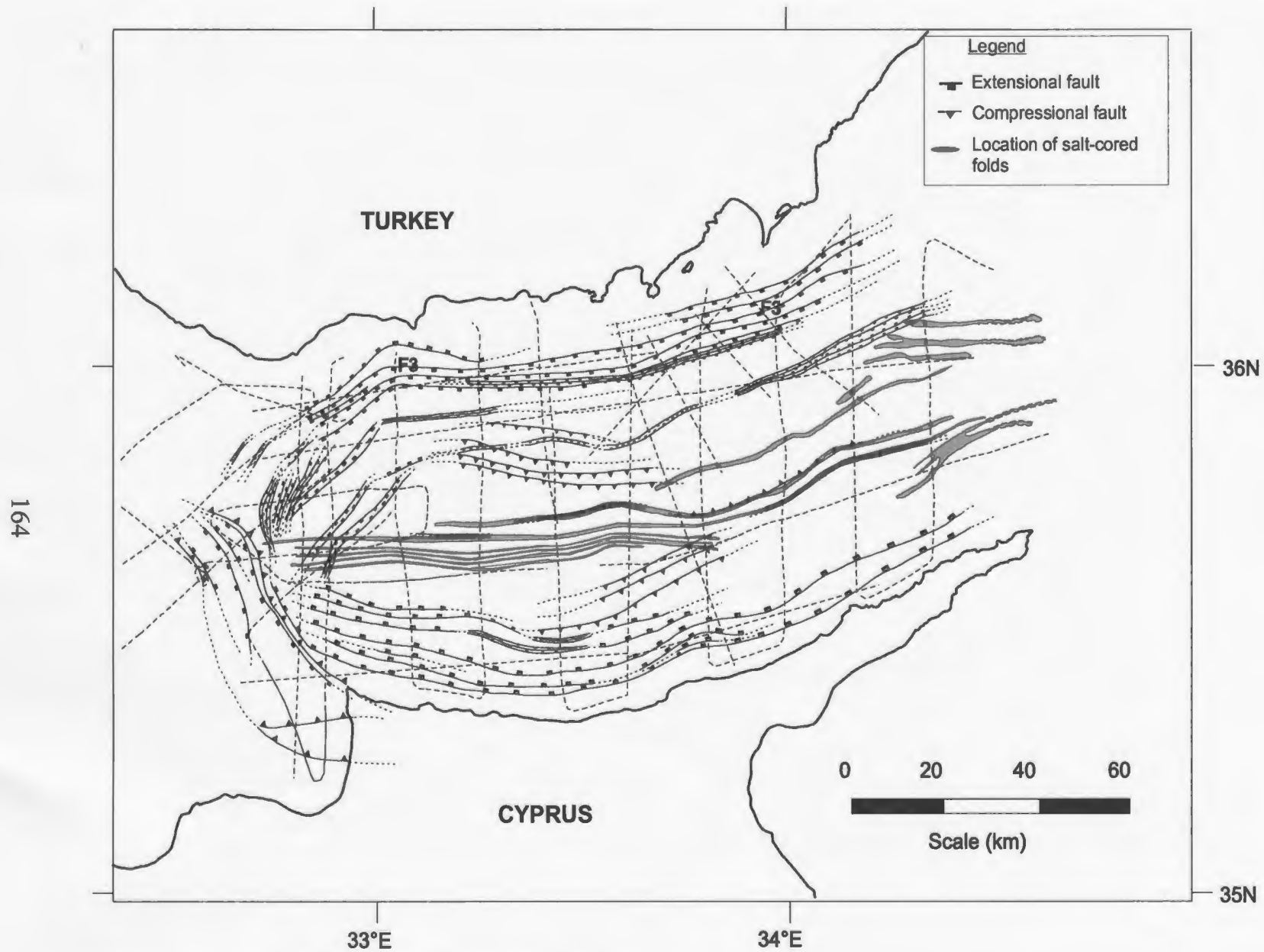


Figure 4.15: Fault map of the Outer Cilicia Basin.

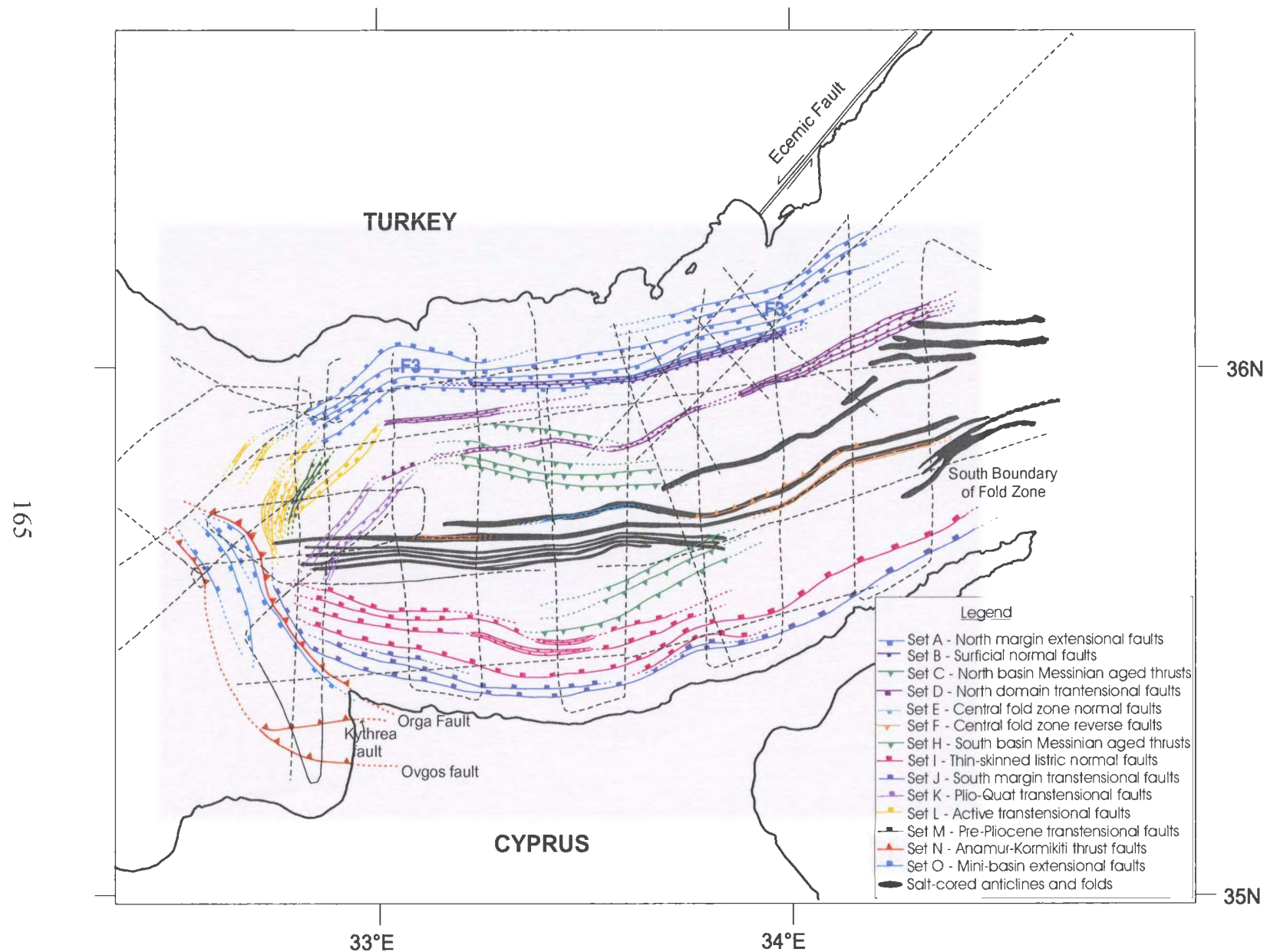


Figure 4.16: Colour-coded fault map of the Outer Cilicia Basin.

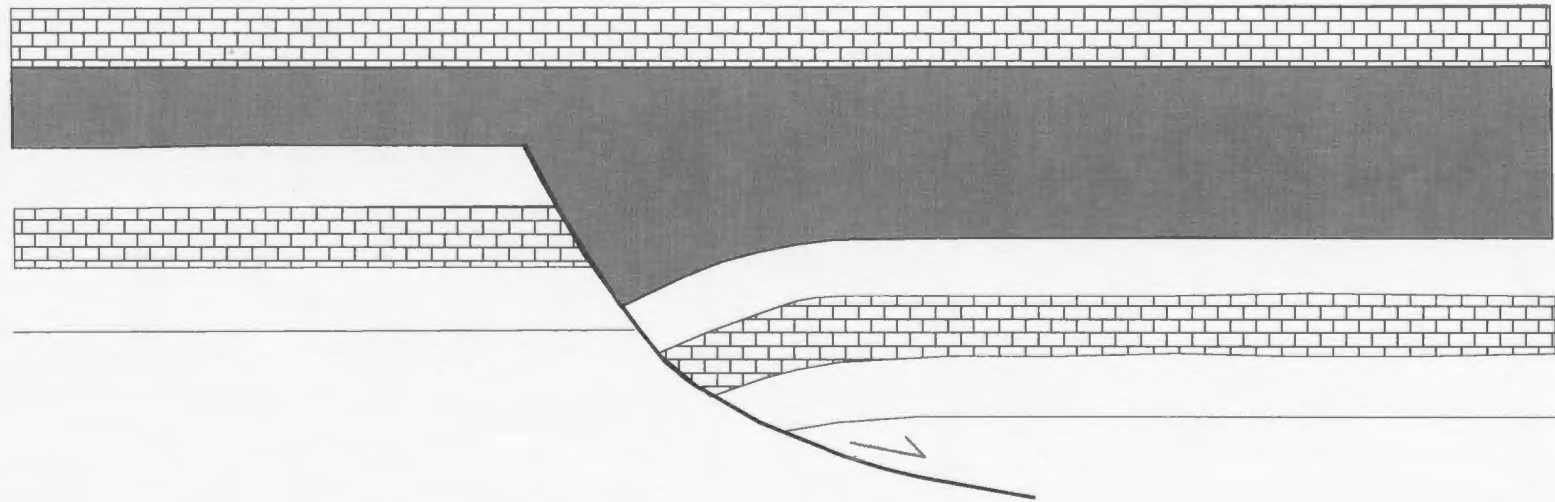


Figure 4.17: Geometry and characteristics of a simplified listric growth fault (edited from Hatcher, 1995).

faults or fault systems is recorded in the sediment layers that are affected by the fault movement. Internal folding, thickening or thinning of the sediment layers can all help distinguish the type and age of the faulting. For example, the sediment deposited in the hanging wall of an active listric normal fault will be dipping, and will thicken, towards the fault plane (see Figure 4.17). These indicators are especially important in areas where the actual fault plane is not well-imaged, and the only indication of the faulting is seen in the geometry of the layers (i.e., thickness and dip). The various fault types each have characteristics to help distinguish and classify them on the seismic data. Extensional faulting is represented as normal faults, in which the hangingwall moves down relative to the footwall. This movement is quite obvious if the slip on the fault is significant or if the fault cuts a well-defined reflector, such as the M-reflector. The movement is also obvious on the listric faults commonly seen in the south part of the basin, due to the fault indicators mentioned above. Compressional faulting is represented mainly as low angle thrust faults, in which the hangingwall moves up relative to the footwall. Indicators for thrust faulting are mainly found in the folded geometry of hangingwall's sediment layers. These layers often form a ramp-flat geometry, with a steeply dipping forelimb and a shallower dipping backlimb (see Figure 4.18). Often the thrusts have a poorly imaged fault trace and detection depends entirely on the ramp-flat geometry of the imaged reflectors. Strike slip faulting is generally more difficult to define on seismic data, unless there is a significant component of dip slip combined with the transverse component. In the Outer Cilicia Basin, the interpreted strike slip faults have a considerable extensional

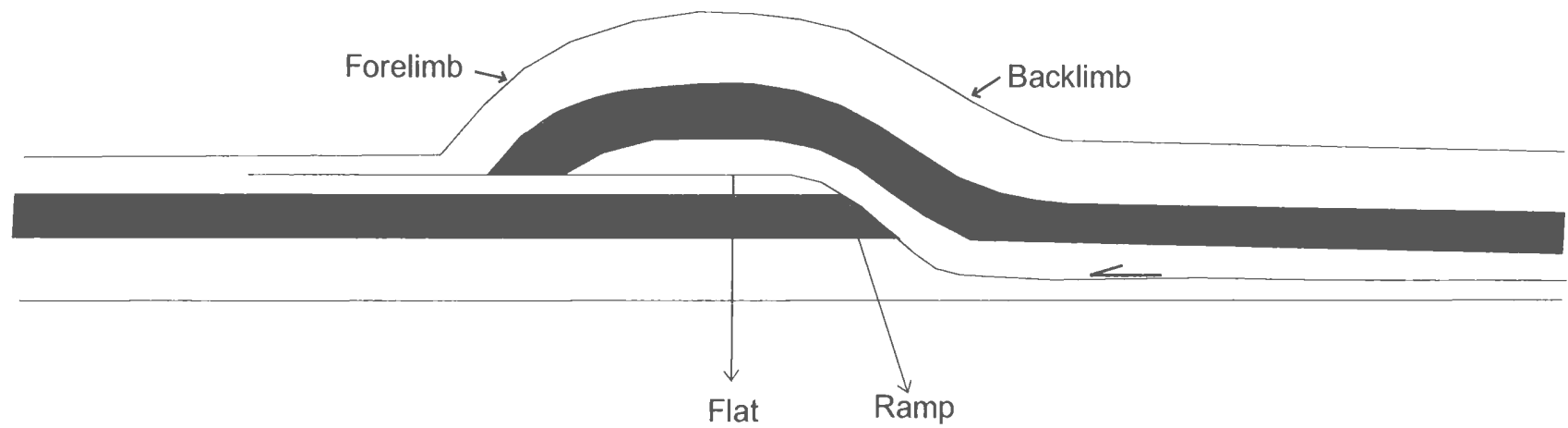


Figure 4.18: Schematic of a fault bend fold with a ramp-flat geometry (edited from Hatcher, 1995).

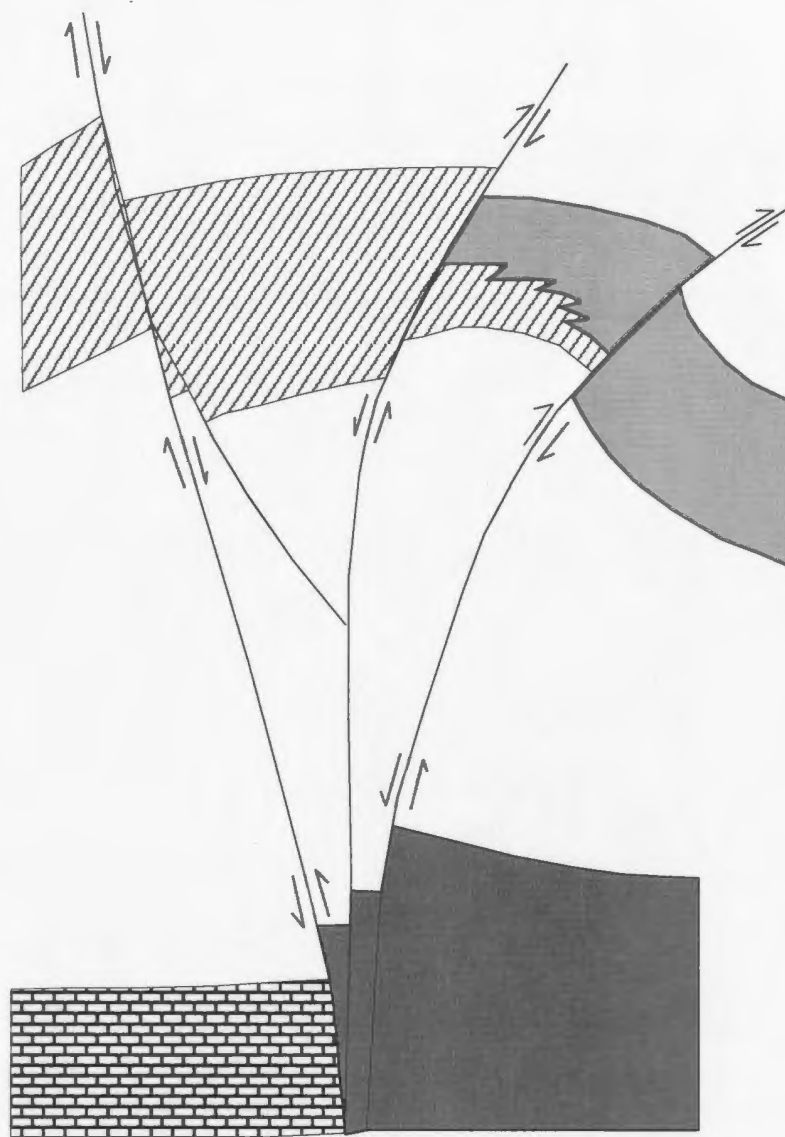


Figure 4.19: Schematic of a strike-slip fault in cross sectional view.
(Edited from Christie-Blick and Biddle, 1985).

component and therefore appear as negative flower structures (Christie-Blick and Biddle, 1985, see Figure 4.19). These flower structures are distinguishable from simple extensional grabens based on several criteria. Flower structures are characterized by upward diverging splays, across which there are often abrupt variations in thickness and facies of a single stratigraphic unit. Other indicators include a varying sense and amount of separation for different horizons along the same fault or for a single horizon across the same fault on successive profiles.

4.3.1 Structural systems found on the Turkish Shelf

The Turkish Shelf is a region dominated by east-west striking extensional faults, most of which throw down to the south. There are two main extensional fault sets: one deeply penetrating fault set (fault set A on Figure 4.16), the other mainly surficial (fault set B on Figure 4.16). In fault set A, there are 3 major faults which can be traced over most of the shelf and a number of others that have a more limited areal extent. Figure 4.20 shows these 3 major faults, labeled as F1, F2 and F3 on line 534. The faults have a general east-west strike, which turns toward the northeast on approach to the Inner Cilicia Basin and towards the south-west near the western boundary of the basin (see Figure 4.16, light blue). From north to south on the shelf, the extensional separation across the M-reflector, for each of the three major faults, progressively increases. This successive drop down of fault blocks creates a step-wise pattern from the shelf into the deeper basin. Toward the east, the narrowing of the fault blocks leads to a fault pattern that produces a steep slope rather than the discrete steps seen farther to the west (compare A1-Figure 5,

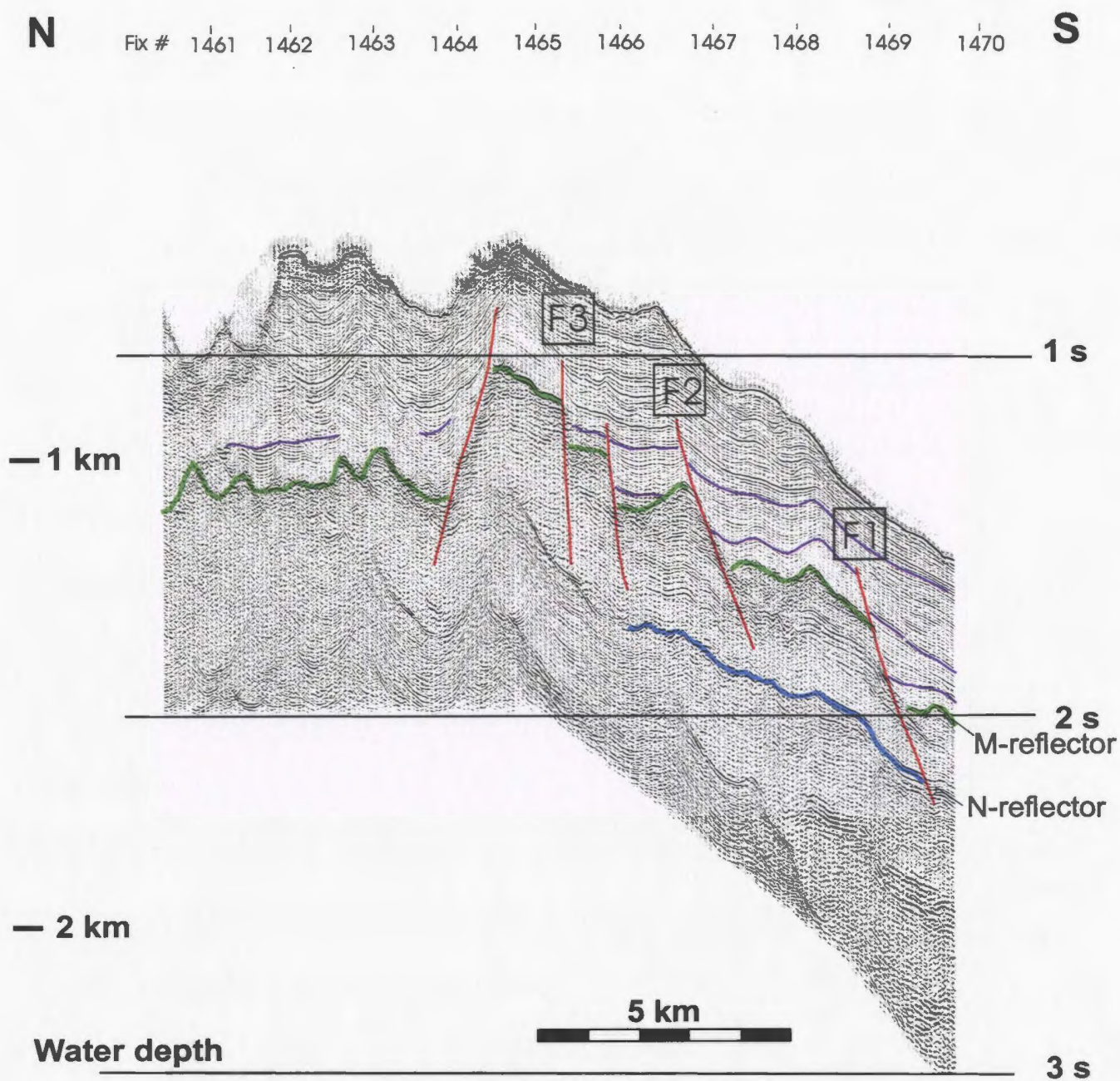


Figure 4.20: Seismic line 534, fix #'s 1461-1470 showing the extensional faults found on the Turkish shelf.

fix # 1354-1359, in the centre of the basin with A1-Figure 3, fix # 1464-1470, at the western end). The fault mapped furthest landward, or F3, has a dip separation across the M-reflector ranging between 125 ms and 200 ms, while the more basin-ward faults have separations of over 400 ms. The dips of the fault planes tend to increase in a landward direction, with a 45 degree dip on the southern-most fault increasing to between 50-70 degrees on the faults farther landward in the basin. An absolute age of these faults is difficult to determine due to the lack of age dating of the sequences affected by the faulting. It is obvious, however, that they successively young in a landward direction. All three faults cut through Unit 3 and Unit 2 (where present), and each dies out within one of the depositional sequences of the Pliocene-Quaternary succession. The most basin-ward fault terminates within sequence C, while F2 continues up to sequence B and F3 continues well into youngest sequence seen in the basin (see A1-Figure 5, fix # 1354-1359). This suggests that while each of the faults were active during some portion of Pliocene-Quaternary time, only the most northerly fault remained active into most recent time. The initiation time of these faults is also difficult to determine due to inability to distinguish thickness changes in the pre-Pliocene-Quaternary units.

In the eastern part of the basin, two additional faults appear north of F3 (see Figure 4.15 and A1-Figure 8, fix # 1241-1245). These faults dip toward the south at angles greater than 45 degrees and have an extensional separation generally less than 100 ms. Although these faults are difficult to track up section, they appear to terminate within sequence A, suggesting they were active into latest Quaternary time. In the western part

of the basin, a north-dipping extensional fault appears just to the north of F3. This fault is associated with up to 300 ms of separation and causes a substantial thickening within sequence A on the north side of the fault (see A1-Figure 3, fix # 1461-1464 and A1-Figure 5, fix # 1352-1354).

Fault set B is made up of a number of presently active normal faults, which cut through only the youngest sequence of the Pliocene-Quaternary succession (see A1-Figure 7, fix # 1254-1256). The fault zone trends east-west and extends mainly along the central and eastern portion of the northern margin (see Figure 4.16, purple). The faults making up set B are morphologically similar to fault set A, but are shallower and associated with significantly less dip separation. Like fault set A, the dip separation on the individual faults increases from north to south across the margin. The location and shallow penetration of the faults suggest that they form due to localized gravity-driven sediment sliding down the steep Turkish slope.

4.3.2 Structural systems found in the Northern Outer Cilicia Basin

There are two dominant fault systems found in the northern Outer Cilicia Basin. The first is an intra-salt, late Miocene age thrust fault family, which occurs mainly in the central region of the northern basin and has an east-west to northwest-southeast orientation (fault set C on Figure 4.16, green). The thrusts verge toward the north and have a gentle southward dip, with an essentially flat base that steepens upwards to a maximum of 5 degrees near the termination point (see A1-Figure 7, fix # 1267-1271). The fault system affects the Messinian evaporite layer, with each fault splay detaching on

the base-salt reflector and terminating well within the layer. Generally, there are 3 to 4 fault splays separated by at least a kilometre at their termination points, and they converge downwards to form an individual fault along the detachment surface. The diverging fault splays create an imbricately stacked thrust system with intervening thrust sheets that overlap one another. The intra-salt horizons also show that the individual thrust sheets exhibit a ramp-flat geometry with a steeply dipping forelimb and more shallowly dipping backlimb.

The second fault system, is an extensional fault family, often associated with a significant transverse component (fault set D on Figure 4.16). In cross sectional view, it appears as a network of relatively steep faults that dip in varying directions and converge at depth (see A1-Figure 5, fix # 1360-1362 and A1-Figure 10, fix # 1103-1107). The fault splays are normally associated with extensional separation but are, in limited occurrence, associated with apparent reverse separation. In plan view, there are a number of fault traces making up this system, each having an east-west to northeast-southwest orientation (see Figure 4.16, purple). The fault trace farther to the south is made up of north and south dipping faults with a significant amount of normal slip of up to 20 ms on the inter-Pliocene-Quaternary sequence boundaries (see A1-Figure 10, fix # 1103-1107 and A1-Figure 1, fix # 93-98). The faults cuts through the three earliest Pliocene-Quaternary sequences and are associated with significant sediment growth predominantly within sequence C, suggesting fault activity occurred during mid-Pliocene-Quaternary time (see A1-Figure 1, fix # 96-98). The width of the fault zone increases toward the

east, accommodated by both additional faults and a greater distance between fault splays (compare A1-Figure 9, fix # 1153-1155 and A1-Figure 10, fix # 1103-1107). This fault zone is tentatively correlated with the Kozan fault zone, which extends from onland Turkey and through the Inner Cilicia Basin, where it is represented by southeast dipping extensional faults that show growth in the lower Pliocene-Quaternary successions (see Figure 2.4) (Aksu et al., 2005).

This fault zone in the north-west portion of the basin lies just south of the shelf to basin boundary (see Figure 4.16 (purple), A1-Figure 5, fix # 1360-1362 and A1-Figure 4, fix # 1445-1447). The system is made up of high angle, north and south dipping faults that converge at depth and terminate upwards within sequence B of the Pliocene-Quaternary succession. There is obvious sediment growth, especially on the most northerly fault, within sequence D suggesting this fault system was active during earliest Pliocene-Quaternary time (see A1-Figure 5, fix # 1360-1362). The faults are associated mainly with normal slip, with the exception of the fault furthest to the south which has apparent normal movement across SB-c, but reverse movement across the M-reflector. The amount of dip slip is generally greater on the M-reflector than on SB-c on the fault furthest to the north (less than 20 ms compared with over 50 ms) and on the dominant southern fault (less than 10 ms compared with up to 30 ms of reverse separation). This evidence of varying sense and amount of separation for different horizons along the same fault plane gives strong indication of a transverse component to the fault movements. Further evidence of the transverse motion can be seen in the changes in thickness and

seismic character within sequence D on opposing sides of the fault system. This fault system appears to correlate with a zone of structural complexity in the central part of the basin associated with the offshore extension of the onland Ececiş fault zone (see Figure 2.4, and A1-Figure 1, fig # 59-71). This zone is made up of a complicated pattern of faulting and fault-related structures, all overlying a pre-Pliocene high. The fault pattern is made of numerous sets of two fault combinations, each of which diverge upwards and dip in opposite directions. These faults are associated with extensional separations, generally less than 10 ms across the M-reflector and inter-Pliocene-Quaternary sequence boundaries. The internal character of the early Pliocene-Quaternary succession show complex folded patterns and internal onlapping unconformities, likely a result of the fault activity. In many cases, the faults separate hanging wall and footwall sediment with noticeably dissimilar seismic characters. This gives a strong indication that strike slip motion is taking place in combination with the extensional activity. Each of the faults terminate within one of the first three sequences of Pliocene-Quaternary succession, suggesting either that fault activity died out prior to the deposition of sequence A or sedimentation rate was much higher than fault slip during the deposition of the sequence.

The southern region of the north basin, leading into the transition to the central fold zone, is characterized by relatively low amplitude folds affecting the Pliocene-Quaternary succession. The folds tend to be salt cored, and therefore can be classified as salt anticlines (Jackson and Talbot, 1991). These folds have wavelengths of up to 5 km and amplitudes generally less than 100 ms in the west and central portion of the basin.

The folds increase in amplitude and frequency toward the east, reaching amplitudes of over 350 ms near the transition to the Inner Cilicia Basin. The folding appears to have occurred mainly during the deposition of sequence B and C, as these sequences show thinning overtop the folds and some degree of thickening in the adjacent synclines (see A1-Figure 10, fix # 1092-1100).

4.3.3 Structural systems found in the central fold zone

The central zone of the Outer Cilicia Basin is dominated by relatively high amplitude salt-cored folds affecting the Pliocene-Quaternary succession, and their related fault systems (see Figure 4.16). The fold zone is best defined in the central portion of the basin but can, with some difficulty, be correlated across the entire Outer Cilicia Basin. A large number of salt -cored folds can be mapped in the eastern area of the basin (see Figure 4.16). These folds form as a result of structural systems that extend from the Inner Cilicia Basin and will, therefore, not be addressed in any great detail in the section.

In the central area of the basin, the fold zone is made up of one major salt anticline, with its associated growth synclines, and several shorter wavelength, generally lower amplitude salt cored folds (see A1-Figure 6, fix # 1325-1332). The main salt anticline is highest in amplitude along line 489, where the time difference between the peak of the anticline and the low in the syncline reaches over 500 ms. The amplitude of the fold decreases in both east and west directions, and eventually loses its structural expression in the west part of the basin. The anticline has surficial expression suggesting the growth of the structure occurs up to the present day. Thickness changes (primarily

thinning over the top of the anticline and thickening within the adjacent synclines) occur within sequences A, B, and C, suggesting that folding activity began after the deposition of sequence D and continued through the deposition of the each of the later sequences.

Two major types of faulting appear to be related to the formation of the major salt anticline. The first is an extensional fault graben, cutting through the Pliocene-Quaternary succession, overlying the apex of the anticline (fault set E on Figure 4.16 (light green) and A1-Figure 7, fix # 1271-1272). The faults dip at high angles, diverge upwards and die out before reaching the sea-floor. Each of the faults detach on the M-reflector and is therefore likely related to thin-skinned, supra-salt extension. These faults are seen only in the central region of the basin. Toward the east, the anticline instead appears to be associated with high angle reverse faulting, which cuts through both the Pliocene-Quaternary succession and the M-reflector (fault set F on Figure 4.16 (orange) and A1-Figure 8, fix # 1214-1216). The primary fault dips toward the north at an angle greater than 45 degrees, and is associated with a 25 ms separation across the M-reflector. In some cases, a south-dipping fault, with a dip of less than 45 degrees and similar amount of separation, forms antithetic to the primary fault, creating an uplifted fault block (see A1-Figure 10, fix #1088-1089). The fault dies out upwards, indicating that it is not currently active. However, the relationship between the faulting and active rising salt structure indicates that the fault may also still be active but represented above its tip point by more ductile deformation in less consolidated sediments.

Directly to the south of the main salt anticline lies a fold belt with numerous, relatively short wavelength, salt cored folds. These folds are also best defined in the central portion of the basin, where the folds extend over a 5 km zone, have wavelengths of about 500 metres and amplitudes up to 150 ms (see A1-Figure 6, fix # 1325-1329). All four sequences of the Pliocene-Quaternary succession, as well as the sea-floor reflector, are affected by the folding, suggesting the structures are presently active. Discontinuous reflectors along the flanks of the folds indicate that the folds may be fault bounded, however it is difficult to determine if the discontinuities are actual fault planes or if they are due to problems imaging the fold steep-sided flanks.

Toward the west, most of the folds making up the zone tend to lose amplitude and some eventually die off. One exception is the fold directly south of the previously described 'main' salt anticline/syncline, which actually increases in amplitude toward the west and becomes the dominant salt anticline of the system (see A1-Figure 5, fix # 1375-1378, and A1-Figure 4, fix # 1430-1432). This fold tends to be asymmetric due to its relationship with a high angle reverse fault system, which cuts through the M-reflector and dies out within sequence A of the Pliocene-Quaternary succession. The reverse fault system is made up of both north and south verging thrusts, which give rise to up to 75 ms of separation on the M-reflector. On A1-Figure 3 (fix # 1481-1483), a fault-related sea floor channel forms at the south side of this fold. The channel has steep edges and is over 100 ms deep, cutting down through sequence 2 of the Pliocene-Quaternary succession.

The fold belt also tends to lose its structural expression toward the east. East of

line 423, the only fold with obvious structural expression lies just to the south of the main salt anticline-syncline (see A1-Figure 10, fix # 1085-1087 and A1-Figure 9, fix # 1169-1171). This fold also appears to be related to a reverse fault system, which cuts through the M-reflector and dies out within sequence A. The fault system is made up of up to four, north- and south-dipping reverse faults, which create an uplifted structure in the early Pliocene-Quaternary sequences and accommodate up to 35 ms of separation on the M-reflector.

The structures described above affect the Messinian evaporite layer and Pliocene-Quaternary succession. Imaging problems and velocity pull up effects, caused by a thickening of high velocity evaporite layer in the central fold zone, make the interpretation of underlying structure fairly difficult. Certain inferences can still be made, however, based on the morphology of the affected sediment layers. A relatively large drop in the time structure on both the N and O- reflectors on the north side of the fold zone suggest the presence of a steeply dipping extensional fault underlying the main salt anticline (see A1-Figure 4, fix # 1427-1431). This fault appears to accommodate up to 300 ms of dip slip and dies out below the M-reflector unconformity. Thickening within Units 2 and 3 to the north of the fault suggests the fault was active throughout the mid to late Miocene. Activity of the fault may have initiated earlier, but a lack of seismic resolution at depth and short record length prevents interpretation of the earlier sequences.

4.3.4 Structural systems found in the Southern Outer Cilicia Basin

The southern domain is dominated by 3 sets of faults: 1) compressional, within the mid-late Miocene successions (fault set H), 2) extensional, within the Pliocene-Quaternary succession (fault set I), and 3) extensional, possibly with a significant transverse component, affecting the entire basin succession, near the transition to the Cyprean shelf (fault set J).

The compressional faulting seen in the south basin is structurally similar to fault set C, previously described for the north basin (see A1-Figure 7, fix # 1280-1285). The faulting is most prominent in the central area of the domain and has a northwest-southeast orientation (see Figure 4.16, green). The thrusts diverge and steepen upwards from a relatively flat detachment surface along the O-reflector. The N-reflector is displaced by the faulting and folded into a ramp-flat geometry similar to that of the inter-salt horizons in the northern and southern domains (see A1-Figure 8, fix # 1203-1210). The M-reflector is also displaced in this area, which may suggest the thrust faults were active up to the end of Miocene time. A more likely interpretation, however, is that the southern thrusts cease activity before the end of Messinian time and the displacement across the M-reflector is caused by Pliocene aged vertical, strike slip faults (see Figure 4.21).

The Pliocene-Quaternary succession is dominantly affected by thin-skinned extensional faults that detach on the M-reflector (fault set I on Figure 4.16, pink). These faults can be classified as listric growth faults, due to their concave upward geometry (see A1-Figure 4, fix # 1413-1420 and A1-Figure 7, fix # 1287-1292). Most of these faults

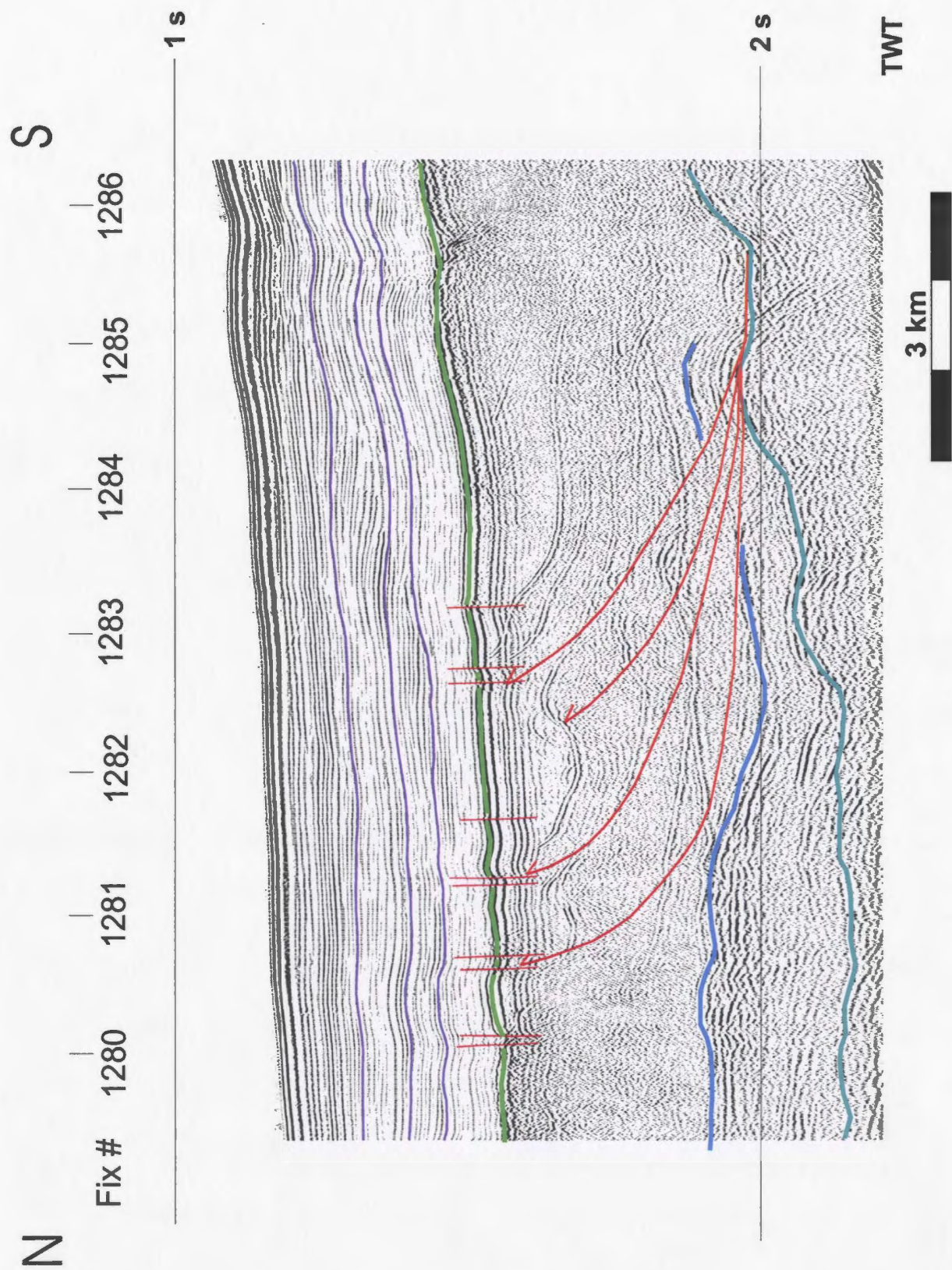


Figure 4.21: Line 467, fix #'s 1280-1286 showing the M-reflector displaced by vertical strike-slip faults.

are currently active and create a sea floor expression that can be described as steps descending into the centre of the basin. These faults tend to be oriented east-west, parallel to the south basin margin. Some fault traces can be correlated along the entire basin margin, while others have a more limited areal extent (see Figure 4.16, fault set I). In cross sectional view, the faults cut through the entire Pliocene-Quaternary succession with dips up to 50 degrees, or steeper, near the top of the fault plane. In some places, these north-dipping faults are associated with south dipping antithetic faults, which generally extend almost to the sea-floor horizon (see A1-Figure 5, fix # 1387-1389). The faults, especially those mapped furthest to the south, are generally associated with a large amount of dip separation (up to 150 ms across the three inter-Pliocene-Quaternary sequence boundaries and 50 ms on the sea floor horizon). The large amount of dip separation, combined with the concave upwards geometry of the fault plane, creates a rotated block geometry in the hangingwall of these faults, especially in the central and western parts of the basin (see A1-Figure 4, fix # 1413-1420). The hangingwall sequences also show modest thickening toward the fault plane. On the faults furthest to the south, the youngest two sequences display the largest percentage of thickening suggesting that fault activity occurred at the time of their deposition. The faults farther to the north are associated with a lesser amount of dip separation and appear to display thickening within sequences B and C, but less within sequence A, suggesting they were active during an earlier time frame (see A1-Figure 4, fix # 1413-1419).

In the footwall of each of the listric faults, the M-reflector is folded into a

relatively low amplitude salt roller which, by definition, is in fault contact with the overburden along the more steeply dipping flank and in conformable stratigraphic contact with the overburden on the opposite flank (Jackson and Talbot, 1991). The amplitude of these salt rollers varies from line to line and for each of the individual listric faults. The highest amplitude rollers appear on line 517, and have amplitudes of up to 180 ms (measured on the M-reflector, from the top of the structure to base of the adjacent low). In some areas, the salt rollers described above are associated with overlying extensional fault grabens instead of a single listric normal fault (see Figure 4.16, fault set I). These graben contain a number of high angle normal faults, which create a drop down or collapse feature on the top of the relative salt highs (see A1-Figure 5, fix # 1389-1391). Although the faults cut through the entire Pliocene-Quaternary succession the amount of dip separation can be quantified only on the sea-floor horizon, where each fault creates about 10 ms of separation. The combined effect of the faulting is a sea-floor depression with walls that display a step wise pattern gradually descending to the centre of the channel, which is about 40 ms deeper than that of the surrounding sea floor.

The transition between the south basin and Cyprean shelf is marked by a system of north-dipping basin-bounding extensional faults, and their associated south dipping antithetic faults (fault set J on Figure 4.16, see A1-Figure 3, fix # 1495-1498 and A1-Figure 4, fix # 1409-1414). The system is generally made up of 2-3 north dipping faults, lying in a 5-8 km zone directly north of the Cyprean shelf. Although these faults are similar in orientation and appearance to the previously described fault set I, they can be

distinguished based on their geometry, higher dip angle and their penetration into the older sequences. These faults cut through Units 1-3 and are associated with a significant amount of separation across each of the sequence boundaries. The amount of separation varies, however, for each of the horizons cut by the same fault and from line to line across the survey area. Across most of the basin, these faults result in between 50 and 200 ms of separation on the M-reflector and between 10 and 100 ms of separation on the Pliocene-Quaternary sequence boundaries. The individual faults merge toward the west with a prominent fault marking the northern boundary of the Kyrenia Range (see A1-Figure 3, fix # 1497-1498). This fault is associated with more than 1100 ms separation across the M-reflector and over 800 ms across the sea-bed reflector. The variation in slip amount, from east to west across the survey area, suggests that there is a significant transverse component associated with the extensional faulting at the southern basin margin.

4.3.5 Structural systems found on the Cyprean Shelf

The Cyprus shelf is a relatively narrow zone that lacks sufficient seismic coverage with our current data-set to provide a detailed interpretation. The seismic data either stops just short of the shelf, or extends onto the shelf as relatively short, east-west directed strike lines. Multiples also create a problem on the shallow shelf and prevent the interpretation of structures much deeper than the M-reflector. That being said, however, it is obvious that the shelf is associated with active structures such as those in which the Pliocene-Quaternary sequences show thickness changes related to an active fold system (see A1-Figure 5, fix # 1399-1405, A1-Figure 4, fix # 1406-1410 and A1-Figure 8, fix #

1189-1197). Sequences A, B, and C each show thinning over the top of the anticlinal structures and thickening in the adjacent synclines. There is also evidence of high angle extensional faulting, primarily present on the flanks of the folded structures. These faults cut through the entire Pliocene-Quaternary succession, as well as the M-reflector, and generally produce between 2 and 8 ms of separation across each of the affected sequence boundaries. The only area of the Cyprean

Shelf that has sufficient seismic coverage to allow inferences regarding its structure to be made is in the western portion of the basin where the shelf merges into the Anamur-Kormakiti zone. This area will be discussed in more detail in the following section.

4.3.6 Structural systems in the Anamur-Kormakiti zone

The Anamur-Kormakiti zone is a structurally complex area, dominated by large scale compressional structures in the pre-Messinian stratigraphy. These compressional structures give rise to significant basement highs, which separate the Outer Cilicia from the deeper Antalya Basin (Figure 2.3). The more recent stratigraphy is primarily affected by extensional faulting, often with a significant transverse component.

The transition from the western Outer Cilicia Basin to the Anamur-Kormakiti complex is characterized by thinning of the late Miocene and Pliocene-Quaternary sequences, dominantly affected by extensional and strike-slip faulting. Figure 4.16 (light purple (set K) yellow (set L)) shows a network of southwest oriented fault traces at the transition, each made up of sets of oppositely verging extensional faults, which dip towards one another and converge at depth (see A1-Figure 16, fix # 156-163 and A1-

Figure 3, fix # 1473-1476). Morphological similarities between these faults and the east-west oriented transtensional faults described from the northern basin domain (set D) suggests that they may be related or extend from the same fault system. The faults in this area are associated with between 5 and 40 ms of normal separation across the affected sequence boundaries and in some cases separate dissimilar seismic characters (see A1-Figure 16, fix # 161-164). The primary difference between the fault traces seen in this area is in the timing of the fault activity, as revealed by the extent of the stratigraphy cut by the each of the faults. This time variance in fault activity is illustrated in Figure 4.16 by colour coding of the fault traces to represent three main time frames. The fault traces labeled as fault set K on Figure 4.16 (light purple) and represented on A1-Figure 16, fix # 163-168, cuts through the late Miocene sequences and terminates within either sequence A or B of the Pliocene-Quaternary succession. It is difficult to tell when this faulting initiated, but the internal seismic configuration of sequence C may indicate that faulting was active when it was deposited. One possible interpretation of the seismic configuration shown in Figure 4.22, is that internal reflectors within sequence C act as sedimentary detachment surfaces. This phenomenon can occur as soft sediment layers effectively detach from an underlying horizon and slide downslope due to movement on a nearby faulting system (personal communication with Dr. Ali Aksu, May 2004). The fault traces labeled as fault set L on Figure 4.16 (dark yellow) and represented on A1-Figure 3, fix # 1473-1476, cut through the M, N and O-reflectors and create channels in the sea floor, suggesting that they are presently active (also see A1-Figure 1, fix # 26-29).

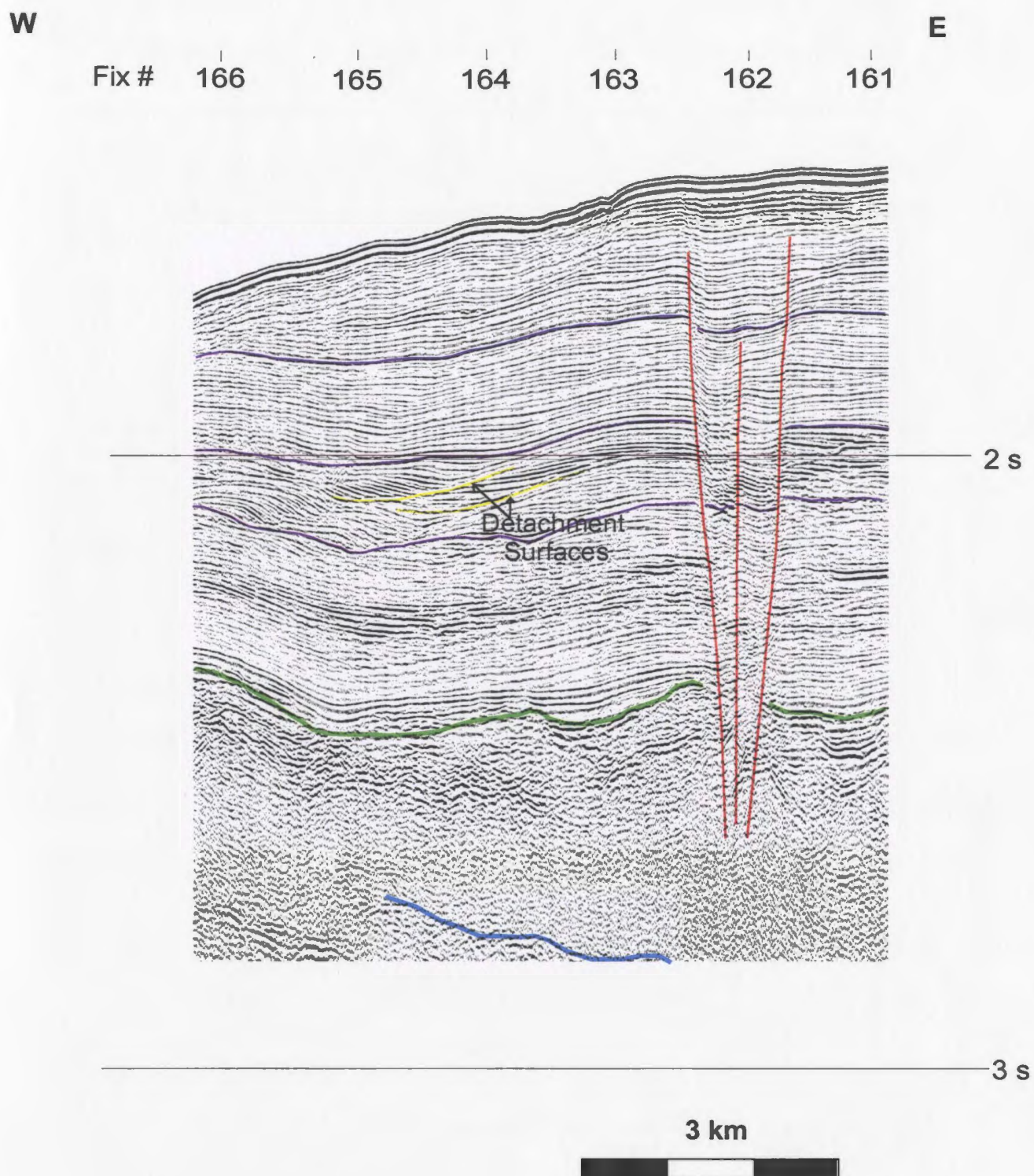


Figure 4.22: Seismic line 23, fix #'s 161-166 showing inter-sequence detachment surfaces in sequence C of the Pliocene-Quaternary succession.

The sea floor channels are 250 ms deep and appear asymmetric on north-south profiles. The north walls are much steeper due to their relationship with high angle normal faults while the southern boundaries are more shallowly dipping, likely related to erosional processes. The faults are responsible for a lesser amount of separation across the other sequence boundaries, generally 2-20 ms of normal separation across the M, N and O reflectors. The earliest episodes of strike-slip faulting in this area can be seen on A1-Figure 14, fix # 1571-1574 and labeled as fault set M on Figure 4.16 (dark green). These faults are north-south oriented, near vertical and cut through the O and N-reflector but die out within the Messinian evaporite layer. They are associated with between 2 and 10 ms of separation across the N-reflector.

The Anamur-Kormakiti complex is divided into two separate segments, based on evidence suggesting it does not form a continuous structure (see Figure 4.23). The bathymetric high representing the northern segment of the complex extends from the onshore Tauride mountain range, but appears to lose expression about 25 km off the south coast of Turkey (compare A1-Figure 1, fix #'s 6-18 to A1-Figure 16, fix #'s 172-182). The southern segment of the Anamur-Kormakiti complex is interpreted as the offshore extension of the Kyrenia mountain range, based on correlation of thrust zones mapped in both areas. These thrusts are shown to have a northwest directed strike on Figure 4.16 (fault set N), which suggests they are more likely continue into the Antalya basin than to curve into the northern part of the complex (see Figure 4.16). This suggests that the northern and southern segments are not connected.

The northern segment extends from the southwest coast of Turkey and is elevated about 400 ms above the sea floor of the Outer Cilicia Basin. The bathymetric expression of the segment dies off about 25 km south of the Turkish coast and just east of the city of Anamur (see Figure 4.23). The boundary between the basement high and the basin is marked by a southwest-oriented fault trace, made up of a set of oppositely dipping normal faults (see A1-Figure 1, fix # 16-19). The faults cut through all definable sequence boundaries and create a 200 ms deep channel on the sea floor.

A 300 ms thick Pliocene-Quaternary succession covers the northern segment of the complex, and is cut by graben bounded by steeply dipping extensional faults creating deep channels on the sea floor (see A1-Figure 1, fix # 6-17). The extensional faults cut through the Pliocene-Quaternary succession and the M-reflector, and are associated with an increasing amount of separation up the fault plane. The sea floor channels are over 100 ms deep and have steep walls, likely created by a combination of fault-related erosional processes. The internal structure of Miocene and earlier sequences within the northern segment is difficult to interpret based on a lack of interpretable seismic reflectors much deeper than the M-reflector. Based on proximity to the onland geology, however, it can be inferred that the basement high is related to an Oligocene south-verging thrust system. Possible evidence for this thrust system can be interpreted farther south in the basin, in an area where each of the Miocene and younger sequences thin towards the western basin boundary (see A1-Figure 14, fix # 1576-1580). The evidence for this thrust system is highly interpretative and is based mainly on a change in reflection character in the pre-

Miocene sequences. The yellow reflector seen on A1-Figure 14, fix # 1576-1580 is present to show the morphology of the thrust faults and is not associated with any particular stratigraphic interval. In the hanging wall of the interpreted thrust, the reflection character is higher amplitude and somewhat more continuous than that of the sequences in the footwall. The spatial relationship between this fault and the transition zone to the Antalya basin also lends support to its presence. Considering the morphological differences between the two basins, it is quite likely that they are separated by some major structural feature within the pre-Miocene stratigraphy.

The southern segment of the Anamur-Kormakiti complex is a northwest-southeast striking bathymetric high, which extends from the north-west coast of Cyprus toward the Antalya Basin (see Figure 4.23). Near Cyprus, the segment has a width of 25 km and is elevated 900 ms above the adjacent sea floor in the Outer Cilicia Basin (see A1-Figure 3, fix # 1498-1513). Toward the northwest, the structure narrows and gradually loses its bathymetric expression, with elevations of just over 400 ms above the Cilicia Basin's seafloor on A1-Figure 14, fix # 1582-1592. The boundary between the southern segment and the Outer Cilicia Basin is marked by an extensional fault, which can be correlated with the fault set J described from the south part of the basin. In map view, the fault trace turns from its east-west orientation, toward the northwest, and finally to a north-south orientation near the centre of the basin. In cross-sectional view, the fault cuts through all definable sequence boundaries, dips at angles greater than 45 degrees and is associated with separations on the M-reflector up to 1000 ms in the southern part of the basin (see

A1-Figure 3, fix # 1496-1498) but just over 100 ms in the centre of the basin (see A1-Figure 14, fix # 1581-1582).

The complex is dominated by three major thrust faults, each of which can be correlated with faults seen onshore in Cyprus (fault set N on Figure 4.16 (brown), A1-Figure 3, fix # 1498-1513). From north to south, the faults correlate with the Orga, Kythrea, and Ovgos faults, respectively. The offshore extension of the Orga fault has a northwest directed strike, oriented parallel to the northeast edge of the bathymetric high (see Figure 4.16). The Kythrea and Ovgos fault zones converge toward the west and are represented as one northwest striking fault trace in the northwest part of the complex (see Figure 4.15 and A1-Figure 3, fix # 1516-1530). Each of the three thrust faults dip toward the north at angles less than 10 degrees and are associated with separations of up to 180 ms on the M-reflector. The M-reflector shows a ramp and flat geometry, associated with each of the individual thrusts, with a relatively steeply dipping forelimb (about 10 degrees) and a more gently dipping back limb (5 degrees or less). Although these faults appear as blind thrusts, as their tip points cannot be carried past the M-reflector, their effect can be seen in the overlying Pliocene-Quaternary succession (see A1-Figure 3, fix # 1498-1513 and A1-Figure 12, fix # 1516-1530). Each of the sequences show a significant amount of the thinning overtop the thrust high, suggesting that the thrust sheets have been active through Pliocene-Quaternary time and continue to move up to the present day.

In the north-west part of the southern segment, the bathymetric highs related to the Orga and Ovgos/Kythrea faults are separated by an extensional fault bounded mini-basin (see Figure 4.23, A1-Figure 13, fix # 1534-1539 and A1-Figure 14, fix # 1584-1591). The basin is bounded on all sides by extensional faults that accommodate significant separation across the sea floor and M-reflector (fault set O on Figure 4.16, light blue). At the eastern basin margin, there are at least two west dipping normal faults creating a step-wise descent into the center of the basin (see Figure 4.16 (light blue), A1-Figure 13, fix # 1536-1540). These faults dip at high angles and accommodate up to 350 ms of separation across the M-reflector. Similarly to the Outer Cilicia Basin, the mini-basin deepens toward the northwest and is asymmetrically filled with late Miocene-Quaternary sedimentary successions. In the northwest part of the basin, the Pliocene-Quaternary succession is over 750 ms thick and overlies a relatively thick Messinian evaporite layer (up to 350 ms). The presence of a Messinian evaporite layer suggests that the basin has been structurally lower than the adjacent highs at least since late Miocene time. The evaporite layer terminates onto the basin's bounding faults and is assumed to pinch out toward the south, as the layer is not present in southeastern part of the basin. In the southeast portion of the mini-basin, a thinned (about 350 ms) Pliocene-Quaternary succession directly overlies the mid-late Miocene rocks (see A1-Figure 13, fix # 1535-1539).

Chapter 5: Discussion

In the previous chapter, the major structural systems of the Outer Cilicia Basin were defined (Figure 4.16) and described in terms of their morphology and time of activity. A tectono-stratigraphic chart for the Outer Cilicia Basin is shown in figure 5.1. This provides a synthesis of the major structural systems described in Chapter 4, including the time during which they were active. Each of these systems was active for a significant time period in the evolution of the Outer Cilicia Basin and is important in understanding the Neogene evolution of this area. In this Chapter, the systems will be discussed in terms of the structural and tectonic forces that control their formation and development.

The main tectonic forces that control the evolution of the Outer Cilicia Basin are related to its plate tectonic setting, as discussed in Chapter 1. The Cilicia Basin lies on the Anatolian microplate and has evolved in the fore-arc setting associated with subduction of the African plate beneath the Anatolian plate. Its evolution, however, is complicated by a rotation in the convergence vector and a change in the mode of convergence, from subduction to collision, since Miocene time. The forces generated at the Anatolian plate boundaries directly, or indirectly, give rise to the compressional, extensional and strike slip structures present in the Outer Cilicia Basin.

Before discussing the major structural systems that define the Neogene-Quaternary evolution of the Outer Cilicia Basin, a brief synthesis of the early evolution of the Cilicia Basin will be given. Although the early evolution cannot be interpreted

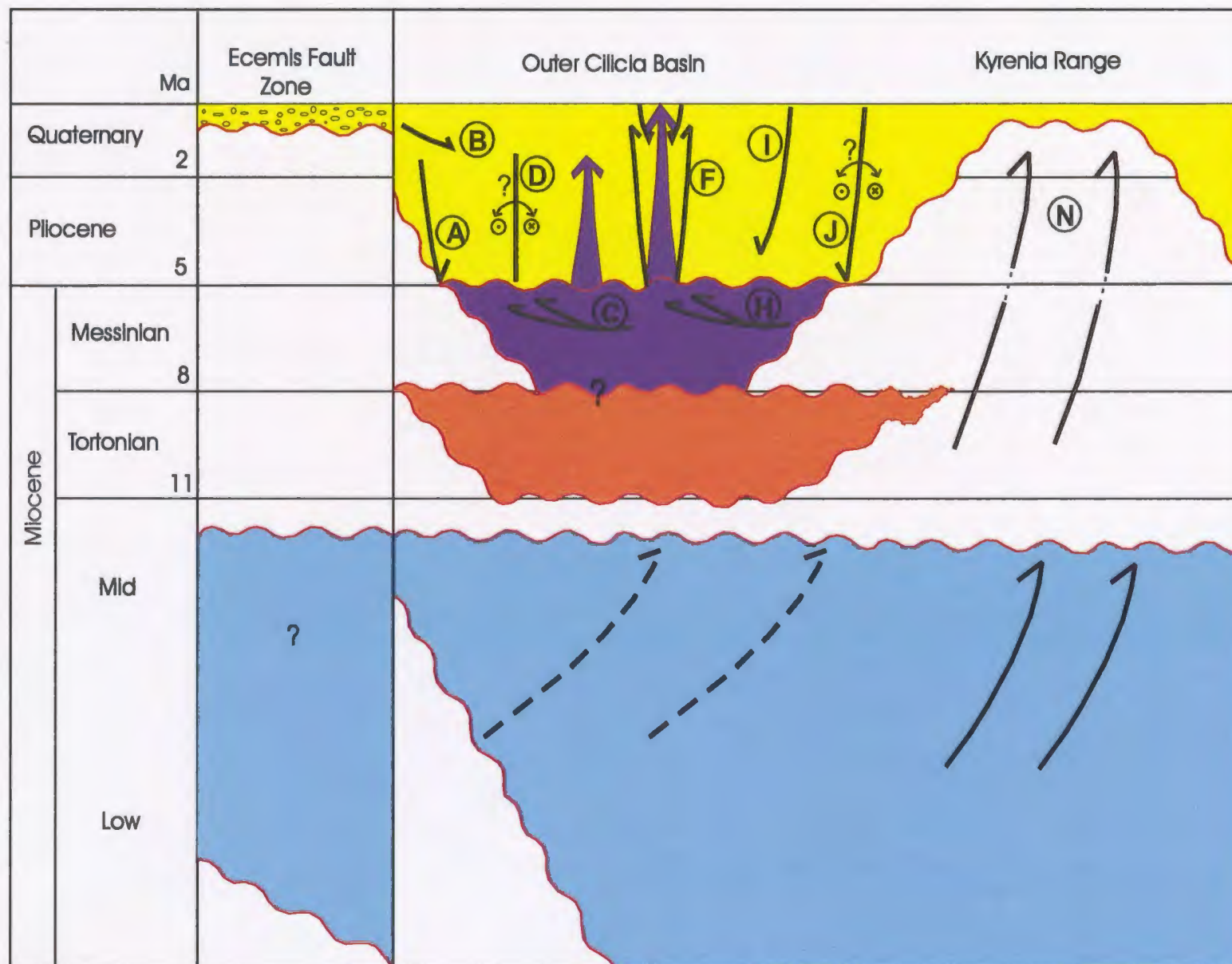


Figure 5.1: Tectonostratigraphic chart representing north-south profile across the centre in the Outer Cilicia Basin.

directly using the current seismic dataset, it is important to address the entire history of the basin. A more detailed description of the Neogene and Quaternary evolution of the Outer Cilicia Basin will be discussed in a later section.

5.1 Pre- to early-Neogene evolution of the Cilicia Basin

The Cilicia Basin evolved in the Oligocene to early Miocene in a foredeep setting in front of the Tauride thrust front (Williams et al., 1995; Calon et al., 2005 a; Aksu et al., 2005). During this early period of subsidence, the Cilicia Basin formed part of a large, continuous basin that contained the present day Adana, Mesaoria and Latakia Basins. Extension in this area likely occurred in response to either load induced flexure resulting from thrusting in the Tauride range (Williams et al, 1995) or in response to differential slip rates on three major faults that meet at a plate triple junction just northeast of this area (Şengör et al., 1985). Şengör et al. (1985) proposed that when strike slip faults meet within the continental lithosphere, incompatibility problems arise due to the buoyancy and low shear strength of the lithosphere. Their kinematic analysis, which considered the rates and directions of plate movements in the area, suggested that oblique, north to northwest directed extension should result in this area. The lower to middle Miocene sedimentary history of this basin involved the deposition of diachronous transgressive sequences (Yetiş et al., 1995).

In the mid- to late-Miocene, a major change occurred which modified the morphology and sediment distribution of the basin. An episode of regional compression

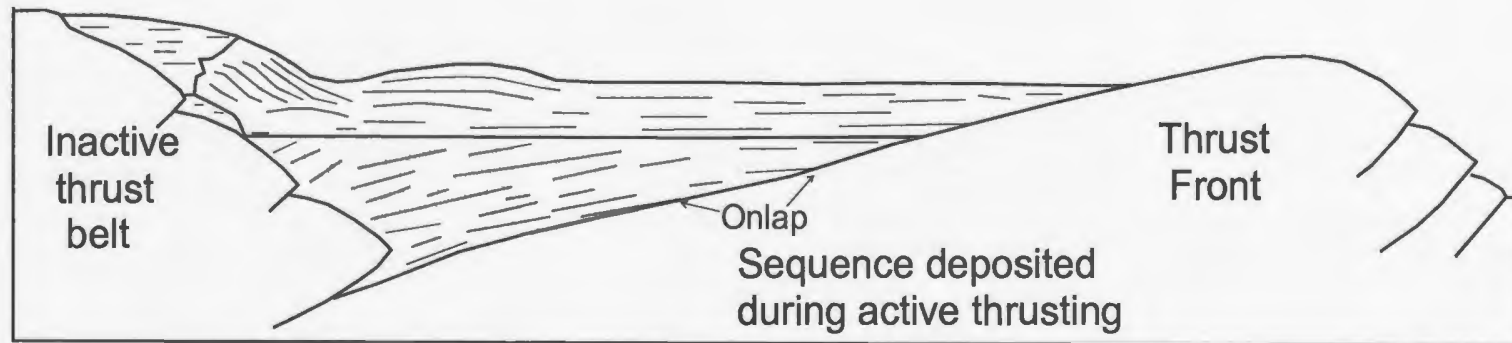
led to the formation of a major fold thrust belt extending from north-east Turkey to west of the island of Cyprus (Anastasakis and Kelling, 1990; Kelling et al., 1987; Robertson and Woodcock, 1986). This thrust belt separated the larger basin into north and south counterparts. Onshore Turkey and Cyprus, the thrust belt is represented as two major mountain ranges; the northeast trending Misis mountains and the east-west trending Kyrenia mountains, respectively. These mountain ranges have similar internal structure and, together with their offshore link, form a genetically related south to south-east verging thrust system. Since late Miocene time, the Cilicia Basin has evolved on the back limb of this thrust system.

In figure 5.2, a north-south profile across the Outer Cilicia Basin is compared with a schematic piggy-back basin, edited from Ori and Friend, 1984. Morphological similarities between the schematic and the profile support the notion that Cilicia basin has evolved on the back limb of the Misis-Kyrenia thrust system, from late Miocene up to present time.

5.2 The major structural systems of the Outer Cilicia Basin

In the previous chapter, five major structural systems were defined within the Outer Cilicia Basin, along with two additional systems in the transition zone between the Cilicia and Antalya Basins. The major structural systems within the Outer Cilicia Basin include: *i*) deep rooted normal faults at basin margins (fault sets A and J, see figure 5.3), *ii*) east-west oriented transtensional faults (fault set D, see figure 5.4), *iii*) Messinian aged

(A)



199

(B)

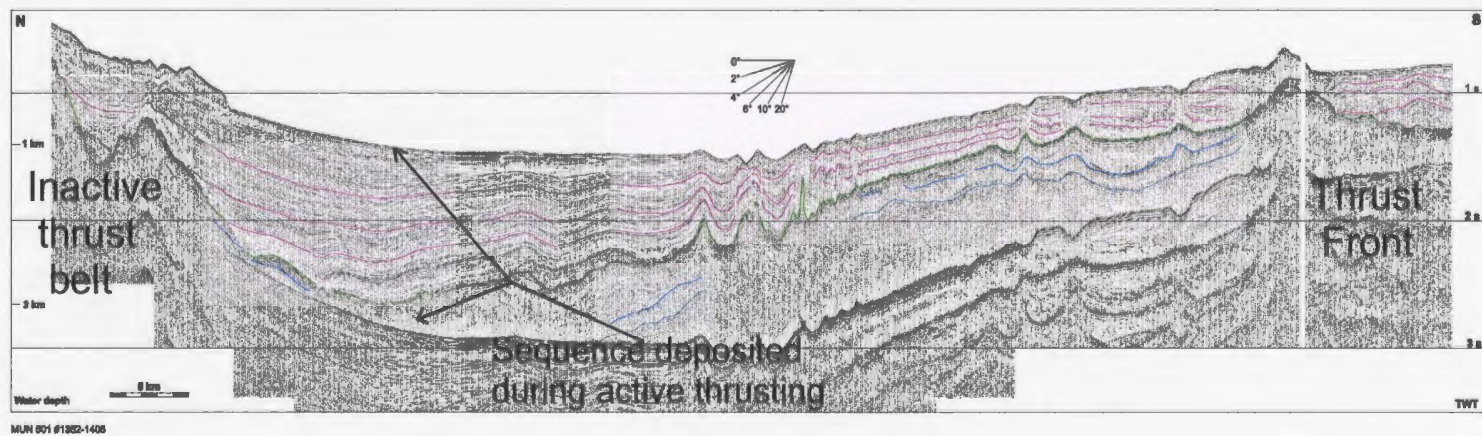


Figure 5.2: (A) Schematic of a basin formed on the back limb of a thrust sheet (not to scale), edited from Ori and Friend (1984). (B) North-South Profile across the Outer Cilicia Basin (line 501, fix #'s 1352-1405).

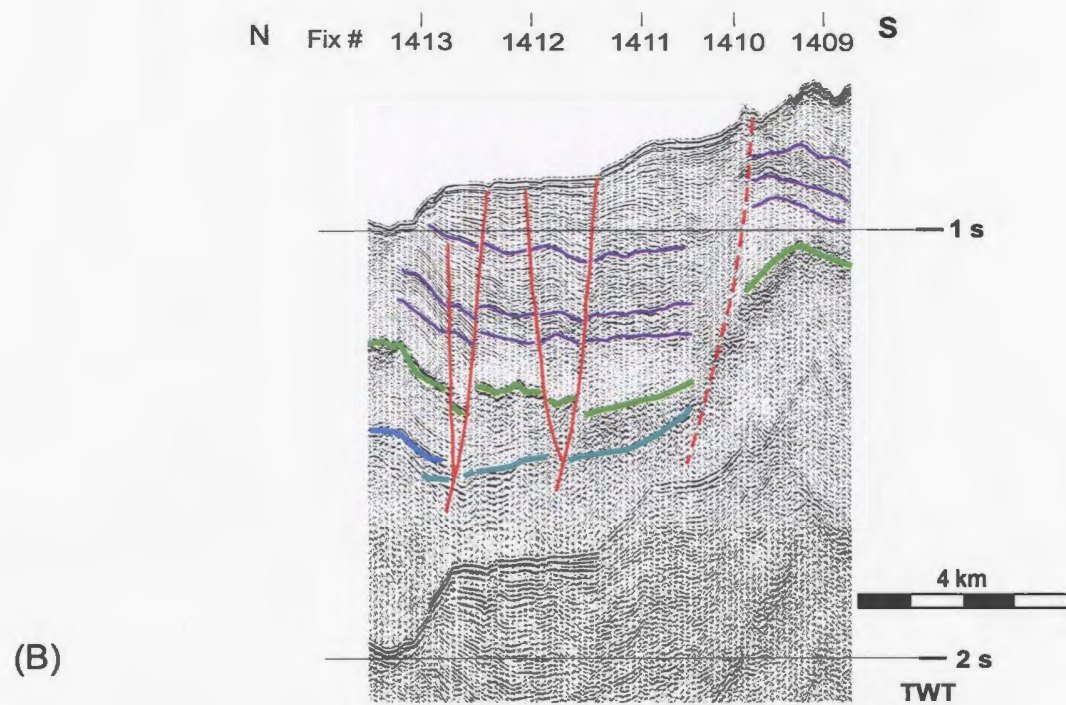
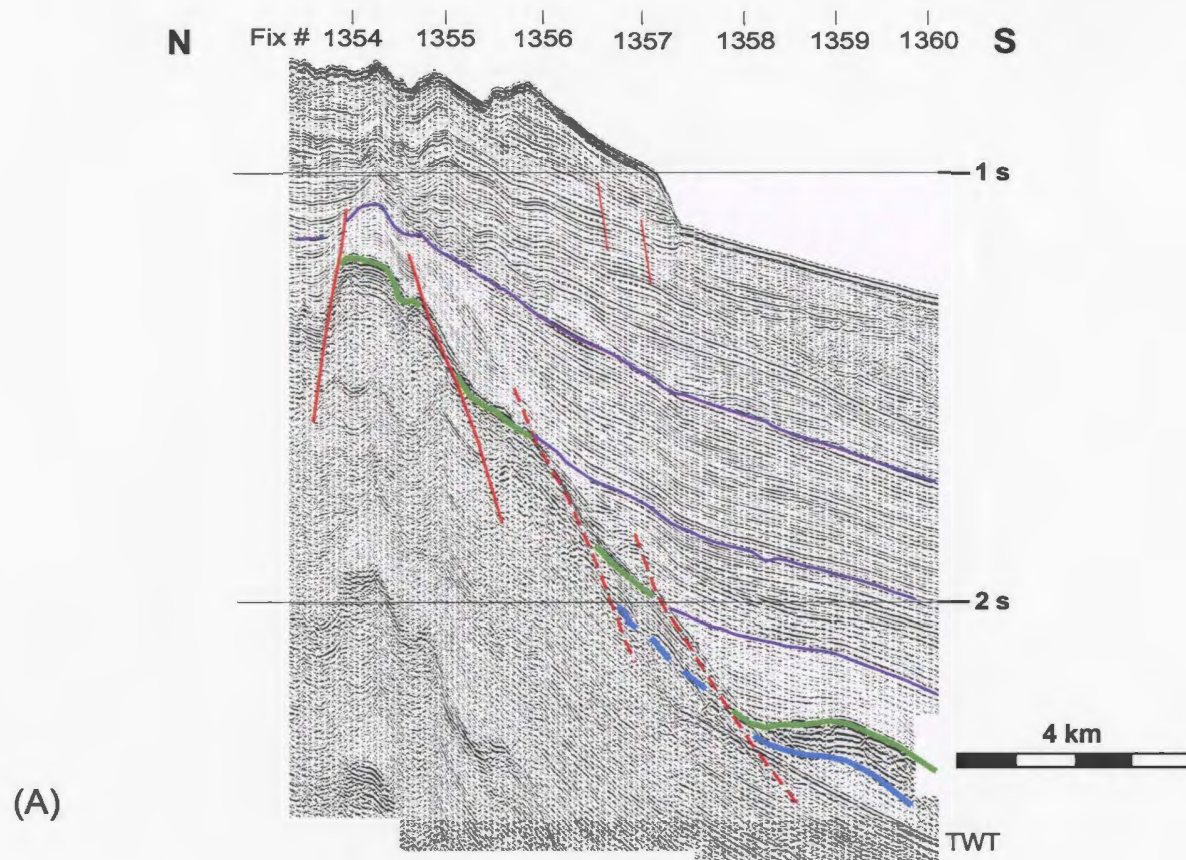


Figure 5.3: (A) Seismic line 534, fix #'s 1354-1360, showing the normal faults at the northern basin margin, (B) Seismic line 517, fix #'s 1409-1473, showing the transtensional faults at the southern basin margin.

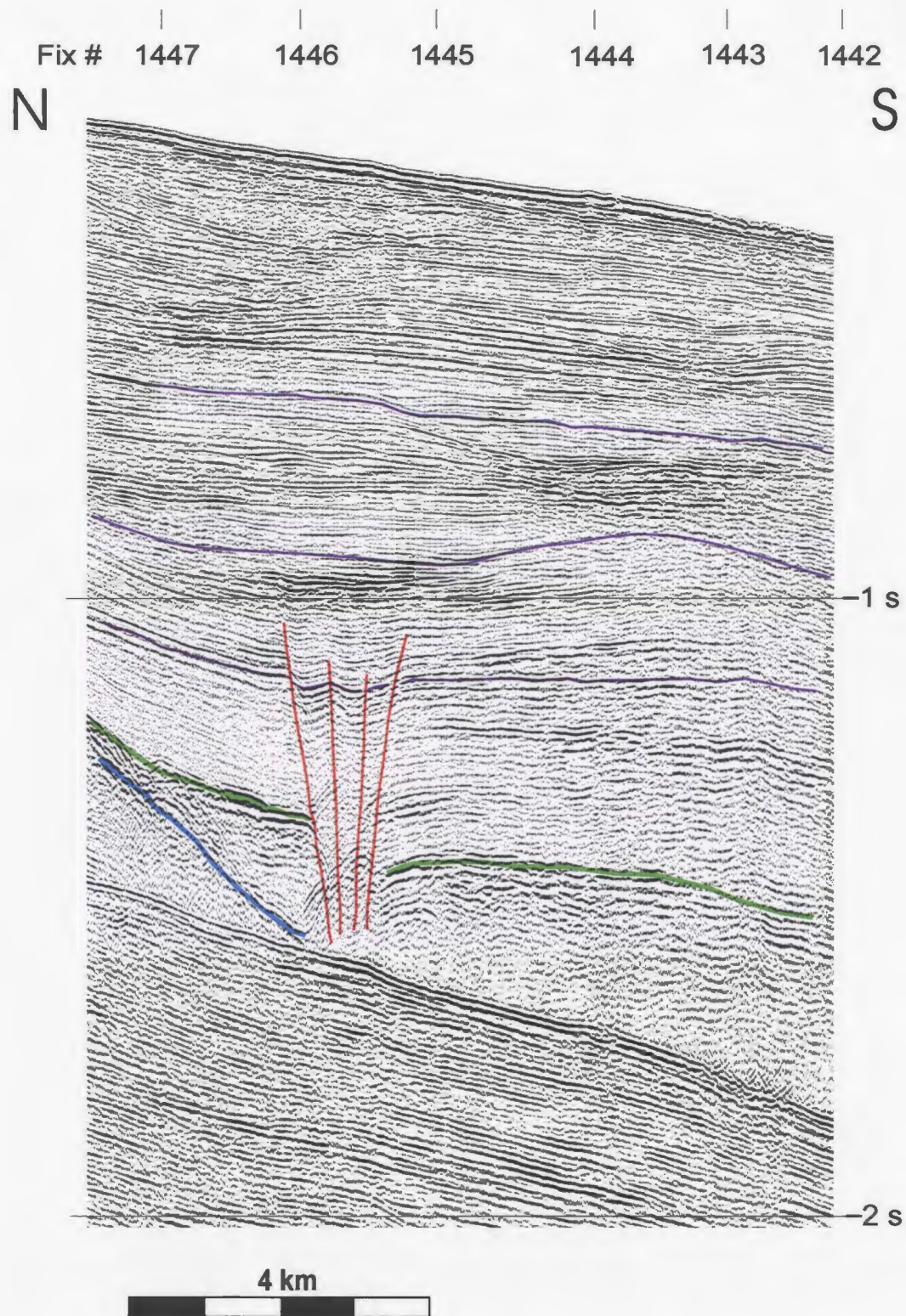


Figure 5.4: Seismic line 517, fix #'s 1442-1447, showing the east-west oriented transtensional fault zone from the northern domain of the Outer Cilicia Basin.

northward-verging thrust fault systems (fault sets C and H, see figure 5.5), *iv*) salt cored anticlines and folds (figure 5.6), *v*) thin-skinned, listric normal faults (fault set I, see figure 5.7). The two additional systems that dominate the transition zone between the Cilicia and Antalya Basins are: *vi*) south to southwest verging compressional faults (fault set N, see figure 5.8), *vii*) north to northeast trending extensional/transtensional faults (faults sets K, L, M, see figure 5.9). The seven structural systems can be loosely divided into two groups based on fundamental differences in the forces that control their development. The first group is made up those structures that develop due to far-field forces, such as surrounding plate motions and plate interactions (systems *i*, *ii*, *vi*, *vii*). The second group is made up of structures that develop primarily due to salt tectonics (systems *iii*, *iv*, *v*).

5.2.1 Structural systems formed due to far-field forces

5.2.1.1 Normal faults at basin margins

Normal faults, with significant extensional separation, are present at both the northern and southern margins of the Outer Cilicia Basin (see figure 5.3). At the northern margin, fault set A accommodates between 1200 ms and 1600 ms of separation across the M-reflector. At the southern margin, fault set J generally accommodates less than 300 ms of separation, with the exception of the far western portion of the basin where the faults are associated with up to 1200 ms of separation. The difference in accommodation amount between the two margins is expected considering the asymmetry of the basin (see figure 5.2). These faults most likely develop due to a combination of strike slip in the

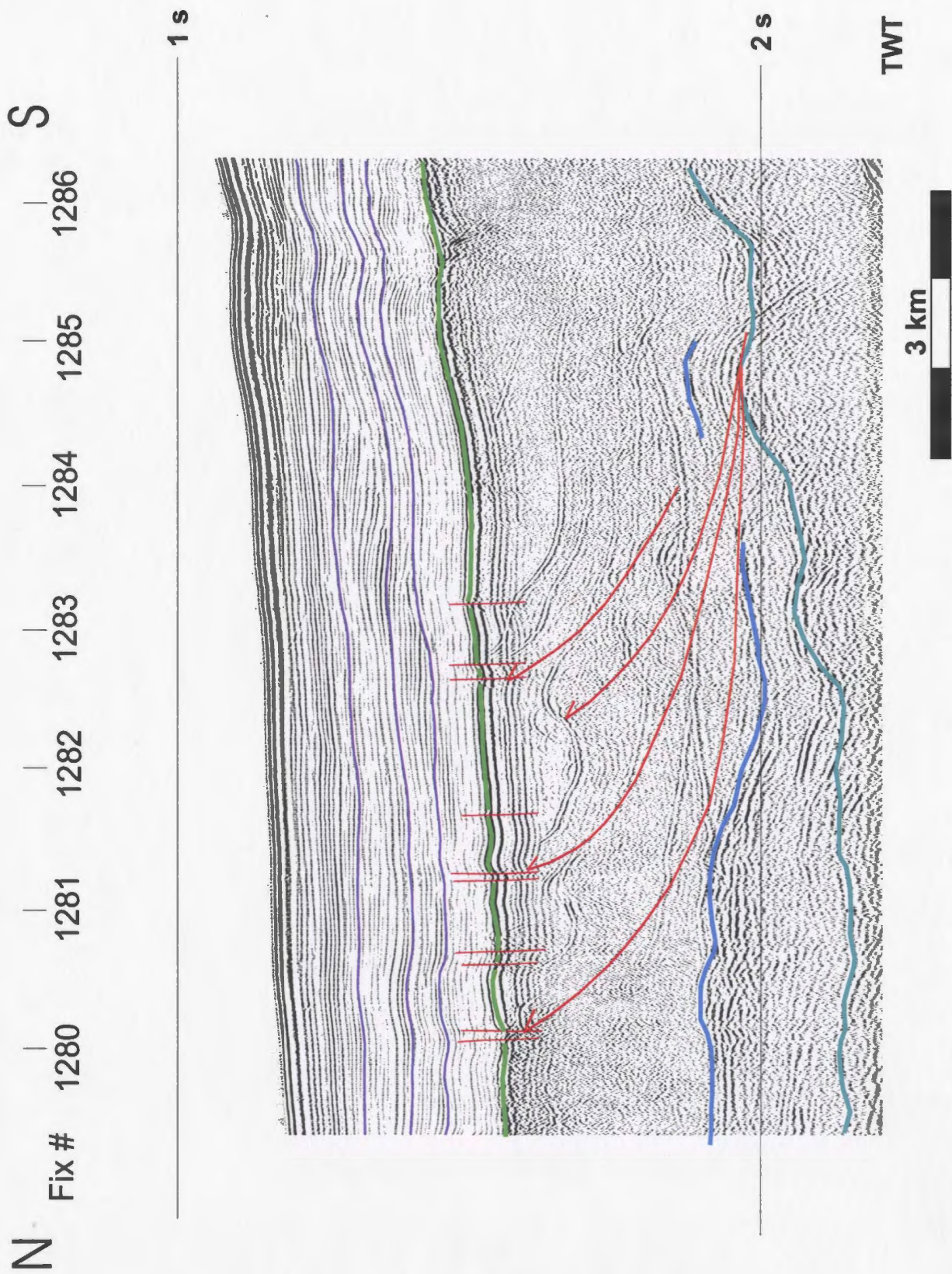


Figure 5.5: Line 467, fix #s 1280-1286 showing Messinian aged north verging thrust faults.

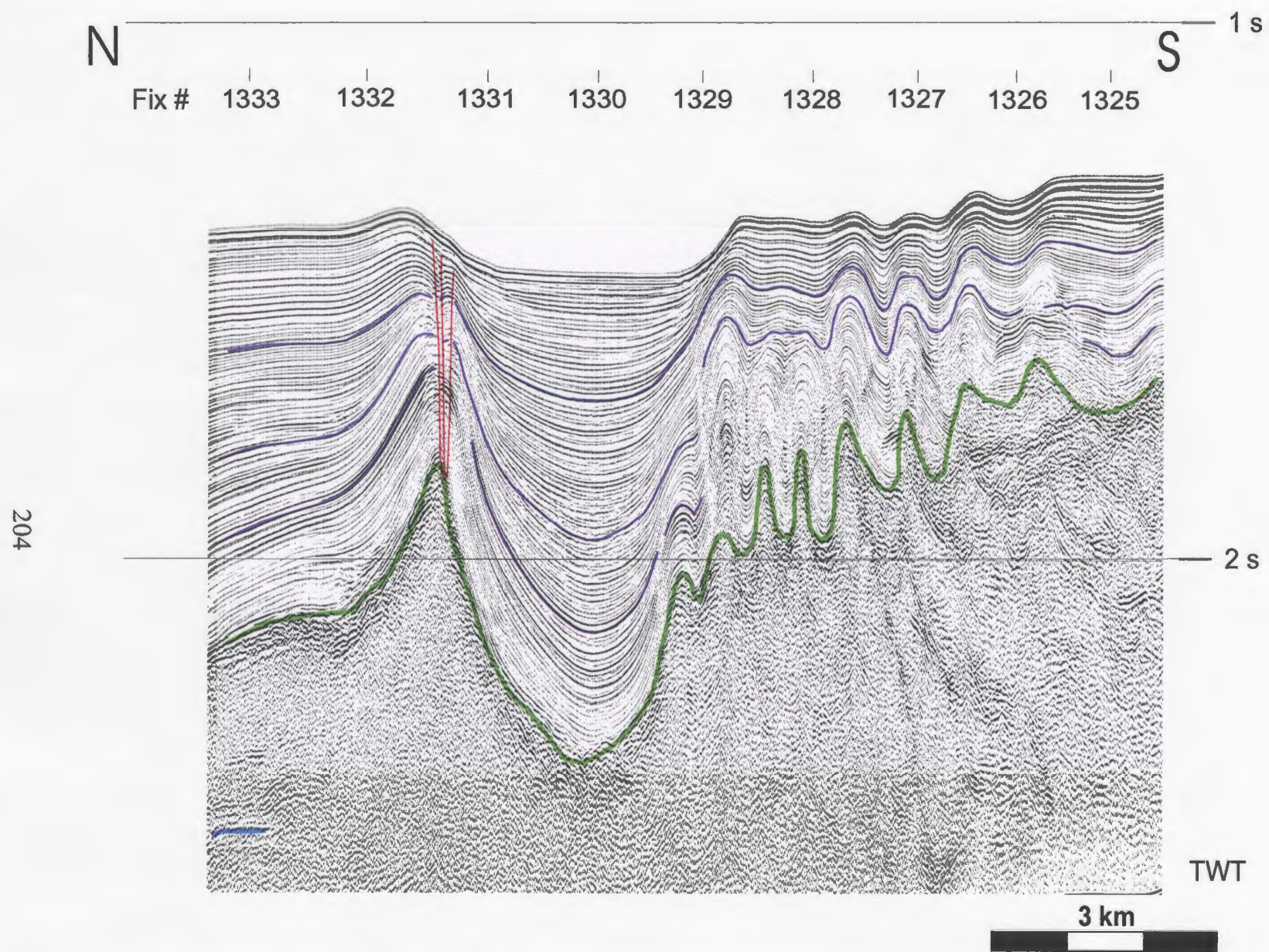


Figure 5.6: Seismic line 489, fix #'s 1325-1333, showing central fold zone of the Outer Cilicia Basin.

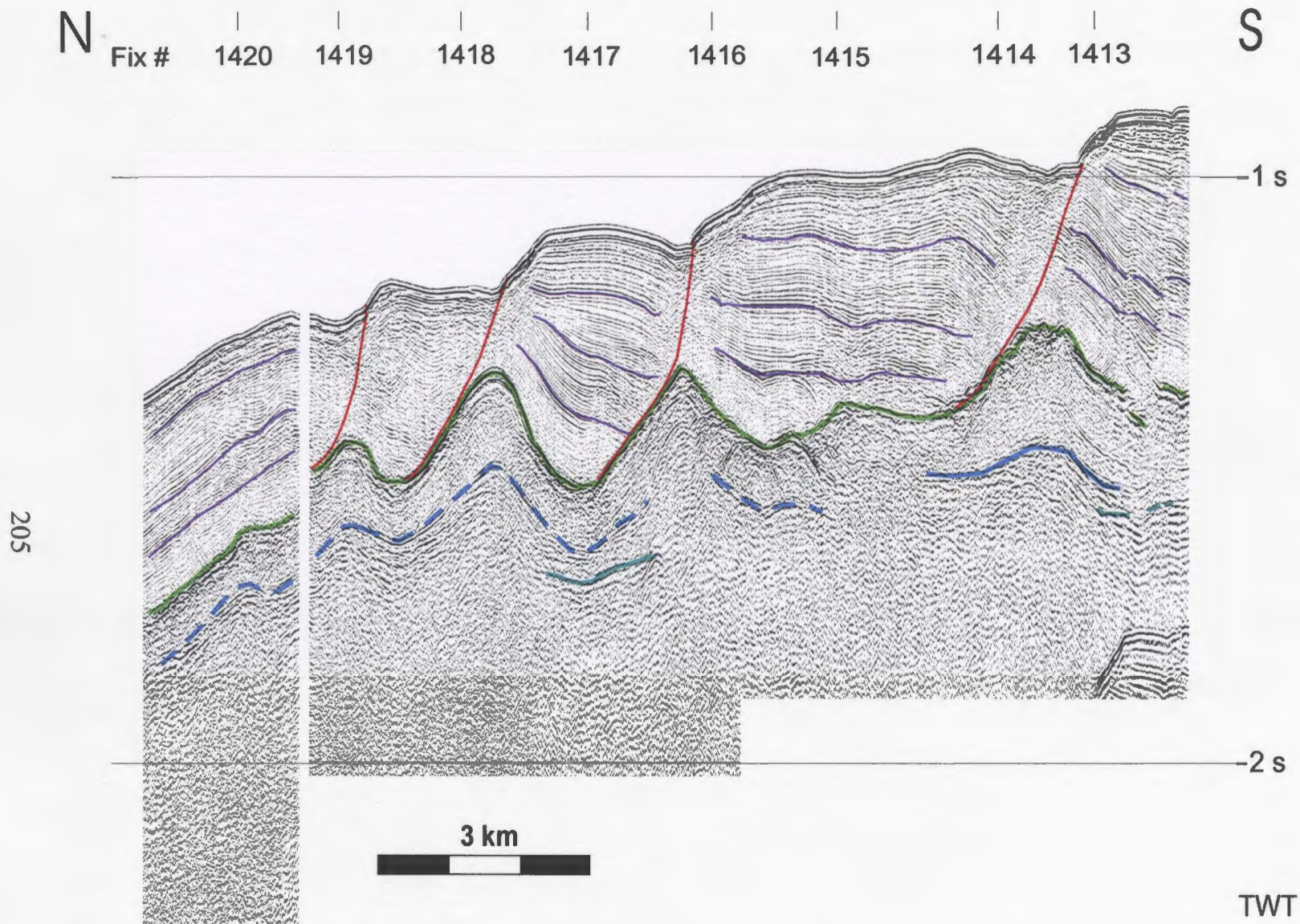


Figure 5.7: Seismic line 517, fix #'s 1413-1420, showing listric growth faults in the southern domain.

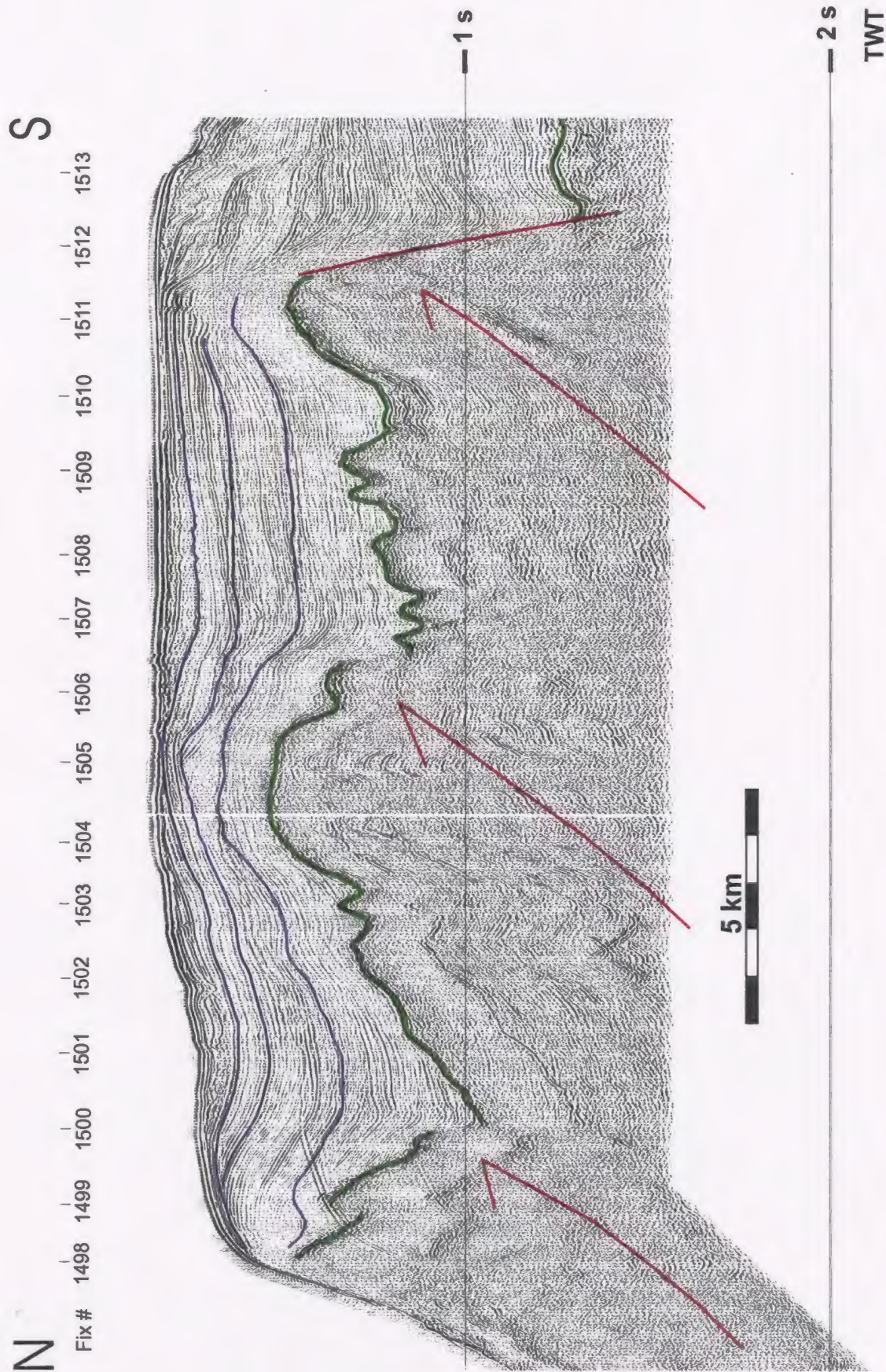


Figure 5.8: Seismic Line 534, fix #'s 1498-1513, showing south verging thrusts in the south segment of the Anamur-Kormakiti complex.

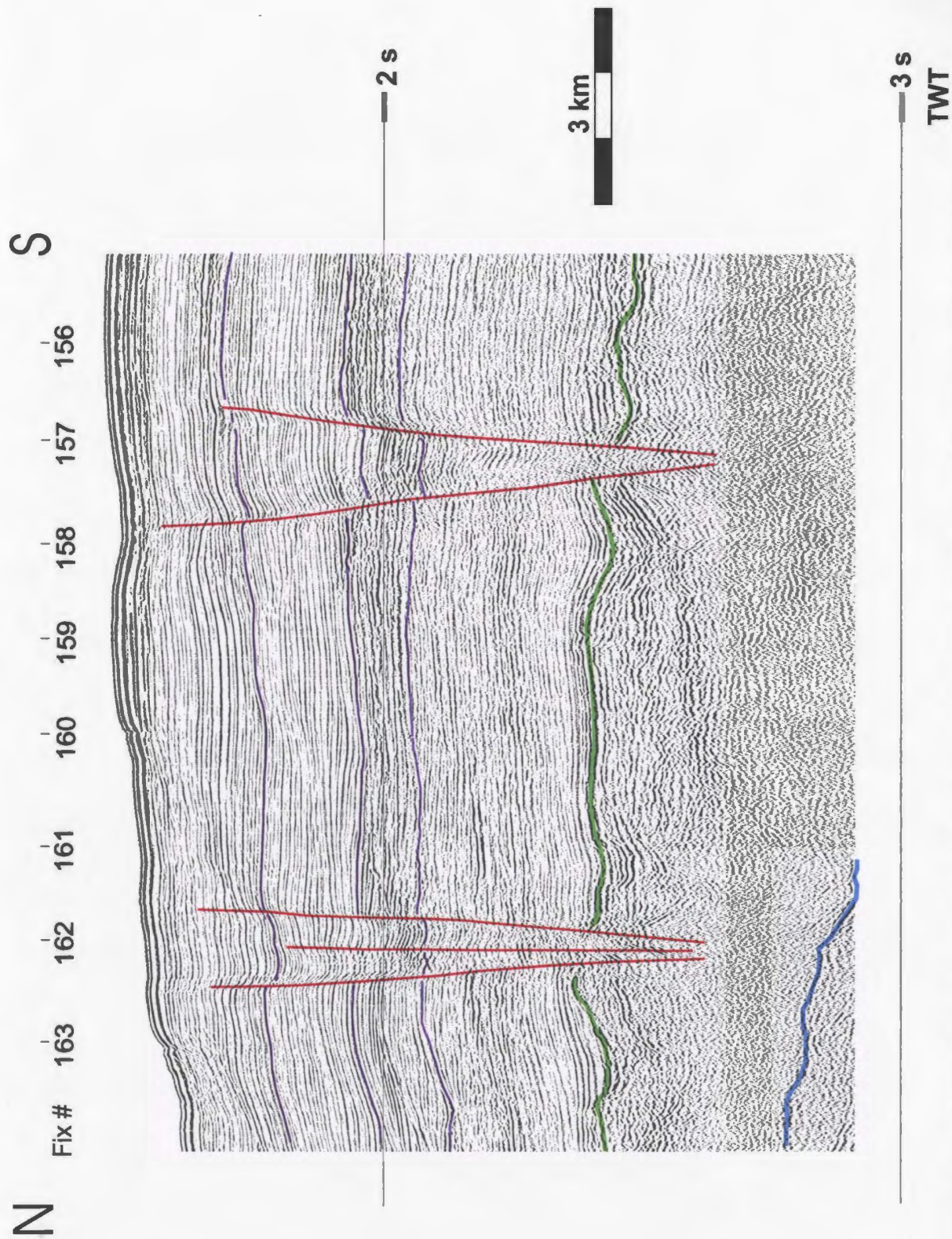


Figure 5.9: Seismic line 23, fix #s 156-164, showing the north to north-east trending transtensional faults from the transition zone between the Outer Cilicia Basin and the Anamur-Kormakiti complex.

basin from these nearby faults. They also acts as a boundary between the primarily transtensional domain within the Outer Cilicia Basin and the contractional domain to the south (also see Aksu et al., 2005). Although there is no clear evidence of strike slip motion across the faults at the northern margin, it is possible that the faults have a strike slip origin overprinted by more recent extension.

While the strike-slip component of these faults can be related to far-field forces, the extensional component of these faults is most likely due to more local forces. The asymmetry of the Outer Cilicia Basin leads to a much steeper shelf along the northern basin margin than at the southern margin. The steep gradient along the Turkish Shelf gives rise to relatively shallow gravity induced normal faulting and sediment sliding in the youngest sequence of the Pliocene-Quaternary succession (fault set B). Although fault sets A and J are earlier and more time extensive, the extensional component of the faults may be explained by a similar mechanism. Northwards up the Turkish margin, the faults penetrate successively younger sedimentary sequences suggesting that fault activity initiated farthest south on the margin, but later jumped to the faults farther to the north as basin progressively tilted toward the north. The extensional component of the faults on the southern margin can be attributed to similar gravity related processes. Although the dip of the margin is significantly less than that seen to the north, it is likely large enough to induce gravity related sliding along the existing strike-slip lineaments.

5.2.1.2 East-west oriented transtensional faults

The northern domain of the Outer Cilicia Basin is dominated by east-west to

northeast-southwest trending transtensional faults (fault set D). Although it is obvious that these faults are associated with a significant transverse and dip slip components, it is difficult to assess the direction of the strike-slip motion as well as the origin of extensional forces in a primarily compressional basin. The westward escape of the Anatolian microplate and the left-lateral motion on the fault splays of the East Anatolian transform fault suggest that these faults are also associated with left-lateral motion. Both fault traces making up fault set D (represented in purple on figure 4.16) have been correlated with onshore fault traces thought to extend from the East Anatolian transform fault; the Ecemis fault zone and the Kozan fault zone. The extension of these fault traces into the Outer Cilicia Basin suggest that splays from the East Anatolian Fault zone extend much farther to the south-west than proposed by earlier workers (see section 1.4.2, Şengör et al., 1985; Şaroğlu et al., 1992; Perincek and Cemen, 1990; Lyberis et al., 1990).

The extensional component of fault set D requires approximately north-south oriented extension in the northern Outer Cilicia Basin. A basin located in the forearc of an active convergent plate boundary would not typically be associated with major extensional forces. Convergence along the Cyprus Arc, however, has been complicated by a 45 degree rotation since late Miocene time, resulting in a counter-clockwise rotation of the Aegean-Anatolian microplate (Le Pichon and Angelier, 1979; Rotstein, 1984). The rotation of the microplate is fairly well documented, but controversy remains over the location of a single pole of rotation (Reilinger et al., 1997; Papazachos, 1999; Rotstein,

1984). The counter-clockwise rotation of Aegean-Anatolian microplate may help explain extensional forces within the Outer Cilicia Basin during Pliocene-Quaternary time. With subduction locked across the central segment of the Cyprus Arc, due to the collision between Cyprus and Eratosthenes seamount, the micro-plate begins to rotate and escape toward the unobstructed Hellenic Arc. Mascle et al. (2000) proposed that the collision along the Cyprus Arc also created a major discontinuity within the African plate creating the Sinai microplate between the African and Arabian plates (see figure 1.8). If this discontinuity continues to the north, cutting through the Aegean-Anatolian microplate, it may further segment the plate and allow the two parts to move more independently (see figure 5.10). The eastern area of the microplate may then rotate around a pole significantly closer to the Outer Cilicia Basin. This tighter rotation may create a situation where north-south directed extension could occur in the basin and be responsible for the dip slip components of fault set D (see figure 5.11).

5.2.1.3 North to northeast trending extensional/ transtensional faults

North to northeast trending transtensional and strike slip faults dominate the transition zone between the Outer Cilicia Basin and the Anamur-Kormakiti complex (fault sets K, L and M). Fault sets K and L are associated with both extensional and strike slip activity and most likely extend from the morphologically similar faults from the northern basin (fault set D). Assuming that the two fault systems are related, a left-lateral motion would be expected to dominate the faults in the transition zone. The only major difference between these faults and those seen in the northern basin

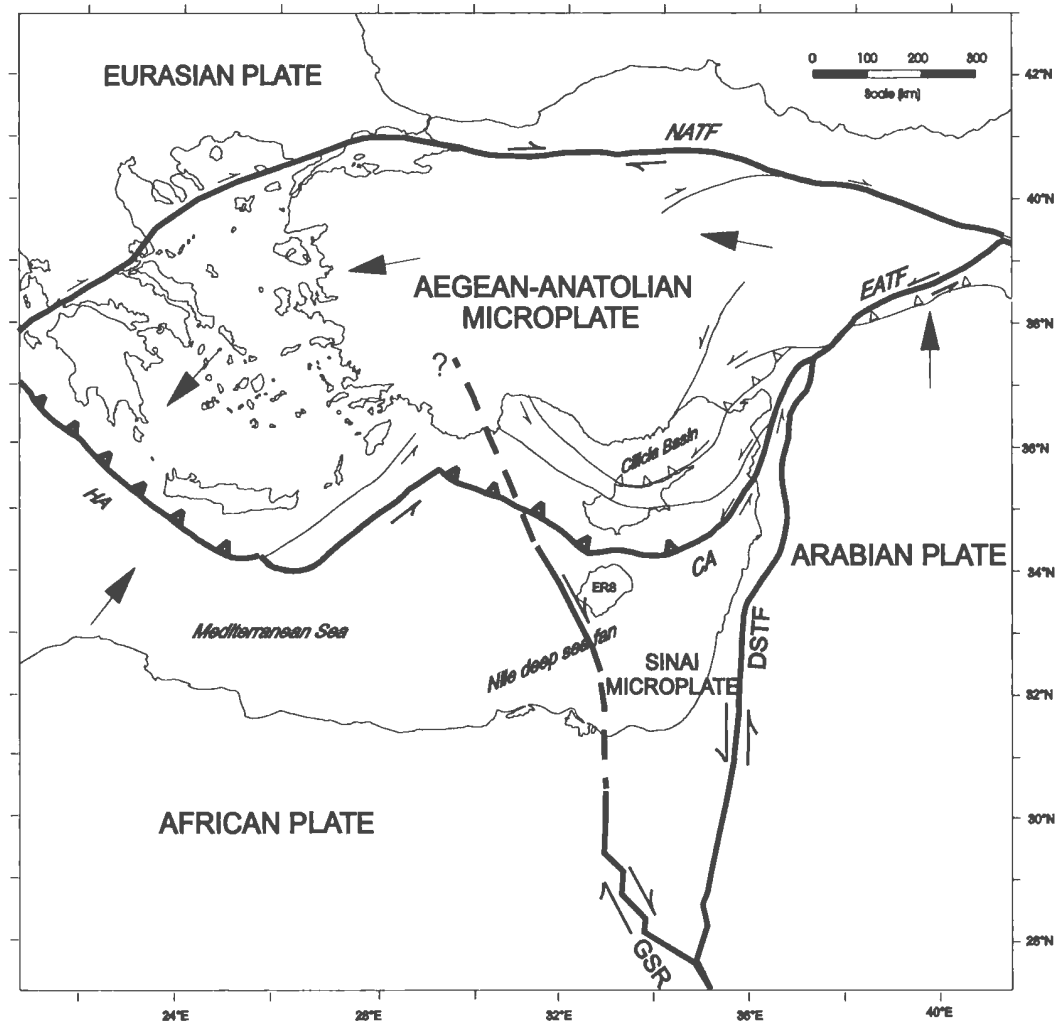


Figure 5.10: Simplified tectonic map of the eastern Mediterranean showing possible extension of the transform fault at the west boundary of Sinai Microplate into the Aegean-Anatolian plate (edited from Aksu et al., 2005). Map compiled from Sengor and Yilmaz (1981), Hancock and Barka (1981), Dewey et al (1986), Mascle et al. (2000). CA = Cyprus Arc, DSTF = Dead Sea transform fault, EATF = East Anatolian Transform Fault, ERS = Eratosthenes seamount, GSR= Gulf of Suez rift system, HA = Hellenic Arc, NATF= North Anatolian Transform fault. Large arrows indicate the sense of plate motion relative to a fixed Eurasian plate; half arrows indicate transform/strike-slip faults.

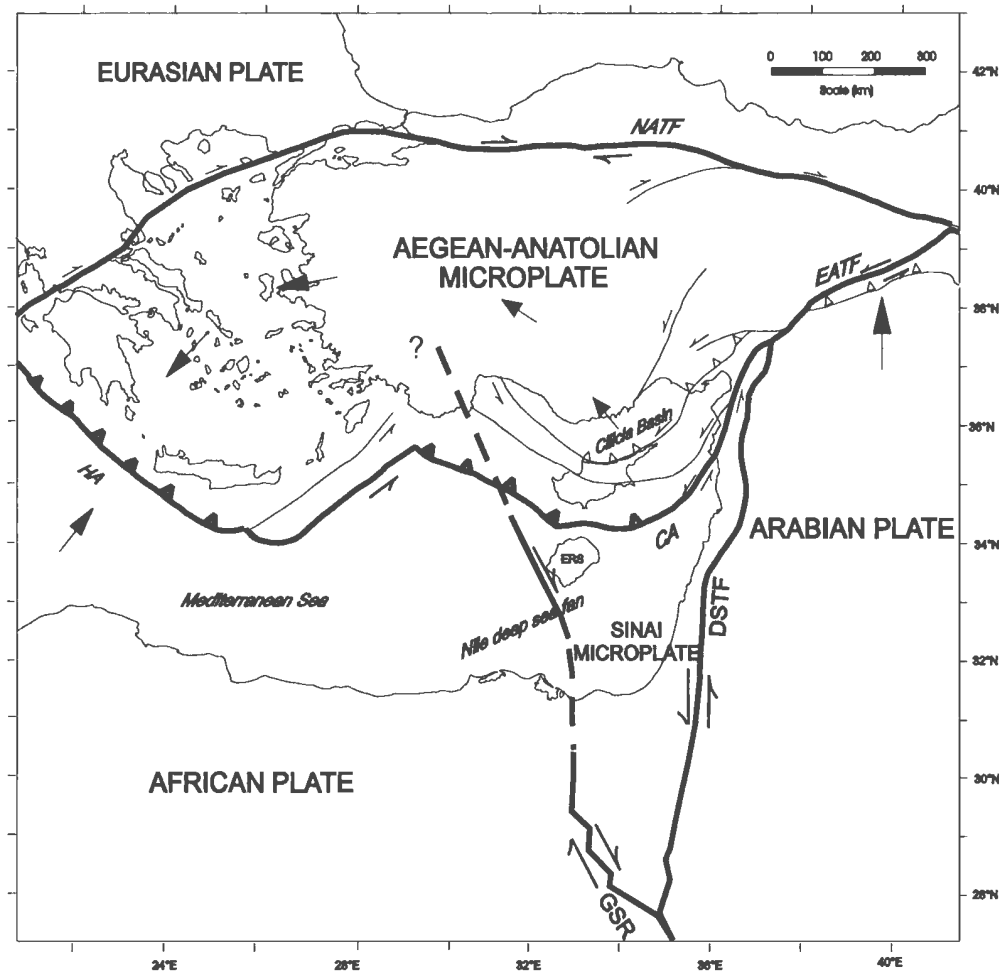


Figure 5.11: Simplified tectonic map of the eastern Mediterranean showing how extension arises in the Outer Cilicia Basin through the counterclockwise rotation of the eastern Aegean-Anatolian plate (edited from Aksu et al., 2005). Map compiled from Sengor and Yilmaz (1981), Hancock and Barka (1981), Dewey et al (1986), Mascle et al. (2000). CA = Cyprus Arc, DSTF = Dead Sea transform fault, EATF = East Anatolian Transform Fault, ERS = Eratosthenes seamount, GSR= Gulf of Suez rift system, HA = Hellenic Arc, NATF= North Anatolian Transform fault. Large arrows indicate the sense of plate motion relative to a fixed Eurasian plate; half arrows indicate transform/strike-slip faults.

is in the timing of fault activity. Fault set K and L remained active throughout Quaternary time, and in some cases up to the present day, while activity on fault set D primarily dies out by the end of Pliocene time. This suggests that any left lateral strike slip accommodation within the Outer Cilicia Basin had transferred to fault sets K and L by Quaternary time. The extensional component of these faults can be explained by a similar mechanism as described for fault set D. The northeast orientation of fault sets K and L, however, indicate that the primary orientation of extensional stress had rotated to northwest-southeast by Quaternary time, in association with the rotation of the Aegean-Anatolian microplate.

Fault set M can be differentiated from the other fault sets in the transition zone based on a number of characteristics. The faults are north-south oriented, most likely purely strike-slip, and were active during a much earlier time frame; ending before the end of Miocene time. Therefore, the forces responsible for these faults are most likely not the same as those associated with the other fault sets seen in this area. There is little evidence to indicate the direction of the strike slip motion across fault set M. Considering the north-south orientation and the timing of the fault activity, it is doubtful if the westward expulsion of the Aegean-Anatolian microplate had a significant impact on these faults. Papazachos and Papaioannou (1999) suggest the presence of a linear, northeast striking fault zone at the south-west coast of Cyprus, interpreted to be associated with a dextral strike slip based on the fault plane solutions of earthquakes (see figure 1.6). This fault zone is directly south of the Anamur-Kormakiti complex and may

therefore induce enough strain in this area to produce faults with a right-lateral strike-slip component. It is unknown, however, if this fault zone was active during the time period associated with fault set M. The evidence of both left and right lateral strike slip faulting in this area throughout the basin's history makes it difficult to determine what the primary orientation of stress would have been in late Miocene time and therefore the direction of motion across these faults.

5.2.1.4 South-southwest verging compressional faults

South-southwest verging reverse faults dominate the Anamur-Kormakiti complex in the far west portion of the basin (fault set N). This system was interpreted as the offshore extension of the Kyrenia range, and therefore likely formed as a result of the same forces responsible for the onshore mountain range. The mountain range is found directly north of and has the same orientation as the Cyprus Arc which marks the boundary between the African plate and Anatolian microplate (see figure 2.4). As described in section 1.4.1.2, the Cyprus Arc is a complicated plate boundary characterized by subduction, collision and strike slip motions. The central segment of the arc is undergoing collisional processes as the Eratosthenes seamount collides with the Anatolian plate (Ben-Avraham et al., 1988,1995). The compressive forces associated with this collision are thought to be responsible for the uplift of Cyprus and thrusting in the Kyrenia range since Pliocene time. The thrusts found in the southern portion of the Anamur-Kormakiti complex also form as a direct result of these forces. Northwest across the complex, the reverse faults are associated with smaller separations and with

bathymetric highs showing less relief. This suggests that the compressive forces responsible for the northwest oriented structures are of a smaller magnitude than the north-south directed forces. This fits with the accepted model of the Cyprean Arc, which suggests collision is occurring along the central segment while the western segment is dominated by either transpressive forces or continued subduction.

5.2.2 Structural systems related to salt tectonics

Salt structures form in sedimentary basins due to the fact that evaporite (or “salt”) layers are generally weaker and less dense than the surrounding sedimentary layers. This allows the evaporite layers to mobilize and deform into complicated structures. The most commonly accepted forces driving salt motion are: 1) differential loading, caused by sediment progradation, erosion or extensional faulting (Jackson and Vendeville, 1994; Koyi, 1996; Ge et al., 1997; Ings et al., 2004; Fort et al., 2004) and 2) gravitational forces, which act primarily in basins that have tilted margins (Fort et al., 2004; Ings et al., 2004). These forces generally induce a basin-ward flow of salt, which can cause failure in the overlying sedimentary layers. The general structure of basins characterized by basin-ward flowing salt is fairly predictable, with of a zone of landward extension and a zone of seaward compression (Koyi, 1996; Ge et al., 1997; Fort et al., 2004; Ings et al., 2004). The actual structures that form in these basins, however, are dependent on numerous variables such as sedimentation rate, tilt angle and salt viscosity (Koyi, 1996; Fort et al., 2004; Ings et al., 2004). Ings et al. (2004) suggested a fairly simplified four phase evolution for basins affected by seaward salt flow driven by both progradation and

gravitational forces. These four phases are: 1) the formation of mini-basins by the evacuation of salt from downwarps into the adjacent upwarps; 2) the formation of extensional and listric normal faults over salt rollers in proximal areas; 3) Seaward translation of rafts (which are overburden fault blocks that move laterally to a degree that are no longer in contact with their associated footwall (Jackson and Talbot, 1994)) and the formation of diapirs at the base of the prograding slope; and 4) salt overthrusts younger sediments beyond its depositional limit to form allochthonous salt nappes. This simplified four phase evolution can help explain some of the structures found in the southern and central zones of the Outer Cilicia Basin.

Both gravitational force and progradation likely play a role in mobilizing the salt layer in the southern domain of the Outer Cilicia Basin. The southern domain is characterized by a fairly thin Pliocene-Quaternary succession overlying a relatively uniformly dipping M-reflector surface. The tilt of the basin generally ranges between 2 and 4 degrees. Although little research has been done to determine the minimum tilt angle that would cause salt to mobilize, models with 4-5 degree tilts have been shown to produce the salt-related structures described above, especially when combined with progradation (Fort et al., 2004). Although there is no significant seismic stratigraphic evidence that progradation occurred in this part of the basin, it is likely that the sediment deposited in the basin was derived from the Kyrenia range and was initially deposited in most landward regions, thereby creating some degree of differential loading.

5.2.2.1 Thin-skinned listric normal faults

Listric normal faults form on the basin-ward flank of relatively low amplitude salt rollers in the southern domain of the Outer Cilicia Basin (fault set I). These faults represent the region of landward extension associated with the basin-ward movement of salt. According to the evolutionary phases proposed by Ings et al. (2004) the layers were first folded into low amplitude folds, forming mini-basins between salt uprisings, followed by the formation of normal faults over the crest of the folds. As described in section 4.3.4, the faults were active during the deposition of the youngest three sequences, but not during the deposition of the earliest Pliocene sequence. Basin-ward salt movement likely began during the deposition of sequence D, leading to the formation of these extensional faults during the deposition of the later sequences. In the central part of the basin, the listric faults are replaced by extensional fault grabens overlying the salt uprisings. These collapse structures most likely form in response to salt withdrawal from the structures as the salt continues to flow downdip. This suggests that the structures are more evolved in the central part of the basin.

The listric faults making up fault set I are more common in the central and western portions of the basin, than farther to the east. This suggests that there may be a correlation between the degree that the margin dips toward the north and the formation of these structures. In the eastern portion of the basin the dip of the margin is generally only 1-2 degrees, while farther west the margin dips more steeply, up to 3-4 degrees. This evidence supports the idea gravitational forces play a major role in the mobilization of

salt in this basin.

5.2.2.2 Salt-cored anticlines and folds

The salt-cored anticlines and folds that dominate the central zone of the Outer Cilicia Basin represent the region of seaward compression associated with basin-ward flow of salt. As described in section 4.3.3., the fold zone is made up of one major salt anticline and associated growth syncline and a region of shorter wavelength, lower amplitude salt cored folds. In some areas, the folds are asymmetrical and associated with high angle reverse faults. According to the evolutionary phases proposed by Ings et al. (2004) the evolution of this area most likely began with layers being folded into low amplitude folds, forming mini-basins between the salt uprisings. As salt continued to flow downslope and feed the system, the amplitude of the salt anticline and folds increased while the mini-basins became more defined and filled with sediment. The high angle reverse faults likely formed at a later stage of development as the northward flow of salt creates sufficient compressive forces to break the overburden. The architecture of sedimentary sequences associated with the rise of these structures indicate that they were developing during the same time frame as the listric normal faults in the southern domain of the basin. The compressional structures are also best developed in areas where the listric faults are most evolved. This verifies that these two systems are indeed related and that they form as parts of the larger system controlled by the movement of salt in this basin.

The location of the fold belt is likely controlled by underlying basement structures. A major fault zone, interpreted as a major extensional fault zone in the pre-late Miocene stratigraphy, lies directly below the location of the main salt anticline (fault set G). Schultz-Ela and Jackson (1996) suggest that basement faulting can influence where salt structures form by influencing the thickness of the sedimentary overburden in the hanging wall and footwall of the fault plane. This variation in thickness can create differential loading on the salt layer causing the salt to rise. This mechanism appears appropriate in the Outer Cilicia Basin, as there is a significant difference in the thickness of the Pliocene-Quaternary succession between the southern and northern domains, which can at least partially be attributed to underlying basement structure. Another possible explanation for the location of the fold belt is that the salt layer thins dramatically, or actually pinches out, in the centre of the basin as indicated by figure 4.12 and A1-Figure 10, fig #'s 1085-1090. The centre of the basin would therefore be at the depositional limit of the salt and therefore the most likely location for compressional structures to form (Ings et al., 2004; Fort et. al., 2004).

5.2.2.3 Northward verging thrust fault systems

Northward verging, low angle thrust faults occur within the Messinian evaporite layer in both the northern and southern domains of the Outer Cilicia Basin (fault sets C and H). The limited time span of fault activity and direction of fault movement (opposite to other compression related structures in the area) suggest that a localized and time-limited stress is responsible for these structures. As discussed above, compressional

structures commonly occur downdip of extensional structures in salt basins, due to the basinward mobilization of salt. In order for the thrust faults of sets C and H to be a part of this type of system, salt movement would have to have occurred in the Outer Cilicia Basin by late Miocene time. As there was only a small amount of sediment deposited in the basin during the salt deposition, sediment progradation was most likely not a significant external force during the Messinian. This leaves only gravitational forces as a possible initiator of the salt movement. The morphology of the basin at the end of Miocene time was most likely different from its present configuration. Considering that the M-reflector is a basin-wide unconformity, it can be assumed that the sea-bed was primarily flat at the beginning of Pliocene time. Thrusting in the Kyrenia range, however, is thought to have resumed during the mid-late Miocene. If the Outer Cilicia Basin was evolving on the back limb of this thrust system during the late Miocene, the basin would be tilted towards the north, similar to its present day configuration.

There has been little research done on the ability of primary salt layers to mobilize exclusively by gravitational force. Fort et al. (2004) suggest that at the Angolan margin, salt mobilization initiated before significant sediment progradation occurred, but they did not substantiate this theory with laboratory experiments. There has, however, been some research done on the flow of salt glaciers, which may be transferrable to the salt layer in the Outer Cilicia Basin. Salt glaciers are sheetlike, salt extrusions flowing from an exposed diapir and spreading beneath air or water (Jackson and Talbot, 1991). During Messinian time, the salt layer in the Outer Cilicia Basin was exposed at the

surface much like present day salt glaciers and therefore may have mobilized in a similar manner. Salt glaciers (the Hormuz salt from southern Iran, for example) have been known to flow downdip without additional external forces, such as heat or loads (Talbot, 1979). The flow of a salt glacier is thought to be facilitated by the infusion of water into the salt layer (Talbot and Rogers, 1980; Wenkert, 1979). Wenkert (1979) suggest that as a salt layer begins to flow, the brittle upper layer will crack allowing water to seep into the salt layer and become trapped. This interstitial liquid effectively softens the salt and allows more rapid flow (Talbot and Rogers, 1980). In the Outer Cilicia Basin, the Messinian salt layer is known to have been deposited during a series of dessications followed by marine invasions. If the salt layer had been cut by faulting or even cracking of the brittle upper layer, water may have penetrated the salt layer during a marine invasion and induced more rapid flow. Water trapped within the thin sediment layers deposited during marine invasions may have also facilitated gravity sliding by acting as detachment surfaces within the evaporite unit.

The internal structure of flowing salt glaciers has also been studied and proves to be analogous to structures seen in orogens, thrust sheets, and submarine slumps (Talbot, 1979, 1981). Talbot (1979, 1981) suggests that the internal structure of a salt glacier is controlled by its flow pattern, which is directly influenced by the regularity of the surface that the salt flows over. Underlying irregularities or discontinuities tend to associated with the main areas of deformation within the salt layer. A1-Figure 1, fix # 1280-1288 shows a possible relationship between the underlying irregular surface and the overlying

thrust faults in the southern Outer Cilicia Basin (fault set H). The thrust faults appear to form directly north of a 15 ms drop across both the N and O-reflectors.

Considering the evidence presented above, fault set C and H appear to have formed in response to a basin-ward mobilization of the salt, similar to that seen in salt glaciers. As the basin tilted toward the north during the late Miocene, gravitational forces caused the salt to flow basin-ward creating the downdip compressional structures in both the northern and southern domains of the basin. There are a few issues that provide challenges to this theory, however, including a lack of updip extensional structures to complement the downdip contraction. The lack of obvious updip extensional structures could result from an inability to map fault traces in the acoustically transparent salt layer. In the central area of the basin, the compressional structures are obvious due to the presence of intra-salt horizons which show the fault's geometry. These intra-salt horizons generally do not extend far enough on the southern margin to be affected by the updip extensional structures, if they are present. It is also possible that the complementary updip extensional structures are represented by early movement on the Pliocene-Quaternary aged, deeply rooted transtensional/ extensional faults that dominate the southern boundary of the basin (fault set J). Another issue that challenges this theory is the evidence that the M-reflector is a basin-wide unconformity, and therefore was most likely not significantly tilted at the end of Miocene time. The model proposed for the formation of the compressional features requires that the sea-floor must be dipping to allow gravitational forces to have a significant impact. It is important to note here that

thrusting in the Kyrenia range was most likely not a constant process, but occurred in stages with numerous episodes of thrusting followed by episodes of erosion and subsidence. Figure 5.12 shows a possible scenario that may help explain the late Miocene evolution of the Cilicia basin. In this scenario, tilting of the basin occurs after the salt layer was deposited during an episode of thrusting in the Kyrenia range. The tilting of the basin forces the salt to migrate basin-ward. As the salt migrates, the depositional limit of the salt also moves basinward and thickening occurs in the central area of the basin. This thickening of the salt layer in the center of the basin produces a top-salt reflector that dips much more gently than the base salt reflector. This scenario provides a possible situation that allows for both tilting of the basin during the late Miocene and basin-wide erosion at the end of the Miocene epoch.

5.3 Neogene Evolution of the Outer Cilicia Basin

The Neogene evolution of the Outer Cilicia Basin is synthesized in two tectono-stratigraphic charts; one representing a north-south profile through the centre of the basin (see figure 5.1), the second representing a profile through the western portion of the basin (see figure 5.13). The two areas share a common evolution, with only minor differences in the Messinian-Quaternary time periods. The relatively uniform nature of the Outer Cilicia Basin allows a fairly concise basin-wide description of the Neogene evolution.

During early to mid-Miocene time, diachronous transgressive sequences were deposited in the foreland region associated with thrusting in the Tauride mountain range.

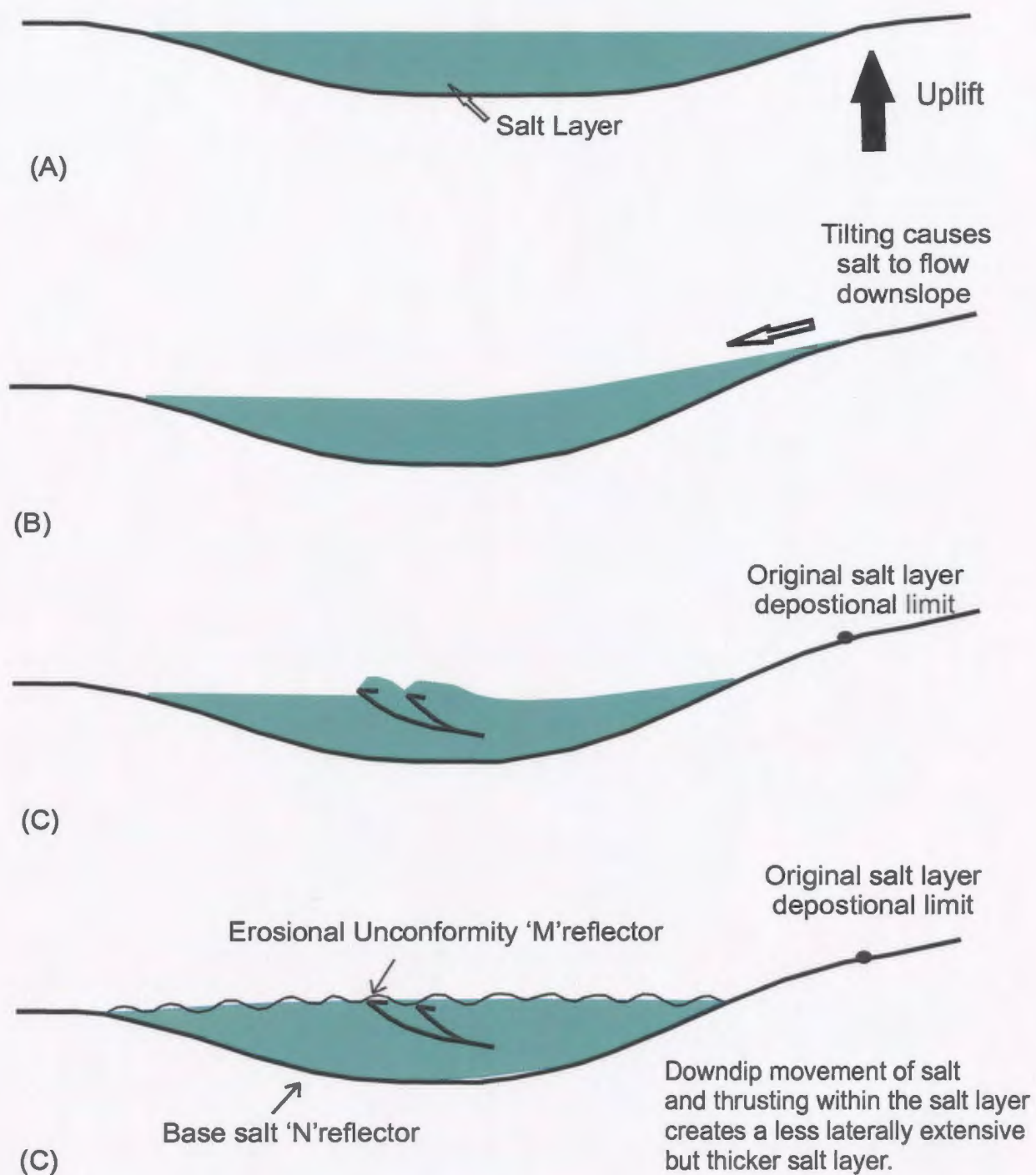


Figure 5.12: Schematic showing the development of Messinian salt layer during late Miocene time, (A) Original basin architecture at the time the salt layer was deposited; (B) Change in basin architecture during thrusting in the Kyrenia range; (C) Initiation of thrust faulting due to the basinward movement of salt; (D) Basinal extent of salt layer at the end of Miocene time.

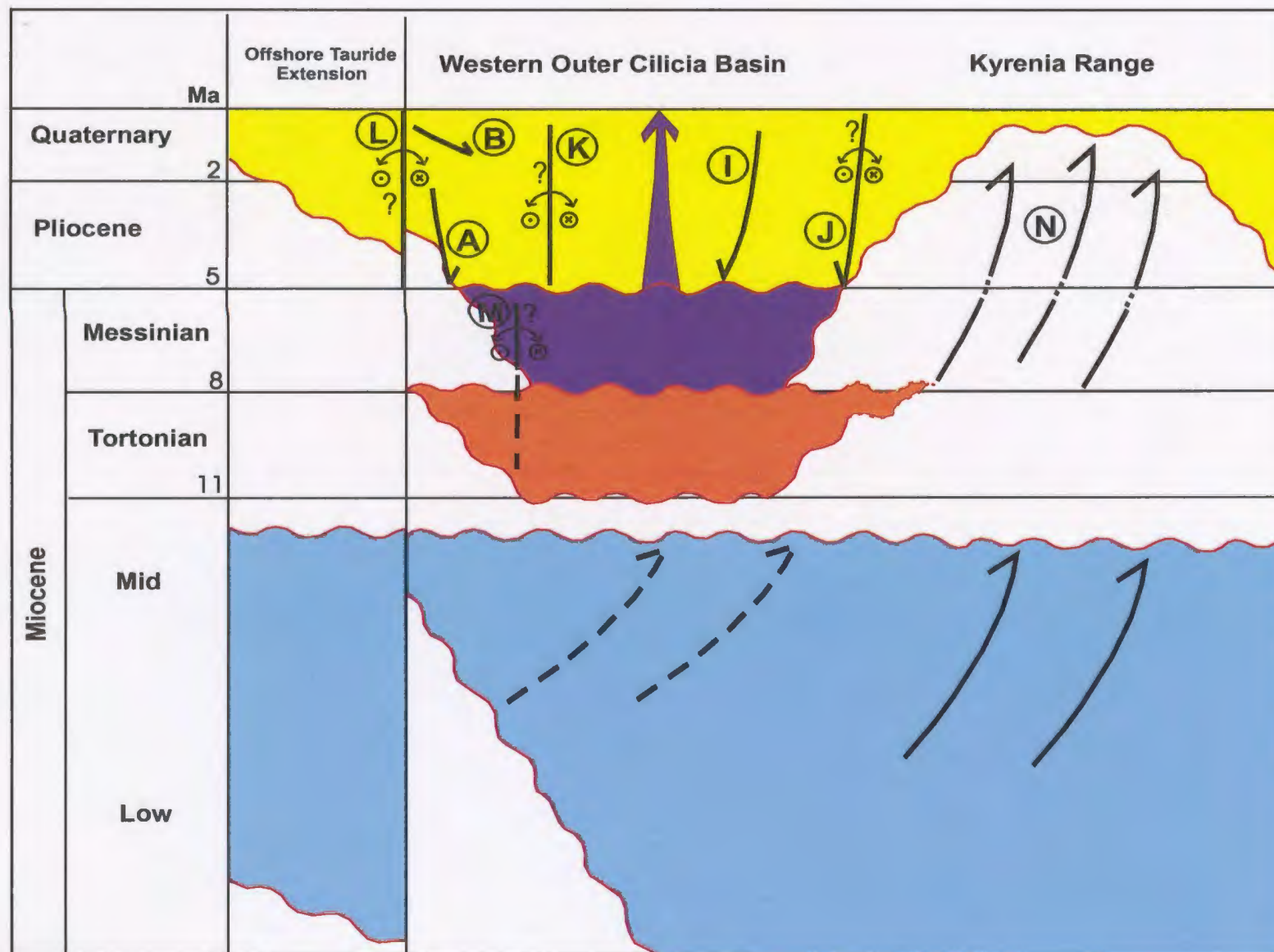


Figure 5.13: Tectono-stratigraphic chart representing north-south profile across the western Outer Cilicia Basin.

These sequences can be correlated across the north-east Mediterranean and are represented in the Outer Cilicia Basin as Unit 3B. Beginning in the mid-late Miocene, regional compression led to the development of a major south to south-east verging thrust belt centered on the present day Misis-Kyrenia lineament (see figure 5.14). Thrust activity initiated in the Misis segment of the thrust belt during the Seravallian-Tortonian and progressed toward the south-west (Aksu et al., 2005; Kelling et al., 1987). The architecture of the Tortonian aged sequences deposited in the Outer Cilicia Basin suggest that thrust activity in the Kyrenia range had also initiated by Tortonian time. These sequences, represented by Unit 3A, pinch out onto the southern margin and show progressive thickening toward the north, indicating deposition in a piggy-back setting. Thrust activity in the western offshore extension of the Kyrenia Range began sometime later, as evidenced by the presence of slices of the Tortonian aged sequences (Unit 3A) within the stratigraphy of the thrust sheets making up the southern segment of the Anamur-Kormakiti complex. This supports the theory of Kelling et al. (1987) that compressional fault activity progressed from the northeast to the southwest along the Misis and Kyrenia lineament. By Messinian time, active thrusting and uplift began along the southern segment of the Anamur-Kormakiti complex. The presence of Messinian-aged strike slip faulting (set M), in the transition zone between the Anamur-Kormakiti complex and Outer Cilicia Basin, indicates that both compression and strike slip activity were occurring simultaneously in this area near the end of Miocene time.

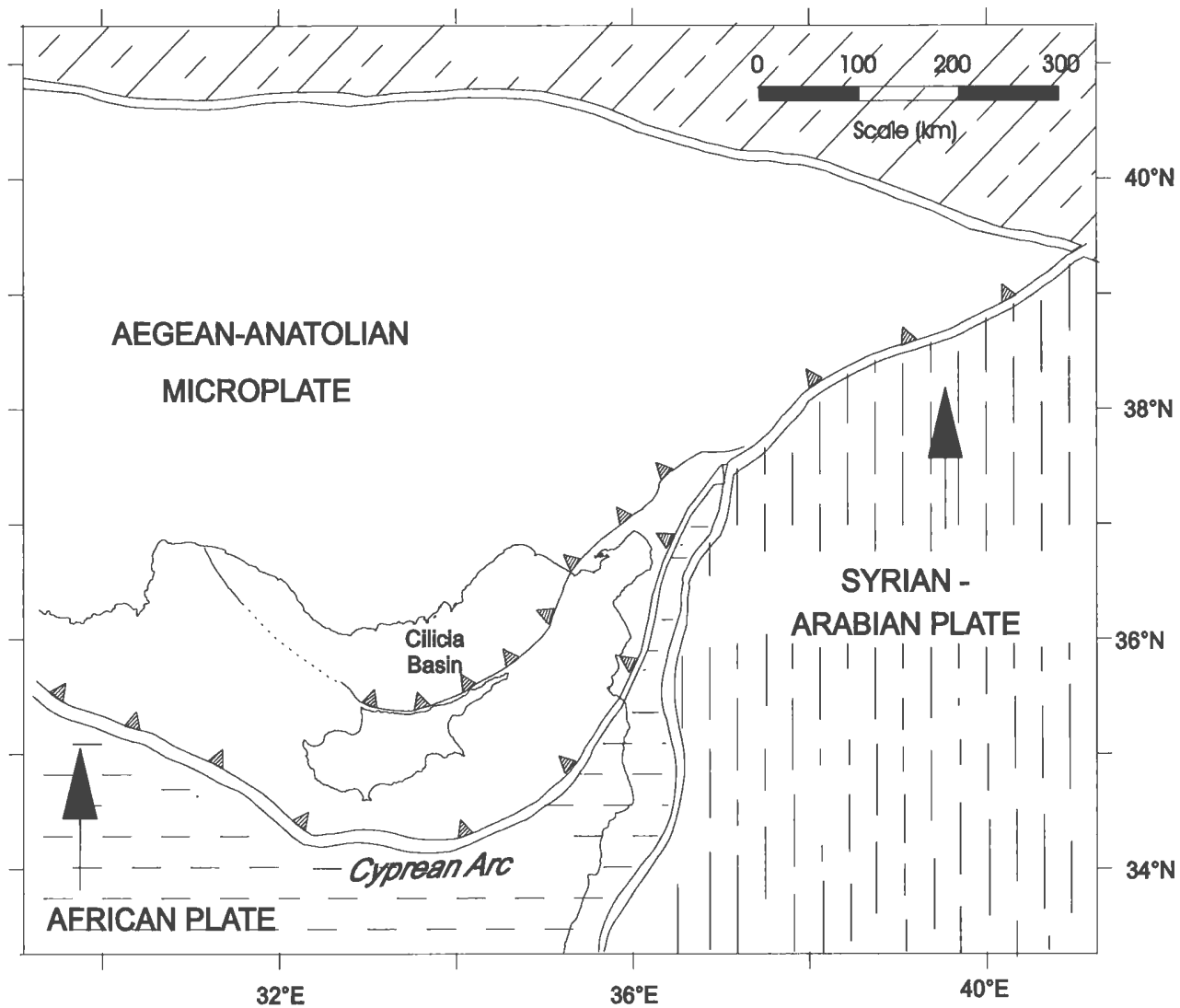


Figure 5.14 : Simplified paleotectonic map of the North-East Mediterranean during mid-Miocene time (edited from Aksu et al., 2005). Map compiled from Sengor and Yilmaz (1981), Hancock and Barka (1981), Dewey et al (1986). Large arrows indicate the sense of plate motion relative to a fixed Eurasian Plate.

The dessication of the entire Eastern Mediterranean Sea caused a thick evaporite layer to be deposited in the basins of the north-east Mediterranean during Messinian time. In the Outer Cilicia Basin, the presence of intra-salt horizons indicate that the evaporite layer was not deposited during a single dessication episode. The intra-salt horizons represent shale, chalk or marl layers deposited in marine conditions during hiatuses in the evaporite deposition. This suggests the evaporite layer was deposited during a number of cycles, involving periods of dessication followed by periods of marine invasion. The periods of marine invasion may have occurred in response to basin subsidence, during times of diminished thrust activity in the Kyrenia range, or in response to eustatic or structural controls. The end of Messinian time is defined by a Mediterranean wide unconformity, represented by major basin-wide erosion in the Outer Cilicia Basin.

The lack of a Messinian evaporite layer along any section of the Misis-Kyrenia lineament suggests that the structure was fully emerged during Messinian time. By the end of the Messinian, thrust activity in the Misis mountains is thought to have ceased based on evidence that the M-reflector, over the crest of the structure, is onlapped by undisturbed Pliocene sediment (Aksu et al., 2005). Activity in the offshore Misis-Kyrenia thrust belt and Kyrenia mountains, however, continued well into Pliocene-Quaternary time. Thrusting in the Kyrenia range caused the southern margin of the Outer Cilicia Basin to tilt towards the north, initiating the downslope flow of salt, sometime before the end of Messinian time. This gravity-driven deformation created the intra-salt thrust faults (set C and H), and displaced the original depositional limit of the salt layer

basinward. Activity on the thrust faults concluded by latest Messinian time, as evidenced by erosion at the top of the thrust sheets across the M-reflector.

The late Miocene was a time of major structural reorganization in the north-east Mediterranean. The collision of the Arabian and Eurasian plate in the mid-Miocene led to the formation of the North and East Anatolian transform faults, facilitating the westward escape of the Anatolian microplate (see figure 5.15) (Şengör et al., 1979,1981,1985). It is difficult to say if the transtensional faults in the northern domain of the Outer Cilicia Basin, which have been interpreted as splays of the East Anatolian transform fault, initiated at this time or later in the basin's evolution. A lack of seismic resolution at depth also makes it difficult to tell if the extensional faults at each of the basin margins initiated during the late Miocene or later in the evolution.

A major transgressive episode signaled the beginning of Pliocene time, as marine conditions were reestablished in the north-east Mediterranean. Sea level rise was thought to be fairly rapid, as the earliest Pliocene sequences in the Outer Cilicia Basin were deposited in full marine conditions (Robertson et al., 1991). The rise in sea level continued throughout the Pliocene, as evidenced by onlapping reflectors progressing higher up the basin margins through the Pliocene succession. The Pliocene and Quaternary sediment distribution in the Cilicia Basin suggests that it was infilled asymmetrically from the sediment source in the north-north-east, with little contribution from Cyprus. The sediment source is from the delta plains of the Seyhan,

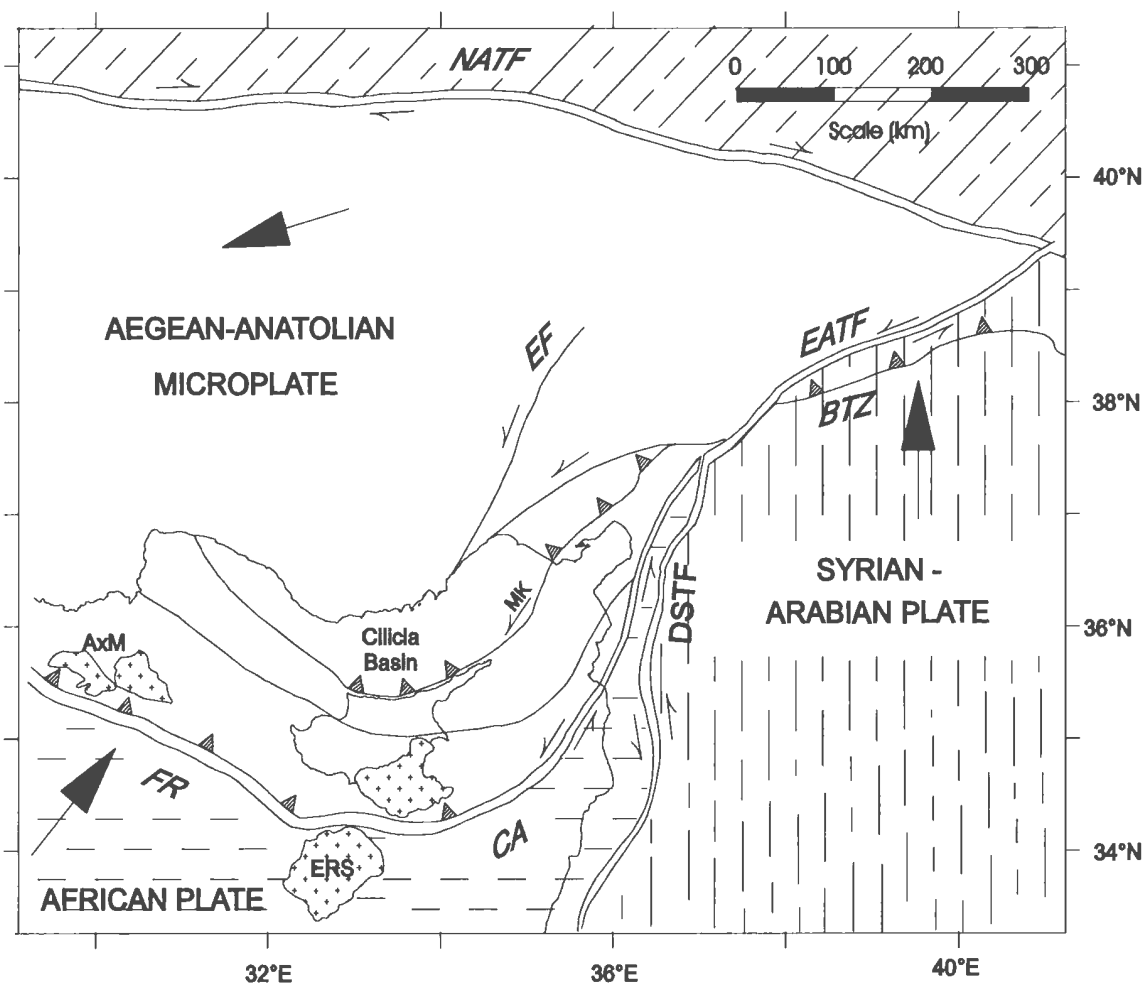


Figure 5.15: Simplified tectonic map of the north-east Mediterranean from Pliocene to present time (edited from Aksu et al., 2005). Map compiled from Sengor and Yilmaz (1981), Hancock and Barka (1981), Dewey et al (1986) AxM=Anaximander mountains, BTZ=Bitlis thrust zone, CA=Cyprus Arc, DSTF=Dead Sea transform, EATF=East Anatolian transform fault, EF=Ecemis fault, ERS=Eratosthenes seamount, MK=Misis Kyrenia thrust belt, NATF=North Anatolian transform fault. Large arrow indicate the sense of plate motion relative to the Eurasian plate; half arrows indicate transform/strike slip faults.

Ceyhan and Taurus and Goksu rivers, which deposit into or just south-west of the Adana basin (Aksu et al., 1992). Any sediment deposited into the basin from the Cyprus margin was most likely derived from erosion of the Kyrenia mountain range. Due to distance from the main sediment source, the Outer Cilicia Basin is relatively underfilled in comparison with the inner part of the basin (Aksu et al., 1992).

Thrusting in the Kyrenia range continued throughout the Pliocene, as evidenced by the geometry of Pliocene sequences over the top of the thrust zones in the offshore extension of the mountain range. Ori and Friend (1984) suggest that the movement of a thrust sheet is also recorded by stratigraphic wedging and unconformities in its associated piggy back basin. Each of the four sequences making up the Pliocene-Quaternary succession in the Outer Cilicia Basin shows wedging or thickening towards the north, suggesting that activity on the Kyrenia thrusts must continue through the Pliocene and up to the present time. The Pliocene also saw activity on the extensional faults at the northern basin margin, resulting primarily from gravity sliding down the steep Turkish shelf.

Subduction processes along the central segment of the Cyprus Arc were interrupted in the early- mid Pliocene, by the collision between the Eratosthenes seamount and Cyprus. This collision has been responsible for the uplift of Cyprus since Pliocene time and, more indirectly, for north-south extension in the Outer Cilicia Basin. With subduction locked to the south, the Anatolian-Aegean microplate rotates counterclockwise to allow subduction along the free-face of the western Hellenic Arc.

This rotation creates an environment of north-south directed extension in the Outer Cilicia Basin and induces extensional activity on the transtensional faults in the northern Outer Cilicia Basin and in the transition zone between the basin and the Anamur-Kormakiti complex.

Progressive tilting of the southern basin margin on the back limb of the Kyrenia thrust front, combined with the progradation of sediment into the southern basin, facilitates the basin-ward flow of salt during Pliocene time. The flow of salt continues through Pliocene-Quaternary time and leads to the formation of salt rollers and listric growth faults in the southern Cilicia Basin as well as salt anticlines and short wavelength folds in the central fold zone. These structures began their development during mid Pliocene-Quaternary time and continue to grow up to the present time.

By early Quaternary time, the majority of fault activity in the northern domain of the Outer Cilicia Basin had ceased. Only the most northerly fault trace of the extensional fault system at the northern basin margin remained active into Quaternary time. Activity on the offshore extensions of the Ecemis and Kozan fault zones also ended before the deposition of the youngest Pliocene-Quaternary sequence. Sequence boundary A acts as an important chrono-stratigraphic boundary marking the end of activity on these splays of the East Anatolian fault. Sedimentation patterns in the northern domain of the Outer Cilicia Basin also changed during Quaternary time. The early sequences of the Pliocene-Quaternary succession are transgressive and represent deposition in a steadily deepening basin. The Quaternary sequences, however, show evidence of progradation, slumping

infilled channels and debris flows. These characteristics are indicative of deposition during a sea level regression. The lack of extensional accommodation on the northern basin margin during the Quaternary, combined with the evidence of sea level regression, suggests that subsidence occurred at relatively slower rate during Quaternary time.

Both the southern margin and Anamur-Kormikiti zone remain structurally active during Quaternary time. In the Anamur-Kormakiti zone, both compressional and transtensional faults are active, continually deforming the Quaternary sediment layers and creating structure on the sea-bed. On the southern margin, the salt structures continue to grow and evolve as the salt layer continuously mobilizes toward the center of the basin.

Chapter 6: Conclusions and Recommendations

6.1 Conclusions

The purpose of this thesis, as stated in section 1.8, was to use reflection seismic data to provide an interpretation of the structurally complex Outer Cilicia Basin. The interpretation of this data provides insight into the evolution of the basin and of the entire Eastern Mediterranean since Miocene time. Using the data outlined on Figure 4.1, the major stratigraphic sequences and structural systems of the Outer Cilicia Basin were defined and described. The basin is dominated by four main stratigraphic sequences, each separated by erosional unconformities: 1) Pliocene-Quaternary aged deep water siliclastics, 2) Messinian aged evaporite, 3) mid- to late-Miocene aged marls and chalks, 4) Oligocene to mid-Miocene aged marls and turbidite deposits. Each of the three youngest sequences was deposited in a piggy back basin setting on the back limb of the Kyrenia thrust system. The oldest sequence was deposited in a foredeep setting in front of the Tauride thrust front, prior to major thrust fault activity along the Kyrenia Range.

The present day structure of the Outer Cilicia Basin results from a long history involving both contractional and extensional tectonics, largely affected by a ductile salt layer. In Chapter 5, the structural systems were divided into two groups based on fundamental differences in the forces that control their development. The first group are the structures that develop primarily due to far-field forces, generated by surrounding plate interactions. This group includes: 1) normal faults at basin margins (fault sets A and J), 2) transtensional faults in both the northern Outer Cilicia Basin and the transition

zone to the Anamur-Kormakiti complex (fault sets D, K and L), and 3) south to south-west verging compressional faults. These structures form independently of each other, in response to the far-field forces, with minor influence from the basin's morphology at the time of their development. For example, the faults at the basin margins evolved due to a combination of strike-slip accommodation, induced by the westward escape of the Anatolian microplate, and surficial sediment sliding down steep basin margins. The second set of structures are those that develop primarily due to salt tectonics. This group includes: 1) late- Miocene- aged northward-verging thrust fault systems (fault sets C and H), 2) salt cored anticlines and folds in the central fold zone , and 3) thin-skinned, listric normal faults in the southern Outer Cilicia Basin (fault set I). These structures form as parts of an inter-related system controlled by the basin-ward movement of salt, primarily driven by gravitational forces and, in some cases, progradational loading.

Studying the relationship between the deposition of the sedimentary sequences and the formation of the structural systems allows a fairly concise basin-wide description of the Neogene evolution of the Outer Cilicia Basin, as described in Section 5.3. The Neogene evolution involved two main phases of deformation: a compressional phase during Miocene time and a transtensional phase during Pliocene-Quaternary time. In Miocene time, the main forces affecting the basin were north-south directed compression resulting from north-south convergence along the Cyprean Arc. The change from compressional to transtensional forces coincides with the initiation of westward escape and rotation of the Aegean-Anatolian microplate near the end of Miocene time (Şengör et

al., 1979,1981,1985). Since that time, the Outer Cilicia Basin has been dominated by transtensional structures, which provide accommodation for the strain induced by the escape and rotation of the microplate. South of the Outer Cilicia Basin, compressional structures continue to dominate the Pliocene-Quaternary succession, onshore Cyprus (Robertson, 1998 a). The transtensional fault zone at the southern basin margin, therefore, acts as a boundary between a primarily contractional domain to the south and a transtensional domain to the north.

6.2 Recommendations

The seismic reflection data available from the Outer Cilicia Basin allows a fairly detailed interpretation of the late Miocene- to Quaternary- aged sequences and correlation of most major structures in the basin. A detailed interpretation of the earlier sequences, however, is prevented by a relatively short seismic record length and lack of seismic resolution at depth. If this area was revisited, some changes could be made to seismic acquisition parameters to increase the resolution below the Messinian salt layer. Larger air guns would increase the signal strength and allow deeper penetration. A larger source-receiver offset or additional receiver channels would also enhance the systems ability to image deep structures. Larger offsets would also increase a seismic processor's ability to remove multiple energy, which cloud over primary reflectors in some key areas.

The seismic coverage of the Outer Cilicia Basin limits the ability to map in the structurally complex areas of the basin, such as the Anamur-Kormikiti zone. Even with increased data volume in this area, the structures are still quite difficult to correlate. A detailed multi-beam bathymetry survey could act as a cheaper alternative to multi-channel seismic in this area, as most of the structures are presently active and have prominent sea-floor expression. The combined interpretation of multi-beam bathymetry and multi-channel seismic data, should give an improved 3-dimensional view of this zone and allow inferences into the evolution of the western part of the Outer Cilicia Basin.

References

- Akay, E., Uysal, S., Poisson, A., Cravette, J., Müller, C., 1985. Antalya Neojen havzasının stratigrafisi. *Bulletin of the Geological Society of Turkey*, 28:105-119.
- Aksu, A. E, Calon, T.J., Hall, J., Mansfield, S., Yaşar, D., 2005. The Cilicia-Adana basin complex, Eastern Mediterranean: Neogene evolution of an active fore-arc basin in an obliquely convergent margin. *Marine Geology*, 221: 121-159.
- Aksu, A.E., Calon, T.J., Piper, D.J.W, Turgut, S, Izdar, E.K., 1992 a. Architecture of late orogenic basins in the eastern Mediterranean Sea. *Tectonophysics*, 210: 191-213.
- Aksu, A.E., Uluğ, A., Piper, D.J.W., Konuk, T.Turgut, S., 1992 b. Quaternary sedimentary history of Adana, Cilicia and Iskenderun Basins, Northeast Mediterranean Sea. *Marine Geology*, 104: 55-71.
- Anastasakis, G., Kelling, G., 1991. Tectonic connection of the Hellenic and Cyprus arcs and related geotectonic elements. *Marine Geology*, 97: 261-277.
- Backus, M.M., 1959. Water Reverberations- their nature and elimination: *Geophysics*, 24, 233-261.
- Ben Avraham, Z., Kempler, D., Ginzburg, A., 1988. Plate convergence in the Cyprean Arc. *Tectonophysics*, 146: 231-240.
- Ben Avraham, Z., Tibor, G., Limanov, A.F., Leybov, M.B., Ivanov, M.K., Tokarev, M.Yu., Woodside, J.M., 1995. Structural and tectonics of the eastern Cyprus Arc. *Marine and Petroleum Geology*, 12: 263-271.
- Ben Avraham, Z., Zobac, M.D., 1992. Transform-normal extension and asymmetric basins: an alternative to pull-apart models. *Geology*, 20: 423-426.
- Biju-Duval, B., Letouzey, J., Montadert, L., 1978. Structure and evolution of the Mediterranean Basins. In K. Hsü, L. Montadert, et al., *Initial Reports of the Deep Sea Drilling Project*, V. 42, Part 1, U.S. Government Printing Office, Washington D.C.: 951-984.
- Bohnhoff, M., Makris, J., Papanikolaou, G., Stavrakakis, G., 2001. Crustal investigation of the Hellenic subduction zone using wide aperture seismic data. *Tectonophysics*, 343: 239-262.

Bridge, C., 2004. Structure and salt tectonics of Messinian evaporites in the Cilicia Basin, eastern Mediterranean. Memorial University of Newfoundland and Labrador, Msc. thesis.

Butler, R.W.H. 1982. The terminology of structures in thrust belts. J. Struct. Geol., 4: 239-245.

Calon, T.J., Hall, J., Aksu, A.E., 2005 a. The Oligocene-Recent evolution of the Mesaoria Basin (Cyprus) and its western marine extension, Eastern Mediterranean. Marine Geology, 221: 95-120.

Calon, T.J., Aksu, A.E., Hall, J., 2005 b. The Neogene evolution of the Outer Latakia and its extension into the Eastern Mesaoria Basin (Cyprus), Eastern Mediterranean. Marine Geology, 221: 61-94.

Christie-Blick, Nicholas, Biddle, K.T., 1985. Deformation and basin formation along strike-slip faults. In: Biddle, K.T., and Christie-Blick, Nicholas, eds., Strike-slip deformation, basin formation, and sedimentation: Society of Economic Paleontologists and Mineralogists Special Publication, 37:1-34.

DeMets, C., Gordon, R.G., Argus, D.F., Stein, S., 1990. Current plate motions. Geophysics Journal International, 101: 425-478.

Dewey, J.F., Hempton, M.R., Kidd, W.S.F., Şaroğlu, F., Şengör, A.M.C., 1986. Shortening of continental lithosphere: the neotectonics of eastern Anatolia - a young collision zone. In: M.P. Coward and A.C. Ries (Eds.), Collision Tectonics. Geological Society Special Publication 19: 3-36.

Dilek, Y., Moores, E.M., 1990. Regional tectonics of the eastern Mediterranean ophiolites. In: J. Malpas, E. M. Moores, A. Panayiotou and C. Xenophontos. *Ophiolites; oceanic crustal analogues; proceedings of the symposium "Troodos 1987"*. Nicosia, Cyprus, Minist. Agric. and Nat. Resour: 295-309.

Ediger, V., Okyar, M., Ergin, M., 1993. Seismic stratigraphy of the fault controlled submarine canyon/valley system on the shelf and upper slope of Anamur Bay, Northeastern Mediterranean Sea. Marine Geology, 115: 129-142.

Ediger, V., Evans, G., Ergin, M., 1997. Recent surficial shelf sediment of the Cilician Basin (Turkey), northeastern Mediterranean. Continental Shelf Research, 17, 13: 1659-1677.

Ergün, M., Okay, S., Sari, C., Oral, E., Ash, M., Hall, J., Miller, H., 2005. Gravity anomalies of the Cyprus Arc and their tectonic implications. *Marine Geology*, 221: 349-358.

Evans, G., Morgan, P., Evans, W.E., Evans, T.R., Woodside, J.M., 1978. Faulting and halokinetics in the northeastern Mediterranean between Cyprus and Turkey. *Geology*, 6: 392-396.

Fort, X., Brun, J.P., Chauvel, F., 2004. Salt tectonics on the Angolan margin, synsedimentary deformation processes. *AAPG Bulletin*, 88, 11: 1523-1524.

Ge, H., Jackson, M.P.A., Vendeville, C., 1997. Kinematics and dynamics of salt tectonics driven by progradation. *AAPG Bulletin*, 81, 3: 398-423.

Gemmer, L., Ings, S., Medvedev, S., Beaumont, C., 2004. Salt Tectonics driven by differential sediment loading: Stability analysis and finite element experiments. *Basin Research*, 16 :199-218.

Görür, N., Sakiñ, M., Barka, A., Akkör, R., Ersoy, 1995. Miocene to Pliocene paleogeographic evolution of Turkey and its surroundings. *Journal of Human Evolution*, 28: 309-324.

Hall, J., Aksu, A.E., Calon, T.J., Yaşar, D., 2005 a. Varying tectonic control on basin development at an active microplate margin: Latakia Basin, Eastern Mediterranean. *Marine Geology*, 221: 15-60.

Hall, J., Aksu, A.E., Calon, T.J., Yaşar, D., 2005 b. Structural evolution of the Latakia Ridge and Cyprus Basin at the front of the Cyprus Arc, Eastern Mediterranean Sea. *Marine Geology*, 221: 261-297.

Hatcher, R.D., 1995. *Structural Geology* (2nd edition). Englewood Cliffs, New Jersey. Prentice-Hall, 525 p.

Hsü, K.J., Cita, M.B. Ryan, W.B.F., 1978. The origin of the Mediterranean evaporites. *In*: K. Hsü, L. Montadert et al. (Eds.), *Initial Reports of the Deep Sea Drilling Project*, 42(1): 1203-1231, US Government Printing Office, Washington.

Hubert-Ferrari, A., Barka, A., Jacques, E., Nalbant, S.S., Meyer, B., Armijo, R., Tapponnier, P., King, G.C.P., 2000. *Nature*, 404: 269-273.

Huguen, C., Mascle, J., Chaunmillion, E., Woodside, J.M., Benkhelil, J., Kopf, A., Volkonskaiia, A., 2001. Deformational styles of the eastern Mediterranean Ridge and surroundings from combined swath mapping and seismic reflection profiling. *Tectonophysics*, 3432: 1-47.

Ings, S., Beaumont, C., Gemmer, L. 2004. Numerical Modeling of Salt Tectonics on Passive Continental Margins: Preliminary assessment of the Effects of Sediment Loading, Buoyancy, Margin Tilt, and Isostasy. 24th Annual GCSSEPM Foundation Bob F. Perkins Research Conference proceedings: 36-68. (On CD Rom - ISSN: 1544-2462).

Intergovernmental Oceanographic Commission (IOC), 1981. International Bathymetric Chart of the Mediterranean. Published by the Head Department of Navigation and Oceanography, Russia under the authority of IOC, 10 sheets.

Jackson, J., Mckenzie, D., 1988. The relationship between plate motions and seismic moment tensors, and the rates of active deformation in the Mediterranean and Middle east, *Geophys. J. R. Astron. Soc.*, 93: 45-73.

Jackson, M.P.A, 1995. Retrospective salt tectonics, in M.P.A Jackson, D.G. Roberts and S. Snelson, eds, *Salt tectonics: a global perspective: AAPG Memoir*, 65: 1-28.

Jackson, M.P.A, Talbot, C.J., 1991. A glossary of salt tectonics. Bureau of Economic Geology. *Geological circular* 91-4: 1-44.

Jackson, M.P.A., Vendeville, B.C., 1994. Regional extension as a geological trigger for diapirism. *Geol. Soc. Ann. Bull.*, 106: 57-73.

Jaffey, N., Robertson, A.H.F., 2001. New sedimentological and structural data from the Ecemis fault zone, southern Turkey: implications for its timing and offset and Cenezoic tectonic escape of Anatolia. *Journal of the Geological Society, London*, 158: 367-378.

Karabıyıjoglu, M., Ciner, A., Monod, O., Deynoux, M., Tuzcu, S., Orçen, S., 2000. Tectonosedimentary evolution of the Miocene Manavgat Basin, western Taurides, Turkey. In: E. Bozkurt, J.A. Winchester and J.D.A. Piper (Eds.), *Tectonics and Magmatism in Turkey and the surrounding area*. Geological Society of London, Special Publication, 173: 271-294.

Karig, D.E., Kozlu, H., 1990. Late Paleogene - Neogene evolution of the triple junction region near Maraş, south-central Turkey. *Journal of the Geological Society, London*, 147: 1023-1034.

- Kelling, G., Gökçen, S.L., Floyd, P.A., Gökçen, N., 1987. Neogene tectonics and plate convergence in the eastern Mediterranean: new data from southern Turkey. *Geology*, 15: 425-429.
- Kempler, D., Garfunkel, Z., 1994. Structure and kinematics in the northeastern Mediterranean: a study of irregular plate boundary. *Tectonophysics*, 234: 19-32.
- Ketin, I., 1988. Comparison between the tectonic units of Cyprus and the southern Taurus-Amanos Mountains. *Metu Journal of Pure and Applied Sciences*, 21, 1-3: 169-182.
- Kiratzi, A., 1993. A study on the active crustal deformation of the North and East Anatolian fault zones. *Tectonophysics*, 225: 191-203.
- Koçyiğit, A., Beyhan, A., 1998. An intracontinental transcurrent structure: the Central Anatolian Fault Zone, Turkey. *Tectonophysics*, 284: 317-336.
- Koyi, H., 1996. Salt flow by aggrading and prograding overburdens. *Geological Society Special Publication*, 100: 243-258.
- Lallemant, S., Truffert, C., Jolivet, L., Henry, P., Chamot-Rooke, N., De Voogd, B., 1994. Spatial transition from compression to extension in the Western Mediterranean Ridge accretionary complex. *Tectonophysics* 234: 33-52.
- Lazear, G.D., 1993, Mixed Phase wavelet estimation using fourth order cumulants: *Geophysics*, 58: 1042-1051.
- Le Pichon X., Angelier, J., 1979. The Hellenic arc and trench system: a key to the neotectonic evolution of the eastern Mediterranean area. *Tectonophysics*, 60:1-42.
- Lyberis, N. 1988. Tectonic Evolution of the Gulf of Suez and the Gulf of Aqaba. *Tectonophysics*, 153: 209-220.
- Lyberis, N., Yurur, T., Chorowicz, J., Kaspoglu, E., Gundogdu, N., 1992. The East Anatolian Fault: an oblique collisional belt. *Tectonophysics*, 204: 1-15.
- Masclé, J., Jongsma, D., Campredon, R., Dercourt J., Glaçon, G., Lecleach, A., Lyberis, N., Malod, J.A., Mitropoulos, D., 1982. The Hellenic margin from eastern Crete to Rhodes: Preliminary Results. *Tectonophysics*, 86: 133-144.

Masclé, A., Le Cleac'h, A., Jongsma, D., 1986. The Eastern Hellenic margin from Crete to Rhodes: Example of progressive collision. *Marine Geology*, 73: 145-168.

McClusky, S., Balassanian, S., Barka, A., Demir, C., Ergintav, S., Georgiev, I., Gurken, O., Hamburger, M., Hurst, K., Kahle, H., Kastens, K., Kekelidze, G., King, R., Kotzev, V., Lenk, O., Mahmoud, S., Mishin, A., Nadariya, M., Ouzounis, A., Paradissis, D., Peter, Y., Prilepin, M., Reilinger, R., Sanli, I., Seeger, H., Tealeb, A., Toksoz, M.N., Veis, G., 2000. Global Positioning system constraints on plate kinematic and dynamics in the eastern Mediterranean and Caucasus. *Journal of Geophysical Research*, 105: 5695-5719.

Mitchum, R.M., Vail, P.R., Sangree, J.B., 1977. Seismic stratigraphy and global changes of sea level, part 6: stratigraphic interpretation of seismic reflection patterns in depositional sequences. In: Payton, C.E. (ed.) *Seismic Stratigraphy-Applications to Hydrocarbon Exploration*. American Association of Petroleum Geologists, Memoirs, 26: 17-133.

Mulder, C.J., Lehner, P., Allen D.C.K., 1975. Structural evolution of the Neogene salt basins in the eastern Mediterranean and the Red Sea. *Geologie en Mijnbouw*, 54: 208-221.

Nur, A., Ben-Avraham, Z., 1978. The Eastern Mediterranean and the Levant: tectonics of continental collision. *Tectonophysics*, 46: 297-311.

Oral, M.B., Reilinger, R.E., Toksöz, M.N., King, R.W., Barka, A.A., Kinik, I., Lenk, O., 1995. Global positioning system offers evidence of plate motions in Eastern Mediterranean. *Eos. Trans. Am. Geophys. Union*, 76, 2: 9-13.

Ori, G.G., Friend, P.F., 1984. Sedimentary basins formed and carried piggyback on active thrust sheets. *Geology*, 12: 475-478.

Özer, B., Bijou-Duval, B., Courrier, P., Letouzey, J., 1974. Geology of Neogene Basins of Antalya, Mut and Adana. *In: Proceedings of the 3rd Petroleum Congress of Turkey*, Turkish Association of Petroleum Geologists, p. 57-84.

Papazachos, B.C., 1999. Seismological and GPS evidence for the Aegean-Anatolia interaction. *Geophysical Research Letters*, 26, 17: 2653-2656.

Papazachos, B.C., Karakostas, V.G., Papazachos, C.B., Scordilis, E.M., 2000. The geometry of the Wadati-Benioff zone and lithospheric kinematics in the Hellenic Arc. *Tectonophysics*, 319: 275-300.

Papazachos, B.C., Papaioannou, Ch.A., 1999. Lithospheric boundaries and plate motions in the Cyprus area. *Tectonophysics*, 308: 193-204.

Perinçek, D., Çemen, I., 1990. The structural relationship between the East Anatolian and Dead Sea fault zones in southeastern Turkey. *Tectonophysics*, 172: 331-340.

Perinçek, D., Eren, A.G., 1990. Origin of the Amik Basin within the strike-slip East Anatolian and Dead Sea fault zones. *In: Proceedings of the 8th Petroleum Congress of Turkey*, Turkish Association of Petroleum Geologists, p. 180-192

Peters, J. M., Hudson, J., 1985. The Pliny and Strabo trenches: Integration of Seismic Reflection data and seabeam Bathymetric maps. *Marine Geology*, 64: 1-17.

Prodehl, C., Fuchs, K., Mechie, J., 1997. Seismic-refraction studies of the Afro-Arabian rift system - a brief review. *Tectonophysics*, 278: 1-13.

Promax 3D reference guide, 1998. A reference guide for Promax geophysical processing software, v.1 and v. 2

Reilinger, R.E., McClusky, S.C., Oral, M.B., King, R.W., Toksoz, M.N., Barka, A.A., Kinik, I., Lenk, O., Sanli, I., 1997. Global positioning system measurements of present-day crustal movements in the Arabia-Africa-Eurasia plate collision zone. *Journal of Geophysical Research*, 102, B5: 9983-9999.

Riad S., Refai, E., Ghalib, M., 1981. Bouger Anomalies and crustal structure in the eastern Mediterranean. *Tectonophysics*, 71: 253-266.

Robertson, A.H.F., 1998 a. Mesozoic-Tertiary tectonic evolution of the easternmost Mediterranean area: integration of marine and land evidence. *In: A.H.F. Robertson, K.-C. Emeis, C. Richter and A. Camerlenghi (Eds.), Proceeding of the Ocean Drilling Program, Scientific Results 160: 723-782.*

Robertson, A.H.F., 1998 b. Tectonic significance of the Eratosthenes Seamount: a continental fragment in the process of collision with a subduction zone in the eastern Mediterranean (Ocean Drilling Program leg 160). *Tectonophysics*, 298: 63-82.

Robertson, A.H.F., 1998 c. Formation and destruction of the Eratosthenes seamount, Eastern Mediterranean Sea, and the implications for collisional processes. *In: A.H.F. Robertson, K.-C. Emeis, C. Richter and A. Camerlenghi (Eds.), Proceeding of the Ocean Drilling Program, Scientific Results 160: 681-699.*

Robertson, A.H.F., Dixon, J.E., 1984. Introduction: aspects of the geological evolution of the Eastern Mediterranean. *In*: The Geological Evolution of the Eastern Mediterranean, J.E. Dixon and A.H.F. Robertson (Eds), Geological Society Special Publication 17: 1-74.

Robertson, A.H.F., Eaton, S., Follows, E.J., McCallum, J.E., 1991. The role of local tectonics versus global sea-level change in the Neogene evolution of the Cyprus active margin. *Spec. Publs. Int. Ass. Sediment*, 12: 331-369.

Robertson A.H.F., Woodcock, N.H., 1986. The role of Kyrenia Range lineament, Cyprus, in the geological evolution of the eastern Mediterranean area. *Royal Society of London Philosophical Transactions, Series A*, V. 317: 141-177.

Rosenbaum, G., Lister, G., Duboz, C., 2002. Relative motions of Africa, Iberia and Europe during Alpine orogeny. *Tectonophysics* 359: 117-129.

Rotstein, Y., 1984. Counterclockwise rotation of the Anatolian block. *Tectonophysics*, 108: 71-91.

Rotstein, Y., Kafka, A., 1982. Seismotectonics of the southern boundary of Anatolia, Eastern Mediterranean Area: subduction, collision and arc jumping. *Journal of Geophysical Research*, 87, B9: 7694-7706.

Royden, L., 1993. The tectonic expression of slab pull at continental convergent boundaries. *Tectonics*, 12: 303-325.

Ryan, W.B.F., Hsü, K.J., et al., 1973. *Init Repts. DSDP*, 13 (pts. 1 and 2), Washington (U.S. Govt printing office)

Sachpazi, M., Hirn A., Clement, C., Haslinger, F., Laigle, M., Kissling, E., Charvis, P., Hello, Y., Lepine, J.C., Sapin, M., Ansorge, J., 2000. Western Hellenic subduction and Cephalonia Transform: local earthquakes and plate transport and strain. *Tectonophysics*, 319: 301-319.

Şaroğlu, F., Emre, O., Kuşçu, I., 1992. The East Anatolian fault zone of Turkey. *Annales Tectonicae* special issue, supplement to Volume VI: 99-125.

Schultz-Ela, D.D., Jackson, M.P.A., 1996. Relation of subsalt structures to suprasalt structures during extension. *American Association of Petroleum Geologists Bulletin*, 80, 12:1896-1924.

Şengör, A.M.C., 1979. Northern Anatolian fault: its age offset and tectonic significance. *J. Geol. Soc. London*, 136: 269-282.

Şengör, A., Canitez N., 1982. The North Anatolian fault. In: *Alpine Mediterranean Geodynamics*, Eds. Berckhemer H., Hsu K., Geodynamic Series, American Geophysical Union, 7: 205-216.

Şengör, A.M.C., Görür, N., Şaroğlu, F., 1985. Strike-slip faulting and related basin formation in zones of tectonic escape: Turkey as a case study. *Society of Economic Paleontologists and Mineralogists, Special Publication 37*: 227-264.

Şengör, A.M.C., Yılmaz, Y., 1981. Tethyan evolution of Turkey: a plate tectonic approach. *Tectonophysics* 75: 181-241.

Smith, S.G., 1977. Diapiric structures in the eastern Mediterranean Cilicia Basin. *Geology*, 5: 705-707.

Talbot, C.J., 1979. Fold trains in a glacier of salt in southern Iran. *Journal of Structural Geology*, 1: 5-18.

Talbot, C.J., 1981. Sliding and other deformation mechanisms in a glacier of salt, South Iran. In: K.R. McClay and N.J. Price, eds., *Thrust and Nappe Tectonics: Geological Society of London Special Publication*, 9: 173-183.

Talbot, C.J., Jarvis, R.J., 1984. Age, budget, and dynamics of an active salt extrusion in Iran. *Journal of Structural Geology*, 6: 521-533.

Talbot, C.J., Rogers, E.A., 1980. Seasonal movements in a salt glacier in Iran: *Science*, 208: 395-397.

Taviani, M., Rossi, S., 1989. Salt-related deformations in the deep Antalya Basin; preliminary results of the Mac Gan Cruise. *Marine Geology*, 87, 1: 5-13.

Vidal, N., Alvarez-Marron, J., Klaeschen, D., 2000. The structure of the Africa-Anatolia plate boundary in the eastern Mediterranean. *Tectonics*, 19, 4: 723-739.

Wenkert, D.D., 1979. The flow of salt glaciers. *Geophysical Research Letters*, 6: 523-526.

Williams, G.D., Ünlügenç, U.C., Kelling, G., Demirkol, C., 1995. Tectonic controls on stratigraphic evolution of the Adana Basin, Turkey. *Journal of Geological Society of London*, 152: 873-882.

Winsor, J., 2004. The Neogene development of the eastern Mediterranean Sea as manifested in and near the Rhodes Basin : an insight into arc-arc junctions. Memorial University of Newfoundland, Msc thesis.

Woodside, J.M., Mascle, J., Huguen, C., Volkonskaia, A., 2000. The Rhodes Basin, a post Miocene tectonic trough. *Marine Geology*, 165: 1-12.

Woodside, J.M., Mascle, J., Zitter, T.A.C., Limonov, A.F., Ergun, M., Volkonskaia, A., shipboard scientists of the PRISMED II Expedition, 2002. The Florence Rise, the western bend of the Cyprus Arc. *Marine Geology*, 185: 177-194.

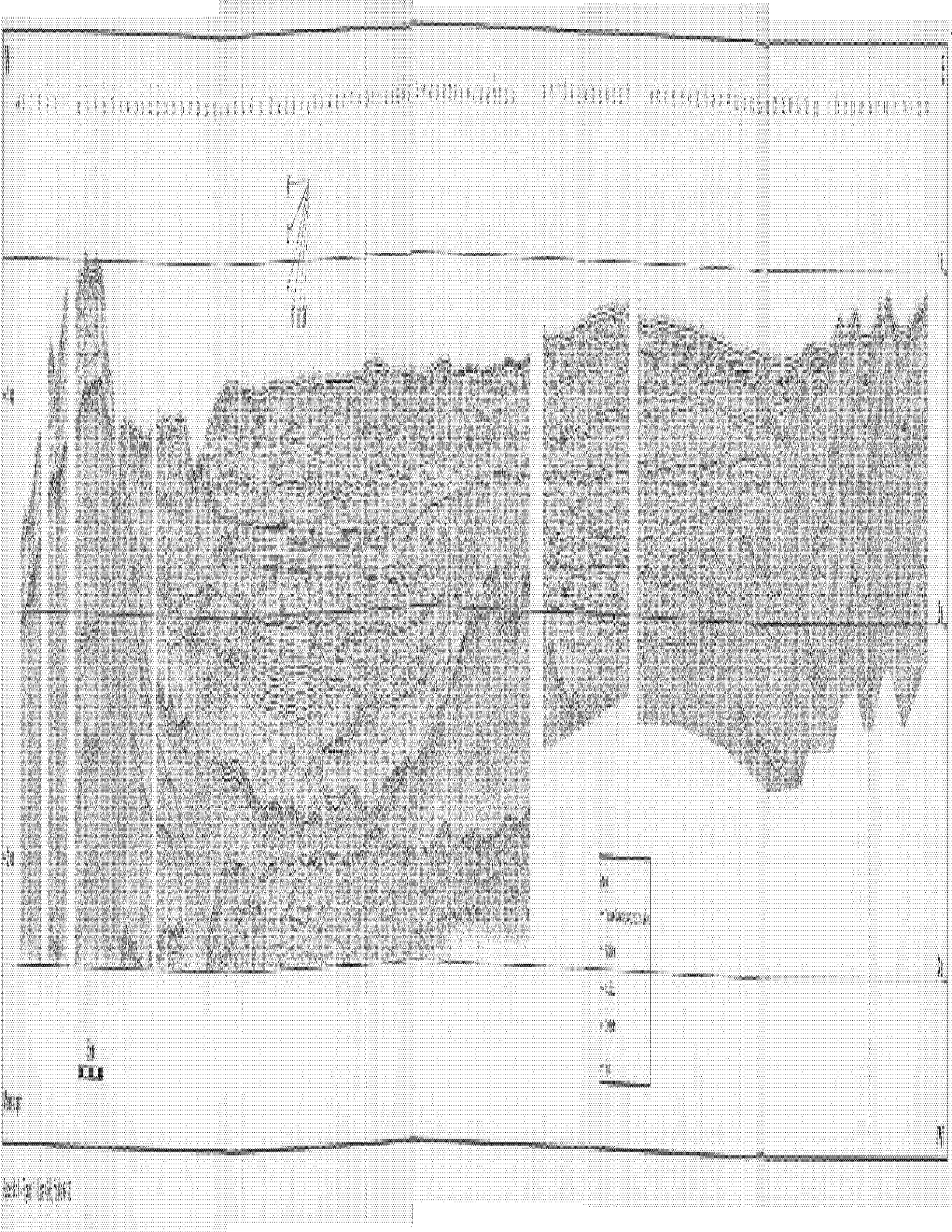
Woodside, J.M., 1977. Tectonic elements and crust of the eastern Mediterranean Sea. *Marine Geophysical Research*, 3: 317-354.

Yalçın, M.N. and Görür, N., 1984. Sedimentological evolution of the Adana basin: Tekeli, O., Göncüoğlu, M.C. ed., *Geology of the Taurus Belt: Proceedings Int. Sym.*, 26-29 Sept., 125-142, Ankara-Turkey.

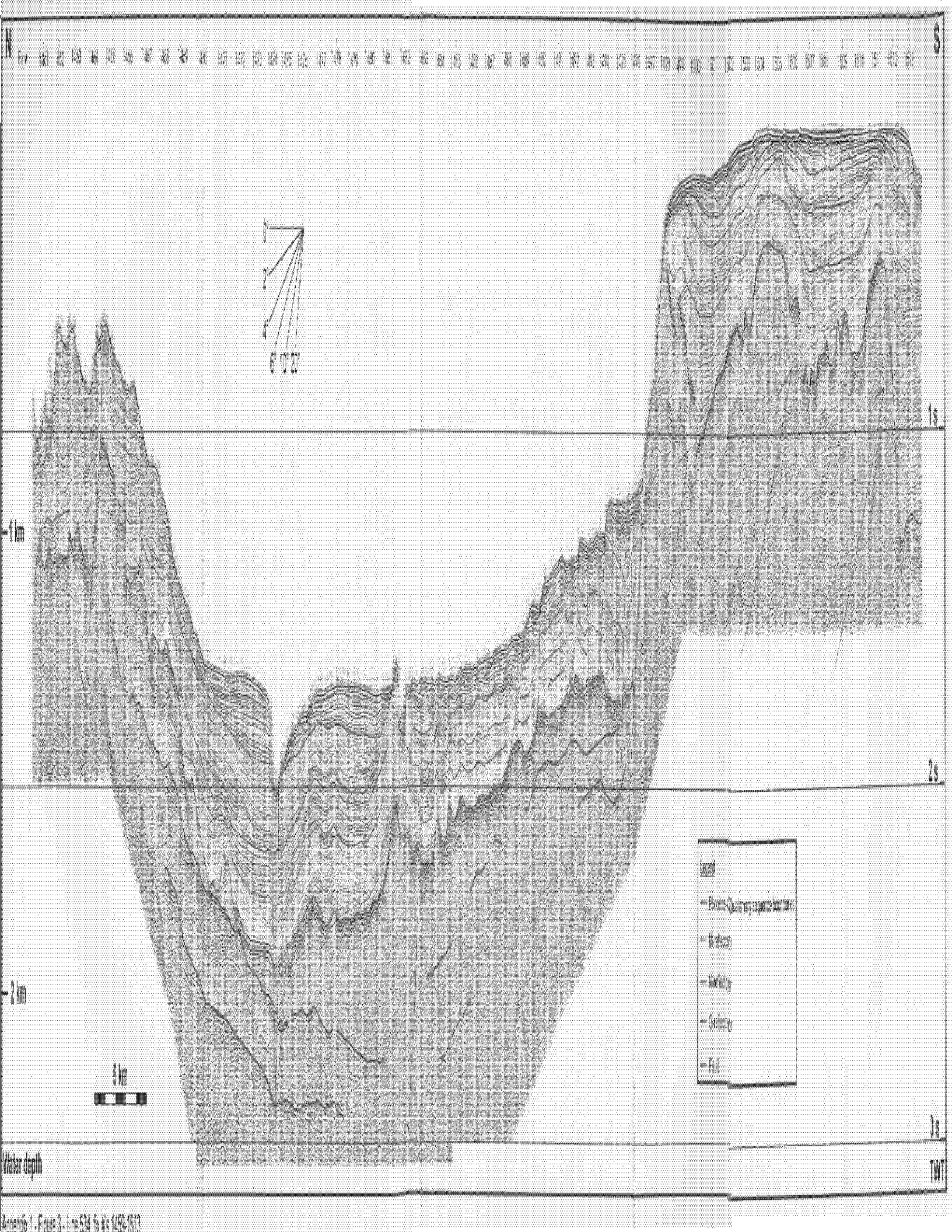
Yetiş, C., Kelling, G., Gökçen, S. I., Baroz, F., 1995. A revised stratigraphic framework for late Cenezoic sequences in the northeastern Mediterranean region. *Geol. Rundsch*, 84: 794-812.

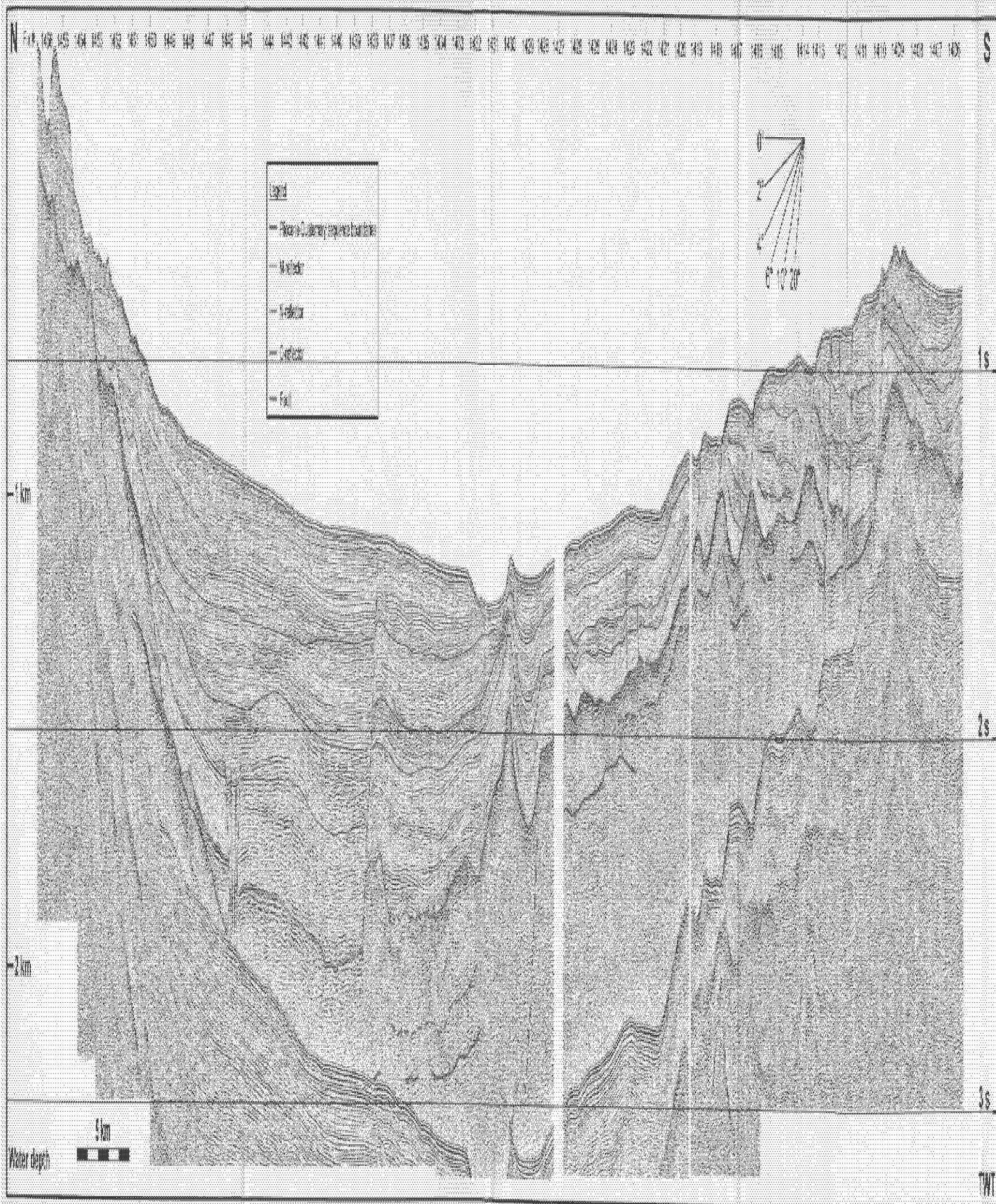
Yilmaz, O., 1987. Seismic data processing. *Society of the Exploration Geophysicists*, Tulsa, Ok. 525p.

Yilmaz, Y., 1993. New evidence and model on the evolution of the southeast Anatolian orogen. *Geological Society of America Bulletin*, 105: 251-271.





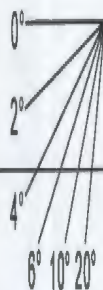
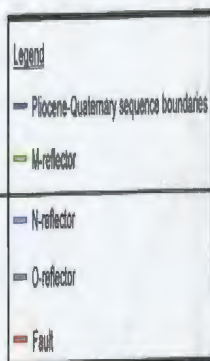




N

S

Fix # 1346 1345 1344 1343 1342 1341 1340 1339 1338 1337 1336 1335 1334 1333 1332 1331 1330 1329 1328 1327 1326 1325 1321 1320 1319 1318 1317 1316 1315 1314 1313 1312 1311 1310 1309 1308 1307 1306 1305 1304



-1 km

1 s

-2 km

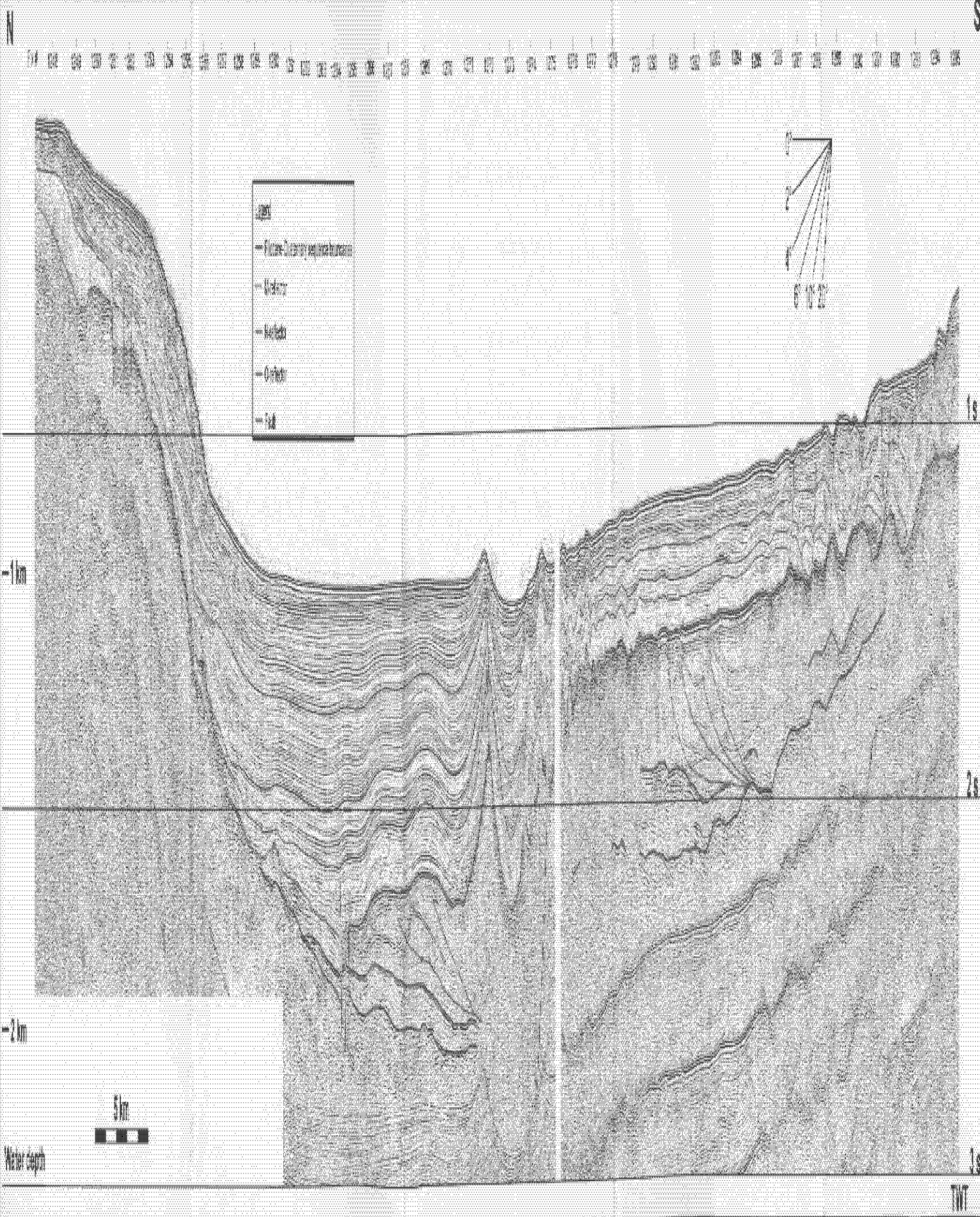
2 s

3 s

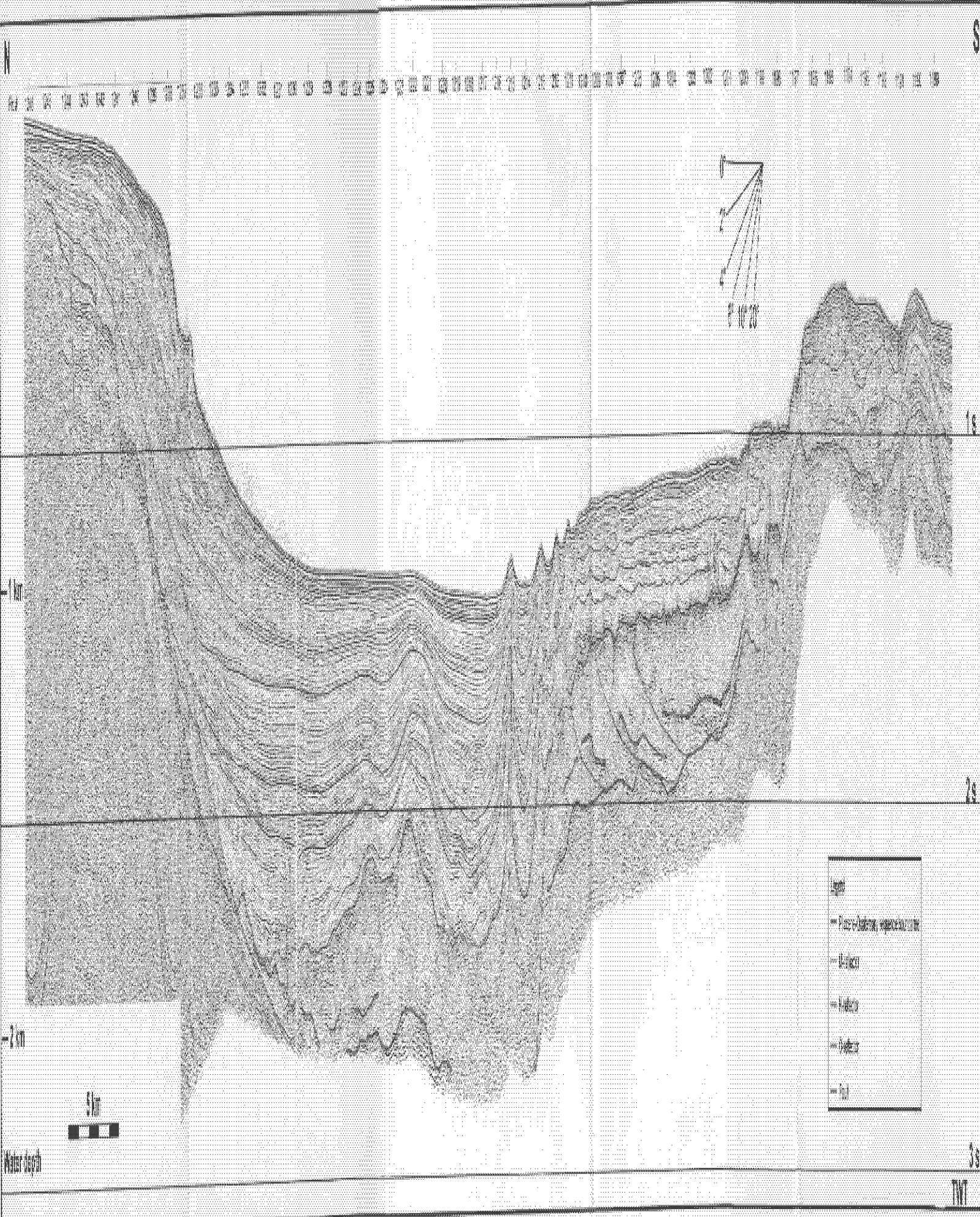
Water depth

5 km

TWT



Appendix 1 - Figure 7 - Line 407 Tr A's 1245-1236



Appendix I - Figure 8 - Line 423, B&W's 1345-1100

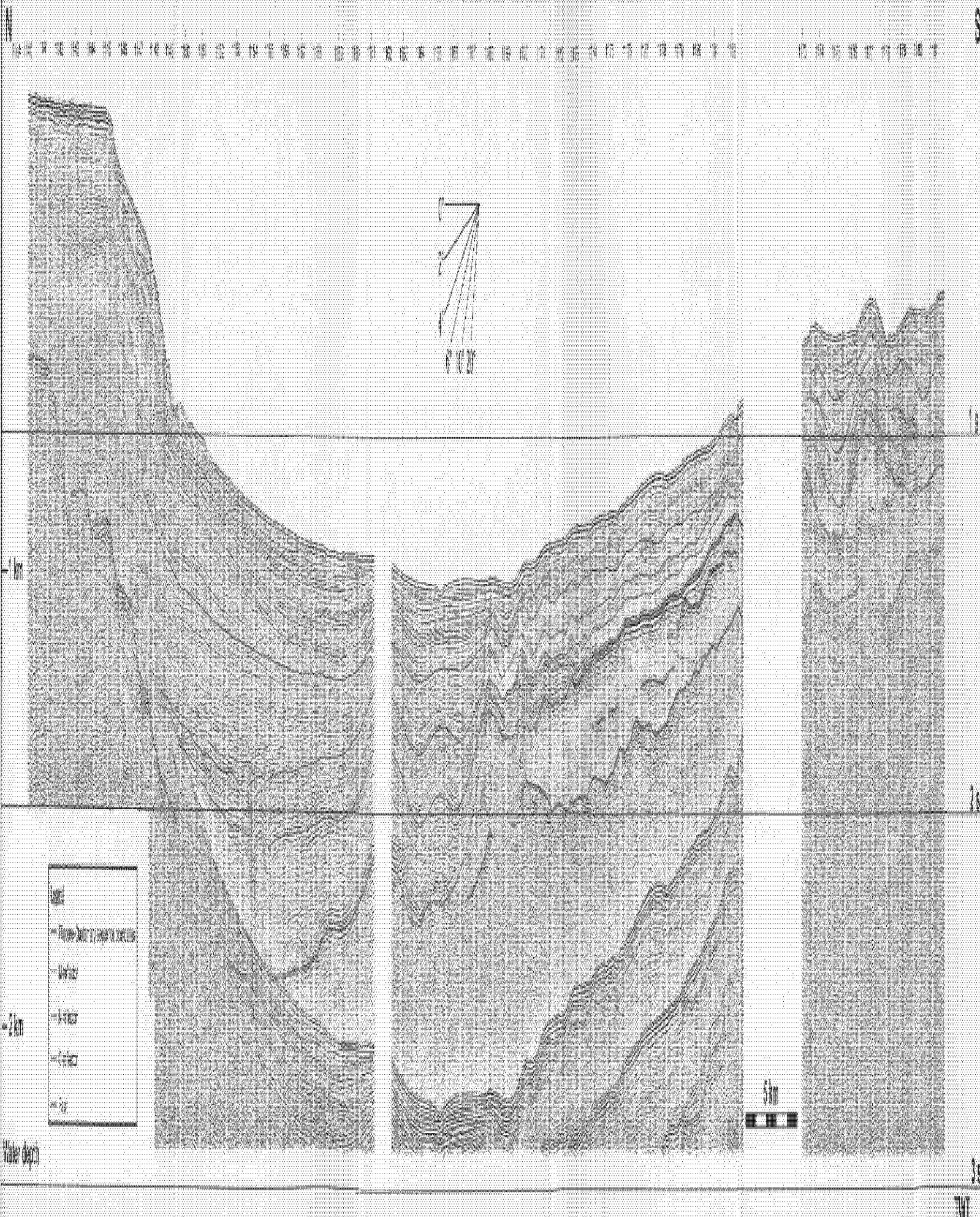
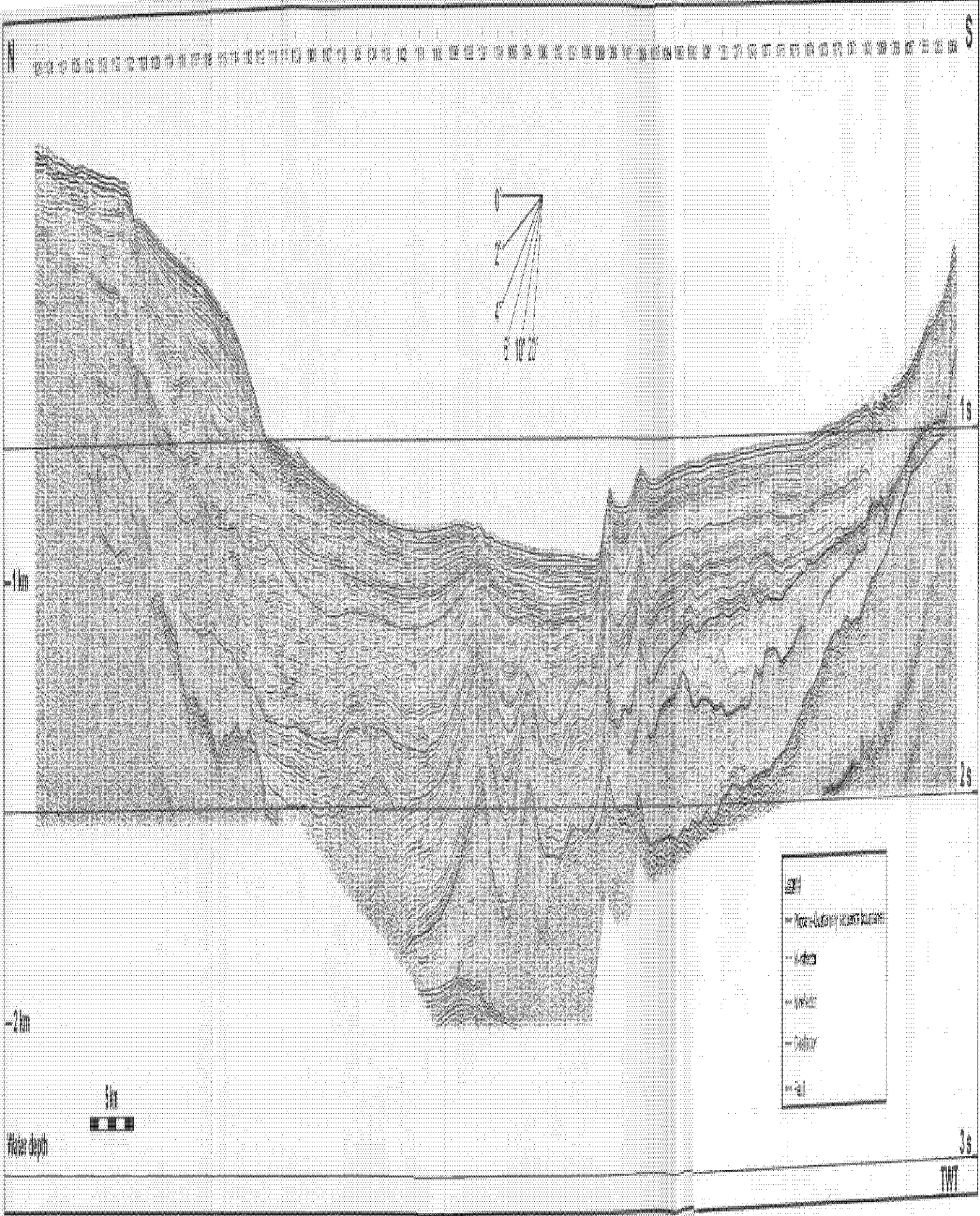


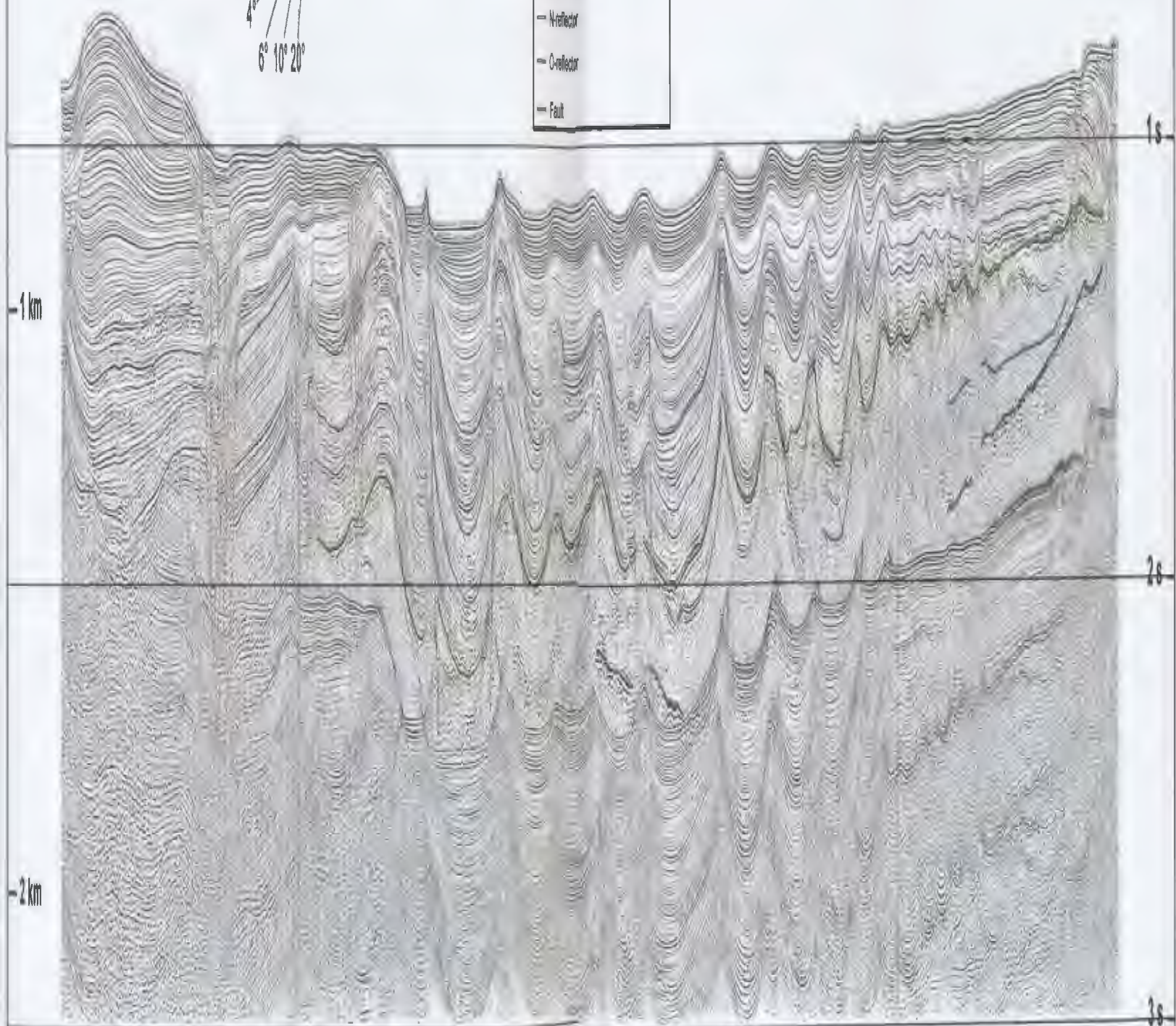
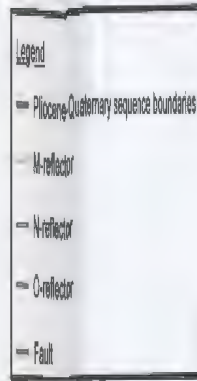
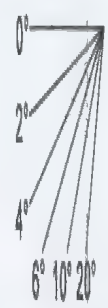
Figure 1. Geological cross-section map of the study area.



N

S

Fix# 1000 1001 1002 1003 1004 1005 1006 1007 1008 1009 1010 1011 1012 1013 1014 1015 1016 1017 1018 1019 1020 1021 1022 1023 1024 1025 1026 1027 1028 1029 1030 1031 1032 1033 1034 1035 1036 1037 1038 1039 1040 1041 1042 1043 1044 1045 1046 1047 1048 1049



1 km

2 km

1s

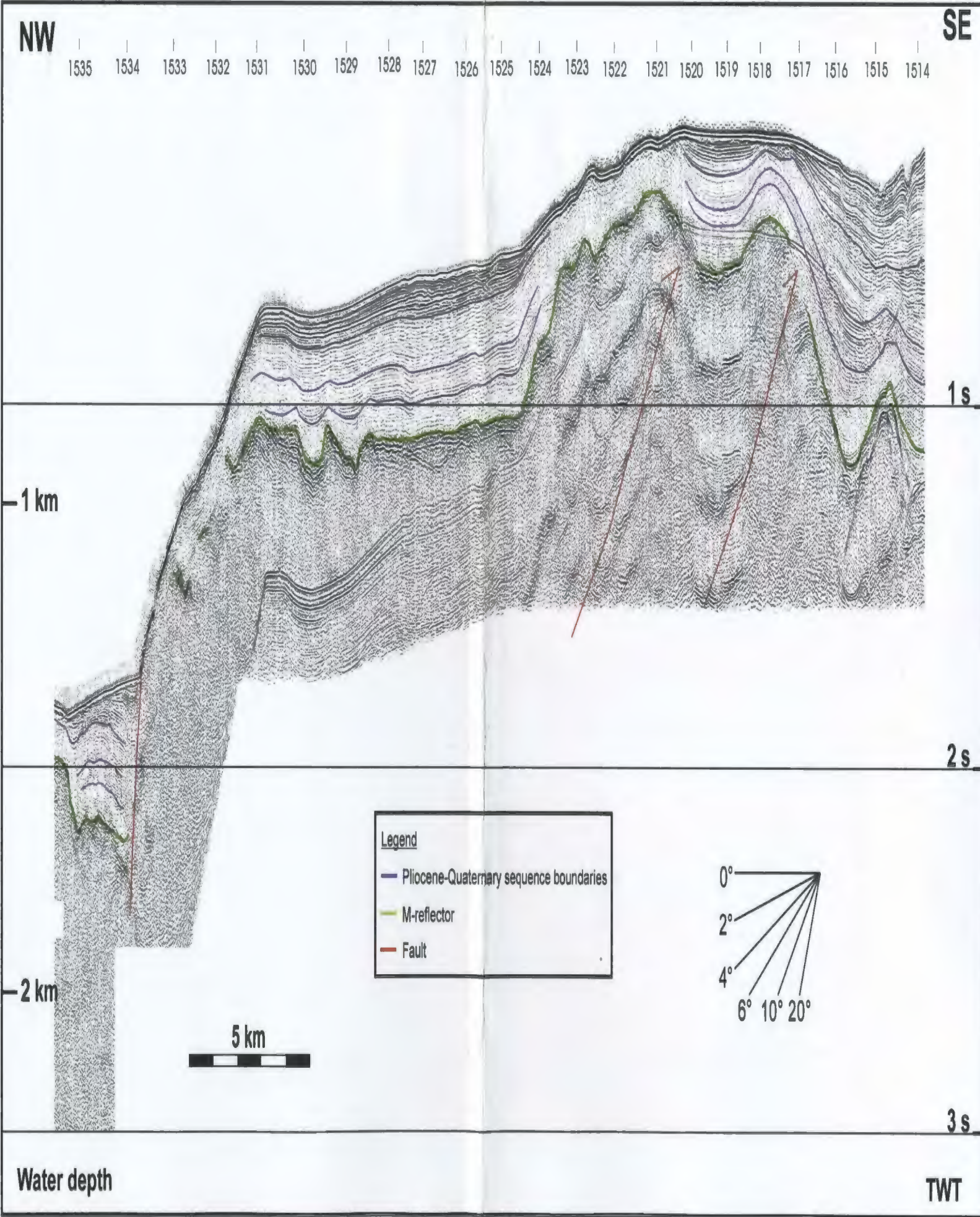
2s

3s



TWT

Appendix 1 - Figure 11 - Line 389, fix #'s 1000-1049

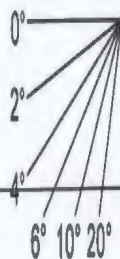
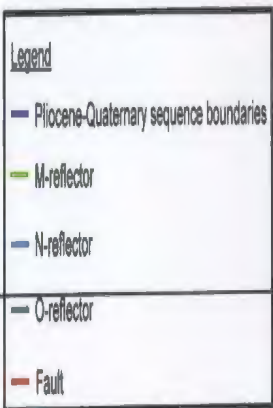


Appendix 1 - Figure 12 - Line 534, fix #'s 1535-1514

NE

SW

Px # 1560 1559 1558 1557 1556 1555 1554 1553 1552 1551 1550 1549 1548 1547 1546 1545 1544 1543 1542 1541 1540 1539 1538 1537 1536 1535



1 km

2 km

1 s

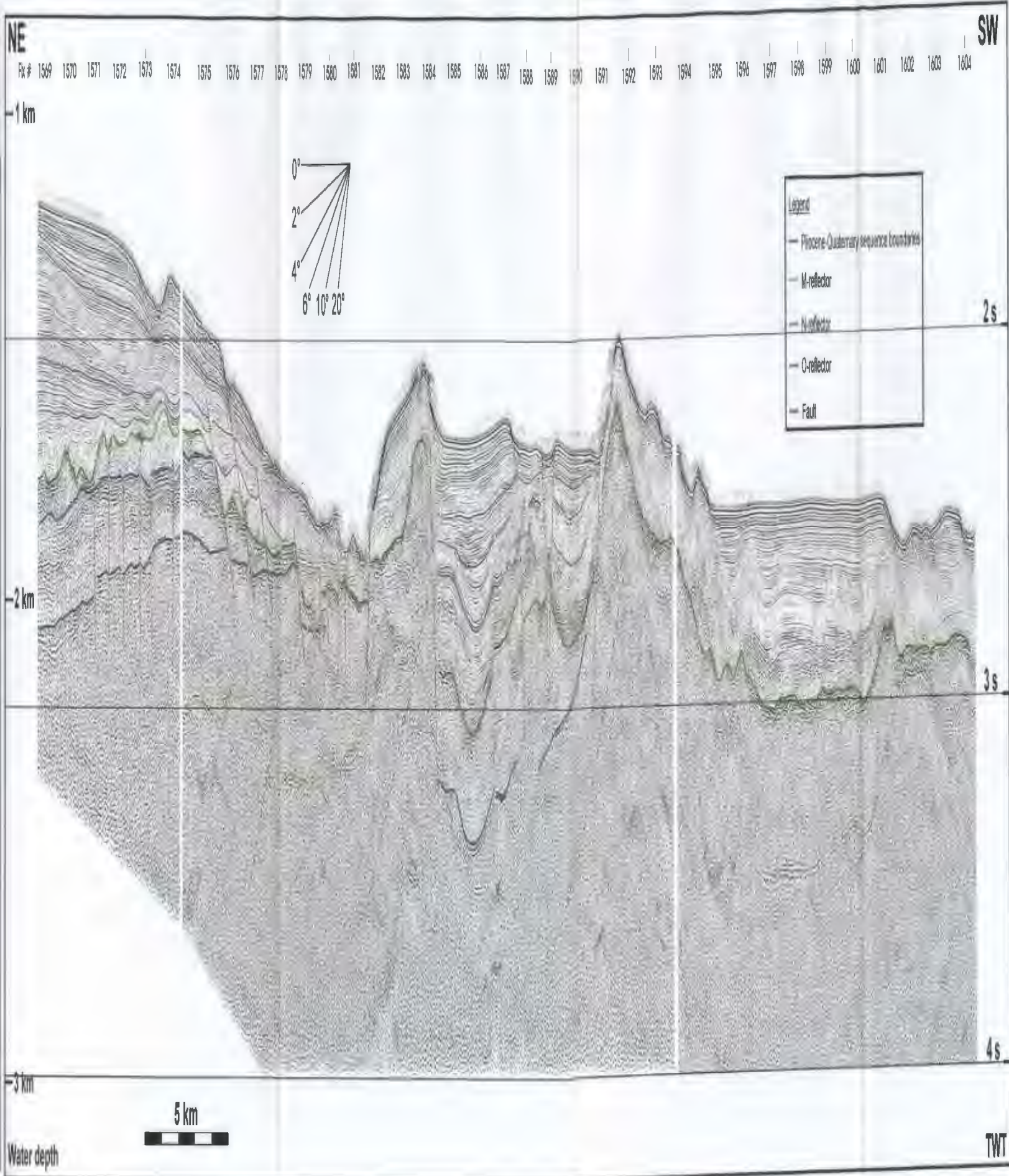
2 s

3 s

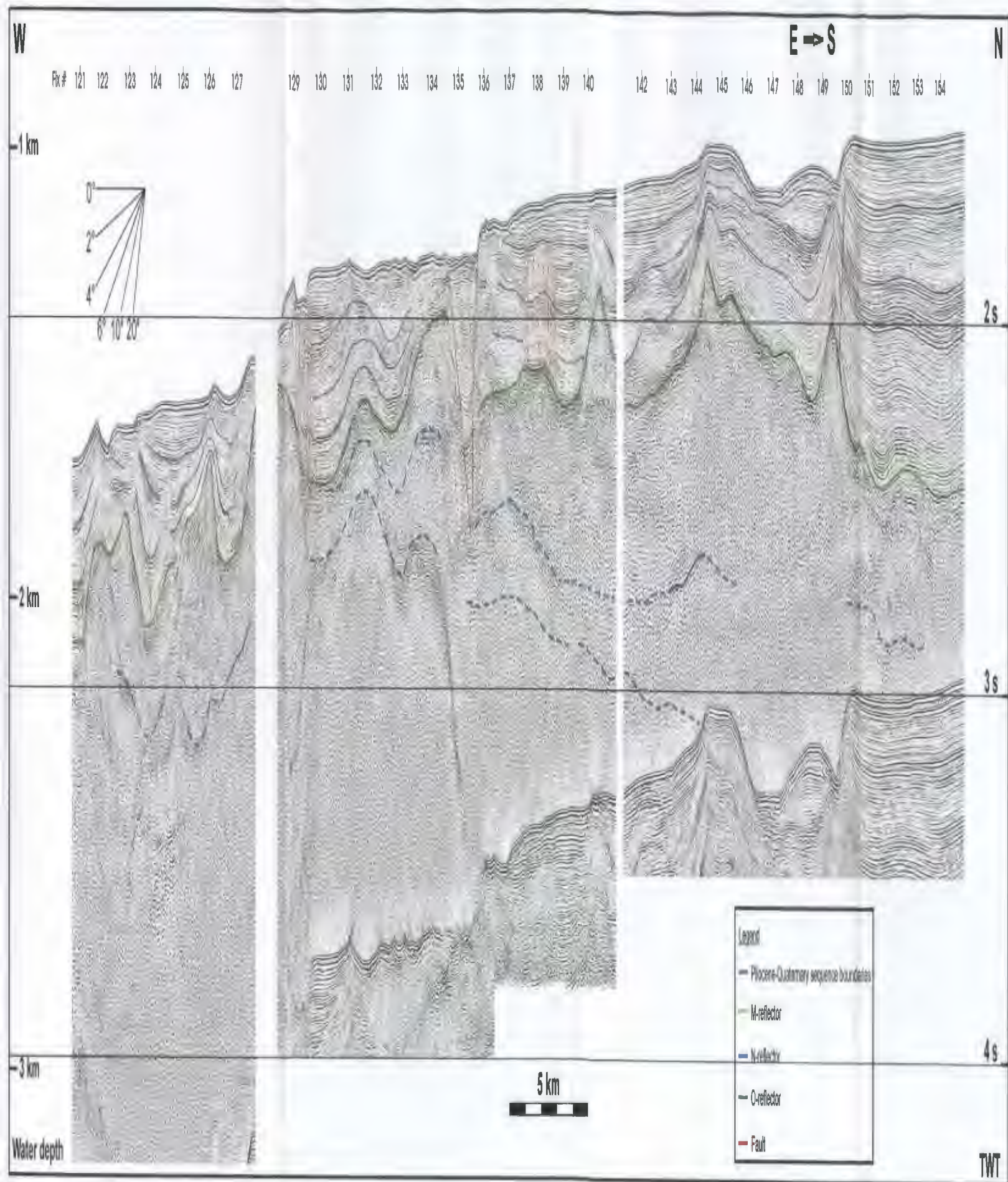
5 km

Water depth

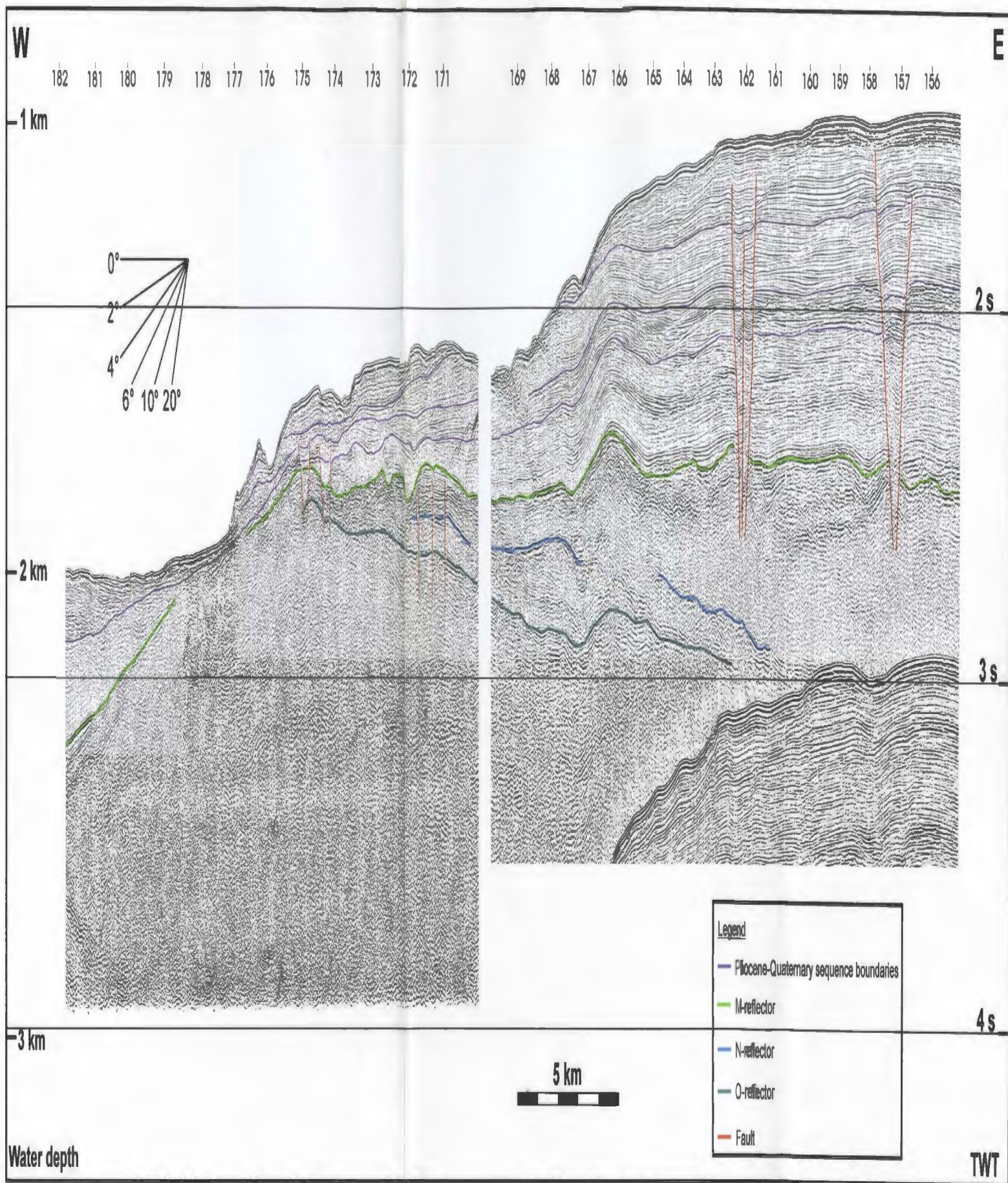
TWT



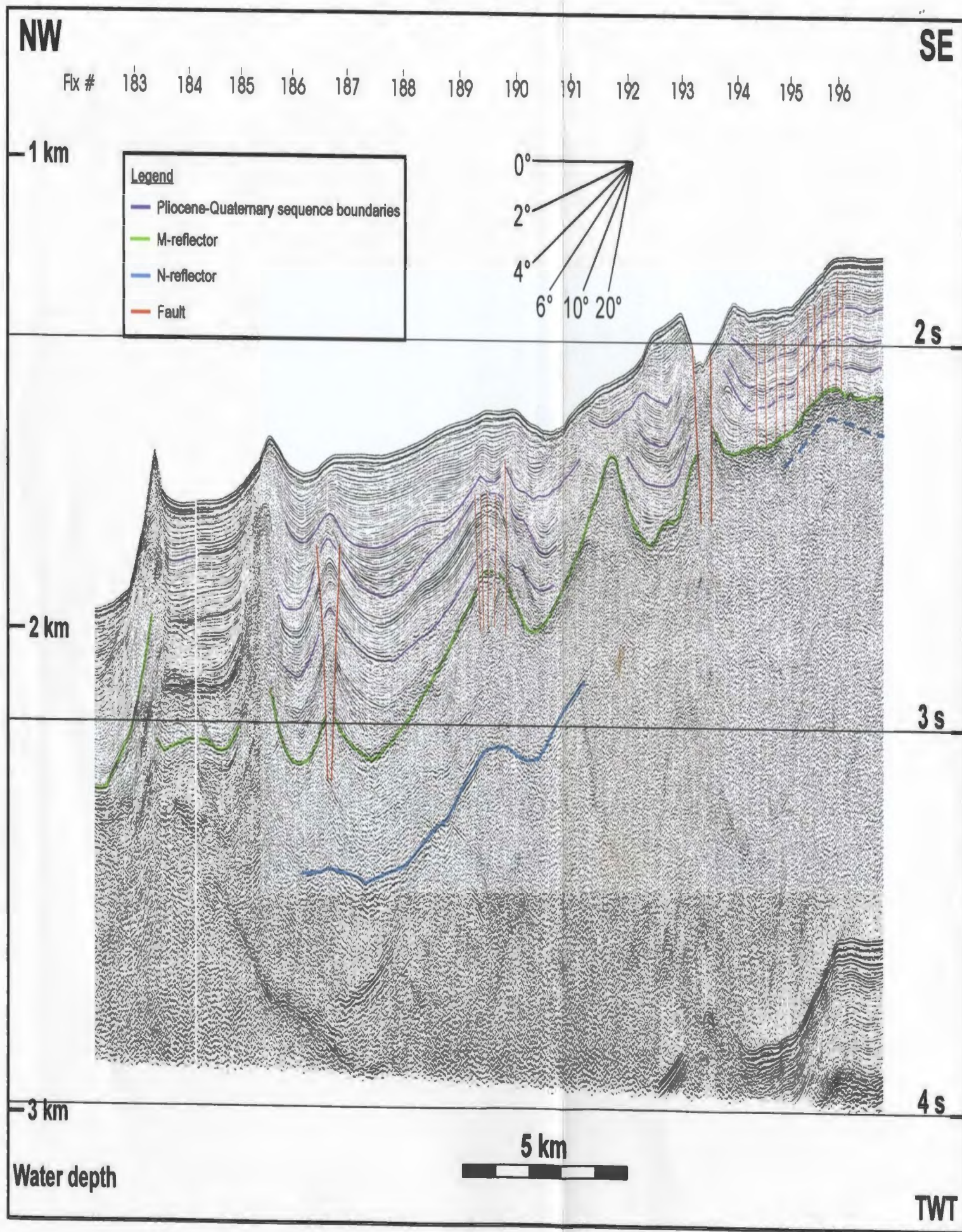
Appendix 1 - Figure 14 - Line 567, fix #'s 1569-1604



Appendix 1 - Figure 15 - Line 23, fix #'s 121-154



Appendix 1 - Figure 16 - Line 23, fix #'s 183-156



Appendix 1 - Figure 17 - Line 23, fix #'s 184-196

TWT

4 s

